Università degli Studi di Ferrara

DOTTORATO DI RICERCA IN SCIENZE DELL'INGEGNERIA

COORDINATORE PROF. STEFANO TRILLO

MODELING OF FRP PULTRUDED STRUCTURES USING LOCKING-FREE FINITE ELEMENTS

DOTTORANDO
DOTT. FABIO MINGHINI

TUTORE
PROF. NERIO TULLINI

TUTORE
DOTT. FERDINANDO LAUDIERO

XX° CICLO

ANNI 2005 - 2007

Modeling of FRP pultruded structures using locking-free finite elements

PhD Thesis by Fabio Minghini

Supervisors:

Prof. Nerio Tullini

Prof. Ferdinando Laudiero

March 2008

Università degli Studi di Ferrara

Dottorato di Ricerca in Scienze dell'Ingegneria

Ingegneria Civile – Tecnica delle Costruzioni

XX ciclo

Examiners:

Prof. Andrea Benedetti, Università di Bologna

Prof. Franco Maceri, Università di Roma "Tor Vergata"

Prof. Simone Secchi, Università di Firenze

Prof. Antonio Tralli, Università di Ferrara

Contents

Introduction

The use of thin-walled composite profiles made of fiber-reinforced polymers (FRP) has been spreading over many engineering applications, especially where characteristics of lightness and durability are of primary importance. In fact, with respect to traditional materials, FRP components may offer significant advantages in assembling, transporting and launching large parts of structures. Moreover, the strong resistance to chemical attacks make them particularly suitable for aggressive environments.

Since the beginning of 1990's, FRP materials, already popular in structural retrofitting, found employment in the field of new structures thanks to the pultrusion technology. The five-story Eyecatcher building (Keller 2002), the footbridges of Aberfeldy (Burgoyne & Head 1993), Pontresina (Keller 1999) and Lleida (Sobrino & Pulido 2002) and, more recently, the 42-meter high tower in Valencia (Rovira *et al.* 2004) probably represent the most noticeable examples in Europe.

Since the year 2003, the research group of Structural Engineering at the University of Ferrara have been studying thin-walled pultruded profiles and their applications. On one hand, numerical simulations of static and dynamic behaviour of FRP composite structures were carried out, and some design proposals for pultruded footbridges (Figs. I.1–I.2, Minghini 2005) and trusses were developed (Dicuonzo *et al.* 2008). On the other hand, experimental analyses of strength and deformability of FRP components were accomplished (Dicuonzo 2008). The acquired know-how addressed the drafting of design code CNR-DT 205/2007, first European example of guidelines entirely devoted to Glass-FRP thin-walled pultruded profiles.

This thesis summarizes the results of three years work on numerical modeling of thin-walled pultruded structures.

…

When dealing with fiber-reinforced plastics, several well-established structural design criteria are to be reconsidered. In fact, performances of FRP pultruded profiles are mainly governed by deformability and buckling phenomena. In particular, the high ratio between longitudinal and transverse shear elastic moduli typically involves local-global instability interaction, closely associated to a significant influence of shear strains. Hence, in the field of numerical formulations, a preliminary 3D modelling becomes necessary to gain insight into the FRP orthotropic behaviour. Nevertheless, when spatial beam assemblages, like bridges and truss structures, are to be analyzed, simple and effective 1D models represent an essential tool to model the structural response. Several researchers developed thin-walled beam models aimed at taking shear

strain effects into account in static and dynamic fields. In general, some cross-section warping functions are introduced in the displacement field (Giavotto *et al.* 1983, Bauchau 1985, Laudiero & Savoia 1990, Park *et al.* 1997, Feo & Mancusi 2005), whereas the exact description requires the solution of an eigenvalue problem (Capurso 1964, De Lorenzis & La Tegola 2003a). On the other hand, in implementing finite element models of spatial assemblages, the continuity conditions of nodal displacements between contiguous beams become more and more complex if many cross-section warping functions are used.

In order to overcome such a drawback, in this work the most simple kinematical model accounting for the shear deformations both due to nonuniform bending and torsion is adopted: i.e. the model based on Timoshenko (1921) bending theory and Reissner (1952) torsion theory, resorting to one single warping function (Gunnlaugsson & Pedersen 1982).

In Chapter 1, Timoshenko-Reissner's model is presented with reference to isotropic beams and its extension to multilayered orthotropic or pultruded profiles is put in evidence. The relationships between strain fields and stress resultants are highlighted, showing that coupling terms between shear resultants and non-uniform torsion may arise due to shear deformations. Analytical solutions to equilibrium equations for profiles subjected to nonuniform bending and torsion are developed. Finally, it is shown that full section properties of FRP pultruded profiles may be estimated using analytical solutions to Timoshenko-Reissner's beam problem in conjunction with experimental results.

In Chapter 2, several displacement interpolation fields based on Timoshenko-Reissner's kinematics are compared (Minghini *et al.* 2005, 2007) with numerical examples found in literature. In particular, some shape functions are obtained from "modified" Hermitian polynomials, that produce a *locking-free* Timoshenko-beam element (Narayanaswami & Adelman 1974). Analogously, numerical interpolations for torsional rotation and cross-section warping are introduced resorting to one Hermitian and six Lagrangian formulations. Analyses of beams with mono-symmetric and non-symmetric cross-section are performed, especially in the presence of coupling terms due to shear deformations, to test convergence rate and accuracy of the different formulations, and underline the decay length of end effects. Profiles made of both isotropic and fiber-reinforced plastic materials are considered. The presented models are compared with beam analytical solutions as well as with results given by 3D numerical models.

Chapter 3 deals with the overall instability analysis of FRP thin-walled beams and frames. In the context of flexural-torsional buckling analysis under lateral forces, it is well-known that a linear displacement field leads, in most cases, to unacceptable over-predictions of the buckling load (Trahair 1993, Kim *et al.* 1996, Pi & Bradford 2001). To overcome this drawback, Timoshenko-Reissner's kinematics is enriched resorting to a second-order approximation (Chang *et al.* 1996) of Rodriguez's tensor of finite rotations (Argyris 1982, Criesfield 1991). The stability conditions are devised by making use of the classical energy criterion which, for practical purposes, reduces to imposing the positive definiteness of the second variation of the total potential energy. Two-node *locking-free* finite elements of the Hermitian family are used. Numerical analyses of orthotropic beams subjected to compressive or lateral forces illustrate

accuracy and convergence properties of the formulation adopted. Finally, buckling analysis of Glass-FRP pultruded frames subjected to in-plane and lateral loads are carried out (Minghini *et al.* 2008a), paying particular attention to the influence of out-of-plane constraint conditions, warping restraints and shear deformations.

In Chapter 4, the same *locking-free* formulation is applied to the vibration analysis of pultruded thin-walled beams and frames (Minghini *et al.* 2008b). Geometric nonlinearities arising from concentrated or distributed surface loads are accounted for. The convergence properties of the adopted element in the presence of flexural-torsional vibrations are highlighted with reference to doubly- and mono-symmetric cross-section Carbon-FRP profiles. Vibration frequencies and mode shapes of Glass-FRP pultruded portal frames are extensively evaluated revealing a frequency crossing between first and second vibration modes at proper values of the applied loads. The influence of frame geometry, shear deformations, participating masses and geometrical effects due to external surface loads is investigated. The chapter ends in a static and dynamic analysis of a GFRP truss footbridge. Buckling and vibration mode shapes are reported and the influence of mass participating to the bridge vibration is emphasized.

Finally, Chapter 5 deals with the modeling of flexible connections in FRP pultruded frames. Joint deformability at beam ends is included by means of a simple manipulation of the elemental stiffness matrix (Shakourzadeh *et al.* 1999). In this way, the joint behaviour associated to membrane, shear, bending and torsion deformations as well as to cross-section warping can be taken into account. The approach is quite general, since any given joint constitutive relation may be implemented. Elastic instability of FRP pultruded portal frames with semirigid connections is analyzed, showing the influence of both in-plane and out-of-plane moment-rotation behaviour of joints, as well as the role played by lateral bracing systems and warping restraints at the column bases.

Figure I.1. Proposal for an FRP footbridge connecting two buildings of the Scientific-Techonolgical Pole of Ferrara University (MSc thesis by Bruzzo PM, Ferrara University 2004).

Figure I.2. Proposals for an FRP footbridge across the river Po di Volano in Ferrara (MSc theses by Bruzzo PM and Minghini F, Ferrara University 2004).

Chapter 1

Linear elastic shear-deformable beams

1.1 Introduction

In order to take shear deformations due to both nonuniform bending and torsion into account, the kinematical model based on Timoshenko (1921) bending theory and Reissner (1952) torsion theory is adopted. The warping function is represented by the well known sectorial coordinate ω deriving from De Saint Venànt solution. Assuming linear elastic behaviour, the relationships between strain fields and stress resultants are obtained for beams with any given cross-section, showing that coupling terms between shear forces acting along the principal directions or between shear and nonuniform torsion may arise due to shear deformations. Then, local governing equations and relevant boundary conditions are deduced variationally from the elastic strain energy expression. The model is particularly tailored to multilayered orthotropic beams, i.e. beams presenting the longitudinal axis coinciding with one of the orthotropy axis, like, for example, the fiber-reinforced plastic (FRP) profiles produced with pultrusion technology. In fact, due to the generally high ratio E/G between longitudinal and transverse shear elastic moduli, these beams may exhibit significant shear strain effects. The beam rigidities for axial, bending, shear and torsion behaviour are evaluated assuming possible differences in staking sequence between web and flange panels, and their expressions are collected in Appendix 1.A.

Analytical solutions to equilibrium equations for profiles subjected to nonuniform bending and torsion are developed. In particular, it is shown that, for open section beams subjected to torsion, neglecting De Saint Venànt contribution enables torsional rotation to be written in polynomial form. Finally, a procedure for the evaluation of the beam full section properties, making use of analytical solutions to Timoshenko-Reissner's problem in conjunction with experimental results, is presented.

1.2 Timoshenko−Reissner's model

An ideal prismatic thin-walled beam is shown in Figure 1.1. An orthogonal, counter-clockwise, reference system $C(x, y, z)$ is assumed, with the origin coinciding with the

cross-section centroid. Axes *x* and *y* correspond to any given couple of orthogonal axes whereas *S* stands for the cross-section shear center. In particular, in this context, point *S* coincides with the classical bending deformation (in the following b.d.) shear center, i.e. the shear center defined by De Saint Venànt's theory (Corradi Dell'Acqua 1992). Moreover (Fig. 1.2), a local reference system $P(n, p)$ is assumed with the origin lying at a given point of the section contour. In-plane displacement components of point *P* in the local reference system are expressed by ξ_P and η_P; moreover, coordinates of point *S* in the local reference system $P(n, p)$ are expressed by:

Figure 1.1. Global reference system.
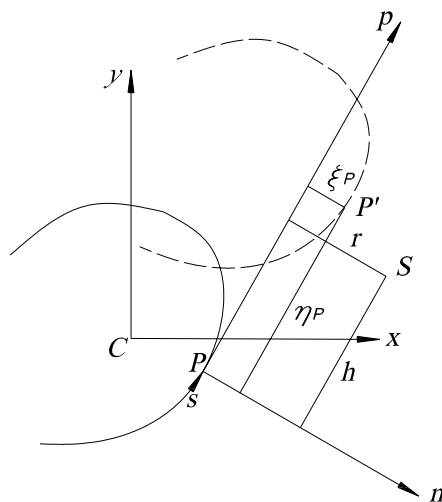
Figure 1.2. Local reference system.

$$r = (x - x_S)\frac{dy}{ds} - (y - y_S)\frac{dx}{ds} \tag{1.1}$$

$$h = (x - x_S)\frac{dx}{ds} + (y - y_S)\frac{dy}{ds} \tag{1.2}$$

where $(dx/ds, dy/ds)$ are contour director cosines at point P.

1.2.1 Kinematical model

Assuming that cross-section in-plane deformations are negligible and reducing the beam to its middle surface, the following kinematical model (Timoshenko 1921; Reissner 1952; Gunnlaugsson & Pedersen 1982; Kim *et al.* 1994; Lin *et al.* 1996) is adopted:

$$u(z,s) = u_S(z) - \varphi_z(z)(y - y_S) \tag{1.3}$$

$$v(z,s) = v_S(z) + \varphi_z(z)(x - x_S) \tag{1.4}$$

$$w(z,s) = w_C(z) - x\varphi_y(z) + y\varphi_x(z) + \omega(s)\Psi(z) \tag{1.5}$$

where u, v, w are the displacement components at point P in x, y, and z directions respectively; u_S and v_S are the shear center displacements in x and y directions; w_C is the cross-section translation due to an axial force; φ_x and φ_y are the flexural rotations about x and y axes, respectively, whereas φ_z represents the torsional rotation about the shear center axis. Finally, function $\omega(s)$ in Eq. 1.5 is the De Saint Venànt warping function whereas $\Psi(z)$ defines the cross-section warping amplitude. In particular, in the case of open sections, the function $\omega(s)$ is assumed to coincide with the sectorial area with respect to S and can be defined by (Vlasov 1961):

$$\frac{d\omega(s)}{ds} - r(s) = 0 \tag{1.6}$$

where r, Eq. 1.1, is the distance between the b.d. shear center S and the local axis p tangent to the middle line at point P. In the case of closed sections, considering Bredt's solution for the shear stress due to torsion, the function $\omega(s)$ is given by:

$$\frac{d\omega(s)}{ds} = r(s) - \frac{f}{t(s)} \tag{1.7}$$

where f is a shear flow constant and t represents the cross-section thickness. The shear flow constant f is obtained by enforcing the monodromy condition for $\omega(s)$ for the closed circuit (Capurso 1964):

$$\oint \frac{d\omega(s)}{ds} ds = \oint r(s)ds - \oint \frac{f}{t(s)}ds = 0 \tag{1.8}$$

Equation 1.8 may be written as:

$$2\Omega - f\alpha = 0 \tag{1.9}$$

giving $f = 2\Omega/\alpha$, where Ω represents the area contained in the contour and $\alpha = \oint ds/t$.

Making use of Eqs. 1.1, 1.3 and 1.4, displacements in the contour direction can be expressed as follows:

$$\eta_p = u\frac{dx}{ds} + v\frac{dy}{ds} = u_S\frac{dx}{ds} + v_S\frac{dy}{ds} + \varphi_z r \tag{1.10}$$

1.2.2 Strain components and stress resultants

Considering that $\varepsilon_s = \varepsilon_n = 0$ along the section contour and observing (Fig. 1.2) that $\gamma_{sn} = d\xi_P/dp + d\eta_P/dn = 0$, the significant components of the first-order strain field are given by:

$$\varepsilon_z = \frac{\partial w}{\partial z} = w'_C - x\varphi'_y + y\varphi'_x + \omega\Psi' \tag{1.11}$$

$$\gamma_{zs} = \frac{\partial w}{\partial s} + \frac{\partial \eta_p}{\partial z} = \left(u'_S - \varphi_y\right)\frac{dx}{ds} + \left(v'_S + \varphi_x\right)\frac{dy}{ds} + \left(\varphi'_z + \Psi\right)\frac{d\omega}{ds} + \varphi'_z\frac{f}{t} \tag{1.12}$$

where prime denotes derivative with respect to z and the last term in Eq. 1.12 refers to closed sections only. Assuming that σ_s and σ_n are negligible with respect to normal stresses acting in the z direction, the non-vanishing components of the stress tensor reduce to the normal stress σ_z and the tangential stress τ_{zs}. Hence, the following stress resultants can be obtained:

$$N = \int_A \sigma_z dA; \quad M_x = \int_A \sigma_z y dA; \quad M_y = -\int_A \sigma_z x dA; \quad M_\omega = \int_A \sigma_z \omega dA \tag{1.13}$$

$$V_x = \int_A \tau_{zx} dA; \quad V_y = \int_A \tau_{zy} dA \tag{1.14}$$

$$M_z = \int_A \tau_{zs} r dA = \begin{cases} \int_A \tau_{zs}\frac{f}{t} dA + \int_A \tau_{zs}\frac{d\omega}{ds} dA = M_{z,closed}^{Bredt} + M_z^\omega & \text{closed sections} \\ \int_A \tau_{zs}\frac{d\omega}{ds} dA = M_z^\omega & \text{open sections} \end{cases} \tag{1.15}$$

where A represents the cross-section area, N, M_x, M_y and M_ω are the axial force, the bending moments and the bimoment and, finally, V_x, V_y and M_z are the shear forces acting in the x and y directions and the total twisting moment, respectively. In Eqs. 1.14, the shear stresses τ_{zx} and τ_{zy} in the global reference system can be written as:

$$\tau_{zx}(z,s) = \tau_{zs}(z,s)\frac{dx}{ds}; \qquad \tau_{zy}(z,s) = \tau_{zs}(z,s)\frac{dy}{ds} \qquad (1.16)$$

In the case of closed section profiles, the twisting moment turns out to be composed by two contributions. The first contribution, $M_{z,closed}^{Bredt}$ (Eq. 1.15a), is ruled by De Saint Venànt (uniform) torsion and may be expressed resorting to the well-known Bredt relation:

$$M_{z,closed}^{Bredt} = \int_A \tau_{zs}\frac{f}{t}dA = (\tau_{zs}t)_B \oint \frac{f}{t}ds = (\tau_{zs}t)_B \oint r\,ds = 2\Omega(\tau_{zs}t)_B \qquad (1.17)$$

where $(\tau_{zs}t)_B$ represents the Bredt (constant) shear flow. The second contribution, M_z^ω (Eq. 1.15a), depending on function $\omega(s)$, is the twisting moment due to nonuniform torsion, or secondary twisting moment.

In the case of open section profiles, Eq. 1.15b, $M_z = M_z^\omega$. In other words, the present kinematical model, identifying the beam with its middle surface, does not provide the primary (or De Saint Venànt) torsion contribution for open section beams. In fact, as is known, the De Saint Venànt solution for open sections implies a linear shear stress distribution within the thickness, with zero value in correspondence of the middle surface, given by:

$$\gamma_{zs} = 2n\varphi_z' \qquad (1.18)$$

where n (Fig. 1.2) is the local co-ordinate orthogonal to the middle surface. Hence, for open sections, the contribution of primary torsion will be included *a posteriori* (Para. 1.2.3).

1.2.3 Constitutive laws

Indicating with E and G longitudinal and transverse elastic moduli respectively, the components of the stress tensor can be expressed as:

$$\sigma_z = E\varepsilon_z \qquad (1.19)$$
$$\tau_{zs} = G\gamma_{zs} \qquad (1.20)$$

1.2.3.1 Behaviour under axial load, bending and bimoment

Inserting Eq. 1.19 into expression 1.13 for the stress resultants, and considering Eq. 1.11 yield:

$$
\begin{Bmatrix} N \\ M_x \\ M_y \\ M_\omega \end{Bmatrix} = E \begin{bmatrix} A & S_x & -S_y & S_\omega \\ & J_x & -J_{xy} & J_{y\omega} \\ & & J_y & -J_{x\omega} \\ \text{Sym} & & & J_\omega \end{bmatrix} \begin{Bmatrix} w'_C \\ \varphi'_x \\ \varphi'_y \\ \Psi' \end{Bmatrix}
\tag{1.21}
$$

where

$$
S_x = \int_A y\,dA\,; \qquad S_y = \int_A x\,dA\,; \qquad S_\omega = \int_A \omega\,dA
\tag{1.22}
$$

are the first area and sectorial moments, respectively;

$$
J_x = \int_A y^2\,dA\,; \qquad J_y = \int_A x^2\,dA\,; \qquad J_\omega = \int_A \omega^2\,dA
\tag{1.23}
$$

are the second area and sectorial moments and, finally,

$$
J_{xy} = \int_A xy\,dA\,; \qquad J_{x\omega} = \int_A x\omega\,dA\,; \qquad J_{y\omega} = \int_A y\omega\,dA
\tag{1.24}
$$

are the product moments of inertia.

Identifying axes x and y with the principal axes of inertia of the cross-section, i.e. $S_x = S_y = J_{xy} = 0$, the further conditions:

$$
S_\omega = 0\,; \qquad J_{x\omega} = 0\,; \qquad J_{y\omega} = 0
\tag{1.25}
$$

make matrix on the right-hand side of Eq. 1.21 diagonal.

1.2.3.2 Torsional behaviour. Comparison between open and closed sections

In the case of closed sections, using Eq. 1.17 for the Bredt-De Saint Venànt twisting moment, Eq. 1.20 for the shear stress and Eq. 1.12 for the shear deformation, and considering the relations 1.8, 1.9 and:

$$
\oint \frac{dx}{ds}\,ds = \oint \frac{dy}{ds}\,ds = 0
\tag{1.26}
$$

yield the following expression:

$$
M_{z,closed}^{Bredt} = \int_A \tau_{zs} \frac{f}{t}\,dA = G\varphi'_z \int_A \frac{f^2}{t^2}\,dA = G\varphi'_z \oint \frac{f^2}{t}\,ds = GJ_B\varphi'_z
\tag{1.27}
$$

where

$$J_B = \oint \frac{f^2}{t} ds = \frac{\left(\oint rds \right)^2}{\oint ds/t} = \frac{4\Omega^2}{\oint ds/t}$$ (1.28)

is the torsional moment of inertia corresponding to Bredt's shear stress.

   In the case of open sections, the classical De Saint Venànt solution of the uniform torsion problem in terms of shear stress is obtained from Eqs. 1.18 and 1.20. The corresponding stress resultant takes the expression:

$$M_{z,open}^{DSV} = GJ_t \varphi_z'$$ (1.29)

where J_t is the well-known De Saint Venànt torsional rigidity for open sections, given by:

$$J_t = \frac{1}{3} \int_0^a t^3 ds$$ (1.30)

where a indicates the length of the cross-section contour. Therefore, the total twisting moment M_z may always be expressed as the sum of two contributions:

$$M_z = M_z^{uniform} + M_z^{\omega}$$ (1.31)

where $M_z^{uniform} = M_{z,closed}^{Bredt}$ or $M_z^{uniform} = M_{z,open}^{DSV}$ in the case of closed or open section, respectively. On the other hand, differently from beams with open section, torsional behaviour of closed section profiles is governed predominantly by Bredt's torsional rigidity. For example purposes, two beams with rectangular cross-section are shown in Figure 1.3. The height is denoted h, the width b, and the wall thickness t. The only difference between the two beams is that the closed cell (Fig. 1.3a) is changed to the open section (Fig. 1.3b) by a slit along the axis of the beam. The Bredt torsional rigidity of the closed section is provided by Eq. 1.28, giving:

$$J_B = 2t \frac{h^2 b^2}{(h+b)}$$ (1.32)

whereas for the open section using Eq. 1.30 leads to:

$$J_t = \frac{2}{3}(h+b)t^3$$ (1.33)

   The differences between closed and open section in uniform torsion is highlighted by the following ratio (Krenk 1998):

$$\frac{J_B}{J_t} = \frac{3h^2b^2}{(h+b)^2 t^2} \cong \frac{hb}{t^2} \gg 1 \tag{1.34}$$

which for a typical thin-walled beam may be several orders of magnitude. As for the nonuniform torsion behaviour, function $\omega(s)$ (Eqs. 1.6, 1.7 with condition 1.25a) for open and closed sections of Figure 1.3 is reported in Figure 1.4. It should be noted that, for the box-beam (Fig. 1.4b), sectorial coordinate distribution provides a self equilibrating axial stress system (Loughlan & Ata 1997). In particular, for a square box-section ($h = b$), the warping is everywhere zero. In such a case the beam is commonly referred to as a *Neuber tube*. In other words, in a box-beam an applied twisting moment is completely equilibrated by Bredt's shear flow. On the contrary, in open sections, which are generally characterized by a very low De Saint Venànt torsional rigidity, warping torsion rigidity is essential to assure the equilibrium under nonuniform torsion. Hence, in the following, Reissner's formulation for nonuniform torsion will be applied for the analysis of open section beams only, whereas torsional stiffness of closed section beams will be totally entrusted to Bredt's shear flow.

1.2.3.3 Shear deformations associated to shear forces and secondary twisting moment

In the case of open section beams, using Eqs. 1.12, 1.14, 1.15b and 1.20, the following relationship connecting shear forces and secondary twisting moment M_z^ω with shear deformations is readily obtained:
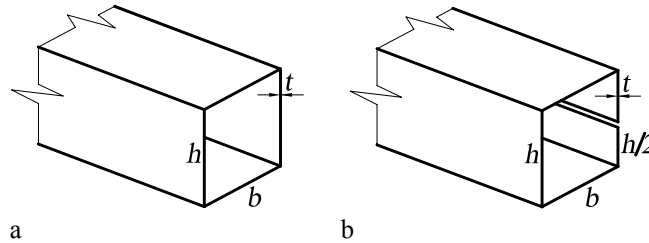
Figure 1.3. Thin-walled beams with (a) closed and (b) open section.

$$|\omega_{closed}| = h/2 \left[b/2 - hb/(h+b) \right] \qquad |\omega_1| = hb \, ; \quad |\omega_2| = 3hb/4 \, ; \quad |\omega_3| = hb/4$$

a   b
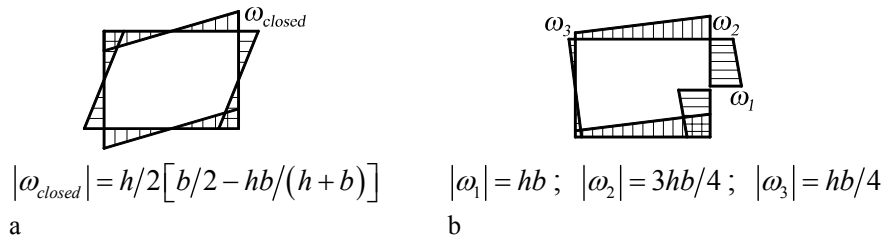
Figure 1.4. Sectorial coordinate distribution (function ω) for the cross-sections of Fig. 1.3.

$$\begin{Bmatrix} V_x \\ V_y \\ M_z^\omega \end{Bmatrix} = G \begin{bmatrix} D_x & D_{xy} & D_{x\omega} \\ & D_y & D_{y\omega} \\ \text{Sym} & & D_\omega \end{bmatrix} \begin{Bmatrix} (u_S' - \varphi_y) \\ (v_S' + \varphi_x) \\ (\varphi_z' + \Psi) \end{Bmatrix} \tag{1.35}$$

where

$$D_x = \int_A \left(\frac{dx}{ds}\right)^2 dA; \qquad D_y = \int_A \left(\frac{dy}{ds}\right)^2 dA; \qquad D_\omega = \int_A \left(\frac{d\omega}{ds}\right)^2 dA \tag{1.36}$$

$$D_{xy} = \int_A \frac{dx}{ds}\frac{dy}{ds} dA; \qquad D_{x\omega} = \int_A \frac{dx}{ds}\frac{d\omega}{ds} dA; \qquad D_{y\omega} = \int_A \frac{dy}{ds}\frac{d\omega}{ds} dA \tag{1.37}$$

Matrix of Eq. 1.35 is in general not diagonal even if axes x and y are identified with the principal directions. In fact, due to shear deformations, off-diagonal terms produce coupling between shear resultants acting into x-z and y-z planes (D_{xy}) and between shear and nonuniform torsion ($D_{x\omega}$, $D_{y\omega}$). In other words, in a shear-deformable beam with generic cross-section, a shear force acting along a principal axis and passing through the b.d. shear center generates an orthogonal shear center displacement component and a torsional rotation. Alternatively, a twisting moment will produce shear center displacements into the principal planes. Off-diagonal terms D_{ij} ($i, j = x, y, \omega$) vanish for doubly-symmetric cross-sections only.

By virtue of Eq. 1.6, shear rigidity D_ω (Eq. 1.36c) associated to nonuniform torsion takes the form:

$$D_\omega = \int_A \left(\frac{d\omega}{ds}\right)^2 dA = \int_A r^2 dA = J_P \tag{1.38}$$

and represents the polar moment of inertia of the cross-section about the shear center.

For closed sections, disregarding the contribution of secondary torsion, Eq. 1.35 becomes:

$$\begin{Bmatrix} V_x \\ V_y \end{Bmatrix} = G \begin{bmatrix} D_x & D_{xy} \\ D_{xy} & D_y \end{bmatrix} \begin{Bmatrix} (u_S' - \varphi_y) \\ (v_S' + \varphi_x) \end{Bmatrix} \tag{1.39}$$

It should be noted that, resorting to Eq. 1.8, shear rigidity D_ω would take the expression:

$$D_\omega = \int_A \left(\frac{d\omega}{ds}\right)^2 dA = \int_A r^2 dA - \int_A \left(\frac{f}{t}\right)^2 dA = J_P - J_B \tag{1.40}$$

know as the "Dirichlet integral" (Baldacci 1983), where J_B is given by Eq. 1.28.

1.2.3.4 Shear flow refinement

Due to the assumed kinematical model, shear strain distribution γ_{zs} provided by Eq. 1.12 may lead to incorrect predictions of the of beam deformability. For example, considering a doubly-symmetric I-section beam subjected to a shear force V_x parallel to the flanges, conditions $dx/ds = 1$ along the flanges and $dx/ds = 0$ along the web would give from Eq. 1.35, by the way of Eq. 1.36a, the following constitutive relation:

$$V_x = GD_x \left(u_S' - \varphi_y \right) = GA_f \left(u_S' - \varphi_y \right) \tag{1.41}$$

where A_f represents the area of the two flanges. The assumption of constant shear strain within the flanges, at the base of Eq. 1.41, makes the shear rigidity $GD_x = GA_f$ overestimated and, consequently, leads to an underestimate of the shear deformation effects. Timoshenko (1921) firstly introduced the concept of shear correction factor. In particular, for rectangular cross-section beams bent into a symmetry plane, he adopted a cross-section area reduced by the factor 2/3. On the other hand, it is to be underlined that the shear factor is not a universal constant for a given cross-section. In fact, it tightly depends on load and restraint conditions and its rigorous evaluation procedure changes according to the particular problem (static or dynamic) to be analyzed. Subsequently, Timoshenko improved his theory (Timoshenko 1922) about vibration problems and provided accurate solutions for rectangular and circular cross-section. Cowper (1966) derived shear factors for various cross-sections with reference to the static problem. In Hutchinson (1981) a highly accurate series solution for a completely free beam of circular cross-section was determined. Leissa and So (1995) developed a Rayleigh-Ritz solution for the circular cross-section and compared their solution to Timoshenko beam theory using Cowper's shear factors. Bert (1973) evaluated the static shear factor for laminated composite cross-section beams with unsymmetric lay-up, giving results consistent with those by Reissner (1972). Bank (1987) and Omidvar (1998) analyzed composite beams made of orthotropic panels and provided useful expressions of the shear factor for commonly used cross-sections. In particular, the formulation of Omidvar reduces to that of Cowper for isotropic material.

It should be recognized that using Timoshenko-Reissner's model requires the definition of shear correction factors associated not only to bending, but also to nonuniform torsion and flexural-torsional coupling due to shear strains. In the following, using classical Vlasov's formulation for the shear stress distribution, the usual procedure, which provides the shear correction factor for a symmetric Timoshenko-beam, is extended to the case of a (isotropic) beam in space.

The virtual work theorem particularized to an infinitesimal beam segment of length *dz* states:

$$\delta L_{v,e} = \delta L_{v,i} \tag{1.42}$$

where $\delta L_{v,e}$ and $\delta L_{v,i}$ indicate external and internal virtual work respectively.

In the presence of both shear resultants and nonuniform torsion, the shear stress distribution in an open section beam is given, in the local reference system *pnz* (Fig. 1.2), by the relation (Vlasov, 1961):

$$\tau_{zs}(z,s) = -\frac{V_x}{J_y t}S_y^* - \frac{V_y}{J_x t}S_x^* - \frac{M_z^\omega}{J_\omega t}S_\omega^* \qquad (1.43)$$

where $S_x^*(s)$, $S_y^*(s)$ and $S_\omega^*(s)$ are the current first area and sectorial moments of the cross-section, given by:

$$S_x^*(s) = \int_0^s ytds'; \qquad S_y^*(s) = \int_0^s xtds'; \qquad S_\omega^*(s) = \int_0^s \omega tds' \qquad (1.44)$$

Using Eq. 1.43, the shear stresses in the global reference system *xyz* can be written as:

$$\tau_{zx}(z,s) = \tau_{zs}(z,s)\frac{dx}{ds}; \qquad \tau_{zy}(z,s) = \tau_{zs}(z,s)\frac{dy}{ds} \qquad (1.45)$$

If two shear forces V_x and V_y (acting at the point S) are alternatively assumed, and the relevant contributions due to shear deformations are considered, left and right hand sides of Eq. 1.42 can be rewritten as follows:

$$dL_{v,e} = V_y\gamma_{zs}(V_x)dz \qquad (1.46)$$

$$dL_{v,i} = dz\int_A \tau_{zs}(V_y)\gamma_{zs}(V_x)dA = dz\int_A \frac{\tau_{zs}(V_y)\tau_{zs}(V_x)}{G}dA \qquad (1.47)$$

Note that, even if V_x and V_y are acting at the b.d. shear centre along principal directions, an orthogonal displacement component will be generated by each resultant due to shear strain effects. Hence, applying the virtual work theorem to the force system V_y, $\tau_{zs}(V_y)$ and to the deformation system $dv_S = \gamma_{zs}(V_x)dz$, $\gamma_{zs}(V_x)$, making use of Eqs. 1.43, 1.46 and 1.47, Eq. 1.42 yields:

$$V_y\gamma_{zs}(V_x) = \frac{1}{G}\frac{V_xV_y}{J_xJ_y}\int_0^a S_x^*S_y^*\frac{ds}{t} = d_{xy}\frac{V_xV_y}{G} \qquad (1.48)$$

Hence, the constitutive relation is finally obtained:

$$\gamma_{zs}(V_x) = \frac{d_{xy}}{G}V_x \qquad (1.49)$$

The outlined procedure (Kim & Kim 2005) provides all the compliance coefficients d_{ij} $(i, j = x, y, \omega)$:

$$d_x = \frac{1}{J_y^2} \int_a S_y^{*2} \frac{ds}{t} ; \qquad d_y = \frac{1}{J_x^2} \int_a S_x^{*2} \frac{ds}{t} ; \qquad d_\omega = \frac{1}{J_\omega^2} \int_a S_\omega^{*2} \frac{ds}{t}$$

$$d_{x\omega} = \frac{1}{J_y J_\omega} \int_a S_y^* S_\omega^* \frac{ds}{t} ; \quad d_{y\omega} = \frac{1}{J_x J_\omega} \int_a S_x^* S_\omega^* \frac{ds}{t} ; \quad d_{xy} = \frac{1}{J_x J_y} \int_a S_x^* S_y^* \frac{ds}{t} \qquad (1.50)$$

Between shear stiffnesses D_{ij} appearing and coefficients d_{ij}, the following relation holds:

$$\begin{bmatrix} D_x & D_{xy} & D_{x\omega} \\ D_{xy} & D_y & D_{y\omega} \\ D_{x\omega} & D_{y\omega} & D_\omega \end{bmatrix} = \begin{bmatrix} d_x & d_{xy} & d_{x\omega} \\ d_{xy} & d_y & d_{y\omega} \\ d_{x\omega} & d_{y\omega} & d_\omega \end{bmatrix}^{-1} \qquad (1.51)$$

where off-diagonal terms D_{ij} vanish for beams having doubly-symmetric cross-section only.

In the case of a closed section beam, the shear stress may be expressed as a sum of two contributions in the form:

$$\tau_{zs}(z,s) = \tau_{zs}^{open}(z,s) + \tau_{zs}^{cut} \qquad (1.52)$$

where τ_{zs}^{open} is the shear stress that would exist if the beam were open because of a longitudinal cut and, disregarding the contribution of nonuniform torsion, is given by:

$$\tau_{zs}(z,s) = -\frac{V_x}{J_y t} S_y^* - \frac{V_y}{J_x t} S_x^* \qquad (1.53)$$

The term τ_{zs}^{cut} in Eq. 1.53 represents a constant shear stress induced by the forces acting along the "cut" edges and is given by (Vlasov 1961):

$$\tau_{zs}^{cut} = -\frac{\oint \tau_{zs}^{open}(z,s) ds/t}{\oint ds/t} \qquad (1.54)$$

Hence, following the same procedure reported for open sections, the virtual work theorem applied to an infinitesimal beam segment leads to the following expressions of shear compliance coefficients:

$$d_x = \oint \tau_{zx}^2 t\, ds ; \qquad d_y = \oint \tau_{zy}^2 t\, ds ; \qquad d_{xy} = \oint \tau_{zx} \tau_{zy} t\, ds \qquad (1.55)$$

1.3 Governing differential equations

A thin-walled beam subjected to a given distribution of external loads is considered. From equilibrium of a beam segment with infinitesimal length dz (Fig. 1.5), the following relations may be written:

$$\frac{\partial N}{\partial z} = -q_z \tag{1.56}$$

$$\frac{\partial V_x}{\partial z} = -q_x \tag{1.57}$$

$$\frac{\partial M_y}{\partial z} = -V_x - m_y \tag{1.58}$$

$$\frac{\partial V_y}{\partial z} = -q_y \tag{1.59}$$

$$\frac{\partial M_x}{\partial z} = V_y - m_x \tag{1.60}$$

$$\frac{\partial M_z}{\partial z} = -m_z \tag{1.61}$$

$$\frac{\partial M_\omega}{\partial z} = M_z^\omega - m_\omega \tag{1.62}$$

where terms multiplied by dz^2 are neglected; q_x, q_y and q_z are distributed external forces in the x, y and z directions, respectively; m_x, m_y and m_z are distributed bending moments about y and x (principal) axes and distributed torsional moment, respectively, and, finally, m_ω represents the distributed bimoment. In the case of beams with open section, remembering Eq. 1.31 and substituting constitutive relations 1.21 (with $S_i = J_{ij} = 0$; $i, j = x, y, \omega$), 1.31 and 1.35 into Eqs. 1.56–1.62, the following set of seven differential equations is obtained:
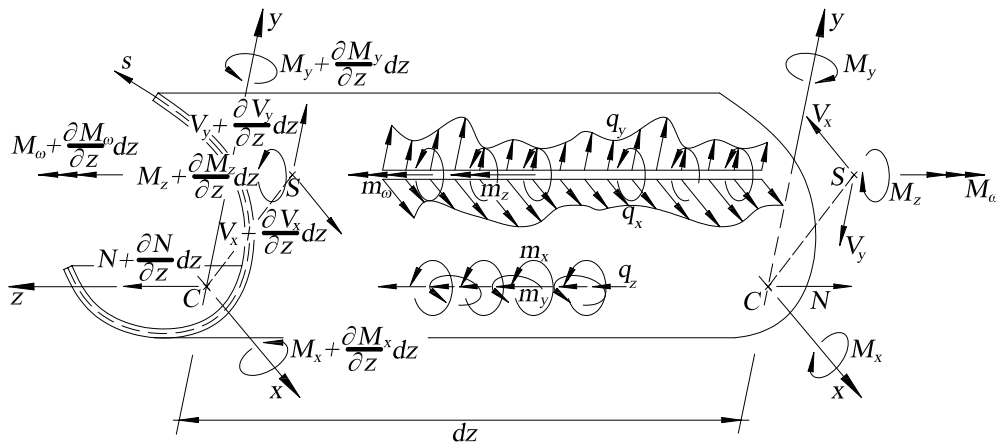
Figure 1.5. Equilibrium of a beam segment under distributed external loads.

$$EAw_C'' = -q_z \tag{1.63}$$

$$GD_x \left(u_S'' - \varphi_y' \right) + GD_{xy} \left(v_S'' + \varphi_x' \right) + GD_{x\omega} \left(\varphi_z'' + \Psi' \right) = -q_x \tag{1.64}$$

$$EJ_y \varphi_y'' + GD_x \left(u_S' - \varphi_y \right) + GD_{xy} \left(v_S' + \varphi_x \right) + GD_{x\omega} \left(\varphi_z' + \Psi \right) = -m_y \tag{1.65}$$

$$GD_{xy} \left(u_S'' - \varphi_y' \right) + GD_y \left(v_S'' + \varphi_x' \right) + GD_{y\omega} \left(\varphi_z'' + \Psi' \right) = -q_y \tag{1.66}$$

$$EJ_x \varphi_x'' - GD_{xy} \left(u_S' - \varphi_y \right) - GD_y \left(v_S' + \varphi_x \right) - GD_{y\omega} \left(\varphi_z' + \Psi \right) = -m_x \tag{1.67}$$

$$GJ_t \varphi_z'' + GD_{x\omega} \left(u_S'' - \varphi_y' \right) + GD_{y\omega} \left(v_S'' + \varphi_x' \right) + GD_\omega \left(\varphi_z'' + \Psi' \right) = -m_z \tag{1.68}$$

$$EJ_\omega \Psi'' - GD_{x\omega} \left(u_S' - \varphi_y \right) - GD_{y\omega} \left(v_S' + \varphi_x \right) - GD_\omega \left(\varphi_z' + \Psi \right) = -m_\omega \tag{1.69}$$

Eqs. 1.63–1.69 represent the equilibrium equations of a shear-deformable thin-walled beam according to Timoshenko-Reissner's theory. In particular, Eq. 1.63, which is uncoupled from each other, is the typical equilibrium equation of a *truss* subjected to a distributed axial load. Eqs. 1.64, 1.65 and 1.66, 1.67 represent the shear-bending problems into *x-z* and *y-z* principal planes, respectively. Finally, Eqs. 1.68 and 1.69 represent the warping-torsion problem.

For doubly-symmetric cross-section beams, the coupling terms of Eq. 1.35 vanish and, consequently, Eqs. 1.63–1.69 reduce to:

$$GD_x \left(u_S'' - \varphi_y' \right) = -q_x \tag{1.70}$$

$$EJ_y \varphi_y'' + GD_x \left(u_S' - \varphi_y \right) = -m_y \tag{1.71}$$

$$GD_y \left(v_S'' + \varphi_x' \right) = -q_y \tag{1.72}$$

$$EJ_x \varphi_x'' - GD_y \left(v_S' + \varphi_x \right) = -m_x \tag{1.73}$$

$$GJ\varphi_z'' + GD_\omega \left(\varphi_z'' + \Psi' \right) = -m_z \tag{1.74}$$

$$EJ_\omega \Psi'' - GD_\omega \left(\varphi_z' + \Psi \right) = -m_\omega \tag{1.75}$$

where Eqs. 1.70–1.71 and 1.72–1.73 are the Timoshenko beam problems referred to *x-z* and *y-z* principal planes, respectively. Due to the lack of coupling terms, these problems and the warping-torsion problem (Eqs. 1.74–1.75) can be solved separately. It should be noted that, neglecting the contribution of primary torsion, the warping-torsion problem for doubly-symmetric cross section beams reduces to the equations

$$GD_\omega \left(\varphi_z'' + \Psi' \right) = -m_z \tag{1.76}$$

$$EJ_\omega \Psi'' - GD_\omega \left(\varphi_z' + \Psi \right) = -m_\omega \tag{1.77}$$

presenting the same structure as the Timoshenko problem of Eqs. 1.70–1.71 (or 1.72–1.73).

For closed section beams, disregarding the contribution of nonuniform torsion, equilibrium equations are given by Eqs. 1.63–1.67 with $D_{x\omega} = D_{y\omega} = 0$.

It is to be underlined that, in the absence of shear deformations, shear resultants and twisting moment due to nonuniform torsion do not descend from shear stresses τ_{zs}. In this case, substituting the first variation of Eqs. 1.58, 1.60 and 1.62 into Eqs. 1.57, 1.59 and 1.61, respectively, considering Eq. 1.29 (open section) and using Eq. 1.21 with $\varphi_y = u_S'$, $\varphi_x = -v_S'$ and $\Psi = -\varphi_z'$ yield:

$$EJ_y u_S'''' = q_x - m_y' \tag{1.78}$$

$$EJ_x v_S'''' = q_y + m_x' \tag{1.79}$$

$$EJ_\omega \varphi_z'''' - GJ_t \varphi_z'' = m_z + m_\omega' \tag{1.80}$$

which are the local equilibrium equations of the Euler-Bernoulli-Vlasov beam theory.

1.3.1 Potential energy

In this section, the functional of the total potential energy will be introduced and it will be shown that equilibrium equations and relevant boundary conditions of Timoshenko-Reissner's model can be derived by making the functional stationary. The potential energy is defined as:

$$\Pi = U - V \tag{1.81}$$

where U represents the elastic strain energy and V is the work made by the external loads. In particular, indicating with ε_{ij} and C_{ijhk} the linear strain tensor and the fourth-order elasticity tensor, respectively, the elastic strain energy may be written as:

$$U = \frac{1}{2} \int_B C_{ijhk} \varepsilon_{ij} \varepsilon_{hk} dV = \frac{1}{2} \int_B \sigma_{ij} \varepsilon_{ij} dV \tag{1.82}$$

where the integrals are extended to the volume of the beam and σ_{ij} represents the Cauchy stress tensor. Bearing in mind strain components 1.11 and 1.12, internal stress resultants 1.13–1.15 and 1.31, constitutive laws 1.19 and 1.20 and, finally, Eqs. 1.16, the elastic strain energy for a beam of length L can be written in the form:

$$\begin{aligned}
U &= \frac{1}{2} \int_B \left(\sigma_z \varepsilon_z + \tau_{zs} \gamma_{zs} \right) dV \\
&= \frac{1}{2} \int_0^L \left[N w_C' + M_y \varphi_y' + M_x \varphi_x' + M_\omega \Psi' + V_x \left(u_S' - \varphi_y \right) + V_y \left(v_S' + \varphi_x \right) \right. \\
&\quad \left. + M_z^\omega \left(\varphi_z' + \Psi \right) + M_z^{uniform} \varphi_z' \right] dz
\end{aligned} \tag{1.83}$$

Making use of constitutive relations 1.21, 1.29 and 1.35 (open section), the following alternative expression of functional U may be derived:

$$U = \frac{1}{2}\int_L E\left(Aw_C'^2 + J_x\varphi_x'^2 + J_y\varphi_y'^2 + J_\omega\Psi'^2\right)dz$$

$$+ \frac{1}{2}\int_L G\left[J\varphi_z'^2 + D_x\left(u_S' - \varphi_y\right)^2 + D_y\left(v_S' + \varphi_x\right)^2 + D_\omega\left(\varphi_z' + \Psi\right)^2\right.$$

$$+ 2D_{xy}\left(u_S' - \varphi_y\right)\left(v_S' + \varphi_x\right) + 2D_{x\omega}\left(u_S' - \varphi_y\right)\left(\varphi_z' + \Psi\right) \tag{1.84}$$

$$\left. + 2D_{y\omega}\left(v_S' + \varphi_x\right)\left(\varphi_z' + \Psi\right)\right]dz$$

With the notations adopted in the previous section, the work of external loads can be written as:

$$V = \int_0^L \left(q_x u_S + q_y v_S + q_z w_C + m_x\varphi_x + m_y\varphi_y + m_z\varphi_z + m_\omega\Psi\right)dz$$

$$+ V_x u_S\big|_0 + V_x u_S\big|_L + V_y v_S\big|_0 + V_y v_S\big|_L + N w_C\big|_0 + N w_C\big|_L + M_x\varphi_x\big|_0 + M_x\varphi_x\big|_L \tag{1.85}$$

$$+ M_y\varphi_y\big|_0 + M_y\varphi_y\big|_L + M_z\varphi_z\big|_0 + M_z\varphi_z\big|_L + M_\omega\Psi\big|_0 + M_\omega\Psi\big|_L$$

As usual in the classical energy criterion, the equilibrium conditions are devised by imposing the stationarity of the potential energy, i.e.:

$$\delta\Pi = 0 \tag{1.86}$$

where symbol δ indicates variation. Substituting Eqs. 1.84–1.85 into Eq. 1.81 and the resulting expression into Eq. 1.86, and performing an integration by part, leads to the local equilibrium equations 1.63–1.69, with the relevant boundary conditions:

$$\left(EAw_C' - N\right)\delta w_C\big|_0^L = 0 \tag{1.87}$$

$$\left[GD_x\left(u_S' - \varphi_y\right) + GD_{xy}\left(v_S' + \varphi_x\right) + GD_{x\omega}\left(\varphi_z' + \Psi\right) - V_x\right]\delta u_S\big|_0^L = 0 \tag{1.88}$$

$$\left(EJ_y\varphi_y' - M_y\right)\delta\varphi_y\big|_0^L = 0 \tag{1.89}$$

$$\left[GD_{xy}\left(u_S' - \varphi_y\right) + GD_y\left(v_S' + \varphi_x\right) + GD_{y\omega}\left(\varphi_z' + \Psi\right) - V_y\right]\delta v_S\big|_0^L = 0 \tag{1.90}$$

$$\left(EJ_x\varphi_x' - M_x\right)\delta\varphi_x\big|_0^L = 0 \tag{1.91}$$

$$\left[GJ\varphi_z' + GD_{x\omega}\left(u_S' - \varphi_y\right) + GD_{y\omega}\left(v_S' + \varphi_x\right) + GD_\omega\left(\varphi_z' + \Psi\right) - M_z\right]\delta\varphi_z\big|_0^L = 0 \tag{1.92}$$

$$\left(EJ_\omega\Psi' - M_\omega\right)\delta\Psi\big|_0^L = 0 \tag{1.93}$$

1.4 FRP multilayered beams

In this section the application of Timoshenko-Reissner's model to multilayered FRP orthotropic beams is presented and stiffness coefficients are given as a function of the laminate stacking sequence.

1.4.1 Basics of laminate mechanics

The constitutive relations for FRP orthotropic thin-walled profiles will be deduced after a brief review of the basic concepts of laminate mechanics.

A generally orthotropic lamina, that is a lamina composed of an orthotropic material in which the geometric and material axes are not aligned, is represented in Figure 1.6. The direction of the reinforcement is indicated with 1, whereas the orthogonal direction is indicated with 2. In the present case, the geometric axes z and s coincide with the longitudinal and (local) cross-section contour directions of an FRP laminated thin-walled beam. The lamina in-plane elasticity equation in the material oriented co-ordinate system 1-2 is given by:

$$\begin{Bmatrix} \sigma_1 \\ \sigma_2 \\ \tau_{12} \end{Bmatrix} = \begin{bmatrix} Q_{11} & Q_{12} & 0 \\ Q_{12} & Q_{22} & 0 \\ 0 & 0 & Q_{66} \end{bmatrix} \begin{Bmatrix} \varepsilon_1 \\ \varepsilon_2 \\ \gamma_{12} \end{Bmatrix} \tag{1.94}$$

where $\gamma_{12} = 2\varepsilon_{12}$ and

$$Q_{11} = E_1/(1 - \nu_{12}\nu_{21}); \qquad\qquad Q_{22} = E_2/(1 - \nu_{12}\nu_{21})$$
$$Q_{12} = \nu_{21}E_1/(1 - \nu_{12}\nu_{21}) = \nu_{12}E_2/(1 - \nu_{12}\nu_{21}); \quad Q_{66} = G_{12} \tag{1.95}$$

In Eqs. 1.95, E_1 and E_2 represent the elasticity moduli in the 1 and 2 direction, respectively, ν_{12} and ν_{21} are Poisson's ratios and, finally, G_{12} is the in-plane shear modulus. In general, the principal material axes (1, 2) are not aligned with the geometric axes (z, s). To obtain the constitutive equation in the geometric system of co-ordinates, a transformation matrix **T** is usually introduced, giving (Vinson & Chou 1974):
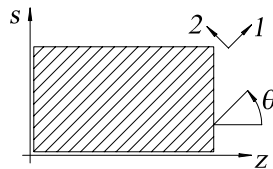
Figure 1.6. Generally orthotropic lamina.

$$\boldsymbol{\sigma} = \begin{Bmatrix} \sigma_z \\ \sigma_s \\ \tau_{zs} \end{Bmatrix} = \mathbf{T}^{-1}\mathbf{QT\varepsilon} = \bar{\mathbf{Q}} \begin{Bmatrix} \varepsilon_z \\ \varepsilon_s \\ \gamma_{zs} \end{Bmatrix} = \begin{bmatrix} \bar{Q}_{11} & \bar{Q}_{12} & \bar{Q}_{16} \\ \bar{Q}_{12} & \bar{Q}_{22} & \bar{Q}_{26} \\ \bar{Q}_{16} & \bar{Q}_{26} & \bar{Q}_{66} \end{bmatrix} \begin{Bmatrix} \varepsilon_z \\ \varepsilon_s \\ \gamma_{zs} \end{Bmatrix} \tag{1.96}$$

where, indicating with θ the angle from the z-axis to the 1-axis, matrix $\mathbf{T}$ takes the form:

$$\mathbf{T} = \begin{bmatrix} \cos^2\theta & \sin^2\theta & \sin 2\theta \\ \sin^2\theta & \cos^2\theta & -\sin 2\theta \\ -\sin 2\theta/2 & \sin 2\theta/2 & \cos 2\theta \end{bmatrix} \tag{1.97}$$

As is known, a laminate is obtained from bonding several laminae together, each with a pre-defined orientation of reinforcement. With reference to the kth lamina of the laminated beam, Eq. 1.96 may be rewritten as follows:

$$\boldsymbol{\sigma}_k = \bar{\mathbf{Q}}_k \boldsymbol{\varepsilon} \tag{1.98}$$

where vector $\boldsymbol{\varepsilon}$ is given by:

$$\boldsymbol{\varepsilon} = \boldsymbol{\varepsilon}^0 + n\boldsymbol{\kappa} = \begin{Bmatrix} \varepsilon_z^0 \\ \varepsilon_s^0 \\ \gamma_{zs}^0 \end{Bmatrix} + n \begin{Bmatrix} \kappa_z \\ \kappa_s \\ \kappa_{zs} \end{Bmatrix} \tag{1.99}$$

In Eq. 1.99, n is the axis normal to the cross-section contour and vectors $\boldsymbol{\varepsilon}^0$ and $\boldsymbol{\kappa}$ collect the middle surface deformations and the midplane curvatures, respectively. Inserting Eq. 1.99 into Eq. 1.98 and summing over all the N layers constituting the composite beam, the following relation is obtained, representing the laminate constitutive law (Vinson & Chou 1974; Jones 1975; Barbero 1999):

$$\begin{Bmatrix} \mathbf{N} \\ \mathbf{M} \end{Bmatrix} = \begin{Bmatrix} N_z \\ N_s \\ N_{zs} \\ M_z \\ M_s \\ M_{zs} \end{Bmatrix} = \begin{bmatrix} \mathbf{A} & \mathbf{B} \\ \mathbf{B} & \mathbf{D} \end{bmatrix} \begin{Bmatrix} \boldsymbol{\varepsilon}^0 \\ \boldsymbol{\kappa} \end{Bmatrix} = \begin{bmatrix} A_{11} & A_{12} & A_{16} & B_{11} & B_{12} & B_{16} \\ A_{12} & A_{22} & A_{26} & B_{12} & B_{22} & B_{26} \\ A_{16} & A_{26} & A_{66} & B_{16} & B_{26} & B_{66} \\ B_{11} & B_{12} & B_{16} & D_{11} & D_{12} & D_{16} \\ B_{12} & B_{22} & B_{26} & D_{12} & D_{22} & D_{26} \\ B_{16} & B_{26} & B_{66} & D_{16} & D_{26} & D_{66} \end{bmatrix} \begin{Bmatrix} \varepsilon_z^0 \\ \varepsilon_s^0 \\ \gamma_{zs}^0 \\ \kappa_z \\ \kappa_s \\ \kappa_{zs} \end{Bmatrix} \tag{1.100}$$

where

$$A_{ij} = \sum_{k=1}^{N} \bar{Q}_{ij}^k \left(t_k - t_{k-1} \right) \tag{1.101}$$

$$B_{ij} = \frac{1}{2} \sum_{k=1}^{N} \overline{Q}_{ij}^{k} \left(t_{k}^{2} - t_{k-1}^{2} \right)$$ (1.102)

$$D_{ij} = \frac{1}{3} \sum_{k=1}^{N} \overline{Q}_{ij}^{k} \left(t_{k}^{3} - t_{k-1}^{3} \right)$$ (1.103)

Note that dimensions of $\mathbf{N}^{T} = \left\{ N_{z} \quad N_{s} \quad N_{zs} \right\}$ and $\mathbf{M}^{T} = \left\{ M_{z} \quad M_{s} \quad M_{zs} \right\}$ are those of a force per unit length and of a moment per unit length, respectively. In Eq. 1.100, $\mathbf{A}$ represents the extensional stiffness matrix, $\mathbf{D}$ is the flexural stiffness matrix, and $\mathbf{B}$ is the bending-stretching coupling matrix. It should be noted that a laminate may have bending−stretching coupling even if the various materials composing the laminae are isotropic. In fact, only when the plate is perfectly symmetric about its middle surface is $\mathbf{B} = \mathbf{0}$, and this requires symmetry in laminae properties, laminae orientation and distance from the midplane. In addition to Eq. 1.100, for some plate or shell composite structures the shear deformability within the thickness is to be taken into account, giving the constitutive relation (Vinson & Chou 1974):

$$\mathbf{V} = \left\{ \begin{array}{c} V_{z} \\ V_{s} \end{array} \right\} = \left[\begin{array}{cc} A_{44} & A_{45} \\ A_{45} & A_{55} \end{array} \right] \left\{ \begin{array}{c} \gamma_{zn} \\ \gamma_{sn} \end{array} \right\}$$ (1.104)

Eqs. 1.100 and 1.104 represent the full system of constitutive equations necessary to study generally orthotropic laminates.

1.4.2 Isotropic equivalence for pultruded beams

In the present analysis, as usual in beam theories, we reduce the beam to its middle surface and, consequently, only the extensional part of the constitutive relation 1.100 is retained, i.e.:

$$\left\{ \begin{array}{c} N_{z} \\ N_{s} \\ N_{zs} \end{array} \right\} = \mathbf{A}\boldsymbol{\varepsilon} = \left[\begin{array}{ccc} A_{11} & A_{12} & A_{16} \\ A_{12} & A_{22} & A_{26} \\ A_{16} & A_{26} & A_{66} \end{array} \right] \left\{ \begin{array}{c} \varepsilon_{z} \\ \varepsilon_{s} \\ \gamma_{zs} \end{array} \right\}$$ (1.105)

where superscript "0" is omitted. Compared with the axial stress resultant N_z, the contribution of N_s may be neglected. Hence, assuming $N_s = 0$, solving for ε_s the second equation of expression 1.105 and substituting the result into first and third equations lead to:

$$\left\{ \begin{array}{c} N_{z} \\ N_{zs} \end{array} \right\} = \left[\begin{array}{cc} A_{11}^{*} & A_{16}^{*} \\ A_{16}^{*} & A_{66}^{*} \end{array} \right] \left\{ \begin{array}{c} \varepsilon_{z} \\ \gamma_{zs} \end{array} \right\}$$ (1.106)

where

$$A_{11}^* = A_{11} - \frac{A_{12}^2}{A_{22}}; \qquad A_{16}^* = A_{16} - \frac{A_{12}A_{26}}{A_{22}}; \qquad A_{66}^* = A_{66} - \frac{A_{26}^2}{A_{22}} \qquad (1.107)$$

Most of the multilayered composite profiles commonly used in civil engineering, as for example FRP beams produced with pultrusion technology, are orthotropic beams having the longitudinal axis coinciding with one of the orthotropy axes. In particular, these profiles are composed by multilayered cross-ply panels with symmetric balanced stacking sequence (for example: $[0°/90°/\pm \theta /0°/90°]_S$, etc., where $\pm \theta$ indicates a possible woven-fabric ply). For such particular laminates $A_{16} = A_{26} = 0$ and Eq. 1.106 gives:

$$N_z(z,s) = A_{11}^*(s)\varepsilon_z(z,s) \qquad (1.108)$$

$$N_{zs}(z,s) = A_{66}(s)\gamma_{zs}(z,s) \qquad (1.109)$$

It should be noted that the previous relations depend on two parameters only. For this reason, some authors introduced the definition of "isotropic equivalence" (Lin *et al.* 1996).

1.4.3 Constitutive relations for pultruded beams

The beam stress resultants are given by:

$$N = \int_0^a N_z ds; \quad M_x = \int_0^a N_z y ds; \quad M_y = -\int_0^a N_z x ds; \quad M_\omega = \int_0^a N_z \omega ds \qquad (1.110)$$

$$V_x = \int_0^a N_{zx} ds; \quad V_y = \int_0^a N_{zy} ds \qquad (1.111)$$

$$M_z = \int_0^a N_{zs} r ds = \begin{cases} \oint N_{zs} \dfrac{f}{t} ds + \oint N_{z\omega} ds = M_{z,closed}^{Bredt} + M_z^\omega & \text{closed sections} \\[4mm] \int_0^a N_{z\omega} ds = M_z^\omega & \text{open sections} \end{cases} \qquad (1.112)$$

where

$$N_{zx}(z,s) = N_{zs}(z,s)\frac{dx}{ds}; \quad N_{zy}(z,s) = N_{zs}(z,s)\frac{dy}{ds}; \quad N_{z\omega}(z,s) = N_{zs}(z,s)\frac{d\omega}{ds} \qquad (1.113)$$

and, according to the definitions introduced in § 1.2.2, N, M_x, M_y and M_ω are the axial force, the bending moments and the bimoment and, finally, V_x, V_y, $M_{z,closed}^{Bredt}$, and M_z^ω are the shear forces, the Bredt-De Saint Venànt twisting moment for closed sections and the twisting moment due to nonuniform torsion, respectively.

Inserting Eq. 1.108 into expressions 1.110 for the stress resultants and considering Eq. 1.11 for the axial strain yield:

$$
\begin{Bmatrix} N \\ M_x \\ M_y \\ M_\omega \end{Bmatrix} = \begin{bmatrix} \overline{EA} & \overline{S_x} & -\overline{S_y} & \overline{S_\omega} \\ & \overline{EJ_x} & -\overline{EJ_{xy}} & \overline{EJ_{y\omega}} \\ & & \overline{EJ_y} & -\overline{EJ_{x\omega}} \\ \text{Sym} & & & \overline{EJ_\omega} \end{bmatrix} \begin{Bmatrix} w'_C \\ \varphi'_x \\ \varphi'_y \\ \Psi' \end{Bmatrix}
\tag{1.114}
$$

where

$$
\overline{EA} = \int_0^a A_{11}^* ds \,; \qquad \overline{S_x} = \int_0^a A_{11}^* y\,ds \,; \qquad \overline{S_y} = \int_0^a A_{11}^* x\,ds \,; \qquad \overline{S_\omega} = \int_0^a A_{11}^* \omega\,ds
\tag{1.115}
$$

$$
\overline{EJ_x} = \int_0^a A_{11}^* y^2 ds \,; \quad \overline{EJ_y} = \int_0^a A_{11}^* x^2 ds \,; \quad \overline{EJ_\omega} = \int_0^a A_{11}^* \omega^2 ds
\tag{1.116}
$$

$$
\overline{EJ_{xy}} = \int_0^a A_{11}^* xy\,ds \,; \quad \overline{EJ_{x\omega}} = \int_0^a A_{11}^* x\omega\,ds \,; \quad \overline{EJ_{y\omega}} = \int_0^a A_{11}^* y\omega\,ds
\tag{1.117}
$$

Identifying axes x and y with the principal axes of inertia of the cross-section, $\overline{S_x} = \overline{S_y} = \overline{EJ_{xy}} = 0$. Moreover, analogously to the case of isotropic beams, we assume $\overline{S_\omega} = \overline{EJ_{x\omega}} = \overline{EJ_{y\omega}} = 0$. Consequently, the following constitutive relation can be written:

$$
\mathbf{S}^T = \text{diag}\left\{ \overline{EA}, \overline{EJ_x}, \overline{EJ_y}, \overline{EJ_\omega} \right\} \mathbf{u}'^T
\tag{1.118}
$$

where $\mathbf{S}^T = \left\{ N, M_x, M_y, M_\omega \right\}$ and $\mathbf{u}'^T = \left\{ w'_C, \varphi'_x, \varphi'_y, \Psi' \right\}$.

For closed sections, remembering the expression $2\Omega = f \oint ds/t$, the following relation holds:

$$
2\Omega \varphi'_z = \oint \gamma_{zs} ds = N_{zs}^{Bredt} \oint A_{66}^{-1} ds
\tag{1.119}
$$

where $N_{zs}^{Bredt} = M_z^{Bredt}/2\Omega$. Hence, the constitutive relation for uniform torsion may be written in the form:

$$
M_z^{Bredt} = \overline{GJ_B} \varphi'_z
\tag{1.120}
$$

where

$$
\overline{GJ_B} = 4\Omega^2 \Big/ \oint A_{66}^{-1} ds
\tag{1.121}
$$

As shown in § 1.2.2, for open section beams the contribution of primary torsion does not follow from the assumed kinematical model. To take such a contribution into account, Kollár (2001a) proposes, for the beam rigidity in uniform torsion, the following approximate expression:

$$\overline{GJ_t} = 4\int_0^a D_{66}\,ds \tag{1.122}$$

where D_{66} is a coefficient on the main diagonal of matrix **D** in Eq. 1.100. For a detailed analysis of multilayered beams in uniform torsion refer to Savoia & Tullini (1993). In the case of constant thickness and same stacking sequence over the cross-section, Eqs. 1.115a, 1.116, 1.121 (1.122) reduce to the expressions:

$$\overline{EA} = EA; \quad \overline{EJ_x} = EJ_x; \quad \overline{EJ_y} = EJ_y; \quad \overline{EJ_\omega} = EJ_\omega; \quad \overline{GJ_B} = GJ_B \left(\overline{GJ_t} = GJ_t\right) \tag{1.123}$$

where $E = A_{11}^*/t$, A and J_i ($i = x$, y, ω, B (t)) are determined in the usual way and, finally, $G = A_{66}/t$ or $G = 12D_{66}/t^3$ for closed or open sections, respectively. Some manufacturers of pultruded profiles report the apparent moduli, obtained by relations $E = \overline{EJ_i}/J_i$ and $G = \overline{GD_i}/D_i$ ($i = x$, y), where rigidities $\overline{EJ_i}$ and $\overline{GD_i}$ are determined by experiments (see § 1.6), $J_i = \int_A i^2\,dA$, and $D_i = 1/d_i$ (see Eq. 1.50a or 1.50b).

As for the constitutive law linking shear resultants and secondary twisting moment to shear deformations, using Eqs. 1.12, 1.109, 1.111 and 1.112, the following relationship is readily obtained for open section beams:

$$\begin{Bmatrix} V_x \\ V_y \\ M_z^\omega \end{Bmatrix} = \begin{bmatrix} \overline{GD_x} & \overline{GD_{xy}} & \overline{GD_{x\omega}} \\ & \overline{GD_y} & \overline{GD_{y\omega}} \\ \text{Sym} & & \overline{GD_\omega} \end{bmatrix} \begin{Bmatrix} u_S' - \varphi_y \\ v_S' + \varphi_x \\ \varphi_z' + \Psi \end{Bmatrix} \tag{1.124}$$

Following the same procedure as for isotropic beams, the shear stiffness coefficients are to be redefined by refining the variation of the shear strain over the cross-section. In particular, writing the shear flow in the form (Kollár & Springer 2003):

$$N_{zs}(z,s) = -\frac{V_x}{EJ_y}\int_0^s A_{11}^* x\,ds' - \frac{V_y}{EJ_x}\int_0^s A_{11}^* y\,ds' - \frac{M_z^\omega}{EJ_\omega}\int_0^s A_{11}^* \omega\,ds' \tag{1.125}$$

the shear rigidity matrix turns out to be given by:

$$\begin{bmatrix} \overline{GD_x} & \overline{GD_{xy}} & \overline{GD_{x\omega}} \\ & \overline{GD_y} & \overline{GD_{y\omega}} \\ \text{Sym} & & \overline{GD_\omega} \end{bmatrix} = \begin{bmatrix} \bar{d}_x & \bar{d}_{xy} & \bar{d}_{x\omega} \\ & \bar{d}_y & \bar{d}_{y\omega} \\ \text{Sym} & & \bar{d}_\omega \end{bmatrix}^{-1} \tag{1.126}$$

where the compliance coefficients on the right-hand side take the form (Kollár 2001a,b; Kollár & Springer 2003):

$$\overline{d}_{ij} = \int_0^a A_{66}^{-1} N_{zi} N_{zj} ds = \int_A \left(1/t A_{66}\right) N_{zi} N_{zj} dA; \quad (i,j = x, y, \omega)$$

(1.127)

In the previous expression, N_{zx}, N_{zy} and $N_{z\omega}$ (Eq. 1.113) represent the shear flows due to unit shear forces along the principal axes x and y and to a unit twisting moment, respectively. For beams with constant thickness and same stacking sequence over the cross-section, Eq. 1.127 reduce to expressions 1.50 divided by $G = A_{66}/t$.

In the case of closed section beams, the shear flow may be expressed as a sum of two contributions in the form:

$$N_{zs}\left(z,s\right) = N_{zs}^{open}\left(z,s\right) + N_{zs}^{cut}$$

(1.128)

where N_{zs}^{open} is the shear flow that would exist if the beam were open because of a longitudinal cut and N_{zs}^{cut} represents a constant shear flow induced by the forces acting along the "cut" edges and is given, disregarding the contribution of nonuniform torsion (Loughlan & Ata 1997), by (Kollár & Springer 2003):

$$N_{zs}^{cut} = -\frac{\oint A_{66}^{-1} N_{zs}^{open}\left(z,s\right) ds}{\oint A_{66}^{-1} ds}$$

(1.129)

Hence, substituting Eqs. 1.125 (first two terms on the right-hand side) and 1.129 into Eq. 1.128, and the resulting expression into Eq. 1.127 ($i, j = x, y$), the following shear rigidity matrix is obtained:

$$\begin{bmatrix} \overline{GD_x} & \overline{GD_{xy}} \\ \overline{GD_{xy}} & \overline{GD_y} \end{bmatrix} = \begin{bmatrix} \overline{d}_x & \overline{d}_{xy} \\ \overline{d}_{xy} & \overline{d}_y \end{bmatrix}^{-1}$$

(1.130)

1.4.4 Stiffness coefficients

The stiffness coefficients determined by means of Eqs. 1.115a, 1.116, 1.121, 1.122 and the shear compliance coefficients given by Eq. 1.127 are reported in Appendix 1.A. Axes x and y were identified with the principal axes of inertia of the cross-section, except for Z- and angle-section, for which the term $\overline{EJ_{xy}}$ was also evaluated. Geometric dimensions are referred to the middle line of the cross-section. Possible differences in mechanical properties between web ("w", coefficients $A_{11,w}^*$, $A_{66,w}$) and flange ("f", coefficients $A_{11,f}^*$, $A_{66,f}$) panels were taken into account. In the case of isotropic beams, the expressions of the stiffness coefficients can be obtained by replacing $A_{11,i}^*$ and $A_{66,i}$ with Et_i and Gt_i ($i = f, w$), respectively. In the following paragraphs, the detailed calculation of the shear compliances is presented for the I- and the C-section beam.

1.4.4.1 I-beam

A FRP profile with doubly-symmetric I-section is considered (Fig. 1.7a).

Figure 1.7. Shear flow in the *I*-section. a: shear force acting in the *x* direction; b: shear force acting in the *y* direction; c: twisting moment.

In the case of a shear force $V_x = 1$ acting along the principal *x*-direction (Fig. 1.7b), the shear flow $N_{zx,w}$ in the web is zero whereas the shear flow $N_{zx,f}$ in the flanges is a quadratic function of the current position s_f along the middle line. In fact, using Eq. 1.125 (first term on the right-hand side) yields:

$$N_{zx,f} = \frac{A_{11,f}^*}{\overline{EJ}_y} \int_0^{s_f} x(s_f) ds_f = \frac{A_{11,f}^*}{\overline{EJ}_y} \int_0^{s_f} (s_f - B/2) ds_f$$
$$= \frac{3s_f(s_f - B)}{B^3}$$

$$s_f \in [0, B] \qquad (1.131)$$

for each flange. In Eq. 1.131, the bending stiffness about the *y*-axis has been given the expression $\overline{EJ}_y = B^3 A_{11,f}^* / 6$ (see Appendix 1.A).

In the case of a shear force $V_y = 1$ acting along the principal *y*-direction (Fig. 1.7c), the shear flow $N_{zy,f}$ in the flanges is a linear function of the current position s_f along the middle line. In particular, using Eq. 1.125 (second term on the right-hand side) yields:

$$N_{zy,f} = \frac{A_{11,f}^*}{\overline{EJ}_x} \int_0^{s_f} y(s_f) ds_f = \frac{A_{11,f}^*}{\overline{EJ}_x} \int_0^{s_f} \pm H/2 \, ds_f$$
$$= \pm \frac{6 A_{11,f}^* s_f}{6BH A_{11,f}^* + H^2 A_{11,w}^*}$$

$$s_f \in [0, B/2] \qquad (1.132)$$

where the bending stiffness about the *x*-axis has been given the expression $\overline{EJ}_x = H^3 A_{11,w}^* / 12 + BH^2 A_{11,f}^* / 2$ (see Appendix 1.A) and signs + and − are referred to

top and bottom flange, respectively. The shear flow $N_{zy,w}$ in the web is a quadratic function of the current position s_w given by:

$$N_{zy,w} = 2N_{zy,f}\left(B/2\right) + \frac{A_{11,w}^*}{EJ_x}\int_0^{s_w} y\left(s_w\right)ds_w$$

$$= \frac{6\left[BHA_{11,f}^* + A_{11,w}^*\left(H - s_w\right)s_w\right]}{H^2\left(6BA_{11,f}^* + HA_{11,w}^*\right)} \qquad\qquad s_w \in\left[0,H\right] \qquad\qquad (1.133)$$

In the case of a twisting moment $M_z = 1$ (Fig. 1.7d), the shear flow due to nonuniform torsion is ruled by warping function ω:

$$\omega\left(s_{f1}\right) = -Hs_{f1}/2 \qquad\qquad s_{f1} \in\left[0,B/2\right] \qquad\qquad (1.134)$$

$$\omega\left(s_{f2}\right) = Hs_{f2}/2 \qquad\qquad s_{f2} \in\left[0,B/2\right] \qquad\qquad (1.135)$$

$$\omega\left(s_{f3}\right) = 0 \qquad\qquad s_{f3} \in\left[0,H\right] \qquad\qquad (1.136)$$

$$\omega\left(s_{f4}\right) = Hs_{f4}/2 \qquad\qquad s_{f4} \in\left[0,B/2\right] \qquad\qquad (1.137)$$

$$\omega\left(s_{f5}\right) = -Hs_{f5}/2 \qquad\qquad s_{f5} \in\left[0,B/2\right] \qquad\qquad (1.138)$$

involving only flange contribution. In particular, using Eq. 1.125 (third term on the right-hand side) yields the following quadratic expression:

$$N_{z\omega} = N_{z\omega,f} = \frac{A_{11,f}^*}{EJ_\omega}\int_0^{s_f}\omega\left(s_f\right)ds_f = \pm\frac{6}{HB^2}s_f\left(\frac{s_f}{B}-1\right) \qquad s_f \in\left[0,B\right] \qquad (1.139)$$

where the warping stiffness has been given the expression $\overline{EJ_\omega} = H^2B^3A_{11,f}^*/24$ (see Appendix 1.A) and signs $+$ and $-$ are referred to top and bottom flange, respectively.

Substituting Eqs. 1.131–1.133 and 1.139 into Eq. 1.127 provides the following shear compliance coefficients:

$$\overline{d}_x = \int_a A_{66,f}^{-1}N_{zx}^2 ds = \frac{2}{A_{66,f}}\int_0^B N_{zx,f}^2 ds = \frac{3}{5BA_{66,f}} \qquad\qquad (1.140)$$

$$\overline{d}_y = \int_a A_{66}^{-1}N_{zy}^2 ds = \frac{6}{5H^2 A_{66,f}A_{66,w}\left(6BA_{11,f}^* + HA_{11,w}^*\right)^2}\left[10BH^2 A_{11,f}^* A_{11,w}^* A_{66,f}\right.$$

$$\left. + H^3 A_{11,w}^{*2}A_{66,f} + 5B^2 A_{11,f}^{*2}\left(BA_{66,w} + 6HA_{66,f}\right)\right] \qquad\qquad (1.141)$$

$$\overline{d}_\omega = \int_a A_{66}^{-1}N_{z\omega}^2 ds = \frac{12}{5BH^2 A_{66,f}} \qquad\qquad (1.142)$$

$$\overline{d}_{xy} = \int_a A_{66}^{-1}N_{zx}N_{zy}ds = 0, \quad \overline{d}_{x\omega} = \int_a A_{66}^{-1}N_{zx}N_{z\omega}ds = 0, \quad \overline{d}_{y\omega} = \int_a A_{66}^{-1}N_{zy}N_{z\omega}ds = 0 \qquad (1.143)$$

A simplified expression for coefficient $\overline{d}_y$ can be obtained by assuming the shear flow $N_{zy,w}$ in the web produced by a unit shear force $V_y = 1$ equal to the constant value $1/H$ (Kollár 2001b, Kollár & Springer 2003). In this case, Eq. 1.141 takes the form:

$$\overline{d}_y = \frac{1}{HA_{66,w}} + \frac{6B^3 A_{11,f}^{*2}}{H^2 A_{66,f}\left(6BA_{11,f}^* + HA_{11,w}^*\right)^2} \tag{1.144}$$

resulting in an underestimate of the compliance coefficient of about 1% for I-section profiles and of about 5% for wide-flange cross-section beams.

1.4.4.2 C-beam

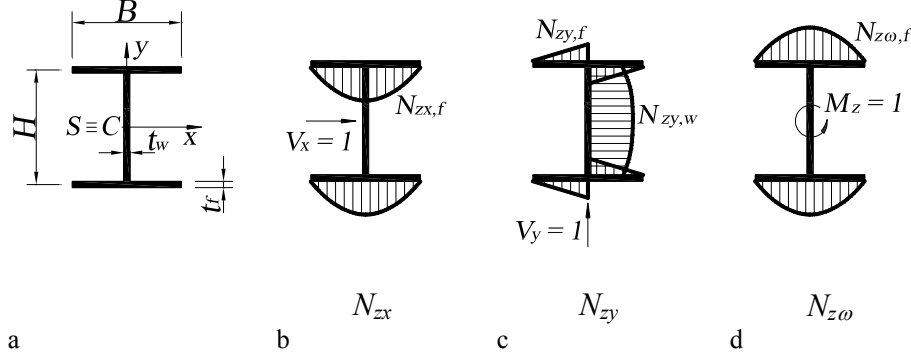A FRP profile with monosymmetric C-section is considered (Fig. 1.8a).
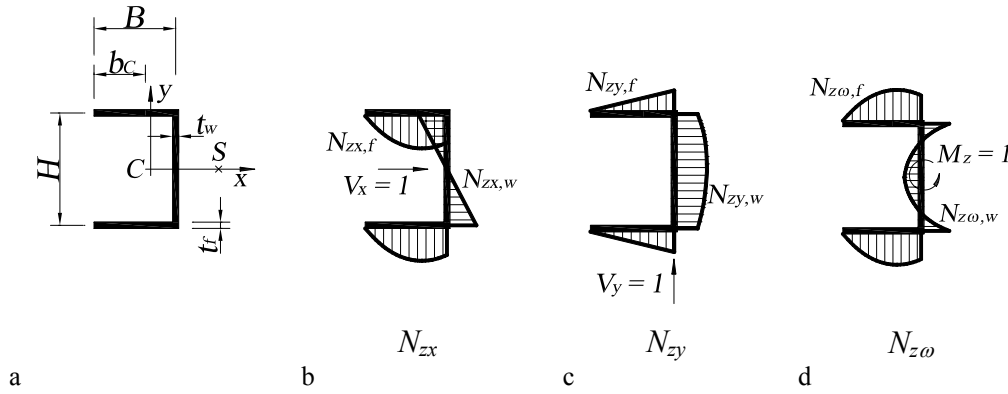
Figure 1.8. Shear flow in the C-section. a: shear force acting in the x direction; b: shear force acting in the y direction; c: twisting moment.

In the case of a shear force $V_x = 1$ acting along the principal x-direction (Fig. 1.8b), the shear flow is quadratic along the flanges and linear along the web. In particular, we have:

$$N_{zx,f} = \frac{A_{11,f}^*}{EJ_y}\int_0^{s_f}\left(B - b_C - s_f\right)ds_f$$
$$= -\frac{3s_f\left[-2BA_{11,f}^*\left(B - s_f\right) + HA_{11,w}^*\left(s_f - 2B\right)\right]}{2B^3\left(BA_{11,f}^* + 2HA_{11,w}^*\right)} \qquad s_f \in [0, B] \tag{1.145}$$

$$N_{zx,w} = N_{zx,f}(B) - \frac{A_{11,w}^*}{EJ_y}\int_0^{s_w} b_C s_w ds_w$$
$$= \frac{3A_{11,w}^*\left(H - 2s_w\right)}{2B\left(BA_{11,f}^* + 2HA_{11,w}^*\right)} \qquad s_w \in [0, H] \tag{1.146}$$

where the relations $\overline{EJ}_y = 2\left[b_C^3 + (B - b_C)^3\right] A_{11,f}^* / 3 + Hb_C^2 A_{11,w}^*$ and $b_C = 1/\overline{EA}\left(B^2 A_{11,f}^* + HBA_{11,w}^*\right)$ (see Appendix 1.A) were adopted.

In the case of a shear force $V_y = 1$ acting along the principal y-direction (Fig. 1.8c), the shear flow is quadratic linear along the flanges and quadratic along the web, assuming the expressions:

$$N_{zy,f} = \frac{A_{11,f}^*}{EJ_x} \int_0^{s_f} y(s_f) ds_f = \frac{A_{11,f}^*}{EJ_x} \int_0^{s_f} \pm H/2 \, ds_f$$

$$= \pm \frac{6A_{11,f}^* s_f}{6BHA_{11,f}^* + H^2 A_{11,w}^*}$$

$$s_f \in [0, B] \qquad (1.147)$$

$$N_{zy,w} = N_{zy,f}(B) + \frac{A_{11,w}^*}{EJ_x} \int_0^{s_w} y(s_w) ds_w$$

$$= \frac{6\left[BHA_{11,f}^* + A_{11,w}^*(H - s_w)s_w\right]}{H^2\left(6BA_{11,f}^* + HA_{11,w}^*\right)}$$

$$s_w \in [0, H] \qquad (1.148)$$

where the bending stiffness about the x-axis has been given the expression $\overline{EJ}_x = H^3 A_{11,w}^* / 12 + BH^2 A_{11,f}^* / 2$ (see Appendix 1.A) and signs $+$ and $-$ are referred to top and bottom flange, respectively.

In the case of a twisting moment $M_z = 1$ (Fig. 1.8d), the shear flow due to nonuniform torsion is ruled by warping function ω:

$$\omega(s) = \frac{1}{2}H\left(B - s - \frac{3B^2 A_{11,f}^*}{6BA_{11,f}^* + HA_{11,w}^*}\right) \qquad s \in [0, B] \qquad (1.149)$$

$$\omega(s) = -\frac{3B^2 A_{11,f}^*(2B + H - 2s)}{2\left(6BA_{11,f}^* + HA_{11,w}^*\right)} \qquad s \in [B, H] \qquad (1.150)$$

$$\omega(s) = \frac{3HBA_{11,f}^*(3B + 2H - 2s) + H^2 A_{11,w}^*(B + H - s)}{2\left(6BA_{11,f}^* + HA_{11,w}^*\right)} \qquad s \in [H, 2B + H] \qquad (1.151)$$

Hence, the shear flow is given by the following quadratic expressions:

$$N_{z\omega,f} = \frac{A_{11,f}^*}{EJ_\omega} \int_0^s \omega(s) ds$$

$$= \pm \frac{3\left[6BA_{11,f}^*(B - s) + HA_{11,w}^*(2B - s)\right]s}{HB^3\left(3BA_{11,f}^* + 2HA_{11,w}^*\right)}$$

$$s \in [0, B] \qquad (1.152)$$

$$N_{z\omega,w} = N_{z\omega,f}(B) + \frac{A^*_{11,w}}{\overline{EJ}_\omega} \int_B^s \omega(s)\,ds$$

$$= \frac{3A^*_{11,w}\left[6B^2 + 6HB + H^2 - 6(2B+H)s + 6s^2\right]}{H^2 B\left(3BA^*_{11,f} + 2HA^*_{11,w}\right)} \qquad s \in [B,H] \qquad (1.153)$$

where the warping stiffness has been given the expression $\overline{EJ}_\omega = H^2 B^3 A^*_{11,f}\left(3BA^*_{11,f} + 2HA^*_{11,w}\right)\big/12\left(6BA^*_{11,f} + HA^*_{11,w}\right)$ (see Appendix 1.A) and signs + and − in Eq. 1.152 are referred to top and bottom flange, respectively.

Finally, substituting Eqs. 1.145−1.148, 1.152 and 1.153 into Eq. 1.127 provides the following shear compliance coefficients:

$$\overline{d}_x = \int_a A_{66}^{-1} N_{zx}^2\,ds = \frac{3}{20B^2 A_{66,f} A_{66,w}\left(BA^*_{11,f} + 2HA^*_{11,w}\right)^2}\Big[4B^3 A^{*2}_{11,f} A_{66,w}$$

$$+14B^2 HA^*_{11,f} A^*_{11,w} A_{66,w} + H^2 A^{*2}_{11,w}\left(16BA_{66,w} + 5HA_{66,f}\right)\Big] \qquad (1.154)$$

$$\overline{d}_y = \int_a A_{66}^{-1} N_{zy}^2\,ds = \frac{6}{5H^2 A_{66,f} A_{66,w}\left(6BA^*_{11,f} + HA^*_{11,w}\right)^2}\Big[10BH^2 A^*_{11,f} A^*_{11,w} A_{66,f}$$

$$+ H^3 A^{*2}_{11,w} A_{66,f} + 10B^2 A^{*2}_{11,f}\left(2BA_{66,w} + 3HA_{66,f}\right)\Big] \qquad (1.155)$$

$$\overline{d}_\omega = \int_a A_{66}^{-1} N_{z\omega}^2\,ds = \frac{3}{5H^2 B^2 A_{66,f} A_{66,w}\left(3BA^*_{11,f} + 2HA^*_{11,w}\right)^2}\Big[36B^3 A^{*2}_{11,f} A_{66,w}$$

$$+ 42HB^2 A^*_{11,f} A^*_{11,w} A_{66,w} + H^2 A^{*2}_{11,w}\left(16BA_{66,w} + 3HA_{66,f}\right)\Big] \qquad (1.156)$$

$$\overline{d}_{xy} = \int_a A_{66}^{-1} N_{zx} N_{zy}\,ds = 0\,, \qquad \overline{d}_{x\omega} = \int_a A_{66}^{-1} N_{zx} N_{z\omega}\,ds = 0 \qquad (1.157)$$

$$\overline{d}_{y\omega} = \int_a A_{66}^{-1} N_{zy} N_{z\omega}\,ds$$

$$= \frac{3\left(30B^3 A^{*2}_{11,f} A_{66,w} + 25HB^2 A^*_{11,f} A^*_{11,w} A_{66,w} - 2H^3 A^{*2}_{11,w} A_{66,f}\right)}{5H^2 BA_{66,f} A_{66,w}\left(6BA^*_{11,f} + HA^*_{11,w}\right)\left(3BA^*_{11,f} + 2HA^*_{11,w}\right)} \qquad (1.158)$$

Simplified expressions for coefficients $\overline{d}_y$ and $\overline{d}_{y\omega}$ can be obtained by assuming the shear flow $N_{zy,w}$ in the web produced by a unit shear force $V_y = 1$ equal to the constant value $1/H$ (Kollár 2001b, Kollár & Springer 2003). In this case, Eqs. 1.155 and 1.158 become:

$$\bar{d}_y = \frac{1}{HA_{66,w}} + \frac{24B^3 A_{11,f}^{*2}}{H^2 A_{66,f}\left(6BA_{11,f}^* + HA_{11,w}^*\right)^2} \tag{1.159}$$

$$\bar{d}_{y\omega} = \int_a A_{66}^{-1} N_{zy} N_{z\omega} ds$$

$$= \frac{3BA_{11,f}^*\left(6BA_{11,f}^* + 5HA_{11,w}^*\right)}{H^2 A_{66,f}\left(6BA_{11,f}^* + HA_{11,w}^*\right)\left(3BA_{11,f}^* + 2HA_{11,w}^*\right)} \tag{1.160}$$

It is to be noted that Eq. 1.159 lightly underestimates the compliance coefficient $\bar{d}_y$ (1% ÷ 5%), whereas Eq. 1.160 strongly overestimates (≥ 50%) the compliance coefficient $\bar{d}_{y\omega}$ for C-beams with narrow flanges.

1.5 Analytical solutions

In this section, a variety of static problems are solved analytically using Timoshenko-Reissner's beam model. In particular, the solutions to uncoupled bending or torsion problems for doubly-symmetric cross-section profiles, as well as to coupled equilibrium equations for monosymmetric or nonsymmetric cross-section beams are presented. The solutions given in the following hold for both isotropic and multilayered orthotropic beams, provided that, in the latter case, equivalent rigidities $\overline{EA}$, $\overline{EJ_i}$, $\overline{GJ_t}$, $\overline{GD_i}$, $\overline{GD_{ij}}$ ($i, j = x, y, \omega$, § 1.4.3) are used. Some of the solutions obtained will be adopted as a reference in the finite element analyses developed in the following chapter.

1.5.1 Beams bent into a plane of symmetry (Timoshenko theory)

Identifying, for example purposes, the y-z plane with a plane of symmetry for the beam, the bending problem 1.72–1.73 reduce, in the absence of distributed forces and moments, to the homogeneous equations:

$$GD_y\left(v_S'' + \varphi_x'\right) = 0 \tag{1.161}$$

$$EJ_x \varphi_x'' - GD_y\left(v_S' + \varphi_x\right) = 0 \tag{1.162}$$

The solutions to Eqs. 1.161–1.162 can be expressed in the following polynomial form:

$$v_S(z) = -\left(A_1 z + A_2 \frac{z^2}{2} + A_3 \frac{z^3}{3} + A_4\right) + 2A_3 \frac{EJ_x}{GD_y} z \tag{1.163}$$

$$\varphi_x(z) = A_1 + A_2 z + A_3 z^2 \tag{1.164}$$

where A_i (i = 1, …, 4) represent a set of independent unknown constants to be determined by imposing four boundary conditions.

1.5.1.1 Cantilever beam subjected to a transversal force at the free end

The cantilever I-section profile of Figure 1.9 is considered.
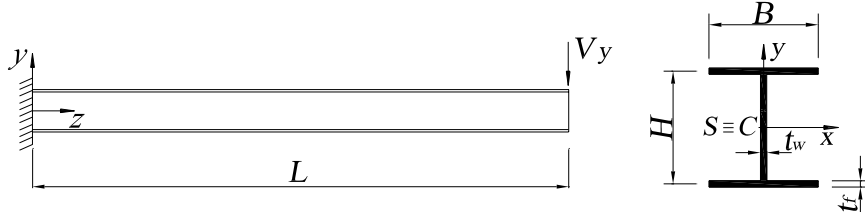
Figure 1.9. Cantilever I-section beam subjected to a transversal force (y direction) at the free end.

Imposing the following four boundary conditions:

$$v_S(0) = 0 \tag{1.165}$$

$$\varphi_x(0) = 0 \tag{1.166}$$

$$M_x(L) = EJ_x \varphi_x'(L) = 0 \tag{1.167}$$

$$V_y(L) = GD_y \left[v_S'(L) + \varphi_x(L) \right] = V_y \tag{1.168}$$

yields the solution:

$$v_S(z) = \left[\frac{1}{GD_y} + \frac{(3L - z)z}{6EJ_x} \right] V_y z \tag{1.169}$$

$$\varphi_x(z) = \frac{(z - 2L)}{2EJ_x} V_y z \tag{1.170}$$

End displacement and rotation are given by:

$$v_S(L) = \left(\frac{1}{GD_y} + \frac{L^2}{3EJ_x} \right) V_y L \tag{1.171}$$

$$\varphi_x(L) = -\frac{L^2}{2EJ_x} V_y \tag{1.172}$$

In the case of a simply-supported beam with a transversal force V_y at midspan, displacement v_S may be readily obtained, due to the problem symmetry, from Eq. 1.169 with the substitutions $L \to L/2$ and $V_y \to V_y/2$ giving:

$$v_S(z) = \left[\frac{1}{2GD_y} + \frac{(3L-2z)z}{24EJ_x} \right] V_y z \tag{1.173}$$

and, consequently, the midspan deflection turns out to be given by:

$$v_S(L/2) = \left(\frac{1}{4GD_y} + \frac{L^2}{48EJ_x} \right) V_y L \tag{1.174}$$

1.5.1.2 Simply-supported beam subjected to two equal transversal forces at z = a and z = L−a

The simply-supported I-section profile of Figure 1.10 is now considered.
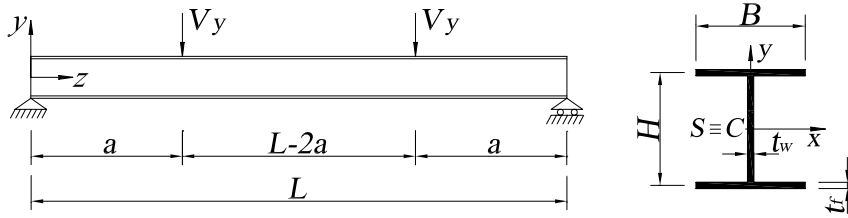
Figure 1.10. Simply-supported I-section beam subjected to two transversal forces (y direction) at $z = a$ and $z = L−a$.

The following eight boundary conditions are to be imposed:

$$v_S(0) = 0 \tag{1.175}$$

$$M_x(0) = EJ_x \varphi_x'(0) = 0 \tag{1.176}$$

$$[\![v_S(a)]\!] = 0 \tag{1.177}$$

$$[\![\varphi_x(a)]\!] = 0 \tag{1.178}$$

$$V_y(0) = GD_y [v_S'(0) + \varphi_x(0)] = V_y \tag{1.179}$$

$$[\![V_y(a)]\!] = [\![GD_y [v_S'(a) + \varphi_x(a)]]\!] = V_y \tag{1.180}$$

$$\varphi_x(L/2) = 0 \tag{1.181}$$

$$M_x(a) = EJ_x \varphi_x'(a) = V_y a \tag{1.182}$$

where symbol $[\![\cdot]\!]$ stands for jump of the argument reported inside. The solution is given by:

$$0 \leq z \leq a$$

$$v_S(z) = \left(\frac{1}{GD_y} - \frac{3a^2 - 3aL + z^2}{6EJ_x} \right) V_y z \tag{1.183}$$

$$\varphi_x(z) = \left(a^2 - aL + z^2 \right) \frac{V_y}{2EJ_x} \tag{1.184}$$

$$a \leq z \leq L/2$$

$$v_S(z) = \left(\frac{1}{GD_y} - \frac{a^2 + 3z(z-L)}{6EJ_x} \right) V_y a \tag{1.185}$$

$$\varphi_x(z) = (2z - L) \frac{V_y a}{2EJ_x} \tag{1.186}$$

Vertical displacements at $z = a$ and $z = L/2$ are given by:

$$v_S(a) = \left(\frac{1}{GD_y} - \frac{4a^2 - 3aL}{6EJ_x} \right) V_y a \tag{1.187}$$

$$v_S(L/2) = \left(\frac{1}{GD_y} + \frac{3L^2 - 4a^2}{24EJ_x} \right) V_y a \tag{1.188}$$

1.5.2 Warping-torsion problem for a doubly-symmetric cross-section beam

In the absence of distributed twisting moment and bimoment, the warping-torsion problem of Eqs. 1.74–1.75 takes the homogeneous form:

$$GJ_t \varphi_z'' + GD_\omega \left(\varphi_z'' + \Psi' \right) = 0 \tag{1.189}$$

$$GD_\omega \left(\varphi_z' + \Psi \right) - EJ_\omega \Psi'' = 0 \tag{1.190}$$

The solution to the fourth-order characteristic equation is represented by two real and opposite eigenvalues and by two null eigenvalues. Hence, torsional rotation and cross-section warping may be given the expressions:

$$\varphi_z(z) = A_1 \cosh(\lambda z) + A_2 \sinh(\lambda z) + A_3 + A_4 z \tag{1.191}$$

$$\Psi(z) = B_1 \sinh(\lambda z) + B_2 \cosh(\lambda z) + B_3 \tag{1.192}$$

where

$$\lambda = \frac{\sqrt{GJ_t}}{\sqrt{EJ_\omega}\sqrt{1 + GJ_t/GD_\omega}} \tag{1.193}$$

is the absolute value of non-zero eigenvalues and A_i ($i = 1, \ldots, 4$), B_i ($i = 1, 2, 3$) are two sets of unknown constants. Substituting Eqs. 1.191–1.192 into equilibrium equations 1.189–1.190 leads to the following relations:

$$B_1 = -\frac{A_1}{\lambda} \frac{GJ_t}{EJ_\omega}$$

$$B_2 = -\frac{A_2}{\lambda} \frac{GJ_t}{EJ_\omega} \tag{1.194}$$

$$B_3 = -A_4$$

revealing that the problem is ruled by four independent constants.

1.5.2.1 Cantilever beam subjected to a twisting moment at the free end

The first torsion problem analyzed concerns the cantilever beam shown in Figure 1.11.
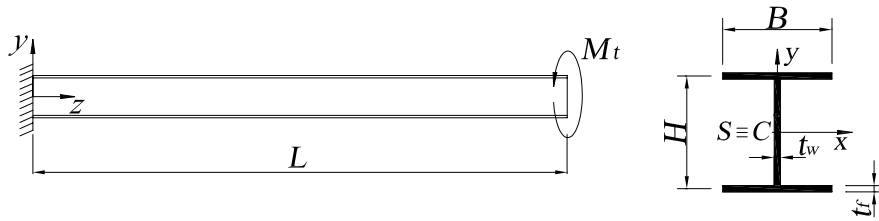
Figure 1.11. Cantilever I-beam subjected to a twisting moment at the free end.

Imposing the following four boundary conditions:

$$\varphi_z(0) = 0 \tag{1.195}$$

$$\Psi(0) = 0 \tag{1.196}$$

$$M_z(L) = GJ_t\varphi_z'(L) + GD_\omega\left[\varphi_z'(L) + \Psi(L)\right] = M_t \tag{1.197}$$

$$M_\omega(L) = EJ_\omega\Psi'(L) = 0 \tag{1.198}$$

yield the solutions:

$$\varphi_z(z) = \frac{M_t}{GJ_t}\left\{z - \frac{EJ_\omega}{GJ_t}\lambda\left[\tanh(\lambda L) - \operatorname{sech}(\lambda L)\sinh(\lambda L - \lambda z)\right]\right\} \tag{1.199}$$

$$\Psi(z) = \frac{M_t}{GJ_t}\left[\frac{\cosh(\lambda L - \lambda z)}{\cosh(\lambda L)} - 1\right] \tag{1.200}$$

End torsional rotation and cross-section warping are given by:

$$\varphi_z(L) = \frac{M_t}{GJ_t}\left[L - \frac{EJ_\omega}{GJ_t}\lambda \tanh(\lambda L)\right] \tag{1.201}$$

$$\Psi(L) = \frac{M_t}{GJ_t}\left[\mathrm{sech}(\lambda L) - 1\right] \tag{1.202}$$

Taking the limit of the two previous equations for $L \to \infty$ yields:

$$\lim_{L \to \infty}\frac{\varphi_z(L)}{L} = -\lim_{L \to \infty}\Psi = \frac{M_t}{GJ_t} \tag{1.203}$$

which corresponds to the well-known De Saint Venànt solution.

1.5.2.2 Simply-supported beam subjected to a twisting moment at midspan

The I-section profile shown in Figure 1.12 is analyzed. The restraints act as flexural-torsional supports, leaving the end-sections free to warp and to rotate about x- and y-axis.
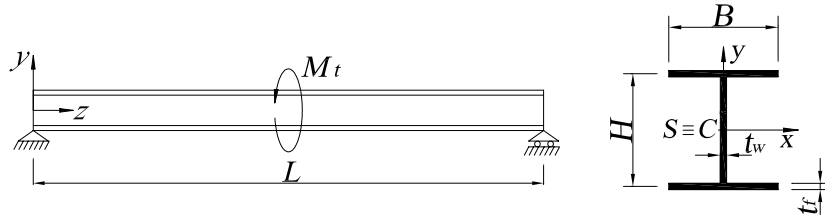
Figure 1.12. Simply-supported I-section beam subjected to a twisting moment at midspan.

The following four boundary conditions hold:

$$\varphi_z(0) = 0 \tag{1.204}$$

$$\Psi'(0) = 0 \tag{1.205}$$

$$\Psi(L/2) = 0 \tag{1.206}$$

$$GJ_t\varphi_z'(0) + GD_\omega\left[\varphi_z'(0) + \Psi(0)\right] = M_t/2 \tag{1.207}$$

The solution is given by ($0 \le z \le L/2$):

$$\varphi_z(z) = \frac{M_t}{2GJ_t}\left[z - \lambda\frac{EJ_\omega}{GJ_t}\mathrm{sech}(\lambda L/2)\sinh(\lambda z)\right] \tag{1.208}$$

$$\Psi(z) = \frac{M_t}{2GJ_t}\left[\mathrm{sech}(\lambda L/2)\cosh(\lambda z) - 1\right] \tag{1.209}$$

At midspan, torsional rotation takes the expression:

$$\varphi_z\left(L/2\right) = \frac{M_t}{2GJ_t}\left[\frac{L}{2} - \lambda\frac{EJ_\omega}{GJ_t}\tanh\left(\lambda L/2\right)\right] \tag{1.210}$$

Taking the limit of Eq. 1.210 for $GJ_t \to 0$ yields the following linear function of $1/EJ_\omega$ and $1/GD_\omega$:

$$\varphi_z\left(L/2\right) = M_t L\left(\frac{L^2}{48EJ_\omega} + \frac{1}{4GD_\omega}\right) \tag{1.211}$$

1.5.2.3 Simply-supported beam subjected to two equal twisting moments at z = L/3 and z = 2L/3

The I-section profile of Figure 1.13 is now considered.
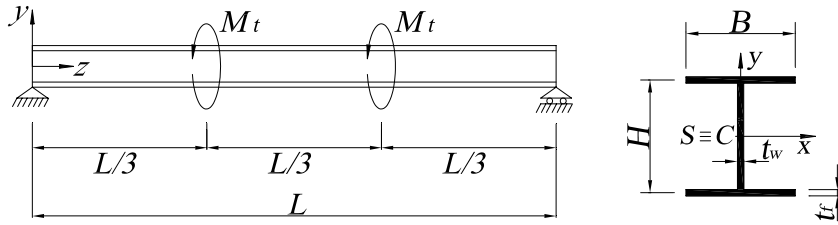
Figure 1.13. Simply-supported I-section beam subjected to two equal twisting moments at $z = L/3$ and $z = 2L/3$.

The set of boundary conditions is composed by Eqs. 1.204–1.207 and by the relations:

$$GJ_t\varphi_z'\left(0\right) + GD_\omega\left[\varphi_z'\left(0\right) + \Psi\left(0\right)\right] = M_t \tag{1.212}$$

$$\left[\!\left[GJ_t\varphi_z'\left(L/3\right) + GD_\omega\left[\varphi_z'\left(L/3\right) + \Psi\left(L/3\right)\right]\right]\!\right] = M_t \tag{1.213}$$

$$\left[\!\left[\varphi_z\left(L/3\right)\right]\!\right] = 0 \tag{1.214}$$

$$\left[\!\left[\Psi\left(L/3\right)\right]\!\right] = 0 \tag{1.215}$$

$$\left[\!\left[\Psi'\left(L/3\right)\right]\!\right] = 0 \tag{1.216}$$

The solution is given by:

$0 \leq z \leq L/3$

$$\varphi_z\left(z\right) = \frac{M_t}{GJ_t}\left\{z + \lambda\frac{EJ_\omega}{GJ_t\left[1 - 2\cosh\left(\lambda L/3\right)\right]}\sinh\left(\lambda z\right)\right\} \tag{1.217}$$

$$\Psi(z) = -\frac{M_t}{GJ_t}\left[1 + \frac{\cosh(\lambda z)}{1 - 2\cosh(\lambda L/3)}\right] \tag{1.218}$$

$$L/3 < z \le L/2$$

$$\varphi_z(z) = \frac{M_t}{GJ_t}\left\{\frac{L}{3} + \lambda\frac{EJ_\omega}{GJ_t}\Big[\sinh(\lambda L/3)\tanh(\lambda L/2)\sinh(\lambda z)\right.$$
$$\left. - \sinh(\lambda L/3)\cosh(\lambda z)\Big]\right\} \tag{1.219}$$

$$\Psi(z) = \frac{M_t}{GJ_t}\Big[\sinh(\lambda L/3)\sinh(\lambda z) - \sinh(\lambda L/3)\tanh(\lambda L/2)\cosh(\lambda z)\Big] \tag{1.220}$$

In particular, for $z = L/3$ and $z = L/2$, φ_z is respectively given by:

$$\varphi_z(L/3) = \frac{M_t}{GJ_t}\left\{\frac{L}{3} + \lambda\frac{EJ_\omega}{GJ_t}\frac{\sinh(\lambda L/3)}{\left[1 - 2\cosh(\lambda L/3)\right]}\right\} \tag{1.221}$$

$$\varphi_z(L/2) = \frac{M_t}{GJ_t}\left[\frac{L}{3} - \lambda\frac{EJ_\omega}{GJ_t}\frac{\sinh(\lambda L/3)}{\cosh(\lambda L/2)}\right] \tag{1.222}$$

Taking the limit of Eqs. 1.221 and 1.222 for $GJ_t \to 0$ leads to the following linear functions of $1/EJ_\omega$ and $1/GD_\omega$:

$$\varphi_z(L/3) = M_t L\left(\frac{5L^2}{162 EJ_\omega} + \frac{1}{3GD_\omega}\right) \tag{1.223}$$

$$\varphi_z(L/2) = M_t L\left(\frac{23L^2}{648 EJ_\omega} + \frac{1}{3GD_\omega}\right) \tag{1.224}$$

1.5.3 Warping-shear coupled problem for a monosymmetric cross-section beam

For C-shaped cross-section beams, the warping-torsion problem and the shear-bending problem referred to the plane orthogonal to the symmetry plane turn out to be coupled. In particular, identifying plane y-z with the symmetry plane ($D_{xy} = D_{y\omega} = 0$), equilibrium equations 1.64, 1.65, 1.68, 1.69 take the homogeneous form:

$$GD_x u_S'' - GD_x \varphi_y' + GD_{x\omega}\varphi_z'' + GD_{x\omega}\Psi' = 0 \tag{1.225}$$

$$-GD_x u_S' + GD_x \varphi_y - EJ_y \varphi_y'' - GD_{x\omega}\varphi_z' - GD_{x\omega}\Psi = 0 \tag{1.226}$$

$$GD_{x\omega} u_S'' - GD_{x\omega}\varphi_y' + \left(GD_\omega + GJ_t\right)\varphi_z'' + GD_\omega\Psi' = 0 \tag{1.227}$$

$$GD_{x\omega} u_S' - GD_{x\omega}\varphi_y + GD_\omega\varphi_z' + GD_\omega\Psi - EJ_\omega\Psi'' = 0 \tag{1.228}$$

The solution to the eight-order characteristic equation is represented by two real and opposite eigenvalues and by six null eigenvalues. Hence, the four displacement fields unknown may be given the expressions:

$$u_S(z) = A_1 \cosh(\lambda z) + A_2 \sinh(\lambda z) + A_3 + A_4 z + A_5 z^2 + A_6 z^3 \tag{1.229}$$

$$\varphi_y(z) = B_1 \sinh(\lambda z) + B_2 \cosh(\lambda z) + B_3 + B_4 z + B_5 z^2 \tag{1.230}$$

$$\varphi_z(z) = C_1 \cosh(\lambda z) + C_2 \sinh(\lambda z) + C_3 + C_4 z + C_5 z^2 + C_6 z^3 \tag{1.231}$$

$$\Psi(z) = D_1 \sinh(\lambda z) + D_2 \cosh(\lambda z) + D_3 + D_4 z + D_5 z^2 \tag{1.232}$$

where

$$\lambda = \frac{\sqrt{GJ_t}}{\sqrt{EJ_\omega}\sqrt{1 - \dfrac{GD_x \cdot GJ_t}{GD_{x\omega}^2 - GD_x \cdot GD_\omega}}} \tag{1.233}$$

is the absolute value of non-zero eigenvalues and A_i, C_i ($i = 1, \ldots, 6$) and B_i, D_i ($i = 1, \ldots, 5$) are four sets of unknown constants. Substituting Eqs. 1.229–1.232 into equilibrium equations 1.225–1.228 enables the displacement fields u_S, φ_y, φ_z, Ψ to be written as a function of eight independent constants, i.e.:

$$u_S(z) = A_1 \cosh(\lambda z) + A_2 \sinh(\lambda z) + A_3 + A_4 z + A_5 z^2 + A_6 z^3 \tag{1.234}$$

$$\varphi_y(z) = A_4 + 2A_5 z + \left(3z^2 - \frac{6EJ_y GD_\omega}{GD_{x\omega}^2 - GD_x GD_\omega}\right)A_6 \tag{1.235}$$

$$\begin{aligned}\varphi_z(z) = &-A_1 \frac{\left(GD_{x\omega}^2 - GD_x GD_\omega + EJ_\omega GD_x \lambda^2\right)}{EJ_\omega GD_{x\omega}\lambda^2}\cosh(\lambda z)\\ &-A_2 \frac{\left(GD_{x\omega}^2 - GD_x GD_\omega + EJ_\omega GD_x \lambda^2\right)}{EJ_\omega GD_{x\omega}\lambda^2}\sinh(\lambda z) + C_3 + C_4 z\end{aligned} \tag{1.236}$$

$$\begin{aligned}\Psi(z) = &A_1 \frac{\left(GD_{x\omega}^2 - GD_x GD_\omega\right)}{EJ_\omega GD_{x\omega}\lambda}\sinh(\lambda z)\\ &+A_2 \frac{\left(GD_{x\omega}^2 - GD_x GD_\omega\right)}{EJ_\omega GD_{x\omega}\lambda}\cosh(\lambda z) - A_6 \frac{6EJ_y GD_{x\omega}}{GD_{x\omega}^2 - GD_x GD_\omega} - C_4\end{aligned} \tag{1.237}$$

1.5.3.1 Cantilever beam subjected to a twisting moment at the free end

The cantilever C-section profile shown in Figure 1.14 is analyzed.
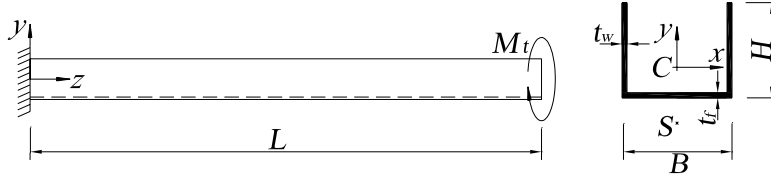
Figure 1.14. Cantilever C-section beam subjected to a twisting moment at the free end.

The following four boundary conditions hold:

$$u_S(0) = 0 \tag{1.238}$$

$$\varphi_y(0) = 0 \tag{1.239}$$

$$\varphi_z(0) = 0 \tag{1.240}$$

$$\Psi(0) = 0 \tag{1.241}$$

$$GJ_t\varphi_z'(L) + GD_{x\omega}\left[u_S'(L) - \varphi_y(L)\right] + GD_\omega\left[\varphi_z'(L) + \Psi(L)\right] = M_t \tag{1.242}$$

$$\varphi_y'(L) = 0 \tag{1.243}$$

$$\Psi'(L) = 0 \tag{1.244}$$

$$GD_x\left[u_S'(L) - \varphi_y(L)\right] + GD_{x\omega}\left[\varphi_z'(L) + \Psi(L)\right] = 0 \tag{1.245}$$

The displacement fields are given by:

$$u_S(z) = \frac{2EJ_\omega GD_{x\omega}\lambda \sinh(\lambda z/2)\cosh(\lambda L - \lambda z/2)}{D_{uS}}M_t \tag{1.246}$$

$$\varphi_y(z) = 0 \tag{1.247}$$

$$\varphi_z(z) = \frac{M_t}{\lambda D_{uS}}\left\{\left(GD_{x\omega}^2 - GD_xGD_\omega\right)\lambda z \cosh(\lambda L)\right.$$
$$\left. - \left(GD_{x\omega}^2 - GD_xGD_\omega + EJ_\omega GD_x\lambda^2\right)\left[\sinh(\lambda L) - \sinh(\lambda L - \lambda z)\right]\right\} \tag{1.248}$$

$$\Psi(z) = -\frac{2\left(GD_{x\omega}^2 - GD_xGD_\omega\right)\sinh(\lambda z/2)\sinh(\lambda L - \lambda z/2)}{D_{uS}}M_t \tag{1.249}$$

with

$$D_{uS} = GD_{x\omega}^2\left(EJ_\omega\lambda^2 - GJ_t\right) + GD_x\left(GD_\omega GJ_t - EJ_\omega GD_\omega\lambda^2 - EJ_\omega GJ_t\lambda^2\right)$$
$$+ \left(GD_{x\omega}^2 - GD_xGD_\omega\right)GJ_t\cosh(\lambda L) \tag{1.250}$$

For $z = L$ Eqs. 1.246, 1.248−1.249 reduce to:

$$u_S(L) = \frac{GD_{x\omega}\tanh(\lambda L)}{\left[GD_{x\omega}^2 - GD_x(GD_\omega + GJ_t)\right]\lambda}M_t \tag{1.251}$$

$$\varphi_z(L) = -\frac{M_t\,\mathrm{sech}(\lambda L)}{GJ_t\lambda\left[GD_{x\omega}^2 - GD_x(GD_\omega + GJ_t)\right]}\left\{\left(GD_{x\omega}^2 - GD_x GD_\omega\right)\sinh(\lambda L)\right.$$
$$\left. -\lambda L\left[GD_{x\omega}^2 - GD_x(GD_\omega + GJ_t)\right]\cosh(\lambda L)\right\} \tag{1.252}$$

$$\Psi(L) = \frac{\mathrm{sech}(\lambda L)-1}{GJ_t}M_t \tag{1.253}$$

1.5.3.2 Simply-supported beam subjected to a twisting moment at midspan

The simply-supported C-section profile shown in Figure 1.15 is analyzed.
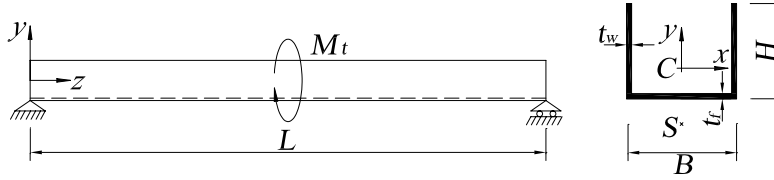
Figure 1.15. Simply-supported C-section beam subjected to a twisting moment at midspan.

The following eight boundary conditions hold:

$$u_S(0) = 0 \tag{1.254}$$

$$\varphi_y'(0) = 0 \tag{1.255}$$

$$\varphi_z(0) = 0 \tag{1.256}$$

$$\Psi'(0) = 0 \tag{1.257}$$

$$GJ_t\varphi_z'(0) + GD_{x\omega}\left[u_S'(0) - \varphi_y(0)\right] + GD_\omega\left[\varphi_z'(0) + \Psi(0)\right] = M_t/2 \tag{1.258}$$

$$\varphi_y(L/2) = 0 \tag{1.259}$$

$$\Psi(L/2) = 0 \tag{1.260}$$

$$GD_x\left[u_S'(0) - \varphi_y(0)\right] + GD_{x\omega}\left[\varphi_z'(0) + \Psi(0)\right] = 0 \tag{1.261}$$

The displacement fields are given by ($0 \le z \le L/2$):

$$u_S(z) = \frac{M_t}{2\lambda}\frac{GD_{x\omega}}{\left[GD_{x\omega}^2 - GD_x(GD_\omega + GJ_t)\right]}\mathrm{sech}(\lambda L/2)\sinh(\lambda z) \tag{1.262}$$

$$\varphi_y(z) = 0 \tag{1.263}$$

$$\varphi_z(z) = -\frac{M_t}{2\lambda^3 EJ_\omega GJ_t \left[GD_{x\omega}^2 - GD_x(GD_\omega + GJ_t) \right]} EJ_\omega \lambda^2 z \left[GD_x(GD_\omega + GJ_t) \right.$$

$$\left. -GD_{x\omega}^2 \right] + GJ_t \left[GD_{x\omega}^2 - GD_x(GD_\omega - EJ_\omega \lambda^2) \right] \text{sech}(\lambda L/2) \sinh(\lambda z) \tag{1.264}$$

$$\Psi(z) = -\frac{M_t}{2\lambda^2} \left\{ \frac{\lambda^2}{EJ_\omega GJ_t} - \frac{(GD_{x\omega}^2 - GD_x GD_\omega) \text{sech}(\lambda L/2) \cosh(\lambda z)}{EJ_\omega \left[GD_{x\omega}^2 - GD_x(GD_\omega + GJ_t) \right]} \right\} \tag{1.265}$$

For $GJ_t \to 0$, Eqs. 1.262 and 1.264 reduce to the polynomial expressions

$$u_S(z) = \frac{M_t z}{2} \frac{GD_{x\omega}}{GD_{x\omega}^2 - GD_x GD_\omega} \tag{1.266}$$

$$\varphi_z(z) = \frac{M_t z}{2} \left[\frac{(3L^2 - 4z^2)}{24EJ_\omega} - \frac{GD_x}{GD_{x\omega}^2 - GD_x GD_\omega} \right] \tag{1.267}$$

1.5.3.3 Simply-supported beam subjected to two equal twisting moments at z = a and z = L−a

The C-section profile of Figure 1.16 is now considered.
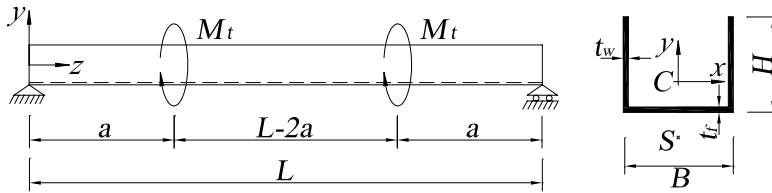
Figure 1.16. Simply-supported C-section beam subjected to a twisting moment at $z = a$ and $z = L−a$.

Imposing the boundary conditions at $z = 0$, a, $L/2$ leads to the following expressions of the displacement parameters ($\varphi_y = 0 \ \forall z$):

$0 \leq z \leq a$

$$u_S(z) = \frac{M_t}{GJ_t} \frac{EJ_\omega GD_{x\omega} \lambda}{(GD_{x\omega}^2 - GD_x GD_\omega)} \text{sech}(\lambda L/2) \cosh(\lambda a - \lambda L/2) \sinh(\lambda z) \tag{1.268}$$

$$\varphi_z(z) = \frac{M_t}{GJ_t \lambda} \{ \lambda z$$

$$-\frac{(GD_{x\omega}^2 - GD_x GD_\omega + EJ_\omega GD_x \lambda^2)}{(GD_{x\omega}^2 - GD_x GD_\omega)} \sinh(\lambda z) \cosh(\lambda a - \lambda L/2) \text{sech}(\lambda L/2) \} \tag{1.269}$$

$$\Psi(z) = \frac{M_t}{GJ_t} \left[\text{sech}(\lambda L/2) \cosh(\lambda a - \lambda L/2) \cosh(\lambda z) - 1 \right] \tag{1.270}$$

$a \leq z \leq L/2$

$$u_S(z) = \frac{M_t}{GJ_t} \frac{EJ_\omega GD_{x\omega} \lambda}{\left(GD_{x\omega}^2 - GD_x GD_\omega\right)} \sinh(a\lambda) \operatorname{sech}(\lambda L/2) \cosh(\lambda L/2 - \lambda z) \tag{1.271}$$

$$\varphi_z(z) = \frac{M_t}{GJ_t} \left\{ a - \frac{EJ_\omega \lambda \sinh(a\lambda)\left[\cosh(\lambda z) + \tanh(\lambda L/2)\sinh(\lambda z)\right]}{GJ_t} \right\} \tag{1.272}$$

$$\Psi(z) = -\frac{M_t}{GJ_t} \sinh(a\lambda) \operatorname{sech}(\lambda L/2) \sinh(\lambda L/2 - \lambda z) \tag{1.273}$$

For $GJ_t \to 0$, lateral displacements and torsional rotations at $z = a$, $L/2$ take the polynomial expressions

$$u_S(a) = u_S(L/2) = \frac{M_t GD_{x\omega} a}{GD_{x\omega}^2 - GD_x GD_\omega} \tag{1.274}$$

$$\varphi_z(a) = M_t a \left[-\frac{\left(4a^2 - 3aL\right)}{6EJ_\omega} - \frac{GD_x}{\left(GD_{x\omega}^2 - GD_x GD_\omega\right)} \right] \tag{1.275}$$

$$\varphi_z(L/2) = M_t a \left[-\frac{\left(4a^2 - 3aL\right)}{24EJ_\omega} - \frac{GD_x}{\left(GD_{x\omega}^2 - GD_x GD_\omega\right)} \right] \tag{1.276}$$

1.5.4 Shear-shear coupled problem for a nonsymmetric cross-section beam

The cantilever Z-section beam shown in Figure 1.17 is finally considered. Since the shear center coincide with the centroid, but axes x and y are not principal, the relations between bending moments and rates of cross-sectional flexural rotation are given by (see Eq. 1.21):

$$M_x = EJ_x \varphi_x' - EJ_{xy} \varphi_y' \tag{1.277}$$

$$M_y = -EJ_{xy} \varphi_x' + EJ_y \varphi_y' \tag{1.278}$$
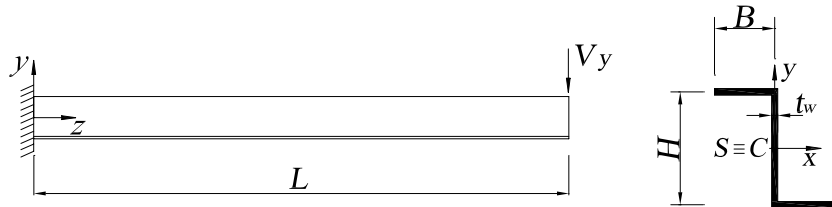
Figure 1.17. Cantilever Z-section beam subjected to a transversal force (y direction) at the free end.

Hence, in the absence of distributed forces and moments, substituting Eqs. 1.277 and 1.278 into Eqs. 1.60 and 1.58, considering Eqs. 1.59 and 1.57 and assuming $D_{x\omega} = D_{y\omega}$ = 0 ($S \equiv C$) lead to the following set of homogeneous equations governing the coupled bending problem into x-z and y-z planes:

$$GD_x \left(u_S'' - \varphi_y' \right) + GD_{xy} \left(v_S'' + \varphi_x' \right) = 0 \tag{1.279}$$

$$-EJ_{xy} \varphi_x'' + EJ_y \varphi_y'' + GD_x \left(u_S' - \varphi_y \right) + GD_{xy} \left(v_S' + \varphi_x \right) = 0 \tag{1.280}$$

$$GD_{xy} \left(u_S'' - \varphi_y' \right) + GD_y \left(v_S'' + \varphi_x' \right) = 0 \tag{1.281}$$

$$EJ_x \varphi_x'' - EJ_{xy} \varphi_y'' - GD_{xy} \left(u_S' - \varphi_y \right) - GD_y \left(v_S' + \varphi_x \right) = 0 \tag{1.282}$$

The solution in terms of the four displacement fields u_S, φ_y, v_S and φ_x, presenting polynomial form, can be written as follows:

$$u_S(z) = \frac{6EJ_{xy}^2 GD_{xy} - 6EJ_x EJ_y GD_{xy} + EJ_{xy} z \left(GD_{xy}^2 - GD_x GD_y \right)(3L - z)}{6 \left(EJ_{xy}^2 - EJ_x EJ_y \right) \left(GD_{xy}^2 - GD_x GD_y \right)} V_y z \tag{1.283}$$

$$\varphi_y(z) = \frac{EJ_{xy} (2L - z)}{2 \left(EJ_{xy}^2 - EJ_x EJ_y \right)} V_y z \tag{1.284}$$

$$v_S(z) = -\frac{6EJ_{xy}^2 GD_x - 6EJ_x EJ_y GD_x + EJ_y z \left(GD_{xy}^2 - GD_x GD_y \right)(3L - z)}{6 \left(EJ_{xy}^2 - EJ_x EJ_y \right) \left(GD_{xy}^2 - GD_x GD_y \right)} V_y z \tag{1.285}$$

$$\varphi_x(z) = \frac{EJ_y (2L - z)}{2 \left(EJ_{xy}^2 - EJ_x EJ_y \right)} V_y z \tag{1.286}$$

Hence, end displacements are given by:

$$u_S(z) = \frac{3EJ_{xy}^2 GD_{xy} - 3EJ_x EJ_y GD_{xy} + EJ_{xy} L^2 \left(GD_{xy}^2 - GD_x GD_y \right)}{3 \left(EJ_{xy}^2 - EJ_x EJ_y \right) \left(GD_{xy}^2 - GD_x GD_y \right)} V_y L \tag{1.287}$$

$$v_S(z) = -\frac{3EJ_{xy}^2 GD_x - 3EJ_x EJ_y GD_x + EJ_y L^2 \left(GD_{xy}^2 - GD_x GD_y \right)}{3 \left(EJ_{xy}^2 - EJ_x EJ_y \right) \left(GD_{xy}^2 - GD_x GD_y \right)} V_y L \tag{1.288}$$

1.6 Test configurations for the evaluation of full section properties of FRP pultruded profiles

An alternative procedure to estimate the full section properties defined in § 1.3 is based on the use of analytical solutions in terms of displacements or torsional rotation in conjunction with experimental results. With reference to pultruded beams with doubly-symmetric cross-section, Roberts & Al-Ubaidi (2002) and Roberts & Masri (2003) suggested a method to evaluate typical full section properties of Timoshenko's bending theory and Vlasov's torsion theory. For example purposes, an I-section FRP pultruded profile is considered in the following. Test configurations and resulting expressions for rigidities $\overline{EJ_i}$, $\overline{GD_i}$ and $\overline{GJ_t}$ ($i = x, y, \omega$), which govern Timoshenko-Reissner's model, are detailed in the following highlighting the errors due to displacement measurement uncerainties.

1.6.1 Four point bending test

A typical four point (major axis) bending test configuration is illustrated in Figure 1.18a (type 1). Substituting measured deflection values $v_1 = |v_S(a)|$, $v_2 = |v_S(L/2)|$ into Eqs. 1.187, 1.188 and solving for $1/\overline{EJ_x}$ and $1/\overline{GD_y}$ yield:

$$\frac{1}{\overline{EJ_x}} = \frac{8(v_2 - v_1)}{a(L-2a)^2 P} \tag{1.289}$$

$$\frac{1}{\overline{GD_y}} = \frac{4a(4a-3L)v_2 - (4a^2 - 3L^2)v_1}{3a(L-2a)^2 P} = \frac{4(3L-4a)}{3(L-2a)^2 P}(\lambda v_1 - v_2) \tag{1.290}$$

where

$$\lambda = \frac{(3L^2 - 4a^2)}{4a(3L-4a)} \tag{1.291}$$

In order to put in evidence the influence of measurement uncertainties Δv_1, Δv_2, Eqs. 1.289–1.290 are rewritten as follows:

$$\frac{1}{\overline{EJ_x}} \pm \Delta\left(\frac{1}{\overline{EJ_x}}\right) = \frac{8}{a(L-2a)^2 P}\left[(v_2 \pm \Delta v_2) - (v_1 \pm \Delta v_1)\right] \tag{1.292}$$

$$\frac{1}{\overline{GD_y}} \pm \Delta\left(\frac{1}{\overline{GD_y}}\right) = \frac{4(3L-4a)}{3(L-2a)^2 P}\left[\lambda(v_1 \pm \Delta v_1) - (v_2 \pm \Delta v_2)\right] \tag{1.293}$$

and, consequently, the errors can be expressed as:
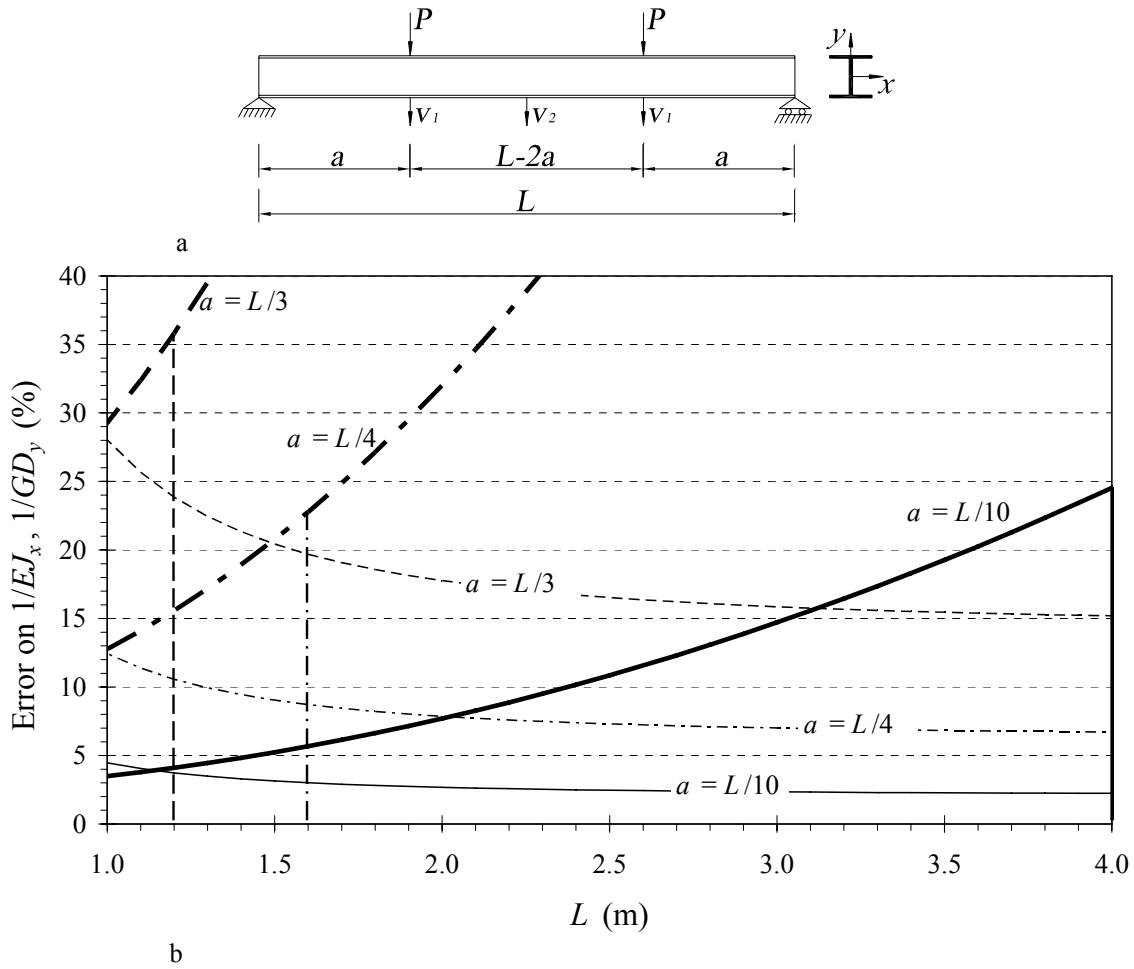
Figure 1.18. a: major axis four point bending test (type 1) on a FRP I-profile with $E = 23$ MPa, $G = 3$ MPa, $H = 200$ mm, $B = 100$ mm and $t = 10$ mm. b: error in the evaluation of bending (thin lines) and shear (thick lines) rigidities versus the beam length for measurement uncertainties $\Delta v_i / v_i = 1\%$ $(i = 1, 2)$.

$$\pm \frac{\Delta\left(1/\overline{EJ_x}\right)}{1/\overline{EJ_x}} = \pm \frac{\left(\Delta v_2 / v_2\right)\left(v_2 / v_1\right)}{\left(v_2 / v_1 - 1\right)} \pm \frac{\left(\Delta v_1 / v_1\right)}{\left(v_2 / v_1 - 1\right)} \tag{1.294}$$

$$\pm \frac{\Delta\left(1/\overline{GD_y}\right)}{1/\overline{GD_y}} = \pm \frac{\left(\Delta v_2 / v_2\right)\left(v_2 / v_1\right)}{\left(v_2 / v_1 - \lambda\right)} \pm \frac{\lambda\left(\Delta v_1 / v_1\right)}{\left(v_2 / v_1 - \lambda\right)} \tag{1.295}$$

Now for a given profile the ratio v_2/v_1 may be estimated by inserting in Eqs. 1.187−1.188 the values of elasticity moduli and geometrical properties reported by the manufacturer. In this case, a narrow-flange profile with $H = 200$ mm, $B = 100$ mm and $t = 10$ mm produced by Fiberline Composites (Design Manual 2003), characterized by $E = 23$ GPa, $G = 3$ GPa, $J_x = 2.36 \times 10^{-5}$ m^4 and $D_y = 1.90 \times 10^{-3}$ m^2, was chosen.

Figure 1.19. a: minor axis four point bending test (type 1). b: error in the evaluation of bending (thin lines) and shear (thick lines) rigidities versus the beam.

Moreover, typical measurement uncertainties $\Delta v_i / v_i = 1\%$ ($i = 1, 2$) were assumed. In Figure 1.18b, errors $\left| \Delta\left(1/\overline{EJ_x}\right) \middle/ \left(1/\overline{EJ_x}\right) \right|$ and $\left| \Delta\left(1/\overline{GD_y}\right) \middle/ \left(1/\overline{GD_y}\right) \right|$, represented by thin and thick lines, respectively, are reported versus the beam length ($1\text{ m} \le L \le 4\text{ m}$) for the three load positions $a = L/3$, $L/4$ and $L/10$. It should be noted that errors on the bending rigidity strongly depend on a, attaining, at $L = 4$ m, the values 15.0%, 6.7% and 2.2% for $a = L/3$, $L/4$ and $L/10$, respectively. Moreover, for a given load position function, $\left| \Delta\left(1/\overline{EJ_x}\right) \middle/ \left(1/\overline{EJ_x}\right) \right|$ lightly decreases with the beam length. Vice versa, errors on the shear rigidity rapidly increase with L. On the other hand, in order to avoid the drawbacks related to disturbed regions, the condition $a \ge 2H$ must be satisfied, giving, for the three cases examined, $L \ge 1.2$ m, 1.6 m and 4.0 m (vertical lines in Fig. 1.18b). Hence, errors $\left| \Delta\left(1/\overline{GD_y}\right) \middle/ \left(1/\overline{GD_y}\right) \right|$ attain the minimum values 36.0%, 22.5% and 24.5% for $a = L/3$, $L/4$ and $L/10$, respectively.

Figure 1.20. a: major axis four point bending test (type 2). b: error in the evaluation of bending (thin line) and shear (thick lines) rigidities versus the beam length.

The same procedure may be used to obtain the full section properties governing bending into the weak plane (Fig. 1.19a). In this case, parameters $J_y = 1.69 \times 10^{-6}$ m^4 and $D_x = 1.60 \times 10^{-3}$ m^2 (Fiberline Design Manual 2003) were introduced into Eqs. 1.187–1.188 to estimate deflections $u_1 = |u_S(a)|$ and $u_2 = |u_S(L/2)|$. Now the ratio J_y/D_x is one order of magnitude lower than J_x/D_y and shear strains are expected to play a less important role. As a consequence, the errors on the shear rigidity turn out to be unacceptable (Fig. 1.19b) and a different test configuration is needed.

With reference to the four point bending test of Figures 1.20a–1.21a (type 2), bending and shear rigidities can be determined using measured deflections $v_1 = |v_S(0)|$ and $v_2 = |v_S(L/2)|$. In particular, the following relations hold ($i, j = x, y$):

$$\frac{1}{\overline{EJ}_i} = \frac{8v_2}{a(L-2a)^2 P} \tag{1.296}$$

$$\frac{1}{\overline{GD}_j} = \frac{4a(4a-3L)v_2 + 3(L-2a)^2 v_1}{3a(L-2a)^2 P} = \frac{(v_1 - \mu v_2)}{3aP} \tag{1.297}$$
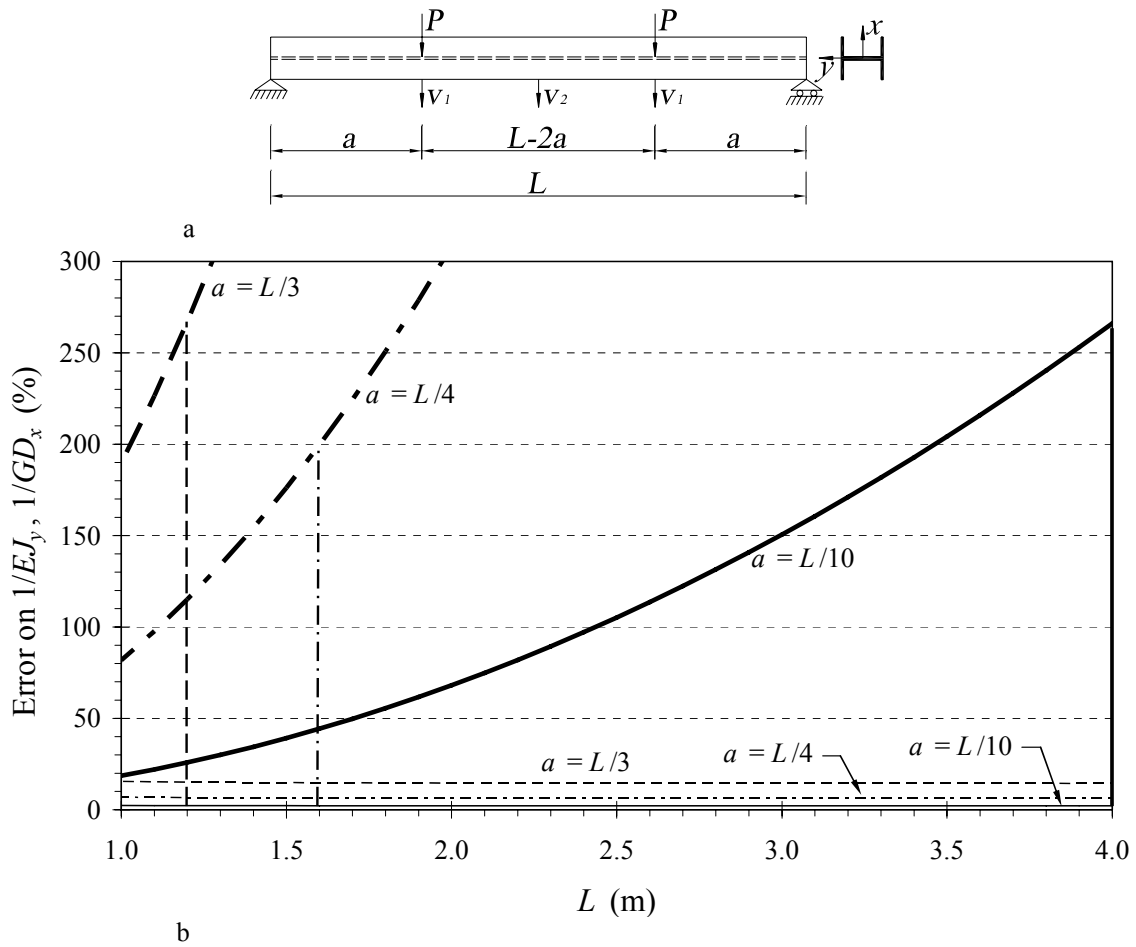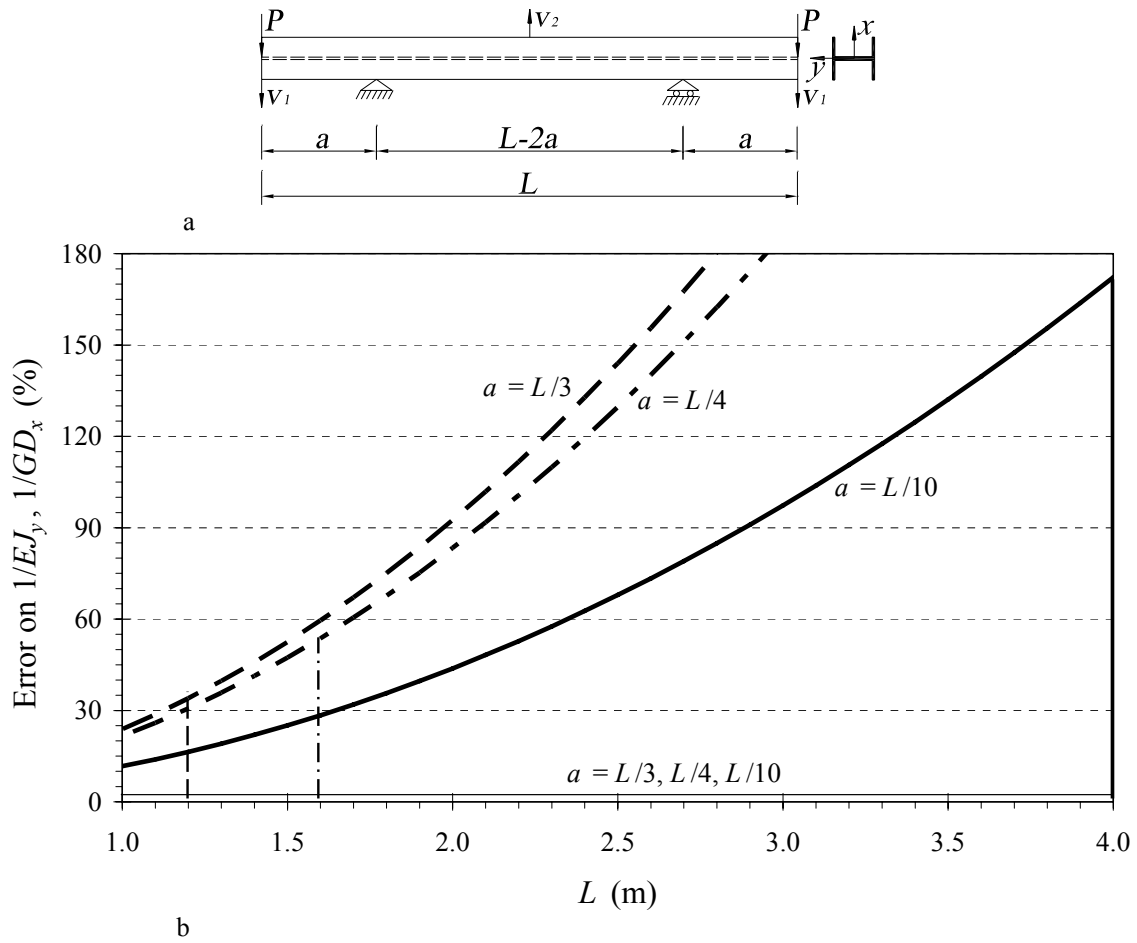
Figure 1.21. a: minor axis four point bending test (type 2). b: error in the evaluation of bending (thin line) and shear (thick lines) rigidities versus the beam length.

with

$$\mu = \frac{4a(3L-4a)}{3(L-2a)^2} \tag{1.298}$$

The error on the shear rigidities can be posed in the form 1.295, whereas the error on bending rigidities is now constantly given by:

$$\pm \frac{\Delta\left(1/\overline{EJ_x}\right)}{1/\overline{EJ_x}} = \pm \frac{\Delta v_2}{v_2} = \pm 0.01 \tag{1.299}$$

The error functions for major and minor axis bending are reported in Figures 1.20b and 1.21b, respectively. It should be noted that rigidities can be predicted more

accurately than in the previous four point test. For example, major axis shear rigidity is affected by minimum errors of about 3.8%, 5.4% and 15.5% for $a = L/3$, $L/4$ and $L/10$, respectively. The error on the minor axis shear rigidity takes, for $a = L/3$, the minimum value of 32.5%, much lower than in four point test of type 1, but still not negligible. On the other hand, for the GFRP narrow-flange I-profile examined, shear deformations on minor axis bending behaviour may be disregarded for practical slenderness values. Vice versa, for wide-flange profiles, for which the ratio J_y/D_x between minor axis geometrical properties is one order of magnitude higher than for narrow-flange beams with same height, shear deformations are generally to be taken into account also in the minor axis bending behaviour. In this case, however, errors on shear rigidities are quite lower. For example, assuming $H = B = 200$ mm, $t = 10$ mm and same material properties as in the previous case, the minimum error on $1/\overline{GD_x}$ for $a = L/3$ is of about 6.3%.
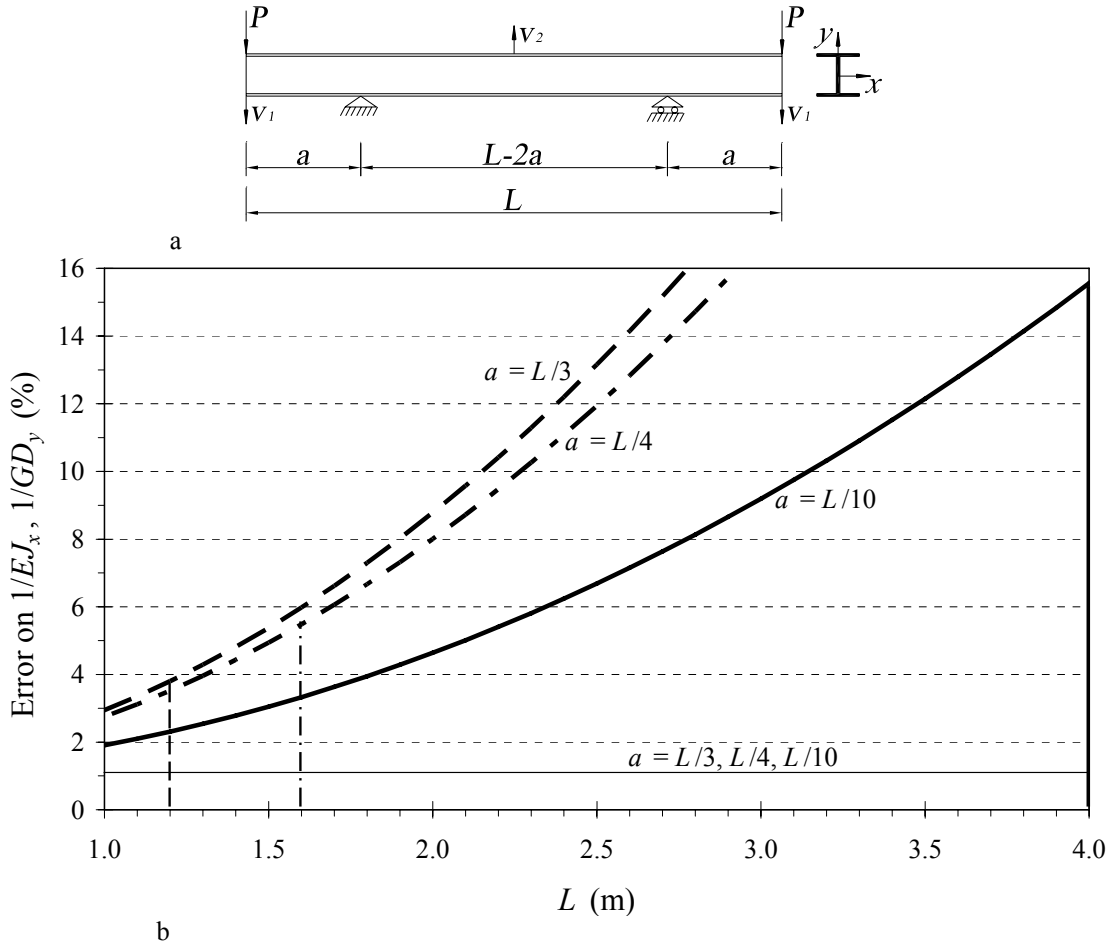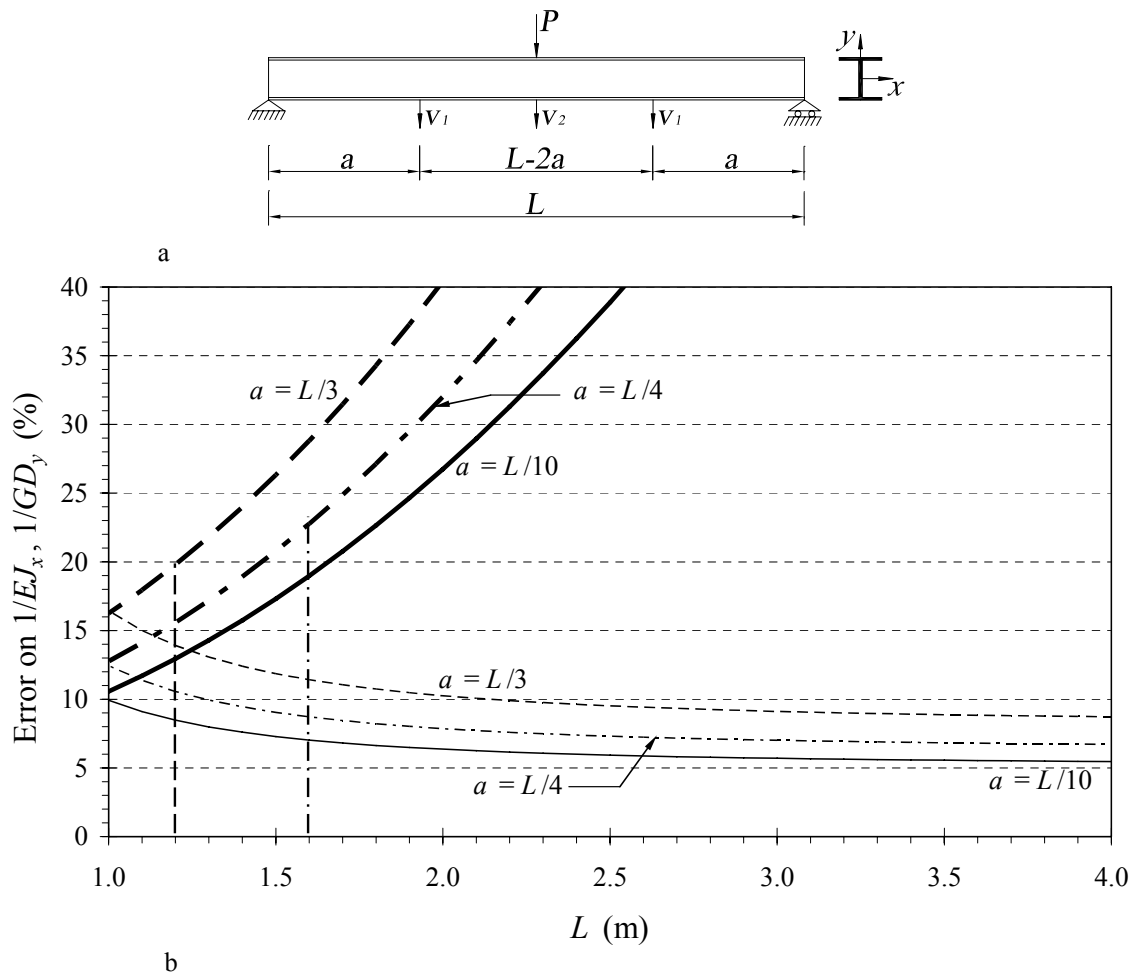

Figure 1.22. a: major axis three point bending test. b: error in the evaluation of bending (thin line) and shear (thick lines) rigidities versus the beam length.
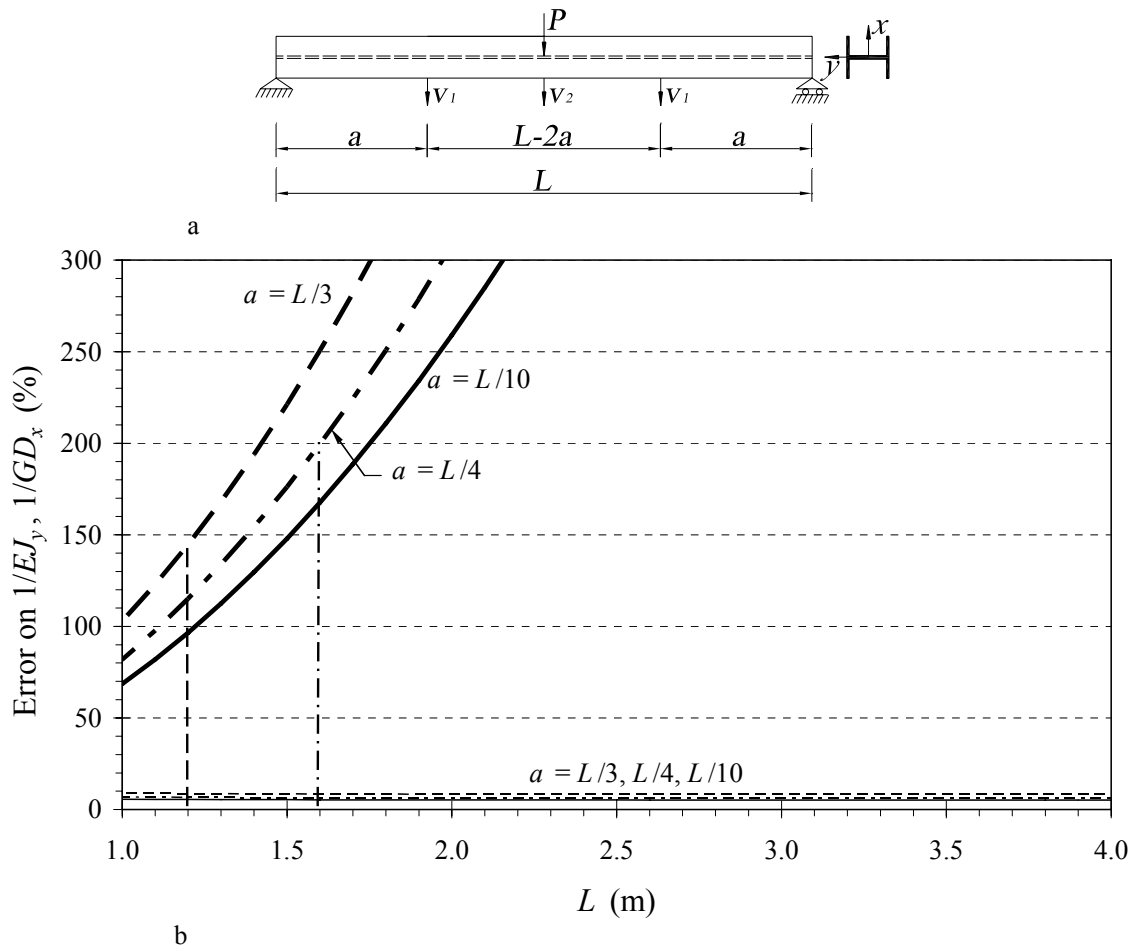
Figure 1.23. a: minor axis three point bending test. b: error in the evaluation of bending (thin line) and shear (thick lines) rigidities versus the beam length.

1.6.2 Three point bending test

A typical three point bending test configuration is illustrated in Figures 1.22a and 1.23a. Substituting measured deflection values $v_1 = |v_S(a)|$ and $v_2 = |v_S(L/2)|$ into Eqs. 1.173 (for $z = a$) and 1.174 and solving for $1/\overline{EJ_i}$ and $1/\overline{GD_j}$ $(i, j = x, y)$ yield now:

$$\frac{1}{\overline{EJ_i}} = \frac{48\left(v_1 - 2av_2/L\right)}{a\left(L^2 - 4a^2\right)P} \tag{1.300}$$

$$\frac{1}{\overline{GD_j}} = \frac{4L^3 v_1 - 4a\left(3L^2 - 4a^2\right)v_2}{aL\left(4a^2 - L^2\right)P} = \frac{4L^3}{aL\left(4a^2 - L^2\right)P}\left(v_1 - \rho v_2\right) \tag{1.301}$$

where

$$\rho = \frac{a\left(3L^2 - 4a^2\right)}{L^3} \tag{1.302}$$

The error on the shear rigidities can still be posed in the form 1.295, whereas the error on the bending rigidity takes the expression:

$$\pm\frac{\Delta\left(1/\overline{EJ}_i\right)}{1/\overline{EJ}_i} = \pm\frac{\left(\Delta v_1/v_1\right)\left(v_1/v_2\right)}{\left(v_1/v_2 - 2a/L\right)} \pm \frac{\left(2a/L\right)\left(\Delta v_2/v_2\right)}{\left(v_1/v_2 - 2a/L\right)} \tag{1.303}$$

Figures 1.22b and 1.23b report the errors versus the beam length in the case of major and minor axis bending, respectively (same narrow-flange profile as the previous figures). In this case, errors on shear rigidities turn out to be unacceptable.

1.6.3 Uniform torsion test

A uniform torsion test (Roberts & Al-Ubaidi 2002) is needed in order to obtain De Saint Venànt torsional rigidity $\overline{GJ}_t$. Indicating measured torsional rotations with $\varphi_{z1} = \varphi_z(a)$ and $\varphi_{z2} = \varphi_z(L-b)$ (Fig. 1.24), the following relation holds:

$$\overline{GJ}_t = \left|\frac{M_t\left(L - a - b\right)}{\varphi_{z1} - \varphi_{z2}}\right| \tag{1.304}$$
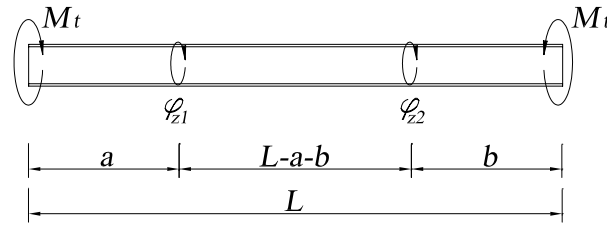
Figure 1.24. Uniform torsion test.

1.6.4 Three and four point torsion tests

Equation 1.208 or Eqs. 1.217, 1.219 can be used, in conjunction with Eq. 1.304, to obtain warping rigidity $\overline{EJ}_\omega$ and shear rigidity $\overline{GD}_\omega$ associated to nonuniform torsion. In particular, for open section (short) beams, neglecting the contribution of primary torsional rigidity $\overline{GJ}_t$ enables $\overline{EJ}_\omega$ and $\overline{GD}_\omega$ to be determined by using the equations for bending and shear rigidities reported in § 1.6.1 and 1.6.2. For example, for a four point torsion test, replacing, in Eqs. 1.289–1.290, v_i ($i = 1, 2$) and P with φ_{zi} and M_t, and $\overline{EJ}_x$, $\overline{GD}_y$ with $\overline{EJ}_\omega$, $\overline{GD}_\omega$ leads to ($a = L/3$):

$$\frac{1}{\overline{EJ_\omega}} = \frac{216\left(\varphi_{z2} - \varphi_{z1}\right)}{L^3 M_t} \tag{1.305}$$

$$\frac{1}{\overline{GD_\omega}} = \frac{23\varphi_{z1} - 20\varphi_{z2}}{L M_t} \tag{1.306}$$

where $\varphi_{z1} = \varphi_z\left(L/3\right)$ and $\varphi_{z2} = \varphi_z\left(L/2\right)$.

Appendix 1.A – Cross-section properties

FRP multilayered beams with orthotropic symmetric lay-up
("w": web; "f": flange)
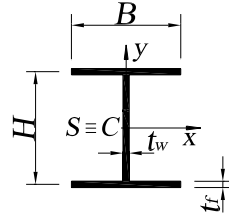
$$\overline{EA} = 2BA^*_{11,f} + HA^*_{11,w}$$

$$\overline{EJ_x} = BH^2 A^*_{11,f}\big/2 + H^3 A^*_{11,w}\big/12$$

$$\overline{EJ_y} = B^3 A^*_{11,f}\big/6$$

$$\overline{EJ_\omega} = H^2 B^3 A^*_{11,f}\big/24$$

$$\overline{GJ_t} = 8BD_{66,f} + 4HD_{66,w}$$

$$\overline{d}_x = 3\big/\left(5BA_{66,f}\right)$$

$$\overline{d}_y = \frac{6}{5H^2 A_{66,f} A_{66,w}\left(6BA^*_{11,f} + HA^*_{11,w}\right)^2}\Big[10BH^2 A^*_{11,f} A^*_{11,w} A_{66,f}$$

$$+ H^3 A^{*2}_{11,w} A_{66,f} + 5B^2 A^{*2}_{11,f}\left(BA_{66,w} + 6HA_{66,f}\right)\Big]$$

$$\overline{d}_\omega = 12\big/\left(5BH^2 A_{66,f}\right)$$

$$\overline{d}_{xy} = \overline{d}_{x\omega} = \overline{d}_{y\omega} = 0$$
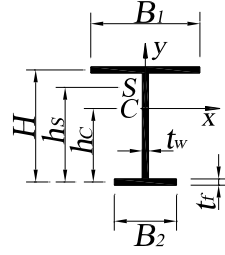
$$\overline{EA} = \left(B_1 + B_2 \right) A_{11,f}^* + H A_{11,w}^*$$

$$\overline{EJ_x} = \left[B_1 \left(H - h_C \right)^2 + B_2 h_C^2 \right] A_{11,f}^* + \left[\left(H - h_C \right)^3 + h_C^3 \right] A_{11,w}^* \Big/ 3$$

$$\overline{EJ_y} = \left(B_1^3 + B_2^3 \right) A_{11,f}^* \Big/ 12$$

$$\overline{EJ_\omega} = B_2^3 H h_S A_{11,f}^* \Big/ 12$$

$$\overline{GJ_t} = 4 \left(B_1 + B_2 \right) D_{66,f} + 4 H D_{66,w}$$

$$h_C = \left(B_1 H A_{11,f}^* + H^2 A_{11,w}^* \Big/ 2 \right) \Big/ \overline{EA}$$

$$h_S = H B_1^3 \Big/ \left(B_1^3 + B_2^3 \right)$$

$$\overline{d}_x = 6 \Big/ \left(5 A_{66,f} \right) \left\{ \left[B_1 \left(1 + \beta_S \right)^2 \right]^{-1} + \left[B_2 \left(1 + 1/\beta_S \right)^2 \right]^{-1} \right\}$$

$$\overline{d}_y = \left(H A_{66,w} \right)^{-1} + \left(12 H^2 A_{66,f} \right)^{-1} \left(B_1 \Big/ \alpha_1^2 + B_2 \Big/ \alpha_2^2 \right)$$

$$\overline{d}_\omega = 6 \Big/ \left(5 H^2 A_{66,f} \right) \left(B_1^{-1} + B_2^{-1} \right)$$

$$\overline{d}_{x\omega} = 6 \Big/ \left(5 H A_{66,f} \right) \left\{ - \left[B_1 \left(1 + \beta_S \right) \right]^{-1} + \left[B_2 \left(1 + 1/\beta_S \right) \right]^{-1} \right\}$$

$$\overline{d}_{xy} = \overline{d}_{y\omega} = 0$$

$$\beta_S = \left(H - h_S \right) \Big/ h_S$$

$$\beta_C = \left(H - h_C \right) \Big/ h_C$$

$$\alpha_1 = 1 + \frac{H A_{11,w}^*}{3 B_1 A_{11,f}^* \left(1 + 1/\beta_C \right)}$$

$$\alpha_2 = 1 + \frac{H A_{11,w}^*}{3 B_2 A_{11,f}^* \left(1 + \beta_C \right)}$$
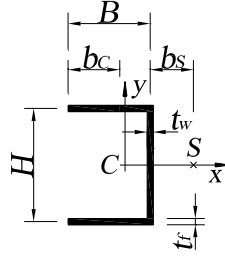
$$\overline{EA} = 2BA_{11,f}^* + HA_{11,w}^*$$

$$\overline{EJ}_x = BH^2 A_{11,f}^* \big/ 2 + H^3 A_{11,w}^* \big/ 12$$

$$\overline{EJ}_y = 2\left[(B-b_C)^3 + b_C^3\right] A_{11,f}^* \big/ 3 + H(B-b_C)^2 A_{11,w}^*$$

$$\overline{EJ}_\omega = b_S B^2 H^2 A_{11,f}^* \left(1 + 2HA_{11,w}^* \big/ 3BA_{11,f}^*\right) \big/ 12$$

$$\overline{GJ}_t = 8BD_{66,f} + 4HD_{66,w}$$

$$b_C = \left(B^2 A_{11,f}^* + HBA_{11,w}^*\right) \big/ \overline{EA}$$

$$b_S = 3B^2 A_{11,f}^* \big/ \left(6BA_{11,f}^* + HA_{11,w}^*\right)$$

$$\overline{d}_x = \int_a A_{66}^{-1} N_{zx}^2 ds = \frac{3}{20B^2 A_{66,f} A_{66,w} \left(BA_{11,f}^* + 2HA_{11,w}^*\right)^2} \Big[4B^3 A_{11,f}^{*2} A_{66,w}$$

$$+ 14B^2 HA_{11,f}^* A_{11,w}^* A_{66,w} + H^2 A_{11,w}^{*2} \left(16BA_{66,w} + 5HA_{66,f}\right) \Big]$$

$$\overline{d}_y = \int_a A_{66}^{-1} N_{zy}^2 ds = \frac{6}{5H^2 A_{66,f} A_{66,w} \left(6BA_{11,f}^* + HA_{11,w}^*\right)^2} \Big[10BH^2 A_{11,f}^* A_{11,w}^* A_{66,f}$$

$$+ H^3 A_{11,w}^{*2} A_{66,f} + 10B^2 A_{11,f}^{*2} \left(2BA_{66,w} + 3HA_{66,f}\right) \Big]$$

$$\overline{d}_\omega = \int_a A_{66}^{-1} N_{z\omega}^2 ds = \frac{3}{5H^2 B^2 A_{66,f} A_{66,w} \left(3BA_{11,f}^* + 2HA_{11,w}^*\right)^2} \Big[36B^3 A_{11,f}^{*2} A_{66,w}$$

$$+ 42HB^2 A_{11,f}^* A_{11,w}^* A_{66,w} + H^2 A_{11,w}^{*2} \left(16BA_{66,w} + 3HA_{66,f}\right) \Big]$$

$$\overline{d}_{y\omega} = \int_a A_{66}^{-1} N_{zy} N_{z\omega} ds$$

$$= \frac{3\left(30B^3 A_{11,f}^{*2} A_{66,w} + 25HB^2 A_{11,f}^* A_{11,w}^* A_{66,w} - 2H^3 A_{11,w}^{*2} A_{66,f}\right)}{5H^2 BA_{66,f} A_{66,w} \left(6BA_{11,f}^* + HA_{11,w}^*\right)\left(3BA_{11,f}^* + 2HA_{11,w}^*\right)}$$

$$\overline{d}_{xy} = \overline{d}_{x\omega} = 0$$
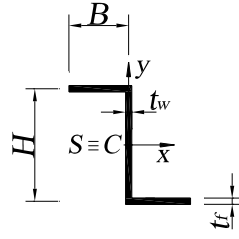
$$\overline{EA} = 2BA_{11,f}^* + HA_{11,w}^*$$

$$\overline{EJ_x} = BH^2 A_{11,f}^* / 2 + H^3 A_{11,w}^* / 12$$

$$\overline{EJ_y} = B^3 A_{11,f}^* / 6$$

$$\overline{EJ_{xy}} = -HB^2 A_{11,f}^* / 2$$

$$\overline{EJ_\omega} = \left\{ B^3 H^2 / \left[12(2B+H)^2 \right] \right\} \left[2\left(B^2 + BH + H^2 \right) A_{11,f}^* \right.$$
$$\left. + 3BHA_{11,w}^* \right]$$

$$\overline{GJ_t} = 8BD_{66,f} + 4HD_{66,w}$$

$$\overline{d}_x = 3 / \left(5BA_{66,f} \right) + H\gamma_x^2 / \left(5A_{66,w} \right)$$

$$\overline{d}_y = \left(HA_{66,w} \right)^{-1} + 4B / \left(15H^2 \delta^2 A_{66,f} \right)$$

$$\overline{d}_\omega = 12 / \left(5BH^2 A_{66,f} \right) + H\gamma_\omega^2 / \left(3A_{66,w} \right)$$

$$\overline{d}_{xy} = -\left(H\delta A_{66,f} \right)^{-1} \frac{2 - 3\alpha_x}{20 - 10\alpha_x} + \left(1 - 1/\delta \right) \gamma_x / \left(5A_{66,w} \right)$$

$$\overline{d}_{x\omega} = \overline{d}_{y\omega} = 0$$

$$\gamma_x = 3(1 - 1/\delta) / 4B$$

$$\gamma_\omega = \frac{3 - 3\alpha_\omega}{(2 - \alpha_\omega) HB}$$

$$\delta = 4\left[1 + HA_{66,w} / \left(6BA_{66,f} \right) \right] - 3$$

$$\alpha_x = \frac{3 - 4B\gamma_x}{3 - 2B\gamma_x}$$

$$\alpha_\omega = \left[1 + HA_{11,w}^* / \left(BA_{11,f}^* \right) \right]^{-1}$$
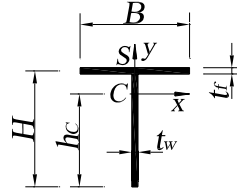
$$\overline{EA} = BA^*_{11,f} + HA^*_{11,w}$$

$$\overline{EJ_x} = B\left(H - h_C\right)^2 A^*_{11,f} + \left[\left(H - h_C\right)^3 + h_C^3\right] A^*_{11,w} \big/ 3$$

$$\overline{EJ_y} = B^3 A^*_{11,f} \big/ 12$$

$$\overline{EJ_\omega} = 0$$

$$\overline{GJ_t} = 4BD_{66,f} + 4HD_{66,w}$$

$$h_C = \left(BHA^*_{11,f} + H^2 A^*_{11,w} \big/ 2\right) \big/ \overline{EA}$$

$$\overline{d}_x = 6 \big/ \left(5BA_{66,f}\right)$$

$$\overline{d}_y = \varsigma \big/ \left(HA_{66,w}\right) + B\gamma_y^2 \big/ \left(12A_{66,f}\right)$$

$$\overline{d}_{xy} = 0$$

$$\gamma_y = \frac{3 - 3\alpha_y}{\left(2 - \alpha_y\right)H}$$

$$\varsigma = \frac{3\left(8 - 9\alpha_y + 3\alpha_y^2\right)}{5\left(2 - \alpha_y\right)^2}$$

$$\alpha_y = \frac{H - h_C}{h_C}$$
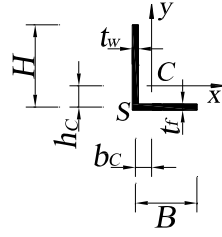
$$\overline{EA} = BA_{11,f}^* + HA_{11,w}^*$$

$$\overline{EJ_x} = Bh_C^2 A_{11,f}^* + \left[(H - h_C)^3 + h_C^3\right] A_{11,w}^* \Big/ 3$$

$$\overline{EJ_y} = \left[(B - b_C)^3 + b_C^3\right] A_{11,f}^* \Big/ 3 + Hb_C^2 A_{11,w}^*$$

$$\overline{EJ_{xy}} = -h_C B \left(B/2 - b_C\right) A_{11,f}^* - b_C H \left(H/2 - h_C\right) A_{11,w}^*$$

$$\overline{EJ_\omega} = 0$$

$$\overline{GJ_t} = 4BD_{66,f} + 4HD_{66,w}$$

$$h_C = \left(H^2 A_{11,w}^* \Big/ 2\right) \Big/ \overline{EA}$$

$$b_C = \left(B^2 A_{11,f}^* \Big/ 2\right) \Big/ \overline{EA}$$
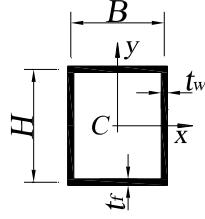
$$\overline{EA} = 2BA_{11,f}^* + 2HA_{11,w}^*$$

$$\overline{EJ}_x = BH^2 A_{11,f}^* \big/ 2 + H^3 A_{11,w}^* \big/ 6$$

$$\overline{EJ}_y = HB^2 A_{11,w}^* \big/ 2 + B^3 A_{11,f}^* \big/ 6$$

$$\overline{EJ}_\omega = 0$$

$$\overline{GJ}_t = 2B^2 H^2 \big/ \left(BA_{66,f}^{-1} + HA_{66,w}^{-1} \right)$$

$$\overline{d}_x = \left(2BA_{66,f} \right)^{-1} + H \left(6B^2 \alpha_x^2 A_{66,w} \right)^{-1}$$

$$\overline{d}_y = \left(2HA_{66,w} \right)^{-1} + B \left(6H^2 \alpha_y^2 A_{66,f} \right)^{-1}$$

$$\overline{d}_{xy} = 0$$

$$\alpha_x = 1 + \frac{HA_{11,w}^*}{3BA_{11,f}^*}$$

$$\alpha_y = 1 + \frac{BA_{11,f}^*}{3HA_{11,w}^*}$$
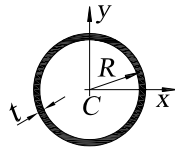
$$\overline{EA} = 2\pi R A_{11}^*$$

$$\overline{EJ_x} = \overline{EJ_y} = \pi R^3 A_{11}^*$$

$$\overline{EJ_\omega} = 0$$

$$\overline{GJ_t} = 2\pi R^3 A_{66}$$

$$\overline{d}_x = \overline{d}_y = \left(\pi R A_{66} \right)^{-1}$$

$$\overline{d}_{xy} = 0$$

Chapter 2

Finite element formulation in linear elastic analysis

2.1 Introduction

In this chapter, several polynomial finite element formulations based on Timoshenko-Reissner's kinematics are presented and compared, with the purpose of identifying numerical models suitable for the analysis of shear-deformable thin-walled beam assemblages.

In 1974, Narayanaswami and Adelman proposed, seemingly for the first time, "modified" Hermitian shape functions for numerical interpolation of transverse displacements and flexural rotations of a Timoshenko (symmetric) beam. These polynomial functions contain a parameter depending on both slenderness and ratio E/G between Young and transverse elastic moduli. By using those interpolating functions, it is possible to re-obtain the stiffness matrix of Timoshenko beam reported by Przemeniecki (1968). Making use of these interpolating functions, Friedman and Kosmatka (1993) and Kosmatka (1995) proposed a finite element to solve dynamic and buckling problems, observing that such an element does not present any *shear locking*. In fact, if the slenderness of the element increases and, consequently, the shear strain influence becomes negligible, the element stiffness matrix approaches the classical stiffness matrix of Euler-Bernoulli beam. This finite element was also adopted in Eisenberger (1994). Afterwards, Reddy (1997) and Ortúzar and Samartín (1998) proposed an alternative procedure to recover these shape functions and compared various finite elements. Mukherjee *et al.* (2001) demonstrated the super convergence properties of this (Timoshenko) finite element. The same element has recently been suggested by Bazoune *et al.* (2003), using a different procedure to obtain the interpolating functions. In the present Chapter, these "modified" Hermitian polynomials are adopted together with Lagrangian polynomials to interpolate transverse displacements and flexural rotations. In particular, a consistent element is adopted using (Lagrangian) third-order polynomials for transverse displacements and second-order polynomials for flexural rotations. Using this element, the bending stiffness matrix and load vector of the cited Hermitian element is re-obtained (Mukherjee *et al.* 2001).

As for the warping-torsion problem, it has been shown in the previous chapter that the closed-form solution can be written in terms of hyperbolic functions. In particular, the solutions of the homogeneous problem for doubly-symmetric cross-section beams were used by Gunnlaugsson and Pedersen (1982), Shakourzadeh *et al.* (1995a) and Lin *et al.* (1996) as interpolating functions for finite element analyses of thin-walled beams with any cross-section. Hu *et al.* (1996) developed a finite element formulation for static and dynamic analysis of nonsymmetric cross-section beams adopting the solutions to Timoshenko-Reissner's model in the presence of shear-warping coupling as interpolating shape functions. The present chapter analyzes the efficiency of some interpolating functions belonging to the families of Hermitian and Lagrangian polynomials. Some of the proposed formulations are consistent; consequently, polynomials interpolating torsional rotations are one order higher than those interpolating cross-section warping. In addition, other formulations are proposed which make use of the same interpolating polynomials for both torsional unknowns.

Numerical examples were performed, concerning thin-walled isotropic and fiber-reinforced (FRP) pultruded beams with monosymmetric and nonsymmetric cross-sections. Coupling between shear and nonuniform torsion, and between shear and bending in two orthogonal (principal) planes were consequently considered.

In the presence of coupling caused by shear deformations, some of the proposed formulations exhibit a high convergence rate and are in very good agreement with both analytical and plate-shell solutions. In particular, the influence of shear strain coupling terms was evaluated for increasing values of the beam length, i.e. when the end effects tend to vanish. A decay length based on the De Saint Venànt principle was obtained following Horgan's proposal (Horgan 1989, Horgan & Simmonds 1994).

The finite element models and the numerical examples presented in this chapter has been recently reported in a paper of Minghini *et al.* (2007).

2.2 Finite element formulation

Collecting the unknown displacement functions of Timoshenko-Reissner's kinematical model (Eqs. 1.3–1.5) by vector:

$$\mathbf{d} = \left\{ w_C(z), u_S(z), \varphi_y(z), v_S(z), \varphi_x(z), \varphi_z(z), \Psi(z) \right\}^T \tag{2.1}$$

and denoting the vector nodal displacements of an ideal beam finite element with:

$$\mathbf{q} = \left\{ w_{C1}, u_{S1}, \varphi_{y1}, v_{S1}, \varphi_{x1}, \varphi_{z1}, \Psi_1, ... \right\}^T \tag{2.2}$$

the displacement field, in the framework of the classical displacement-based finite element method, can be approximated in the form:

$$\mathbf{d}(z) = \mathbf{N}(z)\mathbf{q} \tag{2.3}$$

where matrix $\mathbf{N}(z)$ assembles the selected shape functions.

By substituting Eq. 2.3 into Eqs. 1.84 and 1.85 of elastic strain energy and work of external loads, and the resulting expressions into Eq. 1.81 of total potential, applying the stationarity condition 1.86 yields a set of equilibrium equations that can be expressed in the canonical form:

$$\mathbf{Kq} = \mathbf{Q} \tag{2.4}$$

where $\mathbf{K}$ represents the element stiffness matrix and $\mathbf{Q}$ is the generalized load vector, given by:

$$\mathbf{Q} = \mathbf{Q}_n + \int_0^L \mathbf{N}^T \mathbf{p} \, dz \tag{2.5}$$

In Eq. 2.5, $\mathbf{Q}_n = \left\{ N_1, V_{x1}, M_{y1}, V_{y1}, M_{x1}, M_{z1}, M_{\omega 1}, ... \right\}^T$ and $\mathbf{p} = \left\{ q_z, q_x, m_y, q_y, m_x, m_z, m_\omega \right\}^T$ indicate nodal force and distributed load vectors, respectively. Equations like 2.4 can be assembled by imposing the continuity displacement conditions at a nodal reference point of adjacent elements: the assemblage point, not necessarily coincident with the centroid. Therefore, a proper coordinate transformation is required (see Appendix 2.C) in order to refer all nodal quantities to the assemblage point (Shakourzadeh *et al*. 1995b, Back & Will 1998).

All the numerical models analyzed in the present chapter are reported in Table 2.I, where "*L*" stands for Lagrangian polynomials (Reddy 1985) and "*H*" indicates "modified" Hermitian shape functions (see § 2.2.1). Each acronym generally consists of two parts, sequentially referring to flexural and torsional interpolations. Moreover, the first numbers in brackets indicate orders of polynomials interpolating lateral displacements or torsional rotations, whereas the second numbers analogously refer to flexural rotations and cross-section warping. When flexure and torsion are described with polynomials of the same family, the acronyms are consequently condensed, as is the case of elements n. 1, 2 and 7.

Table 2.I. Polynomial orders of the numerical models adopted.
(*L*): Lagrangian interpolation; (*H*): Hermitian interpolation.

Finite element	Acronym	Transverse displacements, u_S and v_S		Flexural rotations, φ_y and φ_x		Torsional rotation, φ_z		Cross-section warping, Ψ	
1	*L*21	*L*	2	*L*	1	*L*	2	*L*	1
2	*L*32		3		2		3		2
3	*H*(3-2)-*L*(1-1)						1		1
4	*H*(3-2)-*L*(2-2)	*H*	3	*H*	2	*L*	2	*L*	2
5	*H*(3-2)-*L*(2-1)						2		1
6	*H*(3-2)-*L*(3-2)						3		2
7	*H*32	*H*	3	*H*	2	*H*	3	*H*	2

Table 2.II. Nodes used to interpolate each displacement field (see Fig. 3).

Finite element	Acronym	w_C	u_S	φ_y	v_S	φ_x	φ_z	Ψ
Nodes reported in Fig. 3								
1	$L21$	1, 2	1, 2, 4	1, 2	1, 2, 4	1, 2	1, 2, 4	1, 2
2	$L32$	1, 2	1, 2, 3, 5	1, 2, 4	1, 2, 3, 5	1, 2, 4	1, 2, 3, 5	1, 2, 4
3	H(3-2)-L(1-1)	1, 2	1, 2	1, 2	1, 2	1, 2	1, 2	1, 2
4	H(3-2)-L(2-2)	1, 2	1, 2	1, 2	1, 2	1, 2	1, 2, 4	1, 2, 4
5	H(3-2)-L(2-1)	1, 2	1, 2	1, 2	1, 2	1, 2	1, 2, 4	1, 2
6	H(3-2)-L(3-2)	1, 2	1, 2	1, 2	1, 2	1, 2	1, 2, 3, 5	1, 2, 4
7	$H32$	1, 2	1, 2	1, 2	1, 2	1, 2	1, 2	1, 2
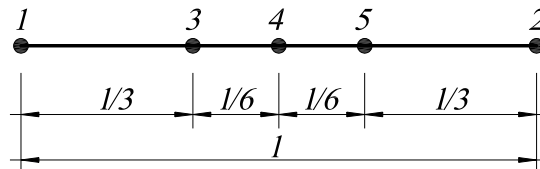
Figure 2.1. Location of the nodes reported in Table 2.II; l indicates the finite element length.

Axial displacements were always interpolated by using linear functions. For instance, element n. 3, i.e. H(3-2)-L(1-1), adopts third-order Hermitian polynomials to interpolate lateral displacements, second-order Hermitian polynomials to interpolate flexural rotations, and first-order Lagrangian polynomials to interpolate both torsional rotations and cross-section warping.

Table 2.II reports the nodes used for numerical interpolation, whereas Figure 2.1 shows their location. When using second- and third-order Lagrangian polynomials, displacements associated to the inner nodes are necessarily to be condensed out.

2.2.1 "Modified" Hermitian shape functions (element H32)

As was shown in § 1.3, local equilibrium equations contain, in general, bending-bending and bending-twisting coupling terms, due to shear strain influence. For doubly-symmetric profiles the equilibrium equations become simpler and bending and torsion turn out to be uncoupled. For example, the homogeneous form of the Timoshenko-beam bent in the *y-z* plane is considered (see Eqs. 1.161−1.162):

$$GD_y\left(v_S'' + \varphi_x'\right) = 0 \tag{2.6}$$

$$EJ_x\varphi_x'' - GD_y\left(v_S' + \varphi_x\right) = 0 \tag{2.7}$$

The analytical solution 1.163−1.164 to Eqs. 2.6 and 2.7 is written in the following in matrix form as a function of the four constants of integration:

$$
\begin{Bmatrix} v_S(z) \\ \varphi_x(z) \end{Bmatrix} = \begin{bmatrix} -z & -z^2/2 & -z^3/3 + 2z\zeta & -1 \\ 1 & z & z^2 & 0 \end{bmatrix} \begin{Bmatrix} A_1 \\ A_2 \\ A_3 \\ A_4 \end{Bmatrix} \tag{2.8}
$$

where $\zeta = EJ_x/GD_y$. Imposing the boundary conditions

$$
v_S(0) = v_{S1}; \quad \varphi_x(0) = \varphi_{x1}; \quad v_S(l) = v_{S2}; \quad \varphi_x(l) = \varphi_{x2} \tag{2.9}
$$

where l stands for the finite element length, yields the relation:

$$
\begin{Bmatrix} v_{S1} \\ \varphi_{x1} \\ v_{S2} \\ \varphi_{x2} \end{Bmatrix} = \begin{bmatrix} 0 & 0 & 0 & -1 \\ 1 & 0 & 0 & 0 \\ -1 & -l^2/2 & -l^3/3 + 2l\zeta & -1 \\ 1 & l & l^2 & 0 \end{bmatrix} \begin{Bmatrix} A_1 \\ A_2 \\ A_3 \\ A_4 \end{Bmatrix} \tag{2.10}
$$

Solving Eq. 2.10 for constants A_1, ..., A_4 and substituting the results into Eq. 2.8 lead to (Reddy 1997):

$$
\begin{Bmatrix} v_S(z) \\ \varphi_x(z) \end{Bmatrix} = \begin{bmatrix} N_{11}^y(z) & N_{12}^y(z) & N_{13}^y(z) & N_{14}^y(z) \\ N_{21}^y(z) & N_{22}^y(z) & N_{23}^y(z) & N_{24}^y(z) \end{bmatrix} \begin{Bmatrix} v_{S1} \\ \varphi_{x1} \\ v_{S2} \\ \varphi_{x2} \end{Bmatrix} \tag{2.11}
$$

where functions $N_{1i}^y(z)$ ($i = 1$, ..., 4), describing transverse displacement v_S, are cubic polynomials of the form:

$$
N_{11}^y = \frac{1}{1+\phi_y}\left[1 - 3\xi^2 + 2\xi^3 + \phi_y(1-\xi)\right] \qquad N_{12}^y = -\frac{l}{1+\phi_y}\xi\left[(1-\xi)^2 + \phi_y(1-\xi)/2\right]
$$
$$
N_{13}^y = \frac{1}{1+\phi_y}\left(3\xi^2 - 2\xi^3 + \phi_y\xi\right) \qquad N_{14}^y = -\frac{l}{1+\phi_y}\xi\left[\xi^2 - \xi - \phi_y(1-\xi)/2\right] \tag{2.12}
$$

whereas functions $N_{2i}^y(z)$ ($i = 1$, ..., 4), describing flexural rotation φ_x, are quadratic polynomials given by:

$$
N_{21}^y = \frac{6\xi}{l(1+\phi_y)}(1-\xi) \qquad\qquad N_{22}^y = \frac{1}{1+\phi_y}\left[1 - 4\xi + 3\xi^2 + \phi_y(1-\xi)\right]
$$

$$N_{23}^y = -\frac{6\xi}{l\left(1+\phi_y\right)}\left(1-\xi\right) \qquad\qquad N_{24}^y = \frac{1}{1+\phi_y}\left(-2\xi+3\xi^2+\phi_y\xi\right) \qquad (2.13)$$

In Eqs. 2.12 and 2.13, $\xi = z/l$ $(0 \le \xi \le 1)$ and the parameter ϕ_y takes the expression:

$$\phi_y = \frac{12EJ_x}{GD_y l^2} \qquad\qquad (2.14)$$

The polynomial functions of Eqs. 2.12 and 2.13 are plotted in Figures 2.2 and 2.3, where the dependency on parameter ϕ_y is pointed out. Using these polynomials as interpolating shape functions for transverse displacement and flexural rotation, the following stiffness matrix is obtained for the Timoshenko beam element (*Interdependent Interpolation Element*, IIE, Reddy 1997):
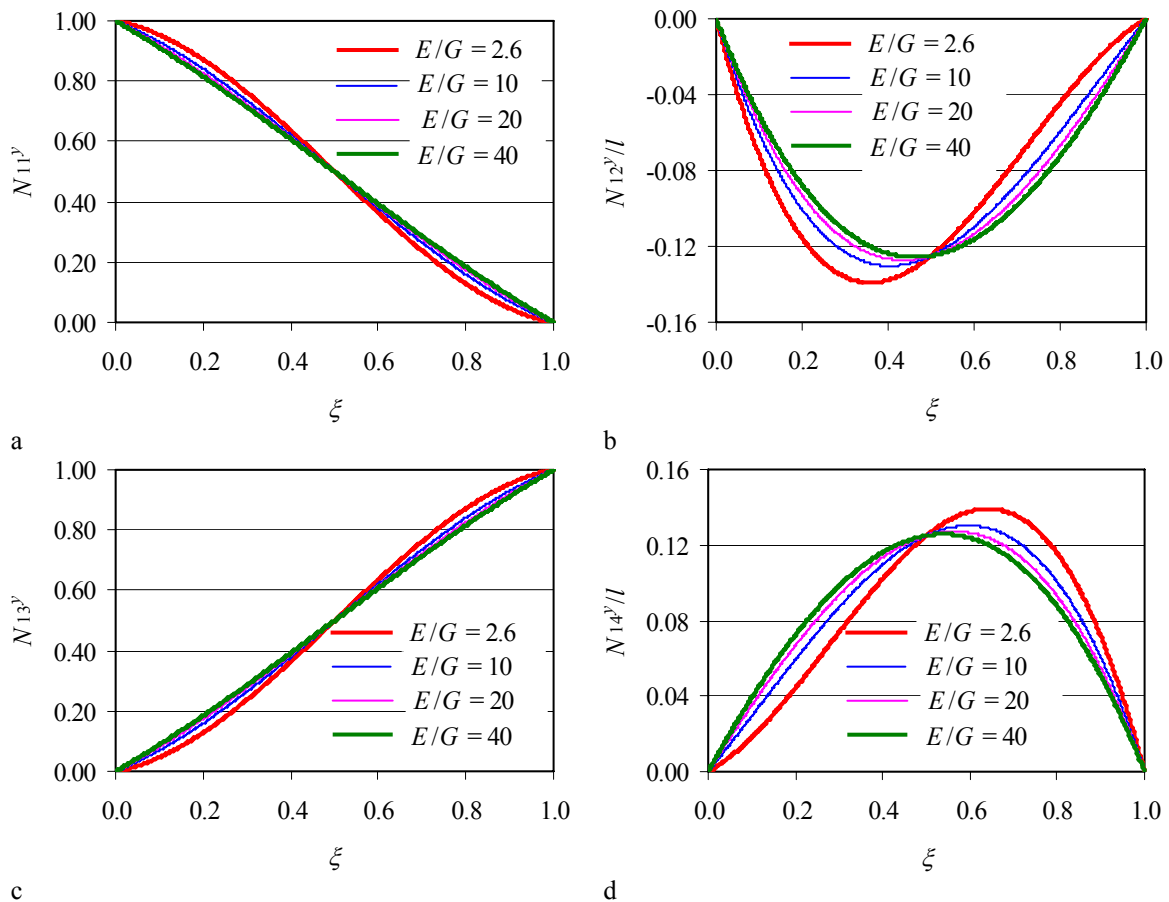
Figure 2.2. Third-order "modified" Hermitian functions describing the transverse displacement v_S (y-z plane) of a (symmetric) Timoshenko beam. Influence of ratio E/G between elastic moduli. a: function N_{11}^y; b: function N_{12}^y/l; c: function N_{13}^y; d: function N_{14}^y/l (Eqs. 2.12).
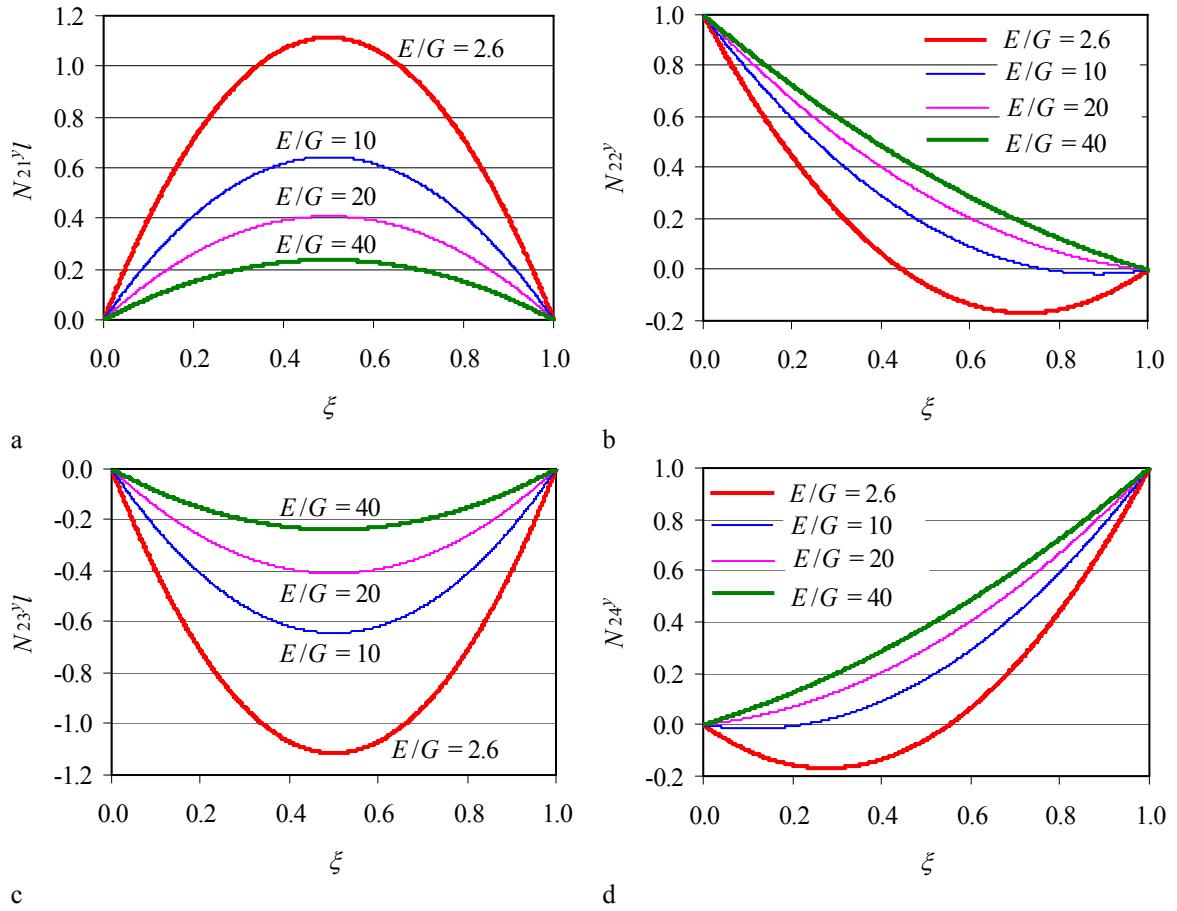
Figure 2.3. Second-order "modified" Hermitian functions describing the flexural rotation φ_x (y-z plane) of a (symmetric) Timoshenko beam. Influence of ratio E/G between elastic moduli. a: function $N_{21}^y l$; b: function N_{22}^y; c: function $N_{23}^y l$; d: function N_{24}^y (Eqs. 2.13).

$$\mathbf{K}_v = \frac{EJ_x}{(1+\phi_y) \cdot l^3} \begin{bmatrix} 12 & -6 \cdot l & -12 & -6 \cdot l \\ & (4+\phi_y) \cdot l^2 & 6 \cdot l & (2-\phi_y) \cdot l^2 \\ & & 12 & 6 \cdot l \\ \text{Sym} & & & (4+\phi_y) \cdot l^2 \end{bmatrix} \tag{2.15}$$

which coincides with the matrix obtained by Przemieniecki (1968) in another way. The corresponding equivalent load vector is obtained from the second term on the right-hand side of Eq. 2.5. In particular, neglecting distributed external bending moment m_x, it results:

$$\int_0^L \mathbf{N}^T \mathbf{p}\, dz = \left\{ ql/2 \quad -ql^2/12 \quad ql/2 \quad ql^2/12 \right\}^T \tag{2.16}$$

which coincides with equivalent load vector of classical Euler-Bernoulli Hermitian element. It should be noted that, when the beam element slenderness, or the shear rigidity GD_y, goes to infinity, coefficient ϕ_y tends to vanish, cubic and quadratic polynomials of Eqs. 2.12–2.13 reduce to the classical third-order Hermitian functions and to their first derivatives, respectively, and the stiffness matrix of Eq. 2.15 reduces to the classical stiffness matrix Euler-Bernoulli's model. Hence, the IIE element is *locking-free* (Kosmatka 1995). Moreover, one single IIE element is able to obtain the exact solutions to the Timoshenko beam problem irrespective of the load distribution, because the finite element approximation space coincides with the space of the exact solutions (Reddy 1997). Therefore, the element is said to be superconvergent (Mukherjee *et al.* 2001).

In the case of bending in the *x-z* plane, the homogeneous form of the Timoshenko beam problem 1.72–1.73 is solved (in terms of transverse displacement u_S and flexural rotation φ_y) by Hermitian polynomials of the same form as Eqs. 2.12–2.13, "modified" by the parameter:

$$\phi_x = \frac{12EJ_y}{GD_x l^2} \tag{2.17}$$

in place of ϕ_y. In particular, shape functions N_{12}^x, N_{14}^x, N_{21}^x and N_{23}^x take opposite signs with respect to N_{12}^y, N_{14}^y, N_{21}^y and N_{23}^y ($i = 1, \ldots, 4$).

As far as torsion is concerned, the homogeneous form of the indefinite equilibrium equations for doubly-symmetric (open) cross-section profiles can be written as follows (see Eqs. 1.189–1.190):

$$GJ_t \varphi_z'' + GD_\omega \left(\varphi_z'' + \Psi' \right) = 0 \tag{2.18}$$

$$EJ_\omega \Psi'' - GD_\omega \left(\varphi_z' + \Psi \right) = 0 \tag{2.19}$$

Because of the warping effects, decaying far from the restraints, the solution is expressed in terms of the hyperbolic functions 1.191–1.192. Torsional rotation and cross-section warping fields within a beam element of length *l* are obtained by imposing the usual boundary conditions $\varphi_z(0) = \varphi_{z1}$, $\Psi(0) = \Psi_1$, $\varphi_z(l) = \varphi_{z2}$, $\Psi(l) = \Psi_2$. Gunnlaugsson and Pedersen (1982), Shakourzadeh *et al.* (1995a) and Lin *et al.* (1996), adopted these functions, together with Eqs. 2.12–2.13, as interpolating functions for the finite element analysis of thin-walled beams with any given cross-section. However, as noted in § 1.3, if the term GJ_t in Eq. 2.18 is neglected, Eqs. 2.18–2.19 turn out to be formally identical to Eqs. 2.6–2.7 and, consequently, φ_z and Ψ may be expressed in terms of Hermitian shape functions of the same form as Eqs. 2.12–2.13, "modified" by the parameter:

$$\phi_\omega = \frac{12EJ_\omega}{GD_\omega l^2} \tag{2.20}$$
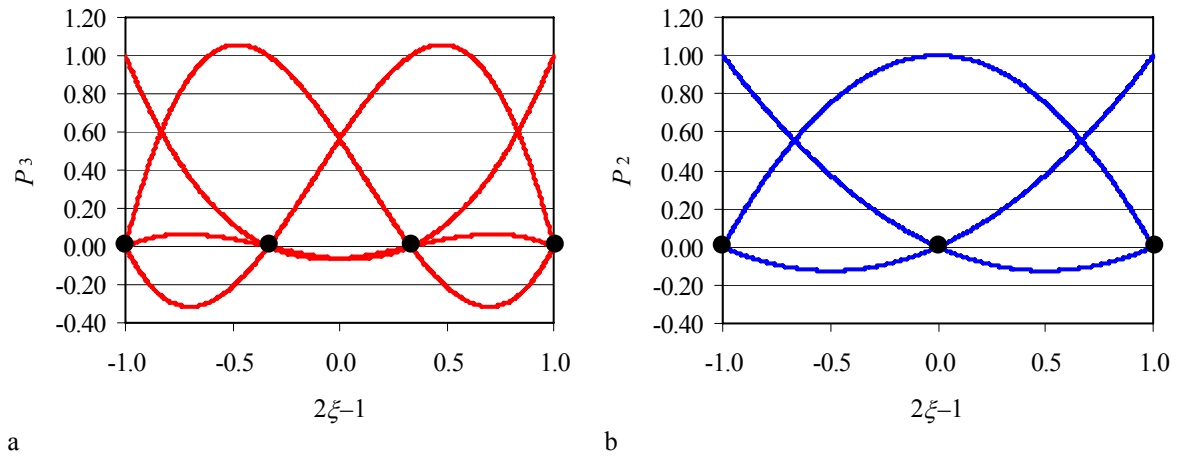
Figure 2.4. Lagrangian shape functions adopted for some of the numerical formulations proposed. a: third-order functions (inner nodes at $\xi = 1/3$ and $\xi = 1/3$). b: second-order functions (inner node at $\xi = 1/2$).

in place of ϕ_y. By substituting polynomials of the form 2.12–2.13 modified by coefficients ϕ_i ($i = x, y, \omega$) into expression 1.84 of the elastic strain energy, the stiffness matrix of $H32$ element (see Appendix 2.A) is obtained. When shear deformations tend to vanish $\phi_i = 0$ ($i = x, y, \omega$) and, correspondingly, the stiffness matrix reduces to the matrix of the Euler-Bernoulli-Vlasov beam model reported Barsoum and Gallagher (1970).

2.2.2 Lagrangian elements L21 and L32

Lagrangian element $L32$ (see Appendix 2.B) is obtained by adopting third- and second-order Lagrangian interpolation (Fig. 2.4a,b). If inner nodes (Fig. 2.1) are condensed out, it is easy to demonstrate (Mukherjee *et al*. 2001) that the $L32$ finite element is characterized by both same bending stiffness matrix (Eq. 2.15) and equivalent load vector (Eq. 2.16) as elements adopting modified Hermitian polynomials. On the other hand, element n. 1 of Table 2.I ($L21$), adopting second- (Fig. 2.4b) and first-order Lagrangian interpolation, coincides, for the flexural part, with the *Consistent Interpolation Timoshenko beam Element* (CIE) introduced by Reddy (1997). Such an element is *locking-free* but, differently from $L32$ and Hermitian elements, is not able to predict the analytical solution of the Timoshenko beam model. Its stiffness matrix can be obtained by using linear interpolating functions only with a reduced integration (RIE element, Reddy 1997). Nevertheless, RIE and $L21$ elements are characterized by different load vectors.

2.3 Numerical examples

2.3.1 Twist of a channel-shaped shear core

The first example concerns a channel-shaped shear core (Fig. 2.5) fully constrained at one end and subjected to a twisting moment at the opposite end. The material is isotropic. This problem was solved by Capurso (1984) and, later, by Tralli (1986) who developed a mixed finite element formulation, and by Back and Will (1998) who used Lagrangian interpolation for all displacement functions. More recently, Kim and Kim (2005) developed an exact beam finite element based on Timoshenko-Reissner's kinematical model; their results, together with the solutions obtained in § 1.5.3.1, are used as comparison terms for the present example.

In this case, coupling occurs between nonuniform torsion and shear. Due to the shape of the cross-section, $D_{y\omega}$ is the only non-vanishing off-diagonal term of the shear rigidity matrix of Eq. 1.51. The problem was solved using six elements for some of the numerical models reported in Table 2.I. Comparison was made with results reported by Tralli (1986) and Back and Will (1998); with a 3D FE model (Fig. 2.6) developed with the aid of SAP2000[®] (2004), and with the analytical solutions (Eqs. 1.246–1.249 and Kim & Kim 2005).

Figure 2.7 shows that, if shear strains are accounted for, the beam solutions – in particular, those provided by elements $L32$, $H(3\text{-}2)$-$L(3\text{-}2)$ and $H32$ – are very accurate even close to the fixed end. In fact, the discrepancy with shell results is less than 0.8% everywhere. The accuracy of results by Tralli is also pointed out in the same figure. Element $L21$ yields the same numerical solutions reported by Back and Will and is characterized by an approximation which is worse than the other present formulations, even if the maximum error is about 2.6%. Compared with the beam analytical solution, the Vlasov model is characterized by an error of about 15% near the fixed end, and about 3.6% at the free end. Hence, in the case of isotropic material, the influence of shear deformations is necessarily to be taken into account in the vicinity of constrained regions.
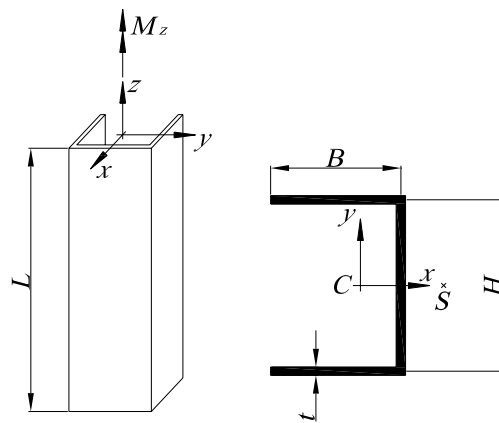
Figure 2.5. Shear wall ($L = 18$ m) fully restrained at one end, subjected to a twisting moment at the opposite end. $M_z = 1 \cdot 10^3$ kNm, $H = 5$ m, $B = 3.5$ m, $t_f = t_w = 0.2$ m, $E = 3 \times 10^7$ kN/m^2, $G = 1.3 \times 10^7$ kN/m^2, $A = 2.4$ m^2, $J_t = 0.032$ m^4, $J_x = 10.83333$ m^4, $J_y = 3.21563$ m^4, $J_\omega = 14.0855$ m^6, $D_\omega = 8.73737$ m^4, $D_x = 0.97471$ m^2, $D_y = 0.914592$ m^2, $D_{y\omega} = -1.15357$ m^3.
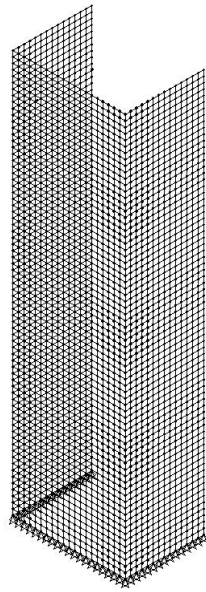
Figure 2.6. 3D numerical model of the shear wall of example 2.3.1.
Orthotropic shell elements 25 cm × 25 cm.
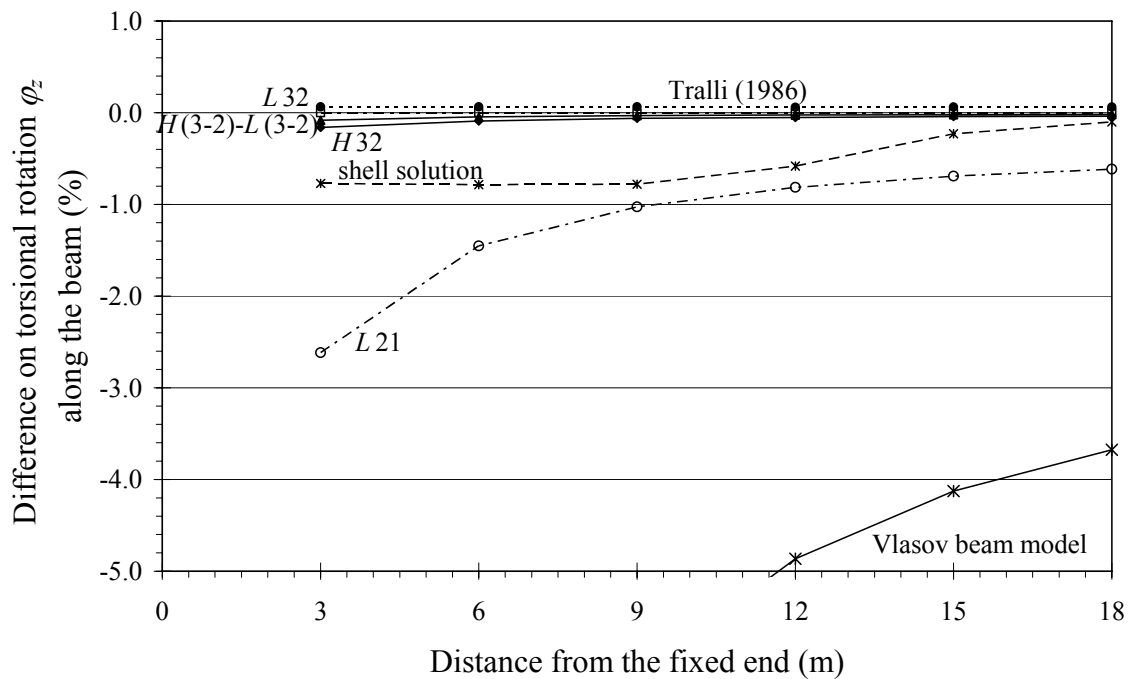
Figure 2.7. Beam of Fig. 2.5 subjected to an end twisting moment. Torsional rotations from proposed numerical beam models (6 elements) and 3D FE model using 4-node shell elements compared with beam analytical solutions (Eq. 1.248 and Kim & Kim 2005). Numerical values reported in Appendix 2.D (Table 2.DI).
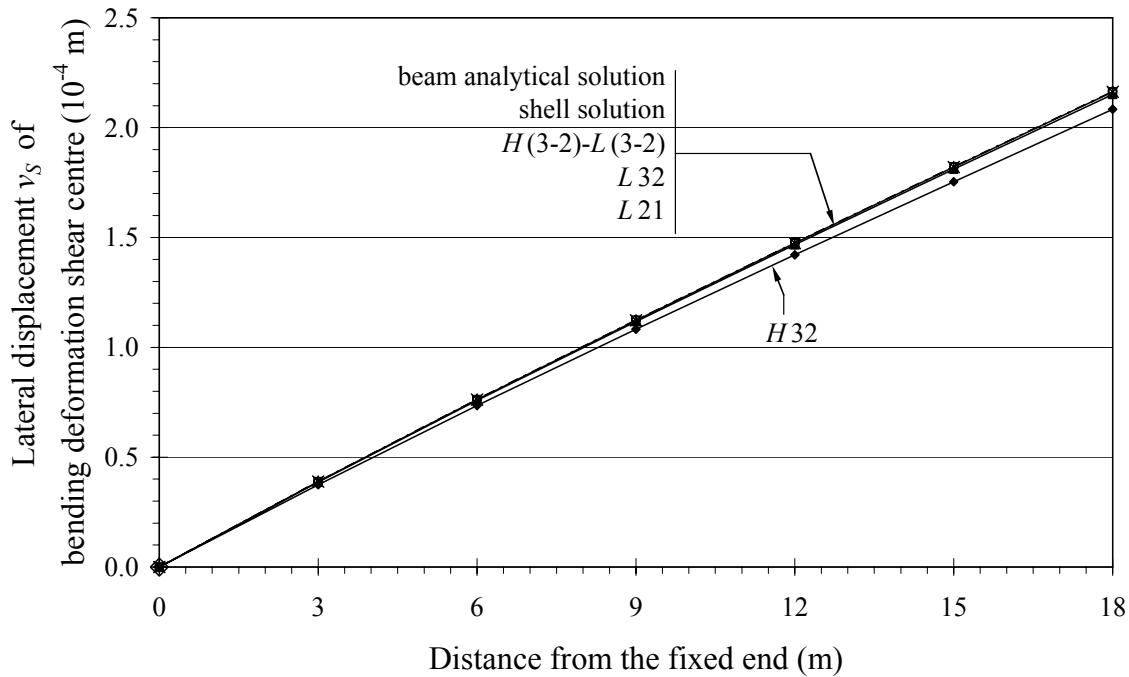
Figure 2.8. Beam of Fig. 2.5 subjected to an end twisting moment. Lateral displacement of the b.d. shear centre caused by nonuniform torsion-shear coupling. Comparison between Timoshenko-Reissner beam theory (Eq. 1.246 and Kim & Kim 2005), some of the present numerical models (6 elements) and shell model. Numerical values are reported in Table 2.CI.

In Figure 2.8, lateral displacements at the b.d. shear centre of the cantilever beam of Figure 2.5 are reported. Numerical results obtained using $H(3\text{-}2)\text{-}L(3\text{-}2)$, $L32$ and $L21$ finite elements approach both the analytical solutions (Eq. 1.246 and Kim & Kim 2005) and the results given by 3D model very well. Also element $H32$ provides good results, showing a maximum error of about 3.65% at a distance $z = 18$ m from the fixed end. Numerical values are reported in Appendix 2.D.

2.3.2 Bending of a cantilever beam into a symmetry plane

If the C-shaped profile of Figure 2.5 is subjected to a shear force V_x acting at the free end along the symmetry axis x, the beam bends into the symmetry plane x-z and the kinematical model 1.3−1.5 reduces to the Timoshenko beam model. In this case, every formulation using "modified" Hermitian shape functions to interpolate transverse displacement u_S and flexural rotation φ_y exactly reproduces the analytical solutions (Eqs. 1.171−1.172) even if one single element is used. Moreover, as was already noted, element $L32$ yields the same bending stiffness matrix as the "modified" Hermitian polynomials and, consequently, the analytical solution as well (Fig. 2.9). On the contrary, more than two $L21$ (*locking-free*) elements are required to obtain acceptable results (Reddy 1997). In fact, as is shown in Figure 2.9, the maximum errors given by one or two $L21$ elements on end-section flexural displacement are about 25% and 6.25% respectively for L/H larger than 20.
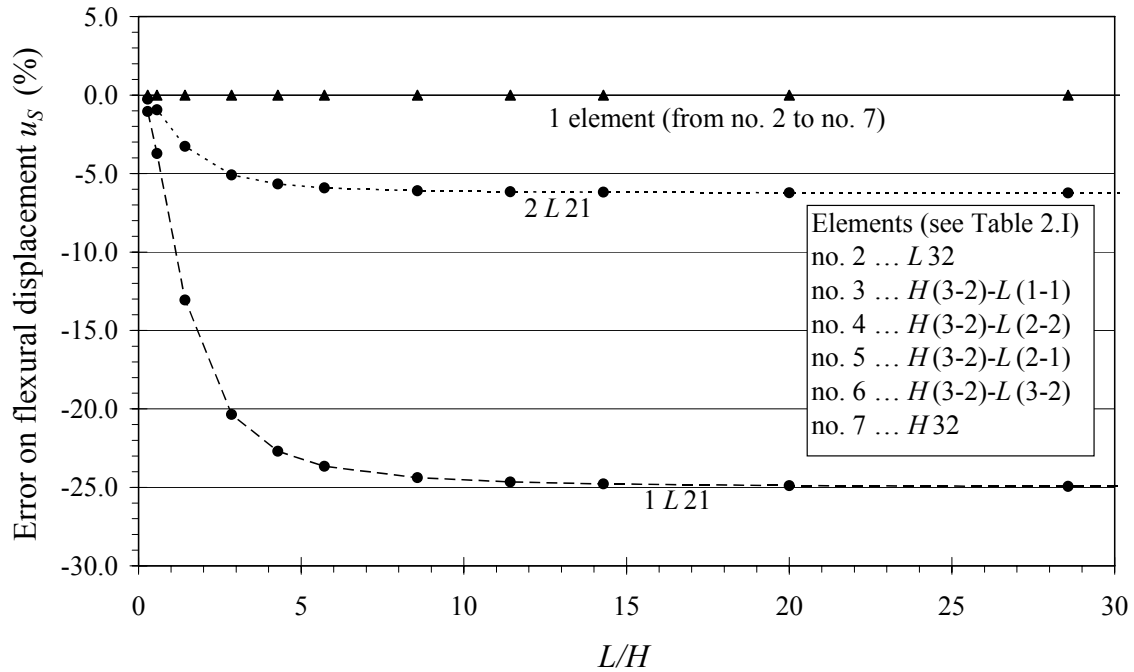
Figure 2.9. End flexural displacement for increasing slenderness of a cantilever C-shaped beam subjected to an end tip force acting in the symmetry plane. Per cent errors are referred to the Timoshenko closed-form solution (Eq. 1.171).

2.3.3 Twist of a monosymmetric beam for increasing slenderness

The torsion problem § 2.3.1 is now examined for increasing beam slenderness. In Figure 2.10, by using Eq. 1.4, the end displacement of the centroid in y direction (see Fig. 2.5) is reported for L/H ranging between 0 and 60. For the purpose of comparison, the closed-form solution to Timoshenko-Reissner's beam model was found for the beam at hand (Eqs. 1.4 and 1.251−1.252) and a shell model was developed using SAP2000®. As is shown in Figure 2.10, the centroidal displacements provided by numerical beam models are very close to the shell solutions even for high slenderness. For instance, using one $H32$ element, the error with respect to shell solution is about 6% for L/H equal to 60. As is to be expected, the displacement of the b.d. shear centre, caused by nonuniform torsion-shear coupling, becomes quickly negligible with respect to the term $\varphi_z(z)(x_C - x_S)$ when the beam length increases.

In Figure 2.11, the bimoment at the restraint from some of the proposed formulations is compared for increasing beam slenderness with the analytical solution to Timoshenko-Reissner's model (first derivative of Eq. 1.249 multiplied by EJ_ω) and with the shell solution, obtained substituting the axial stress values at the 3D-model base into Eq. 1.13d. It should be noted that, for $L \leq 15\,H$, one single beam finite element well predicts the bimoment value at the restraint.

Due to shear strain effects, if a shear force V_y is applied at the end b.d. shear centre, the C-shaped profile undergoes a torsional rotation φ_z (Fig. 2.12). In particular, due to Betti-Maxwell's reciprocity theorem, the torsional rotation φ_z produced by a unit shear

force V_y at the free end section numerically coincides with the lateral displacement v_S produced by a unit twisting moment M_z at the same section (Eq. 1.246). It can be
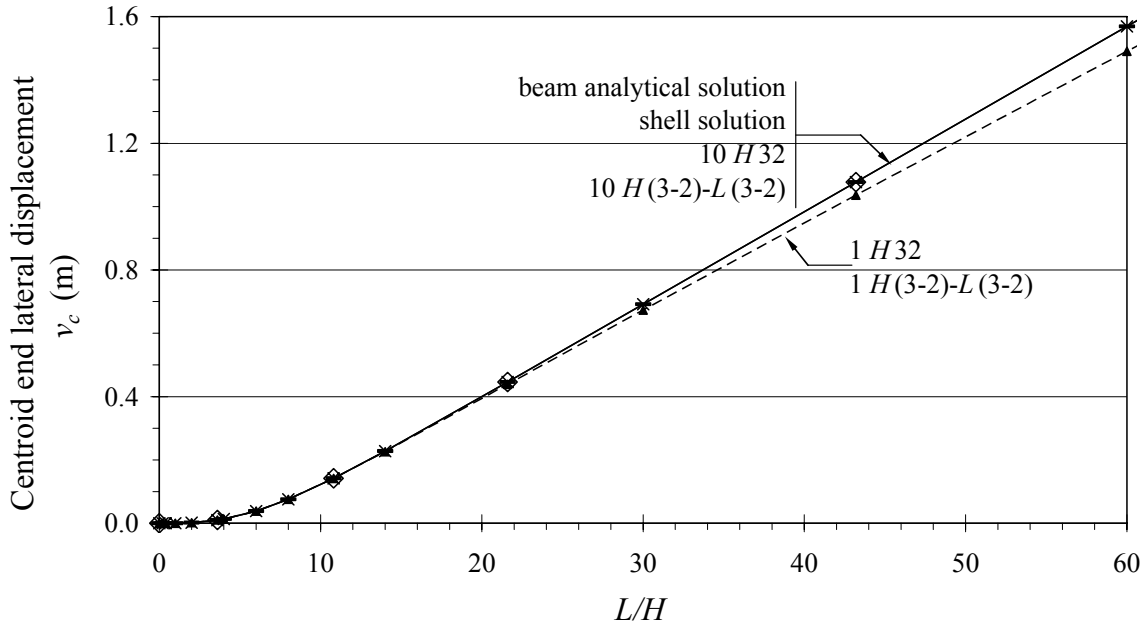
Figure 2.10. Monosymmetric cantilever profile (cross-section reported in Fig. 2.5) subjected to an end twisting moment. End section centroidal displacement along lateral (y) direction for increasing slenderness. Comparison between Timoshenko-Reissner's theory (Eq. 1.4), some of the present numerical formulations (1 and 10 elements) and shell model.
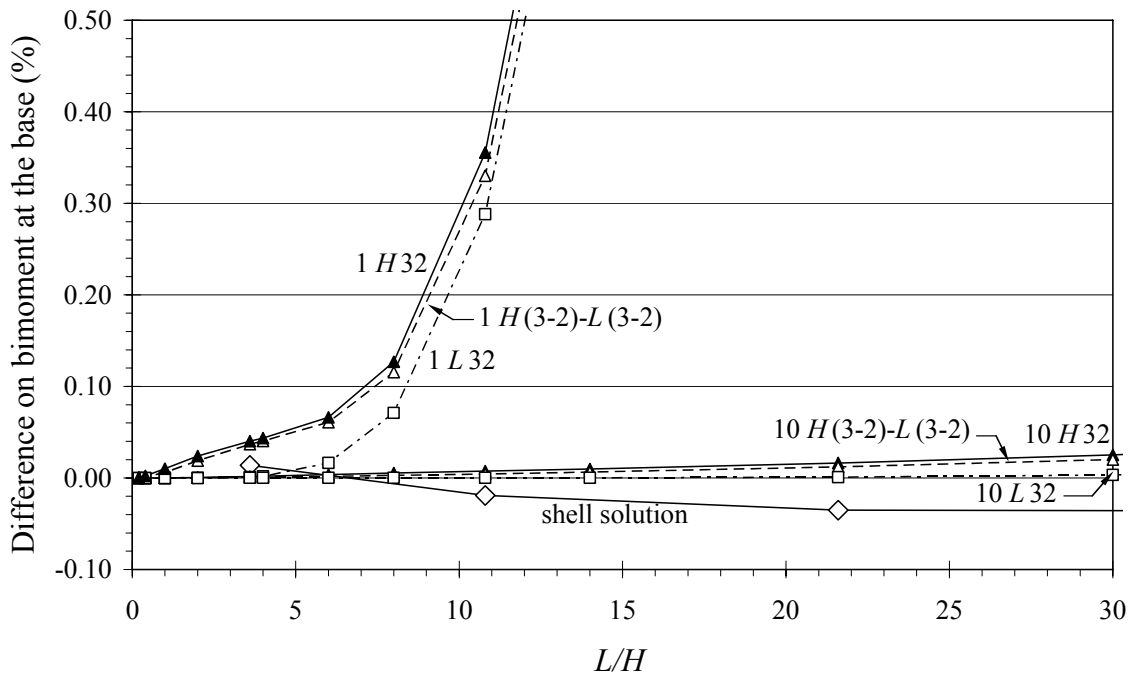
Figure 2.11. Bimoment at the base from proposed numerical beam models and 3D FE model using 4-node shell elements compared with beam analytical solution (first derivative of Eq. 1.249 multiplied by EJ_ω).

observed that the rotation φ_z at the free end given by Timoshenko-Reissner's theory ("analytical solution" in Fig. 2.12, Eq. 1.251) tends to an asymptotic value when the beam length L approaches the value L^*, at which the restraint effects become substantially negligible. If the beam (homogeneous) equilibrium equations are rearranged to give an eigenvalue problem (see § 1.5.3), the length L^* can be defined according to the relation:

$$L^* = \ln(R)/|\lambda|_{min} \qquad (2.21)$$

where R is the decay ratio of the end effects and λ_{min} is the minimum non-vanishing eigenvalue. For the problem at hand, substituting the cross-section properties (caption of Fig. 2.5) into Eq. 1.233, $|\lambda|_{min} = 0.0313$ was obtained and therefore, assuming $R = 100$ (Horgan 1989, Horgan & Simmonds 1994) yields $L^* \cong 147$ m.

Figure 2.12 also shows the values of φ_z at the free end obtained by using one beam finite element only. If elements with Lagrangian interpolation ($L21$, H(3-2)-L(3-2), $L32$) are used, the solutions tend to diverge; in particular, adopting one element H(3-2)-L(3-2), the torsional rotation $\varphi_z(V_y)$ goes to infinity according to the following limit:

$$\lim_{L \to \infty} \frac{\varphi_z(V_y)}{L} = \frac{1}{9GD_y} \frac{D_{y\omega}}{(D_\omega + J_t)} V_y \qquad (2.22)$$
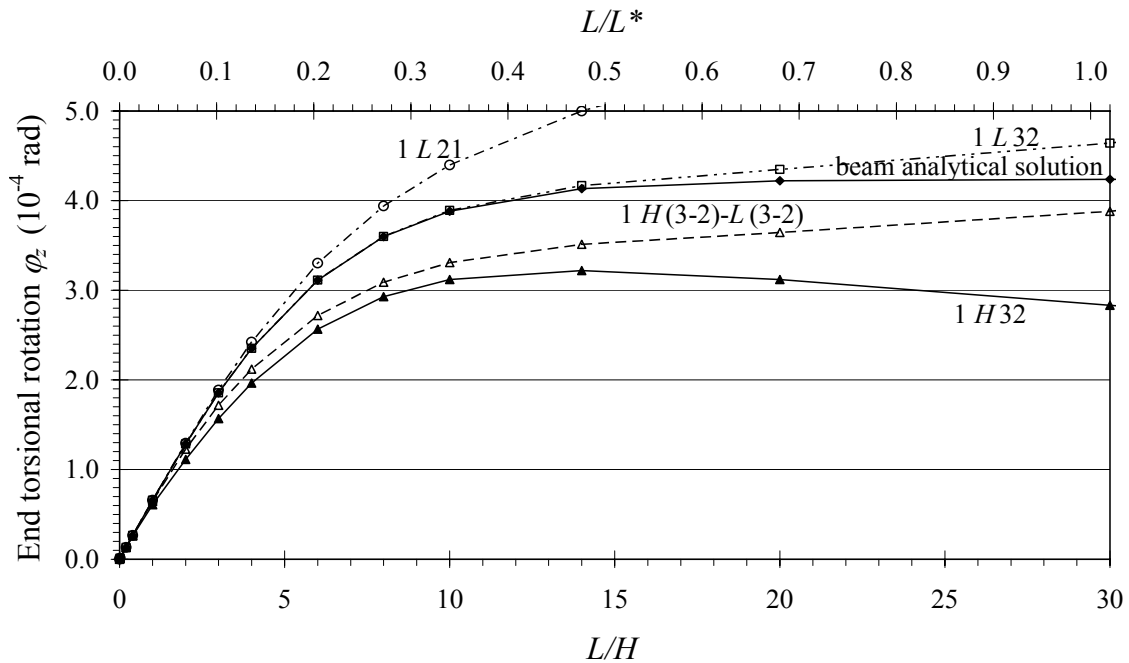
Figure 2.12. Monosymmetric cantilever profile (cross-section in Fig. 2.5) subjected to an end shear force orthogonal to the symmetry axis and passing through the b.d. shear centre. End torsional rotation for increasing slenderness. Comparison between Timoshenko-Reissner's beam theory (Eq. 1.251) and some of the present numerical models.
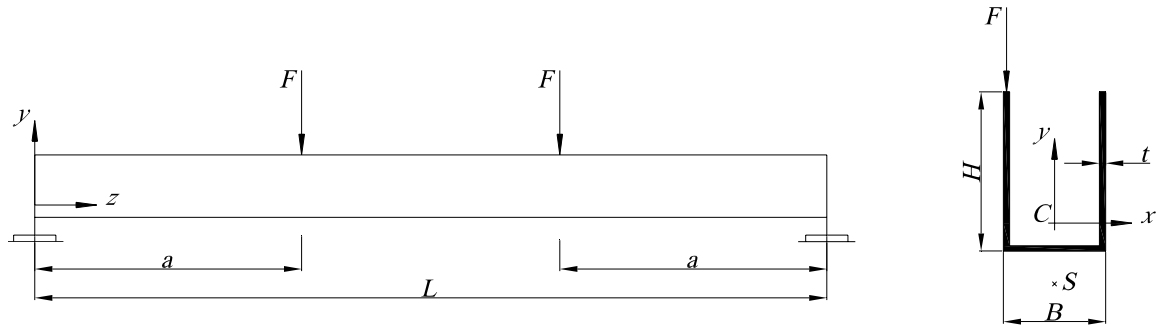
Figure 2.13. FRP orthotropic channel profile with unidirectional lay-up subjected to two eccentric
forces. $H = 0.25$ m, $B = 0.15$ m, $t = 4.45 \times 10^{-3}$ m, $L = 2$ m, $a = 0.7$ m,
$E_L = 141.4 \times 10^9$ Nm^{-2}, $G_{TL} = 6.0 \times 10^9$ Nm^{-2}, $F = 1$ N,
$J_x = 1.96125 \times 10^{-5}$ m^4, $J_y = 1.37709 \times 10^{-5}$ m^4, $J_\omega = 8.29634 \times 10^{-8}$ m^6,
$J_t = 1.90929 \times 10^{-8}$ m^4, $D_x = 5.4144 \times 10^{-4}$ m^2, $D_y = 1.86573 \times 10^{-3}$ m^2,
$D_\omega = 1.69323 \times 10^{-5}$ m^4, $D_{x\omega} = -5.72356 \times 10^{-5}$ m^3.

On the contrary, the solution provided by one H32 element tends to vanish for increasing slenderness because the relevant stiffness matrix reduces to the classical Euler-Bernoulli-Vlasov beam matrix (see Appendix 2.A).

2.3.4 Simply-supported FRP profile with monosymmetric cross-section subjected to eccentric lateral forces

This example was examined to validate the numerical models when shear deformations play a significant role. An FRP orthotropic channel profile with unidirectional lay-up subjected to two transverse eccentric forces was analyzed (Fig. 2.13). End conditions consist of pinned joints with torsional restraints. Young modulus $E_L = 141.4 \times 10^9$ Nm^{-2} and shear modulus $G_{TL} = 6.0 \times 10^9$ Nm^{-2} are assumed. The problem was proposed by Feo & Mancusi (2005), who developed a very accurate beam model for thin-walled composite profiles. They adopted a displacement field containing a number N_S of additional warping functions (supplementing function ω) up to 10, so that no correcting shear factors were required. Following the mentioned paper, 10 finite elements were used for each of the following fields: $0 < z < a$; $a < z < (L-a)$; $(L-a) < z < L$ (Fig. 2.13). A 3D model was also implemented using orthotropic shell elements (SAP2000$^{®}$ 2004). Finally, the closed-form solution to Timoshenko-Reissner's beam model was found using Eqs. 1.183, 1.185 for displacement in the plane of symmetry and Eqs. 1.269, 1.272 for torsional rotation due to load eccentricity.

In Table 2.III, torsional rotations at mid span, given by H(3-2)-L(3-2) and H32 finite elements, are compared with the results obtained by Feo and Mancusi when using a number $N_S = 0$, 4, 7 and 10 additional warping functions and with the analytical solutions to Vlasov and Timoshenko-Reissner's models. The results of Vlasov theory are re-obtained by Feo and Mancusi for $N_S = 0$. In the present example, the influence of shear deformations is significant. In fact, if shear strain effects are totally neglected, the error is about 30%. In particular, if the bending-torsion coupling term $D_{x\omega}$ is neglected,

the error on φ_z at the mid span still is of about 10%. For this example, the proposed formulations give errors less than 0.5% with respect to 3D model and capture analytical solution to Timoshenko-Reissner's model very well.

Table 2.III. Torsional rotation at mid span of the FRP profile shown in Fig. 2.13. Some of the present formulations (30 finite elements), Vlasov, Timoshenko-Reissner and Feo & Mancusi (2005) beam models are compared with shell model.

		Torsional rotation φ_z at mid span ($\times 10^{-6}$ rad)	Differences with respect to the shell solution (%)
Vlasov beam model		1.8648	−29.6
Timoshenko-Reissner's beam model		2.6610	0.4
Feo & Mancusi (2005)	$N_S = 0$	1.8648	−29.6
	$N_S = 4$	2.5559	−3.4
	$N_S = 7$	2.6485	∼ 0.0
	$N_S = 10$	2.6487	∼ 0.0
Present analysis	$H(3\text{-}2)\text{-}L(3\text{-}2)$	2.6607	0.4
	$H32$	2.6601	0.4
	$H32$ with $D_{x\omega} = 0$	2.3768	−10.3
Shell model		2.6501	

Figure 2.14. I-shaped isotropic cantilever beam subjected to a twisting moment at the free end. $H =$ 0.25 m, $B = 0.15$ m, $t_w = t_f = t = 2.5 \times 10^{-2}$ m, $L = 5$ m, $E = 2\times 10^8$ kN/m^2, $G = 8.14\times 10^7$ kN/m^2, $M_z = 25$ kNm, $J_\omega = 1.7798\times 10^{-7}$ m^6, $J_t = 2.7344\times 10^{-6}$ m^4, $D_\omega = 9.7656 \times 10^{-5}$ m^4.
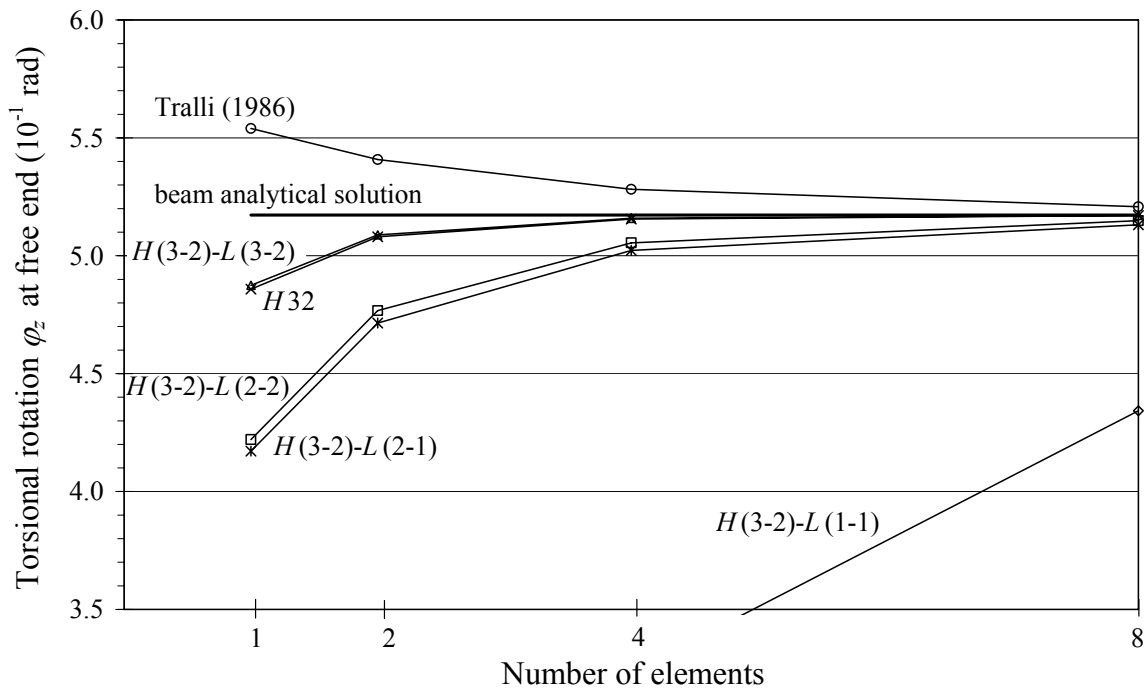
Figure 2.15. End torsional rotation for the beam shown in Fig. 2.14.
Convergence rate of the proposed numerical formulations.

2.3.5 Convergence rate for a slender isotropic cantilever beam with doubly-symmetric cross-section subjected to a constant twisting moment

This case (Fig. 2.14) was analyzed by Tralli (1986) and by Back & Will (1998). The analytical solution corresponding to kinematical model 1.3–1.5 is given by Eqs. 1.199–1.200 in terms of torsional rotation and cross-section warping. In particular, at the end section, $\varphi_z(L) = 0.5173$ rad and $\Psi(L) = -0.1123$ rad m^{-1} was obtained, respectively.

Figure 2.15 shows the solution in terms of torsional rotation φ_z at the free end given by Tralli, the analytical solution and the results offered by the proposed formulations for different discretizations. Uncoupling between torsion and bending (due to double symmetry) makes element $L21$ and $L32$ provide the same results as $H(3-2)$-$L(2-1)$ and $H(3-2)$-$L(3-2)$ elements, respectively. The model proposed by Tralli is characterized by convergence from above. As for the proposed formulations, it can be observed that convergence of element $H(3-2)$-$L(1-1)$ is very poor, whereas the other formulations present a faster convergence. In particular, $H(3-2)$-$L(2-1)$ element gives an error of 8.86% and 2.90% using 2 and 4 finite elements respectively. The corresponding errors for element $H(3-2)$-$L(2-2)$ are about 7.85% and 2.29% respectively. The fully-Hermitian element $H32$ and $H(3-2)$-$L(3-2)$ element are characterized by almost the same convergence rate and seem to offer more accurate results. For instance, the errors given by $H32$ element are about 6.08% and 1.79% if one or two finite elements are adopted.

2.3.6 Twist of a doubly-symmetric beam for increasing slenderness

The torsion problem reported in § 2.3.5 was reconsidered to test the accuracy of the highest order elements when the beam slenderness L/H goes to infinity. In other words, the ability of the formulation proposed to reproduce the De Saint Venànt solution is investigated.

End torsional rotations obtained by using 1 or 2 H(3-2)-L(3-2) and H32 finite elements are compared (Fig. 2.16) with the analytical solution 1.199. Errors for a slenderness equal to 40 are about 8% and 3% when adopting 1 or 2 elements, respectively. Moreover, element H(3-2)-L(3-2) always approaches the analytic solution better than the Hermitian element H32, even if differences become negligible when two elements are adopted. Per cent errors given by one or two H32 elements for $L/H \rightarrow \infty$ are also reported. In particular, the limit values of the end torsional rotation for one or two H32 elements are:

$$\lim_{L \to \infty} \frac{\varphi_z}{L}\bigg|_{1\text{FE}} = \frac{8M_z}{9GJ_t}; \quad \lim_{L \to \infty} \frac{\varphi_z}{L}\bigg|_{2\text{FE}} = \frac{16M_z}{17GJ_t} \tag{2.23}$$

giving, with respect to De Saint Venànt solution, errors of about -11.0% and -5.9% respectively.

Values of end cross-section warping obtained by using 1 or 2 H(3-2)-L(3-2) and H32 finite elements are compared (Fig. 2.17) with analytical solution 1.200. The limit values of the end cross-section warping for one or two H32 elements are:
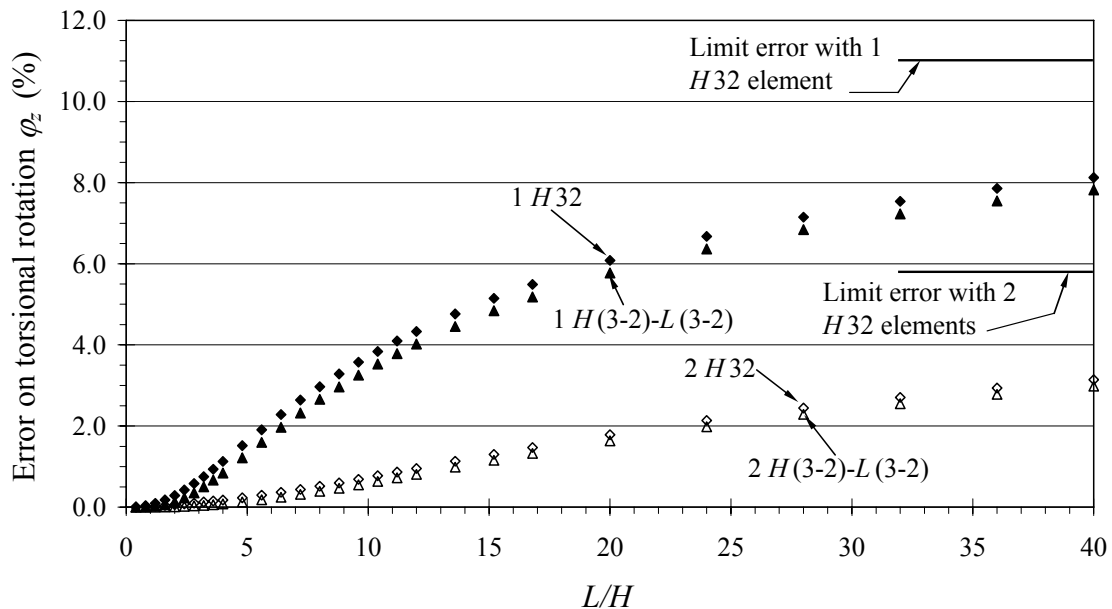
Figure 2.16. End torsional rotation for the torsion problem reported in Fig. 2.14. Per cent error (absolute values) of two proposed formulations for increasing values of slenderness L/H.
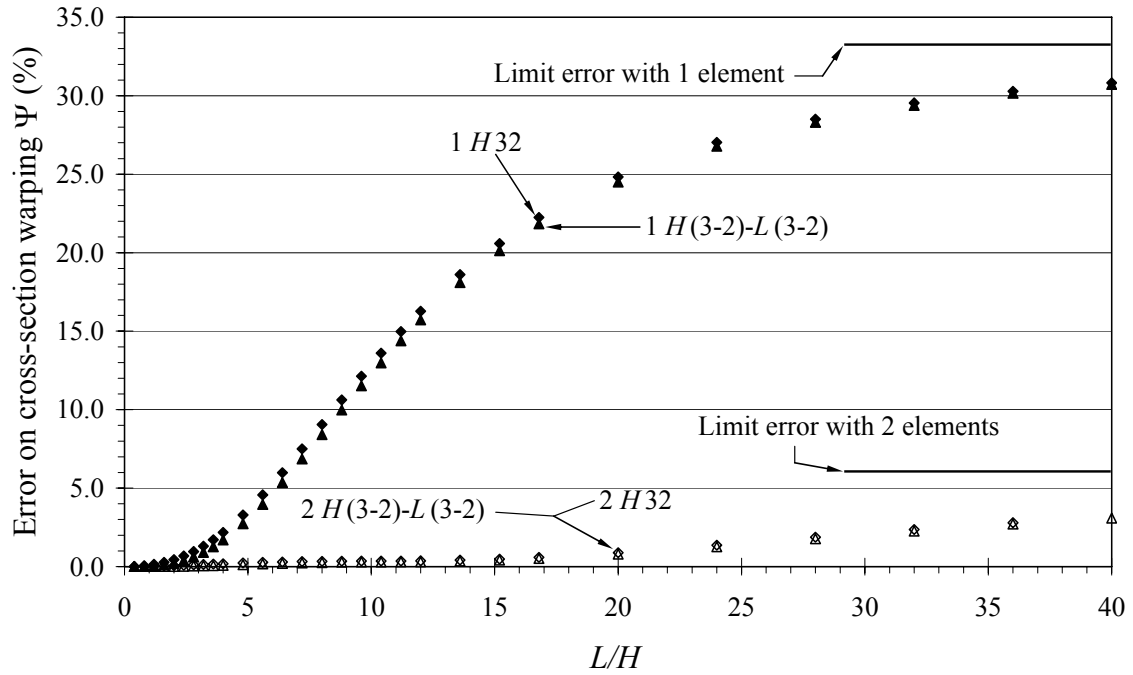
Figure 2.17. End cross-section warping for the torsion problem reported in Fig. 2.14. Per cent error (absolute values) of two proposed formulations for increasing values of slenderness L/H.

Table 2.IV. FRP I-shaped profiles: stiffness coefficients of the laminates (web and flanges). A_{ij} and D_{ij} units are 10^6 Nm^{-1} and Nm respectively.

Lay-up $1 \rightarrow [\pm45_2^f/0_{12}/\pm45_2^f]$

$$\mathbf{A}_{layup1} = \begin{bmatrix} 215.17 & 32.74 & 0 \\ & 48.17 & 0 \\ \text{Sym} & & 36.01 \end{bmatrix} \quad \mathbf{D}_{layup1} = \begin{bmatrix} 45.30 & 19.53 & 0 \\ & 25.26 & 0 \\ \text{Sym} & & 20.61 \end{bmatrix}$$

Lay-up $2 \rightarrow [0_{20}]$

$$\mathbf{A}_{layup2} = \begin{bmatrix} 297.75 & 5.82 & 0 \\ & 19.41 & 0 \\ \text{Sym} & & 9.10 \end{bmatrix} \quad \mathbf{D}_{layup2} = \begin{bmatrix} 99.25 & 1.94 & 0 \\ & 6.47 & 0 \\ \text{Sym} & & 3.03 \end{bmatrix}$$

Table 2.V. Rigidities of the two analyzed orthotropic profiles. Cross-section dimensions: $H = B = 5 \times 10^{-2}$ m, $t_w = t_f = 2 \times 10^{-3}$ m.

	$\overline{GJ_t}$ (Nm^2)	$\overline{EJ_\omega}$ (Nm^4)	$\overline{GD_\omega}$ (Nm^2)
Lay-up 1	12.20	2.58	1728.48
Lay-up 2	1.80	3.57	436.80
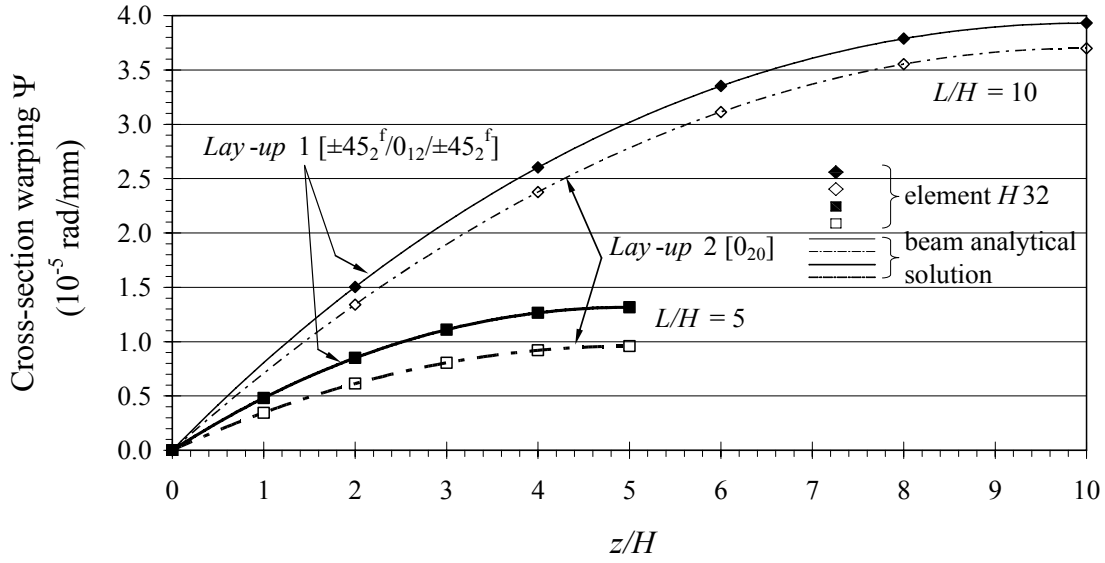
Figure 2.18. Cross-section warping of an orthotropic I-shaped beam with two different lay-ups and for two different slenderness ratios. Numerical and analytical solutions.

$$\lim_{L \to \infty} \Psi\big|_{1\text{FE}} = -\frac{2M_z}{3GJ_t} \, ; \quad \lim_{L \to \infty} \Psi\big|_{2\text{FE}} = -\frac{16M_z}{17GJ_t} \quad\quad\quad\quad (2.24)$$

giving, with respect to De Saint Venànt solution, errors of about 33.0% and 5.9% respectively.

2.3.7 Multilayered cantilever beam subjected to constant twisting moment

An I-shaped multilayered orthotropic cantilever beam made of graphite epoxy, subjected to an end twisting moment $M_z = 1.2$ Nm, was considered, characterized by two symmetric lay-ups $[0_{20}]$ and $[\pm 45_2^{\,f}/0_{12}/\pm 45_2^{\,f}]$, where apex "f" stands for woven fabric. In this case, torsion, extension and bending turn out to be uncoupled. Hence, by introducing torsion, warping and shear rigidities of the orthotropic beam, Eqs. 1.199−1.200 can still be used to determine torsional rotation and cross-section warping.

The rigidities ($\overline{GJ_t}$, $\overline{EJ_\omega}$ and $\overline{GD_\omega}$) were evaluated according to the relations reported in Appendix 1.A using laminate extensional (A_{ij}) and bending (D_{ij}) stiffness coefficients reported in Table 2.IV (values from Kollár & Springer 2003) and cross-section dimensions reported in the caption of Table 2.V. Web and flange mechanical properties were assumed to be the same. Numerical values of rigidities are reported in Table 2.V for the two beam lay-ups.

Figure 2.18 shows the cross-section warping for the orthotropic I-shaped beam with two different slenderness ratios. Numerical results obtained using six $H32$ elements and the analytical solutions given by Eq. 1.200 show very good agreement.

2.3.8 Z-shaped orthotropic cantilever beam subjected to a centroidal force at the free end

The last example was aimed at verifying the accuracy of the proposed formulations in the presence of a non symmetric cross-section. In particular, a Z-shaped orthotropic cantilever beam with unidirectional lay-up subjected to a shear force acting along the y direction at the shear centre of the end section was analyzed (Fig. 2.19). For the purpose of simplicity, the orthogonal (non principal) reference system shown in Figure 2.19 was adopted and, consequently, the elastic strain energy 1.84 is to be supplemented with the term:

$$-\frac{1}{2}\int_L 2EJ_{xy}\varphi'_x\varphi'_y dz \qquad\qquad (2.25)$$

Due to the coincidence of the shear centre with the centroid, the only non-vanishing coefficients of the shear rigidity matrix appearing in Eq. 1.51 turn out to be D_x, D_y, D_ω and D_{xy} (Fig. 2.19).

Following the same scheme of previous examples, numerical (beam) solutions were compared with results given by Timoshenko-Reissner's theory (Eqs. 1.283, 1.285) and by a shell model adopting 4-node (orthotropic) finite elements (SAP2000[®] 2004). The shear force V_y produces a displacement u_S in the x direction and a cross-section rotation φ_y about the y axis, partly given by shear strains coupling, and partly due to the combined flexure.

Actually, elements from 3 to 7 in Table 2.I (using "modified" Hermitian shape functions for flexural displacements) and the same $L32$ element reproduce the (polynomial) analytical solution and are in excellent agreement with the shell solution (Fig. 2.20) even if one beam element only is adopted. Furthermore, the accuracy of numerical results does not depend on the beam slenderness. On the contrary, results given by one $L21$ element are significantly far from the shell solution; in fact, for L/H larger than 20, they are constantly affected by an error of 25%.
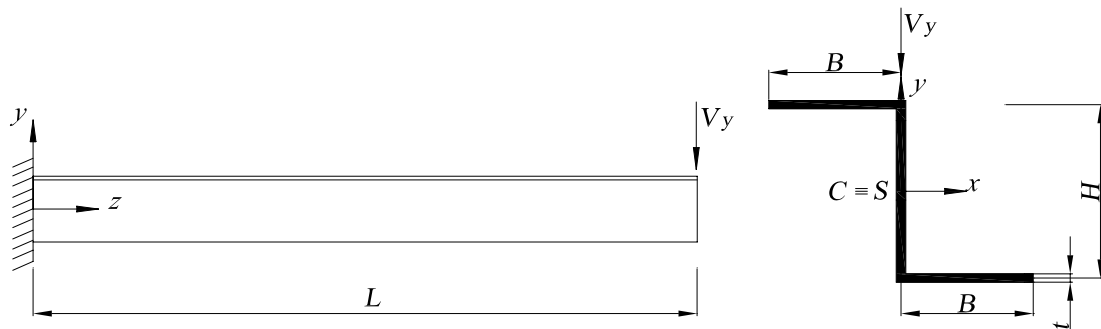
Figure 2.19. Z-shaped orthotropic cantilever beam (unidirectional lay-up) subjected to the end centroidal shear force V_y. $H = 0.2$ m, $B = 0.1$ m, $t = 0.01$ m, $E_L = 2 \times 10^{10}$ daN/m^2, $G_{LT} = E_L/7$, $V_y = 50$ daN, $J_x = 2.6667 \times 10^{-5}$ m^4, $J_y = 6.6667 \times 10^{-6}$ m^4, $J_{xy} = -1 \times 10^{-5}$ m^4, $J_t = 1.3333 \times 10^{-7}$ m^4, $J_\omega = 4.7529 \times 10^{-8}$ m^6, $D_x = 1.49398 \times 10^{-3}$ m^2, $D_y = 1.9642 \times 10^{-3}$ m^2, $D_{xy} = -1.3392 \times 10^{-4}$ m^2, $D_\omega = 1.19048 \times 10^{-5}$ m^4.
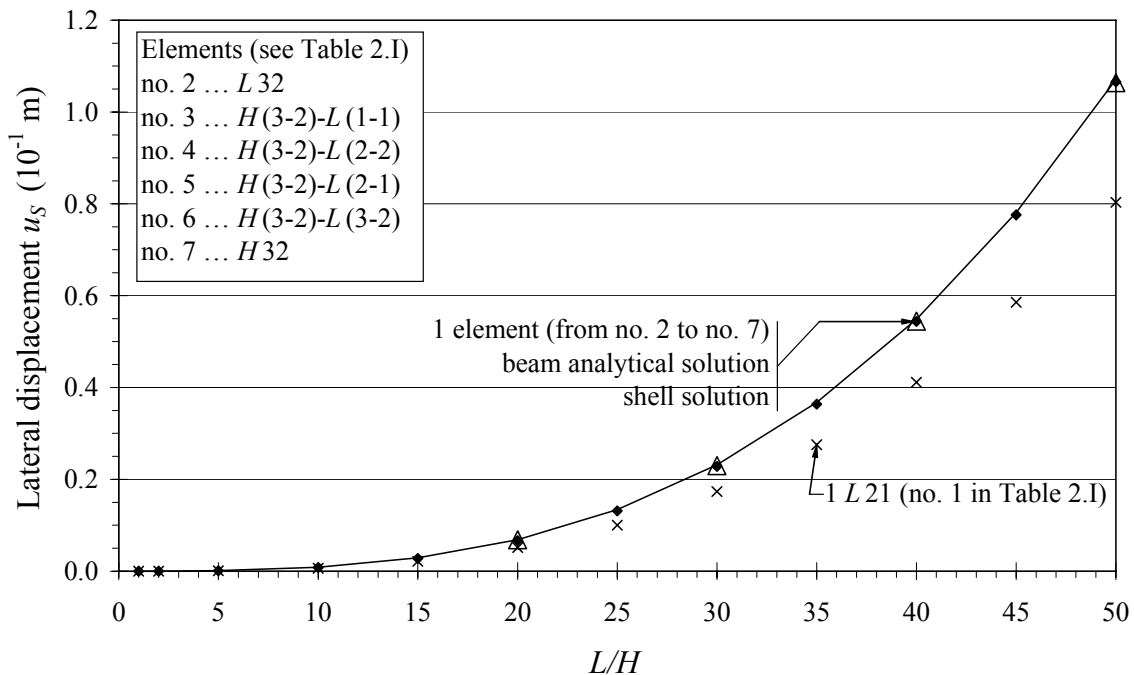
Figure 2.20. Z-shaped cantilever beam of Fig. 2.19 subjected to a centroidal tip force: lateral displacement u_S in x direction versus beam slenderness. The proposed formulations ($\blacklozenge$, $\times$) are compared with solutions given by Timoshenko-Reissner beam theory (solid line, Eq. 1.283) and by a shell model ($\triangle$).

2.4 Conclusions

Seven finite element models for thin-walled beams were compared. They were obtained using different polynomial interpolations of the displacement fields. The kinematical model based on Timoshenko-Reissner theory and described in Chapter 1 was adopted, so as to account for shear strain effects of nonuniform bending and torsion with the use of one single warping function. As is well known, beam theories are certainly less effective than 3D approaches in modelling local effects, especially in the case of orthotropic materials, which exhibit a much slower decay. Perhaps, local-global instability interaction of pultruded profiles is the most stringent example of the necessity of a preliminary 3D modelling. Nevertheless, when FRP spatial assemblages (typically bridges and truss structures) are to be analyzed and proper continuity displacement conditions are to be imposed at the inner nodes, simple and effective (beam) models represent an essential tool to analyze the structure as a whole.

The numerical (beam) models included: two formulations ($L21$, $L32$) adopting a fully Lagrangian interpolation of displacement fields; one fully Hermitian ($H32$) formulation and, finally, four ($H(3-2)-L(1-1)$, $H(3-2)-L(2-1)$, $H(3-2)-L(2-2)$, $H(3-2)-L(3-2)$) formulations adopting Hermitian polynomials for flexural displacements and rotations, and Lagrangian polynomials for torsional rotation and cross-section warping.

The Hermitian shape functions were "modified" by a parameter (depending on E/G ratio) which goes to zero when the shear strain influence vanishes. Polynomials used to

interpolate flexural displacement fields derive from the solution of the (homogeneous) Timoshenko beam problem, whereas polynomials interpolating torsion displacement fields represent the solution of the homogeneous warping-torsion problem, restricted to doubly-symmetric cross-section beams in the absence of the De Saint Venànt contribution.

As for flexural behaviour, all finite elements compared are *locking-free*. Moreover, elements using Hermitian interpolation and element *L*32 are characterized by the same bending stiffness matrix and provide exact solutions to the Timoshenko beam model.

Several examples were illustrated in order to evaluate convergence rate and accuracy of the proposed formulations with respect to both Timoshenko-Reissner beam theory and 3D (shell) models. In particular, finite elements *L*32 and *H*(3-2)-*L*(3-2) exhibited the highest convergence rate and, together with element *H*32, were in excellent agreement with shell solutions even in the case of monosymmetric and nonsymmetric cross-sections. The shear strain effects become particularly significant for FRP profiles characterized by large E/G ratios; they were accurately predicted in the presence of couplings between shear and nonuniform torsion even for long profiles. It was confirmed that the Vlasov beam model provides satisfactory results for practical purposes in the case of isotropic materials only.

In the presence of shear strain coupling, a decay length of end effects was defined, based on the De Saint Venànt principle.

Element *H*32 seems to offer greater computational advantages because it does not require static condensation. Furthermore, its stiffness matrix contains explicit parameters indicating the shear strain influence; if those parameters are set equal to zero, the matrix of the classical Euler-Bernoulli-Vlasov beam model (Barsoum & Gallagher 1970) is re-obtained.

Appendix 2.A – Stiffness matrix of element *H*32

The 14×14 stiffness matrix of *H*32 element ("modified" Hermitian interpolation for both flexural and torsional displacements) is given by:

$$
\mathbf{K}^{H32} = \begin{bmatrix}
\mathbf{K_w} & \mathbf{0} & \mathbf{0} & \mathbf{0} \\
\mathbf{0} & \mathbf{K_u} & \mathbf{K_{uv}} & \mathbf{K_{u\omega}} \\
\mathbf{0} & \mathbf{K_{vu}} & \mathbf{K_v} & \mathbf{K_{v\omega}} \\
\mathbf{0} & \mathbf{K_{\omega u}} & \mathbf{K_{\omega v}} & \mathbf{K_\omega}
\end{bmatrix}
\tag{2.A.1}
$$

where:

$$
\mathbf{K_w} = \frac{EA}{l} \begin{bmatrix} 1 & -1 \\ \text{Sym} & 1 \end{bmatrix}
\qquad \text{(axial extension)} \tag{2.A.2}
$$

$$
\mathbf{K_u} = \frac{EJ_y}{l^3 (1+\phi_x)} \begin{bmatrix}
12 & 6l & -12 & 6l \\
 & (4+\phi_x)l^2 & -6l & (2-\phi_x)l^2 \\
 & & 12 & -6l \\
\text{Sym} & & & (4+\phi_x)l^2
\end{bmatrix}
\quad \text{(bending in the } x\text{-}z \text{ plane)} \tag{2.A.3}
$$

$$
\mathbf{K_v} = \frac{EJ_x}{l^3 (1+\phi_y)} \begin{bmatrix}
12 & -6l & -12 & -6l \\
 & (4+\phi_y)l^2 & 6l & (2-\phi_y)l^2 \\
 & & 12 & 6l \\
\text{Sym} & & & (4+\phi_y)l^2
\end{bmatrix}
\quad \text{(bending in the } y\text{-}z \text{ plane)} \tag{2.A.4}
$$

$$
\mathbf{K_\omega} = \frac{1}{60l^3 (1+\phi_\omega)^2} \begin{bmatrix}
12P_1 & -6lP_2 & -12P_1 & -6lP_2 \\
 & P_3 l^2 & 6lP_2 & -l^2 P_4 \\
 & & 12P_1 & 6lP_2 \\
\text{Sym} & & & P_3 l^2
\end{bmatrix}
\quad \text{(torsion)} \tag{2.A.5}
$$

Coefficients P_i ($i = 1, \ldots, 4$) in Eq. (2.B.5) take the following expressions:

$$
P_1 = 60EJ_\omega (1+\phi_\omega) + GJ_t l^2 (6+10\phi_\omega + 5\phi_\omega^2) \tag{2.A.6}
$$

$$
P_2 = 60EJ_\omega (1+\phi_\omega) + GJ_t l^2 \tag{2.A.7}
$$

$$
P_3 = 60EJ_\omega (4+5\phi_\omega + \phi_\omega^2) + GJ_t l^2 (8+10\phi_\omega + 5\phi_\omega^2) \tag{2.A.8}
$$

$$
P_4 = 60EJ_\omega (-2-\phi_\omega + \phi_\omega^2) + GJ_t l^2 (2+10\phi_\omega + 5\phi_\omega^2) \tag{2.A.9}
$$

Off-diagonal submatrices of $\mathbf{K}^{H32}$ are given by:

$$\mathbf{K_{uv}} = \mathbf{K_{vu}^{T}} = \frac{GD_{xy}\phi_x\phi_y}{4l\left(1+\phi_x\right)\left(1+\phi_y\right)}\begin{bmatrix} 4 & -2l & -4 & -2l \\ 2l & -l^2 & -2l & -l^2 \\ -4 & 2l & 4 & 2l \\ 2l & -l^2 & -2l & -l^2 \end{bmatrix} \tag{2.A.10}$$

(x-shear–y-shear coupling)

$$\mathbf{K_{u\omega}} = \mathbf{K_{\omega u}^{T}} = \frac{GD_{x\omega}\phi_x\phi_\omega}{4l\left(1+\phi_x\right)\left(1+\phi_\omega\right)}\begin{bmatrix} 4 & -2l & -4 & -2l \\ 2l & -l^2 & -2l & -l^2 \\ -4 & 2l & 4 & 2l \\ 2l & -l^2 & -2l & -l^2 \end{bmatrix} \tag{2.A.11}$$

(x-shear–warping coupling)

$$\mathbf{K_{v\omega}} = \mathbf{K_{\omega v}^{T}} = \frac{GD_{y\omega}\phi_y\phi_\omega}{4l\left(1+\phi_y\right)\left(1+\phi_\omega\right)}\begin{bmatrix} 4 & -2l & -4 & -2l \\ -2l & l^2 & 2l & l^2 \\ -4 & 2l & 4 & 2l \\ -2l & l^2 & 2l & l^2 \end{bmatrix} \tag{2.A.12}$$

(y-shear–warping coupling)

and turn out to be null matrices for doubly-symmetric cross-section beams only. Neglecting shear deformations yields $\phi_x = \phi_y = \phi_\omega = 0$ and, consequently, matrix $\mathbf{K}^{H32}$ reduces to the stiffness matrix of the Euler-Bernoulli-Vlasov beam (Barsoum & Gallagher 1970).

Appendix 2.B – Stiffness matrix of element *L*32

The 23×23 stiffness matrix of *L*32 element is given by:

$$\mathbf{K}^{L32} = \begin{bmatrix} \mathbf{K}_{en} & \mathbf{K}_{ei} \\ \mathbf{K}_{ie} & \mathbf{K}_{in} \end{bmatrix} \tag{2.B.1}$$

where, with reference to the finite element of Figure 2.1, $\mathbf{K}_{en}$, $\mathbf{K}_{in}$ and $\mathbf{K}_{ei}$ $(=\mathbf{K}_{ie}^{T})$ collect the stiffness coefficients of the end nodes (1, 2), of the inner nodes (3, 4, 5), and the relative stiffnesses, respectively.

In particular, the 14×14 matrix $\mathbf{K}_{en}$ is given by:

$$\mathbf{K}_{en} = \begin{bmatrix} \mathbf{K}_{en,\mathbf{w}} & \mathbf{0} & \mathbf{0} & \mathbf{0} \\ \mathbf{0} & \mathbf{K}_{en,\mathbf{u}} & \mathbf{K}_{en,\mathbf{uv}} & \mathbf{K}_{en,\mathbf{u\omega}} \\ \mathbf{0} & \mathbf{K}_{en,\mathbf{vu}} & \mathbf{K}_{en,\mathbf{v}} & \mathbf{K}_{en,\mathbf{v\omega}} \\ \mathbf{0} & \mathbf{K}_{en,\mathbf{\omega u}} & \mathbf{K}_{en,\mathbf{\omega v}} & \mathbf{K}_{en,\mathbf{\omega}} \end{bmatrix} \tag{2.B.2}$$

where:

$$\mathbf{K}_{en,\mathbf{w}} = \frac{EA}{l} \begin{bmatrix} 1 & -1 \\ \text{Sym} & 1 \end{bmatrix} \qquad \text{(axial extension)} \tag{2.B.3}$$

$$\mathbf{K}_{en,\mathbf{u}} = \frac{GD_x}{l} \begin{bmatrix} 37/10 & 83l/120 & -13/40 & -7l/120 \\ & 7EJ_y/3GD_x + 2l^2/15 & 7l/120 & EJ_y/3GD_x - l^2/30 \\ & & 37/10 & -83l/120 \\ \text{Sym} & & & 7EJ_y/3GD_x + 2l^2/15 \end{bmatrix} \tag{2.B.4}$$

(bending in the *x*-*z* plane)

$$\mathbf{K}_{en,\mathbf{v}} = \frac{GD_y}{l} \begin{bmatrix} 37/10 & -83l/120 & -13/40 & 7l/120 \\ & 7EJ_x/3GD_y + 2l^2/15 & -7l/120 & EJ_x/3GD_y - l^2/30 \\ & & 37/10 & 83l/120 \\ \text{Sym} & & & 7EJ_x/3GD_y + 2l^2/15 \end{bmatrix} \tag{2.B.5}$$

(bending in the *y*-*z* plane)

$$\mathbf{K}_{en,\boldsymbol{\omega}} = \frac{GD_{\omega}}{l}\begin{bmatrix} \dfrac{37}{10}\left(1+\dfrac{GJ_t}{GD_{\omega}}\right) & -\dfrac{83}{120}l & -\dfrac{13}{40}\left(1+\dfrac{GJ_t}{GD_{\omega}}\right) & \dfrac{7}{120}l \\[2mm] & \dfrac{7EJ_{\omega}}{3GD_{\omega}}+\dfrac{2}{15}l^2 & -\dfrac{7}{120}l & \dfrac{EJ_{\omega}}{3GD_{\omega}}-\dfrac{1}{30}l^2 \\[2mm] & & \dfrac{37}{10}\left(1+\dfrac{GJ_t}{GD_{\omega}}\right) & \dfrac{83}{120}l \\[2mm] \text{Sym} & & & \dfrac{7EJ_{\omega}}{3GD_{\omega}}+\dfrac{2}{15}l^2 \end{bmatrix} \qquad (2.B.6)$$

<div align="center">(torsion)</div>

Off-diagonal submatrices of $\mathbf{K}_{en}$ are given by:

$$\mathbf{K}_{en,\mathbf{uv}} = \mathbf{K}_{en,\mathbf{vu}}^T = \frac{GD_{xy}}{l}\begin{bmatrix} 37/10 & -83l/120 & -13/40 & 7l/120 \\ 83l/120 & -2l^2/15 & 7l/120 & l^2/30 \\ -13/40 & -7l/120 & 37/10 & 83l/120 \\ -7l/120 & l^2/30 & -83l/120 & -2l^2/15 \end{bmatrix} \qquad (2.B.7)$$

<div align="center">(x-shear–y-shear coupling)</div>

$$\mathbf{K}_{en,\mathbf{u\omega}} = \mathbf{K}_{en,\boldsymbol{\omega}\mathbf{u}}^T = \frac{GD_{x\omega}}{l}\begin{bmatrix} 37/10 & -83l/120 & -13/40 & 7l/120 \\ 83l/120 & -2l^2/15 & 7l/120 & l^2/30 \\ -13/40 & -7l/120 & 37/10 & 83l/120 \\ -7l/120 & l^2/30 & -83l/120 & -2l^2/15 \end{bmatrix} \qquad (2.B.8)$$

<div align="center">(x-shear–warping coupling)</div>

$$\mathbf{K}_{en,\mathbf{v\omega}} = \mathbf{K}_{en,\boldsymbol{\omega}\mathbf{v}}^T = \frac{GD_{y\omega}}{l}\begin{bmatrix} 37/10 & -83l/120 & -13/40 & 7l/120 \\ -83l/120 & 2l^2/15 & -7l/120 & -l^2/30 \\ -13/40 & -7l/120 & 37/10 & 83l/120 \\ 7l/120 & -l^2/30 & 83l/120 & 2l^2/15 \end{bmatrix} \qquad (2.B.9)$$

<div align="center">(y-shear–warping coupling)</div>

The 9×9 matrix $\mathbf{K}_{in}$ is given by:

$$\mathbf{K}_{in} = \begin{bmatrix} \mathbf{K}_{in,\mathbf{u}} & \mathbf{K}_{in,\mathbf{uv}} & \mathbf{K}_{in,\mathbf{u\omega}} \\ \mathbf{K}_{in,\mathbf{vu}} & \mathbf{K}_{in,\mathbf{v}} & \mathbf{K}_{in,\mathbf{v\omega}} \\ \mathbf{K}_{in,\boldsymbol{\omega}\mathbf{u}} & \mathbf{K}_{in,\boldsymbol{\omega}\mathbf{v}} & \mathbf{K}_{in,\boldsymbol{\omega}} \end{bmatrix} \qquad (2.B.10)$$

where:

$$\mathbf{K}_{in,\mathbf{u}} = \frac{GD_x}{l} \begin{bmatrix} 54/5 & 9l/10 & -297/40 \\ & 16EJ_y/3GD_x + 8l^2/15 & -9l/10 \\ \text{Sym} & & 54/5 \end{bmatrix} \tag{2.B.11}$$

(bending in the x-z plane)

$$\mathbf{K}_{in,\mathbf{v}} = \frac{GD_y}{l} \begin{bmatrix} 54/5 & -9l/10 & -297/40 \\ & 16EJ_x/3GD_y + 8l^2/15 & 9l/10 \\ \text{Sym} & & 54/5 \end{bmatrix} \tag{2.C.12}$$

(bending in the y-z plane)

$$\mathbf{K}_{in,\boldsymbol{\omega}} = \frac{GD_\omega}{l} \begin{bmatrix} \frac{54}{5}\left(1+\frac{GJ_t}{GD_\omega}\right) & -\frac{9}{10}l & -\frac{297}{40}\left(1+\frac{GJ_t}{GD_\omega}\right) \\ & \frac{16EJ_\omega}{3GD_\omega}+\frac{8}{15}l^2 & \frac{9}{10}l \\ \text{Sym} & & \frac{54}{5}\left(1+\frac{GJ_t}{GD_\omega}\right) \end{bmatrix} \tag{2.B.13}$$

(torsion)

Off-diagonal submatrices of $\mathbf{K}_{in}$ are given by:

$$\mathbf{K}_{in,\mathbf{uv}} = \mathbf{K}_{in,\mathbf{vu}}^T = \frac{GD_{xy}}{l} \begin{bmatrix} 54/5 & -9l/10 & -297/40 \\ 9l/10 & -8l^2/15 & -9l/10 \\ -297/40 & 9l/10 & 54/5 \end{bmatrix} \tag{2.B.14}$$

(x-shear–y-shear coupling)

$$\mathbf{K}_{in,\mathbf{u\omega}} = \mathbf{K}_{in,\boldsymbol{\omega}\mathbf{u}}^T = \frac{GD_{x\omega}}{l} \begin{bmatrix} 54/5 & -9l/10 & -297/40 \\ 9l/10 & -8l^2/15 & -9l/10 \\ -297/40 & 9l/10 & 54/5 \end{bmatrix} \tag{2.B.15}$$

(x-shear–warping coupling)

$$\mathbf{K}_{in,\mathbf{v\omega}} = \mathbf{K}_{in,\boldsymbol{\omega}\mathbf{v}}^T = \frac{GD_{y\omega}}{l} \begin{bmatrix} 54/5 & -9l/10 & -297/40 \\ -9l/10 & 8l^2/15 & 9l/10 \\ -297/40 & 9l/10 & 54/5 \end{bmatrix} \tag{2.B.16}$$

(y-shear–warping coupling)

Finally, the 14×9 matrix $\mathbf{K}_{ei}$ $(=\mathbf{K}_{ie}^T)$ takes the form:

$$\mathbf{K}_{ei} = \mathbf{K}_{ie}^T = \begin{bmatrix} \mathbf{0} & \mathbf{0} & \mathbf{0} \\ \mathbf{K}_{ei,\mathbf{u}} & \mathbf{K}_{ei,\mathbf{uv}} & \mathbf{K}_{ei,\mathbf{u\omega}} \\ \mathbf{K}_{ei,\mathbf{vu}} & \mathbf{K}_{ei,\mathbf{v}} & \mathbf{K}_{ei,\mathbf{v\omega}} \\ \mathbf{K}_{ei,\mathbf{\omega u}} & \mathbf{K}_{ei,\mathbf{\omega v}} & \mathbf{K}_{ei,\mathbf{\omega}} \end{bmatrix} \qquad (2.B.17)$$

where:

$$\mathbf{K}_{ei,\mathbf{u}} = \frac{GD_x}{l} \begin{bmatrix} -189/40 & 11l/30 & 27/20 \\ -33l/40 & -8EJ_y/3GD_x + l^2/15 & 3l/40 \\ 27/20 & -11l/30 & -189/40 \\ -3l/40 & -8EJ_y/3GD_x + l^2/15 & 33l/40 \end{bmatrix} \qquad (2.B.18)$$

(bending in the *x-z* plane)

$$\mathbf{K}_{ei,\mathbf{v}} = \frac{GD_y}{l} \begin{bmatrix} -189/40 & -11l/30 & 27/20 \\ 33l/40 & -8EJ_x/3GD_y + l^2/15 & -3l/40 \\ 27/20 & 11l/30 & -189/40 \\ 3l/40 & -8EJ_x/3GD_y + l^2/15 & -33l/40 \end{bmatrix} \qquad (2.B.19)$$

(bending in the *y-z* plane)

$$\mathbf{K}_{ei,\mathbf{\omega}} = \frac{GD_\omega}{l} \begin{bmatrix} -\dfrac{189}{40}\left(1+\dfrac{GJ_t}{GD_\omega}\right) & -\dfrac{11}{30}l & \dfrac{27}{20}\left(1+\dfrac{GJ_t}{GD_\omega}\right) \\ \dfrac{33}{40}l & -\dfrac{8EJ_\omega}{3GD_\omega}+\dfrac{1}{15}l^2 & -\dfrac{3}{40}l \\ \dfrac{27}{20}\left(1+\dfrac{GJ_t}{GD_\omega}\right) & \dfrac{11}{30}l & -\dfrac{189}{40}\left(1+\dfrac{GJ_t}{GD_\omega}\right) \\ \dfrac{3}{40}l & -\dfrac{8EJ_\omega}{3GD_\omega}+\dfrac{1}{15}l^2 & -\dfrac{33}{40}l \end{bmatrix} \qquad (2.B.20)$$

(torsion)

Off-diagonal submatrices of $\mathbf{K}_{ei}$ $(=\mathbf{K}_{ie}^T)$ are given by:

$$\mathbf{K}_{ei,\mathbf{uv}} = \frac{GD_{xy}}{l} \begin{bmatrix} -189/40 & -11l/30 & 27/20 \\ -33l/40 & -l^2/15 & 3l/40 \\ 27/20 & 11l/30 & -189/40 \\ -3l/40 & -l^2/15 & 33l/40 \end{bmatrix} \qquad (2.B.21)$$

$$\mathbf{K}_{ei,\mathbf{vu}} = \frac{GD_{xy}}{l} \begin{bmatrix} -189/40 & 11l/30 & 27/20 \\ 33l/40 & -l^2/15 & -3l/40 \\ 27/20 & -11l/30 & -189/40 \\ 3l/40 & -l^2/15 & -33l/40 \end{bmatrix}$$

(2.B.22)

(*x*-shear–*y*-shear coupling)

$$\mathbf{K}_{ei,\mathbf{u\omega}} = \frac{GD_{x\omega}}{l} \begin{bmatrix} -189/40 & -11l/30 & 27/20 \\ -33l/40 & -l^2/15 & 3l/40 \\ 27/20 & 11l/30 & -189/40 \\ -3l/40 & -l^2/15 & 33l/40 \end{bmatrix}$$

(2.B.23)

$$\mathbf{K}_{ei,\mathbf{\omega u}} = \frac{GD_{x\omega}}{l} \begin{bmatrix} -189/40 & 11l/30 & 27/20 \\ 33l/40 & -l^2/15 & -3l/40 \\ 27/20 & -11l/30 & -189/40 \\ 3l/40 & -l^2/15 & -33l/40 \end{bmatrix}$$

(2.B.24)

(*x*-shear–warping coupling)

$$\mathbf{K}_{ei,\mathbf{v\omega}} = \frac{GD_{y\omega}}{l} \begin{bmatrix} -189/40 & -11l/30 & 27/20 \\ 33l/40 & l^2/15 & -3l/40 \\ 27/20 & 11l/30 & -189/40 \\ 3l/40 & l^2/15 & -33l/40 \end{bmatrix}$$

(2.B.25)

$$\mathbf{K}_{ei,\mathbf{\omega v}} = \frac{GD_{y\omega}}{l} \begin{bmatrix} -189/40 & -11l/30 & 27/20 \\ 33l/40 & l^2/15 & -3l/40 \\ 27/20 & 11l/30 & -189/40 \\ 3l/40 & l^2/15 & -33l/40 \end{bmatrix}$$

(2.B.26)

(*y*-shear–warping coupling)

In order to obtain a 14×14 stiffness matrix, the degrees of freedom of inner nodes are to be condensed out by means of the following standard transformation:

$$\mathbf{K}_{cond}^{L32} = \mathbf{K}_{en} - \mathbf{K}_{ei}\mathbf{K}_{in}^{-1}\mathbf{K}_{ie} = \mathbf{K}_{en} - \mathbf{K}_{ei}\mathbf{K}_{in}^{-1}\mathbf{K}_{ei}^{T}$$

(2.B.27)

Appendix 2.C – Coordinate transformation to take the assemblage point eccentricity into account

Displacement components 1.3–1.5 are referred partly to the centroid and partly to the shear center. Hence, before assembling the global structural matrix, all quantities are to be defined with respect to a single reference point: typically the centroid (Back & Will 1998). On the other hand, in spatial truss structures the assemblage point of noncollinear elements often does not coincide neither with the centroid nor with the shear center (Fig. 2.CI). Hence, to refer all degrees of freedom to the assemblage point, a coordinate transformation is needed. In particular, by virtue of Eqs. 1.3–1.5, for each connected element the following transformation holds (Shakourzadeh *et al.* 1995b):
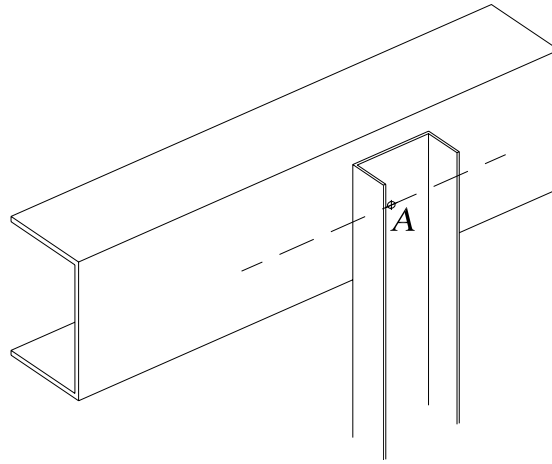
Figure 2.CI. Assembly of thin-walled profiles.

$$
\begin{Bmatrix} w \\ u \\ v \\ \varphi_z \\ \varphi_x \\ \varphi_y \\ \Psi \end{Bmatrix}_{C,S}
=
\begin{bmatrix}
1 & 0 & 0 & 0 & -y_A & x_A & \overline{\omega} \\
 & 1 & 0 & (y_A - y_S) & 0 & 0 & 0 \\
 & & 1 & -(x_A - x_S) & 0 & 0 & 0 \\
 & & & 1 & 0 & 0 & 0 \\
 & & & & 1 & 0 & (x_A - x_S) \\
 & 0 & & & & 1 & (y_A - y_S) \\
 & & & & & & 1
\end{bmatrix}
\begin{Bmatrix} w \\ u \\ v \\ \varphi_z \\ \varphi_x \\ \varphi_y \\ \Psi \end{Bmatrix}_{A}
\qquad (2.C.1)
$$

where the relation $\overline{\omega} = \omega_A + x_S y_A - x_A y_S$ (Corradi Dell'Acqua 1992) links the warping function referred to the shear center to that referred to the assemblage point.

Appendix 2.D – Numerical solutions for example 2.3.1

Channel-shaped shear core of § 2.3.1 (Fig. 2.5). Comparison between numerical results and beam analytical solution in terms of torsional rotations (Eq. 1.248, Kim & Kim 2005) and lateral displacements of b.d. shear centre (Eq. 1.246, Kim & Kim 2005). See Table 2.I and Table 2.II for details on proposed beam finite elements.

Table 2.DI. Numerical solutions concerning example of § 2.3.1.

Compared formulations		Distance from the fixed end (m)					
		3	6	9	12	15	18
Torsional rotation φ_z (rad × 10^{-3})	Mesh of 6 beam finite elements						
	$L21$	0.1882	0.6595	1.354	2.215	3.185	4.210
	$L32$	0.1930	0.6692	1.368	2.233	3.207	4.236
	$H(3\text{-}2)\text{-}L(3\text{-}2)$	0.1931	0.6689	1.368	2.232	3.207	4.236
	$H32$	0.1930	0.6686	1.367	2.232	3.206	4.235
	Tralli (1986)	0.1934	0.6696	1.369	2.234	3.209	4.239
	Analytical beam solution						
	Eq. 1.248	0.1933	0.6692	1.368	2.233	3.207	4.236
	One exact beam finite element						
	Kim and Kim (2005)	0.1933	0.6692	1.368	2.233	3.207	4.236
	Shell model	0.1918	0.6639	1.358	2.220	3.200	4.232
Lateral displacement v_S of b.d. shear centre (m × 10^{-4})	Mesh of 6 beam finite elements						
	$L21$	0.3893	0.7628	1.124	1.476	1.822	2.165
	$L32$	0.3890	0.7623	1.123	1.475	1.821	2.163
	$H(3\text{-}2)\text{-}L(3\text{-}2)$	0.3869	0.7583	1.117	1.467	1.811	2.152
	$H32$	0.3748	0.7344	1.082	1.421	1.754	2.084
	Analytical beam solution						
	Eq. 1.246	0.3890	0.7623	1.123	1.475	1.821	2.163
	One exact beam finite element						
	Kim and Kim (2005)	0.3890	0.7623	1.123	1.475	1.821	2.163
	Shell model	0.3694	0.7480	1.114	1.474	1.828	2.180

Chapter 3

Buckling analysis

3.1 Introduction

In the field of structural applications, the performance of FRP profiles is basically ruled by deformability and buckling phenomena. In particular, the high ratio between the longitudinal elasticity modulus and the transverse elasticity modulus typically involves local-global buckling interaction, closely related to a strong influence of shear deformations. At present, an extensive bibliography is available, referring to both experimental (Brooks & Turvey 1995, Davalos *et al.* 1997, Barbero *et al.* 2000, Barbero & Malek 2000, Qiao *et al.* 2003, Mottram *et al.* 2003, Mottram 2004) and theoretical (Sherbourne & Kabir 1995, Kollár 2001a, Lee & Kim 2001, Sapkás & Kollár 2002, Lee & Kim 2002, Lee *et al.* 2002, Roberts 2002, Cortínez & Piovan 2002, Roberts & Masri 2003, De Lorenzis & La Tegola 2005, Kim *et al.* 2007a,b) investigations into buckling phenomena; in particular, some practical design expressions were provided (Barbero & DeVivo 1999, Pecce & Cosenza 2000) which represent a useful tool to handle a rather complex material. In recent beam models, the classical hypothesis of transversal rigidity was removed (Volovoi *et al.* 1999, De Lorenzis & La Tegola 2003b) to analyze local-global buckling interaction of beams with particular open cross-sections. The extension of these models to generic cross-section profiles and the relative applications probably represent the greatest challenge in the analysis of FRP structures. To this purpose, a preliminary 3D modelling is essential to gain insight into FRP buckling phenomena; yet, simple and effective 1D (beam) models are necessary when displacement continuity conditions are to be imposed at the inner nodes of spatial assemblages.

In this chapter, a beam model for overall buckling analysis of FRP open-section beams under conservative static loads is presented. It is well known that, in the context of buckling analysis, accuracy is greatly affected by the order of approximation of the displacement field. For instance, for some load conditions like axial load or uniform bending, buckling is well predicted by adopting a linear approximation. On the contrary, in the case of beams subjected to lateral loads, a second-order displacement field is required (Kim *et al.* 1996, Pi & Bradford 2001). As a matter of fact, in the present chapter reference is made to the displacement field proposed by Chang *et al.* (1996) and, more recently, by Cortínez & Piovan (2006) and Piovan & Cortínez (2007) which,

in turn, can be obtained from Rodriguez's matrix of finite rotations (Argyris 1982, Criesfield 1991) by retaining terms up to the second-order. The model adopted takes the shear strain influence on nonuniform torsion and bending into account: in fact, the linear part of the assumed kinematics coincides with Timoshenko-Reissner's beam model (see Chapter 1) where one single warping function is adopted.

The assumed stability criterion is based on the positive definiteness of the second variation of the potential energy (Washizu 1982). The displacement field is interpolated by means of *locking-free* finite elements of type *H*32 (see § 2.2.1) resorting to "modified" Hermitian polynomials. The geometric stiffness matrix developed is reported in Appendix 3.A for two common load conditions. For shear-undeformable doubly-symmetric cross-section beams it reduces, after some manipulation, to the matrix of the classical Euler-Bernoulli-Vlasov model (Barsoum & Gallagher 1970), provided that in-plane second-order displacement components are neglected.

In order to validate the numerical model, orthotropic beams with doubly- and monosymmetric cross-sections were analyzed. Convergence properties and accuracy were verified in the case of profiles subjected to axial loads as well as to lateral forces. The influence of shear deformations and of the location of applied loads with respect to the shear centre was pointed out. Comparisons were made with analytical solutions (Kollár 2001a,b, Cortínez & Piovan 2002), numerical solutions (Cortínez & Piovan 2006) and approximate formulas (Sapkás & Kollár 2002, Clark & Hill 1960) given in literature. Finally, finite element stability analyses of frames made of FRP pultruded thin-walled members, subjected to combined horizontal and vertical loads, were performed. Buckling interaction curves were determined for various out-of-plane restraint conditions. Some aspects concerning buckling of frames having shear flexible members were previously discussed by Mottram and Aberle (2002) and Aristizábal-Ochoa (2004, 2007), where the authors make use of the stability equations of the Timoshenko beam problem. In these works, however, the flexural-torsional buckling of members was not considered. In the last mentioned paper (Aristizábal-Ochoa 2007) the effects of the connection stiffness and of the column shear force induced by the axial load are taken into account, but the influence of restrained warping is ignored and columns show doubly symmetric cross-sections only. In this chapter, one- and three-bay portal frames made of doubly- and monosymmetric profiles are analyzed for changing span to height ratios, pointing out the occurrence of different mode shapes, the stiffening effect of warping restraints and the influence of shear deformations. The numerical analyses detailed in the following have been recently presented in a paper of Minghini *et al.* (2008a).

3.2 Variational formulation of the stability problem

In this section, a brief review of the basic concepts of structural stability is presented. In particular, the linearized stability problem is formulated by making use of the classical energy criterion. To this purpose, the virtual work theorem is written putting in evidence the possible different forms of the internal virtual work.

3.2.1 Virtual work theorem

The Eulerian (spatial) formulation of the motion equation is given by:

$$\text{div}\boldsymbol{\sigma} + \mathbf{f} = \rho\dot{\mathbf{v}} \tag{3.1}$$

where $\boldsymbol{\sigma}$ represents the Cauchy stress tensor, $\mathbf{f}$ the vector of the body forces, ρ the mass density and, finally, $\dot{\mathbf{v}}$ is the material derivative of the spatial velocity field $\mathbf{v}$. By virtue of the fundamental lemma of variational calculus, Eq. 3.1 can be rewritten in the following weak (integral) form:

$$\int_V \left(\text{div}\boldsymbol{\sigma} + \mathbf{f} - \rho\dot{\mathbf{v}}\right) \cdot \delta\mathbf{u} \, dV = 0 \tag{3.2}$$

where V is the body volume, $\mathbf{u}$ represents the displacement field and symbol δ indicates variation. In particular, the generic variation $\delta\mathbf{u}$ coincides with the variation $\delta\phi$ of the deformation. By using the known relation:

$$\text{div}\boldsymbol{\sigma} \cdot \delta\mathbf{u} = \sigma_{ij,i}\delta u_j = \left(\sigma_{ij}\delta u_j\right)_{,i} - \sigma_{ij}\left(\delta u_j\right)_{,i} = \text{div}\left(\boldsymbol{\sigma}\delta\mathbf{u}\right) - \boldsymbol{\sigma} \cdot \text{grad}\delta\mathbf{u} \tag{3.3}$$

and the Gauss' theorem:

$$\int_V \text{div}\left(\boldsymbol{\sigma}\delta\mathbf{u}\right) dV = \int_{\partial V} \boldsymbol{\sigma}\delta\mathbf{u} \cdot \mathbf{n} \, dA = \int_{\partial V} \boldsymbol{\sigma}\mathbf{n} \cdot \delta\mathbf{u} \, dA = \int_{\partial V} d\mathbf{p} \cdot \delta\mathbf{u} \tag{3.4}$$

Eq. 3.2 takes the form:

$$\int_{\partial V} d\mathbf{p} \cdot \delta\mathbf{u} + \int_V \left(\mathbf{f} - \rho\dot{\mathbf{v}}\right) \cdot \delta\mathbf{u} \, dV = \int_V \boldsymbol{\sigma} \cdot \text{grad}\delta\mathbf{u} \, dV \tag{3.5}$$

where ∂V indicates the contour of volume V, $\mathbf{n}dA = d\mathbf{A}$ is the generic (oriented) infinitesimal area element of ∂V into a small interval of the spatial point P, $\mathbf{n}$ represents the vector normal to area dA at P, and, finally, $d\mathbf{p} = \boldsymbol{\sigma}d\mathbf{A}$ is the surface force transmitted through the area $d\mathbf{A}$. The left-hand side of Eq. 3.5 is the external virtual work δL_e, i.e. the work of the external loads including the "lost forces" $-\rho\dot{\mathbf{v}}$, whereas the right-hand side of Eq. 3.5 represents the internal virtual work δL_i. By virtue of the symmetry of Cauchy's stress tensor, the following relation holds:

$$\begin{aligned}
\delta L_i &= \int_V \boldsymbol{\sigma} \cdot \text{grad}\delta\mathbf{u} \, dV = \int_V \boldsymbol{\sigma} \cdot \text{grad}^T\delta\mathbf{u} \, dV \\
&= \int_V \boldsymbol{\sigma} \cdot \tfrac{1}{2}\left(\text{grad}\delta\mathbf{u} + \text{grad}^T\delta\mathbf{u}\right) dV = \int_V \boldsymbol{\sigma} \cdot \delta\boldsymbol{\varepsilon} \, dV
\end{aligned} \tag{3.6}$$

where $\delta\boldsymbol{\varepsilon} = 1/2\left(\text{grad}\delta\mathbf{u} + \text{grad}^T\delta\mathbf{u}\right)$ is the virtual tensor of infinitesimal strain related to the spatial configuration. Eq. 3.5 represents the spatial formulation of the virtual work theorem. It should be noted that a material formulation of the theorem may be obtained

by introducing the following relation between spatial (dV) and material (dV_0) infinitesimal elements of volume:

$$dV = \mathrm{J} dV_0 \tag{3.7}$$

in which $\mathrm{J} = \det\mathbf{F} = \det(\mathrm{Grad}\boldsymbol{\phi})$ is the Jacobian of the deformation gradient. In fact, substituting Eq. 3.7 into Eq. 3.6 yields:

$$\delta L_i = \int_{V_0} \mathrm{J}\boldsymbol{\sigma} \cdot \tfrac{1}{2}\left(\mathrm{grad}\,\delta\mathbf{u} + \mathrm{grad}^T \delta\mathbf{u}\right) dV_0 = \int_{V_0} \boldsymbol{\tau} \cdot \tfrac{1}{2}\left(\mathrm{grad}\,\delta\mathbf{u} + \mathrm{grad}^T \delta\mathbf{u}\right) dV_0 \tag{3.8}$$

where $\boldsymbol{\tau} = \mathrm{J}\boldsymbol{\sigma}$ is known as Kirchhoff's tensor or Trefftz's tensor.

An expression of the virtual work theorem analogous to Eq. 3.5 can be obtained by making use of the Lagrangian (material) formulation of the motion equation. In particular, the following relation holds:

$$\int_{V_0} \left(\mathrm{Div}\mathbf{P} + \mathbf{f}_0 - \rho_0 \dot{\mathbf{v}}_{\mathrm{Ref}}\right) \cdot \delta\mathbf{u}\, dV_0 = 0 \tag{3.9}$$

where the two-point tensor $\mathbf{P} = \mathrm{J}\boldsymbol{\sigma}\mathbf{F}^{-T}$ is the first Piola-Kirchhoff stress tensor, whereas $\mathbf{f}_0 = \mathrm{J}\mathbf{f}$, $\rho_0 = \mathrm{J}\rho$ and $\mathbf{v}_{\mathrm{Ref}} = \mathbf{v}\circ\boldsymbol{\phi}^{-1}$ are the material fields of body forces, mass density and velocity, respectively. By means of tensor $\mathbf{P}$ vector $d\mathbf{p} = \boldsymbol{\sigma}d\mathbf{A}$ can be usefully expressed as $d\mathbf{p} = \mathbf{P}d\mathbf{A}_0 = \mathbf{P}\mathbf{N}dA_0$, where $d\mathbf{A}_0$ is the generic (oriented) material area element and $\mathbf{N}$ represents the vector normal to area dA_0. Hence, by virtue of Gauss's theorem, Eq. 3.9 leads to the following expression of the virtual work theorem:

$$\int_{\partial V_0} d\mathbf{p} \cdot \delta\mathbf{u} + \int_{V_0} \left(\mathbf{f}_0 - \rho_0 \dot{\mathbf{v}}_{\mathrm{Ref}}\right) \cdot \delta\mathbf{u}\, dV_0 = \int_{V_0} \mathbf{P} \cdot \delta\mathbf{H}\, dV_0 \tag{3.10}$$

where $\mathbf{H} = \mathrm{Grad}\mathbf{u}$ is the material gradient of the displacement field. Left- and right-hand sides still represent the external and the internal virtual work, respectively. Noting that tensors $\mathbf{H}$ and $\mathbf{F}$ are linked by the relation $\mathbf{H} = \mathbf{F} - \mathbf{I}$, where $\mathbf{I}$ represents the identity tensor (shifter), the internal virtual work may be rewritten as:

$$\delta L_i = \int_{V_0} \mathbf{P} \cdot \delta\mathbf{H}\, dV_0 = \int_{V_0} \mathbf{P} \cdot \delta\mathbf{F}\, dV_0 \tag{3.11}$$

On the other hand, performing the pull-back of Cauchy's stress tensor gives the following material tensor:

$$\mathbf{S} = \mathrm{J}\mathbf{F}^{-1}\boldsymbol{\sigma}\mathbf{F}^{-T} \tag{3.12}$$

known as the second Piola-Kirchhoff stress tensor. Observing that $\mathbf{P} = \mathbf{F}\mathbf{S}$, the internal virtual work takes the alternative form:

$$\delta L_i = \int_{V_0} \mathbf{FS} \cdot \delta \mathbf{F} dV_0 = \int_{V_0} \mathbf{S} \cdot \mathbf{F}^T \delta \mathbf{F} dV_0 = \int_{V_0} \mathbf{S} \cdot \frac{1}{2} \left(\mathbf{F}^T \delta \mathbf{F} + \delta \mathbf{F}^T \mathbf{F} \right) dV_0$$
$$= \frac{1}{2} \int_{V_0} \mathbf{S} \cdot \delta \mathbf{C} dV_0 = \frac{1}{2} \int_{V_0} \mathbf{S} \cdot \delta \left(\mathbf{C} - \mathbf{I} \right) dV_0 = \int_{V_0} \mathbf{S} \cdot \delta \mathbf{E} dV_0 \tag{3.13}$$

where $\mathbf{C} = \mathbf{F}^T \mathbf{F} = \mathbf{I} + \mathbf{I}^T \mathbf{H} + \mathbf{H}^T \mathbf{I} + \mathbf{H}^T \mathbf{H}$ is the right Cauchy-Green deformation tensor, whereas $\mathbf{E} = 1/2 \left(\mathbf{C} - \mathbf{I} \right)$ is the Green-Lagrange strain tensor.

3.2.2 Total potential energy

A hyperelastic continuum under static load conditions ($\rho_0 \dot{\mathbf{v}}_{\text{Ref}} = \rho \dot{\mathbf{v}} = 0$) is considered, for which a potential function $w(\mathbf{E})$, named strain energy density, may be defined as follows:

$$\mathbf{S} = \frac{\partial w}{\partial \mathbf{E}} \tag{3.14}$$

Introducing Eq. 3.14 into Eq. 3.13, the internal virtual work may be written as:

$$\delta L_i = \int_{V_0} \mathbf{S} \cdot \delta \mathbf{E} dV_0 = \int_{V_0} \frac{\partial w}{\partial \mathbf{E}} \cdot \delta \mathbf{E} dV_0 = \delta \int_{V_0} w dV_0 = \delta U \tag{3.15}$$

where U represents the elastic strain energy. Moreover, in the presence of conservative external loads, another potential function V can be defined so that the external virtual work takes the expression:

$$\delta L_e = \delta V \tag{3.16}$$

By using Eqs. 3.15–3.16, the virtual work theorem reduces to the well known equation:

$$\delta \Pi = 0 \tag{3.17}$$

where $\Pi = U - V$ represents the total potential energy. As we have seen in Chapter 1 (§ 1.3.1), making functional Π stationary is equivalent to solve the local equilibrium equations with the relevant boundary conditions for the problem at hand.

In the case of infinitesimal displacements, the linear-elastic constitutive law linking Cauchy's stress tensor $\boldsymbol{\sigma}$ to the tensor $\boldsymbol{\varepsilon} = 1/2 \left(\text{grad}\,\mathbf{u} + \text{grad}^T \mathbf{u} \right)$ may be defined by means of a fourth-order tensor $\mathbb{C}$ as follows:

$$\mathbb{C} : \boldsymbol{\varepsilon} \notin \text{Sym} \to \boldsymbol{\sigma} = \mathbb{C}[\boldsymbol{\varepsilon}] \notin \text{Sym} \tag{3.18}$$

in which the tension is assumed to be null in the reference (material) configuration. For a hyperelastic body, the strain energy density $w(\boldsymbol{\varepsilon})$ is defined as:

$$\boldsymbol{\sigma} = \frac{\partial w}{\partial \boldsymbol{\varepsilon}} \tag{3.19}$$

Obviously, the following relation holds:

$$\boldsymbol{\varepsilon} \cdot \mathbb{C}[\boldsymbol{\varepsilon}] \geq 0 \qquad \forall \boldsymbol{\varepsilon} \geq 0 \tag{3.20}$$

The series expansion of Π into a small interval of a generic configuration $\mathbf{u}_0$ yields:

$$\Pi(\mathbf{u}_0 + \delta\mathbf{u}) = \Pi(\mathbf{u}_0) + \delta\Pi(\mathbf{u}_0) + \delta^2\Pi(\mathbf{u}_0) + R(\mathbf{u}_0) \tag{3.21}$$

where $R(\mathbf{u}_0)$ collects higher-order terms than the second-order, i.e.:

$$\lim_{\alpha \to 0} \frac{|R(\alpha\mathbf{u}_0)|}{\alpha^2} = 0 \tag{3.22}$$

If $\mathbf{u}_0$ represents an equilibrium configuration, remembering Eq. 3.17, Eq. 3.21 reduces to:

$$\Pi(\mathbf{u}_0 + \delta\mathbf{u}) - \Pi(\mathbf{u}_0) \simeq \delta^2\Pi(\mathbf{u}_0) = \int_V \delta\boldsymbol{\varepsilon} \cdot \mathbb{C}[\delta\boldsymbol{\varepsilon}] \, dV > 0 \qquad \forall \delta\mathbf{u} \tag{3.23}$$

Hence, the total potential energy attains a minimum in correspondence of equilibrium configurations.

3.2.3 Energy criterion of stability

By virtue of Koiter's theorems, the positive definiteness of $\delta^2\Pi$ is a necessary condition for stability. In the case of finite displacements, the nonlinearity of Π may lead to bifurcation points along the fundamental equilibrium path. In order to detect such critical conditions, a series expansion of $w(\mathbf{E}_0)$ with respect to the fundamental configuration $\mathbf{E}_0$ is performed, giving:

$$w(\mathbf{E}_0) = \left.\frac{\partial w}{\partial \mathbf{E}}\right|_0 \mathbf{E} + \frac{1}{2}\mathbf{E} \cdot \left.\frac{\partial^2 w}{\partial \mathbf{E}^2}\right|_0 \mathbf{E} + \ldots = \mathbf{S}_0 \cdot \mathbf{E} + \frac{1}{2}\mathbf{E} \cdot \mathbb{C}[\mathbf{E}] + \ldots \tag{3.24}$$

where

$$\mathbf{S}_0 = \left.\frac{\partial w}{\partial \mathbf{E}}\right|_0 ; \qquad \mathbb{C} = \left.\frac{\partial^2 w}{\partial \mathbf{E}^2}\right|_0 \tag{3.25}$$

Therefore, the strain energy turns out to be given by:

$$
\begin{aligned}
U &= \int_{V_0} \left\{ \mathbf{S}_0 \cdot \mathbf{E} + \frac{1}{2}\mathbf{E} \cdot \mathbb{C}[\mathbf{E}] + \ldots \right\} dV_0 = \frac{1}{2}\int_{V_0} \mathbf{S}_0 \cdot \left(\mathbf{I}^T\mathbf{H} + \mathbf{H}^T\mathbf{I} + \mathbf{H}^T\mathbf{H} \right) dV_0 \\
&+ \frac{1}{2}\int_{V_0} \left\{ \frac{1}{2}\left(\mathbf{I}^T\mathbf{H} + \mathbf{H}^T\mathbf{I} + \mathbf{H}^T\mathbf{H} \right) \cdot \mathbb{C}\left[\frac{1}{2}\left(\mathbf{I}^T\mathbf{H} + \mathbf{H}^T\mathbf{I} + \mathbf{H}^T\mathbf{H} \right) \right] \right\} dV_0 + \ldots \\
&= \int_{V_0} \mathbf{S}_0 \cdot \boldsymbol{\varepsilon} \, dV_0 + \int_{V_0} \left\{ \mathbf{S}_0 \cdot \boldsymbol{\varepsilon}^{(2)} + \frac{1}{2}\boldsymbol{\varepsilon} \cdot \mathbb{C}[\boldsymbol{\varepsilon}] \right\} dV_0 + \ldots \\
&= \delta U + \frac{1}{2}\delta^2 U + \ldots
\end{aligned}
\tag{3.26}
$$

where, with material notations, tensors $\boldsymbol{\varepsilon} = 1/2\left(\text{Grad}\,\mathbf{u} + \text{Grad}^T\mathbf{u}\right) = 1/2\left(\mathbf{I}^T\mathbf{H} + \mathbf{H}^T\mathbf{I}\right)$ and $\boldsymbol{\varepsilon}^{(2)} = 1/2\left(\text{Grad}^T\mathbf{u}\,\text{Grad}\,\mathbf{u}\right) = 1/2\left(\mathbf{H}^T\mathbf{H}\right)$ indicate linear and second-order strain fields. Neglecting the contribution $\int_{V_0} -\rho_0 \dot{\mathbf{v}}_{\text{Ref}} \cdot \delta\mathbf{u} \, dV_0$ of inertial forces in the left-hand side of Eq. 3.10 and indicating with $\mathbf{p}_0 = \mathbf{p}\,dA/dA_0$ the external force per unit undeformed area, potential V of conservative surface and body forces may be written, into a small interval of the fundamental configuration, in the following form:

$$
\begin{aligned}
V &= \delta V + \frac{1}{2}\delta^2 V + \ldots \\
&= \int_{\partial V_0} \mathbf{p}_0 \cdot \delta\mathbf{u}\,dA_0 + \int_{V_0} \mathbf{f}_0 \cdot \delta\mathbf{u}\,dV_0 + \frac{1}{2}\left(\int_{\partial V_0} \mathbf{p}_0 \cdot \delta^2\mathbf{u}\,dA_0 + \int_{V_0} \mathbf{f}_0 \cdot \delta^2\mathbf{u}\,dV_0 \right) + \ldots
\end{aligned}
\tag{3.27}
$$

where $1/2\,\delta^2\mathbf{u}$ is the second variation of the displacement field. Hence, the total potential energy for a system subjected to conservative external loads takes the expression:

$$\Pi = \delta U - \delta V + \frac{1}{2}\delta^2 U - \frac{1}{2}\delta^2 V + \ldots = \delta\Pi + \frac{1}{2}\delta^2\Pi + \ldots \tag{3.28}$$

Finally, the critical conditions are devised by imposing the positive definiteness of the second variation of the total potential energy:

$$\frac{1}{2}\delta^2\Pi = \frac{1}{2}\delta^2 U - \frac{1}{2}\delta^2 V \geq 0 \tag{3.29}$$

3.2.3.1 Linearized stability problems

Under the assumption of small displacements, Kirchhoff's and Piola-Kirchhoff's stress tensors referred to the fundamental (pre-buckling) configuration reduce to Cauchy's stress tensor. Hence, taking Eq. 3.26 into account, the second variation of the elastic strain energy can be given the following expression:

$$\frac{1}{2}\delta^2 U = \frac{1}{2}\int_{V_0} C_{ijhk}\varepsilon_{ij}^{(1)}\varepsilon_{hk}^{(1)}dV_0 + \int_{V_0}\sigma_{ij}^0\varepsilon_{ij}^{(2)}dV_0 \tag{3.30}$$

where $\varepsilon_{ij}^{(1)}$ and $\varepsilon_{ij}^{(2)}$ are the components of tensors $\boldsymbol{\varepsilon}$ and $\boldsymbol{\varepsilon}^{(2)}$, respectively. Substituting Eq. 3.30 into Eq. 3.29 and considering Eq. 3.27, the necessary condition for stability turns out to be given by:

$$\frac{1}{2}\delta^2\Pi = \frac{1}{2}\delta^2\Pi_E + \frac{1}{2}\delta^2\Pi_G \geq 0 \tag{3.31}$$

where

$$\frac{1}{2}\delta^2\Pi_E = \frac{1}{2}\int_{V_0} C_{ijhk}\varepsilon_{ij}^{(1)}\varepsilon_{hk}^{(1)}dV_0 \tag{3.32}$$

represents the elastic strain energy already given in Chapter 1 and

$$\frac{1}{2}\delta^2\Pi_G = \int_{V_0}\sigma_{ij}^0\varepsilon_{ij}^{(2)}dV_0 - \frac{1}{2}\int_{\partial V_0} p_i^0\delta^2 u_i dA_0 - \frac{1}{2}\int_{V_0} f_i^0\delta^2 u_i dV_0 \tag{3.33}$$

is the potential energy due to the second-order effects of pre-critical stresses and external surface and body loads. Any critical load must satisfy the condition

$$\frac{1}{2}\delta^2\Pi_E + \frac{1}{2}\delta^2\Pi_G = 0 \tag{3.34}$$

As usual in linearized stability problems, the effects of pre-buckling deformations are ignored in the following analyses. In any case, it should be remembered that pre-buckling displacements of a beam under lateral loads can properly be neglected when the two principal second area moments are quite distant form each other. If this is not the case, pre-buckling displacements can have a very significant influence on lateral buckling loads (Trahair 1993, Roberts 2002, Machado & Cortínez 2005).

3.3 Transformation matrix for finite rotations

3.3.1 Rodriguez's formula

In order to derive the displacement field and the corresponding strain field to be used in Eqs. 3.32–3.33 for the formulation of the stability equation 3.34, a transformation rule for a vector in space when undergoing a rotation of finite (not infinitesimal) amplitude is established first, following the works of Argyris (1982) and Criesfield (1991). In particular, a rotation of amplitude ϑ about a *fixed* axis defined by the unit vector $\mathbf{e}$ is considered (Fig. 3.1). Such rotation transforms vector $\mathbf{r}_0 \equiv (P_0 - O)$ into vector $\mathbf{r} \equiv (P - O)$. Point C is the center of rotation, whereas R represents the radius of the circle centred in C and passing through P_0 and P. Directions of $\mathbf{r}_0$ and $\mathbf{e}$ form an angle α. Vector ϑ, known in literature as the rotational "*pseudo-vector*", is defined as:

$$\vartheta^T = \{\varphi, \chi, \psi\} = \vartheta\mathbf{e} \tag{3.35}$$

where φ, χ and ψ represent its component in a Cartesian system *Oxyz* and $\vartheta = (\vartheta^T \vartheta)^{1/2}$. It is to be underlined that, differently from the case of infinitesimal rotations, components φ, χ and ψ cannot be interpreted as component rotations about the Cartesian axes x, y and z.

The goal of the present section is to define a relation of the form:

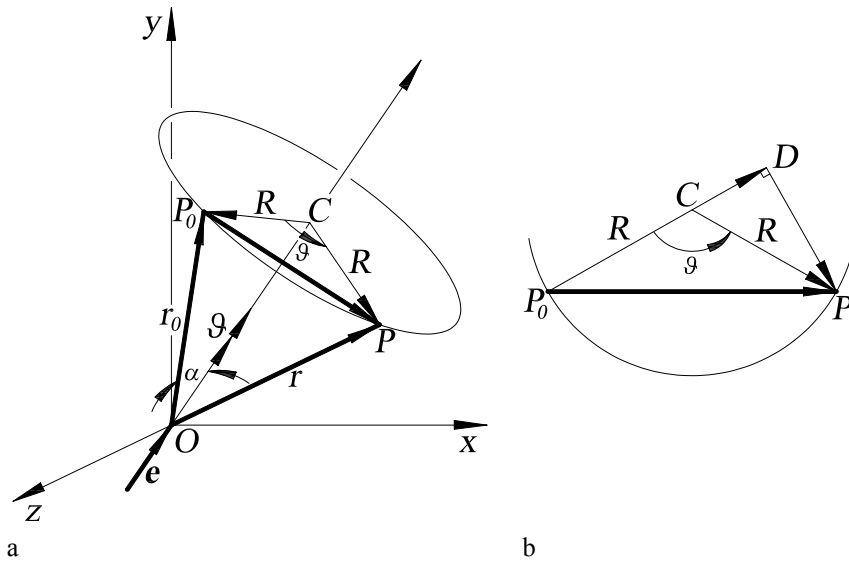$$\mathbf{r} = \mathbf{R}(\vartheta)\mathbf{r}_0 \tag{3.36}$$

Figure 3.1. Transformation of vector $\mathbf{r}_0$ into vector $\mathbf{r}$ by means of a generic finite rotation with *pseudo-vector* ϑ.

where $\mathbf{R}(\vartheta)$ represents the matrix of finite rotation and is, in general, a nonlinear function of ϑ. To this purpose, vector $\mathbf{r}$ is written as (Fig. 3.1a):

$$\mathbf{r} = \mathbf{r}_0 + (P - P_0) \tag{3.37}$$

where (Fig. 3.1b)

$$(P - P_0) = (D - P_0) + (P - D) \tag{3.38}$$

Since vector $(P - D)$ is drawn orthogonal to $(D - P_0)$, its norm is given by:

$$\|P - D\| = R \sin \vartheta \tag{3.39}$$

Observing that

$$\|\mathbf{e} \times \mathbf{r}_0\| = \|\mathbf{r}_0\| \sin \alpha = R \tag{3.40}$$

and using Eq. 3.39 lead to:

$$(P - D) = \sin \vartheta (\mathbf{e} \times \mathbf{r}_0) = \frac{\sin \vartheta}{\vartheta} (\boldsymbol{\vartheta} \times \mathbf{r}_0) \tag{3.41}$$

From Figure 3.1, vector $(D - P_0)$ is orthogonal to both $\mathbf{e}$ and $(\mathbf{e} \times \mathbf{r}_0)$. Moreover, its norm is equal to:

$$\|D - P_0\| = R(1 - \cos \vartheta) = 2R \sin^2 \frac{\vartheta}{2} \tag{3.42}$$

Hence, noting that

$$\|\mathbf{e} \times (\mathbf{e} \times \mathbf{r}_0)\| = R \tag{3.43}$$

the following relation holds:

$$(D - P_0) = 2 \sin^2 \frac{\vartheta}{2} (\mathbf{e} \times (\mathbf{e} \times \mathbf{r}_0)) = \frac{1}{2} \frac{\sin^2 (\vartheta/2)}{(\vartheta/2)^2} (\boldsymbol{\vartheta} \times (\boldsymbol{\vartheta} \times \mathbf{r}_0)) \tag{3.44}$$

Substituting Eqs. 3.41 and 3.44 into Eq. 3.38 and the resulting expression into Eq. 3.37 yields:

$$\mathbf{r} = \mathbf{r}_0 + \frac{\sin \vartheta}{\vartheta} (\vartheta \times \mathbf{r}_0) + \frac{1}{2} \frac{\sin^2 (\vartheta/2)}{(\vartheta/2)^2} (\vartheta \times (\vartheta \times \mathbf{r}_0)) \tag{3.45}$$

Setting

$$\mathbf{S}(\vartheta) = \begin{bmatrix} 0 & -\psi & \chi \\ \psi & 0 & -\varphi \\ -\chi & \varphi & 0 \end{bmatrix} \tag{3.46}$$

make easy to demonstrate that:

$$\vartheta \times \mathbf{r}_0 = \mathbf{S}\mathbf{r}_0; \qquad \vartheta \times (\vartheta \times \mathbf{r}_0) = \mathbf{S}^2 \mathbf{r}_0 \tag{3.47}$$

Finally, inserting Eqs. 3.47 into Eq. 3.45 leads to:

$$\mathbf{r} = \mathbf{r}_0 + \frac{\sin \vartheta}{\vartheta} \mathbf{S}\mathbf{r}_0 + \frac{1}{2} \frac{\sin^2 (\vartheta/2)}{(\vartheta/2)^2} \mathbf{S}^2 \mathbf{r}_0 = \mathbf{R}(\vartheta) \mathbf{r}_0 \tag{3.48}$$

where

$$\mathbf{R}(\vartheta) = \mathbf{I} + \frac{\sin \vartheta}{\vartheta} \mathbf{S} + \frac{1}{2} \left(\frac{\sin \vartheta/2}{\vartheta/2} \right)^2 \mathbf{S}^2 \tag{3.49}$$

is the rotation matrix searched for. It is simple to observe that $\mathbf{R}\mathbf{R}^T = \mathbf{I}$, i.e. the rotation matrix is orthogonal. Expression 3.49 is known as the Rodriguez formula. An alternative formulation of $\mathbf{R}$ frequently adopted in literature is reported in the following (Argyris 1982, Criesfield 1991, Kim *et al.* 2001):

$$\mathbf{R}(\boldsymbol{\omega}) = \mathbf{I} + \frac{1}{1 + 1/4\, \boldsymbol{\omega}^T \boldsymbol{\omega}} \left[\mathbf{S}(\boldsymbol{\omega}) + \frac{1}{2} \mathbf{S}(\boldsymbol{\omega})^2 \right] \tag{3.50}$$

which is obtained from Eq. 3.49 by using the relation:

$$\boldsymbol{\omega} = \omega \mathbf{e} = 2 \tan \frac{\vartheta}{2} \mathbf{e} = 2 \frac{\tan (\vartheta/2)}{\vartheta} \vartheta \tag{3.51}$$

The *pseudo-vector* $\boldsymbol{\omega}$ of Eq. 3.51 is defined by:

$$\boldsymbol{\omega}^T = \{ \omega_x, \omega_y, \omega_z \} \tag{3.52}$$

where the Cartesian components ω_x, ω_y and ω_z are known as the Rodriguez rotation parameters, whereas matrix $\mathbf{S}(\omega)$, taking the same form of $\mathbf{S}(\vartheta)$, is given by:

$$\mathbf{S}(\omega) = \begin{bmatrix} 0 & -\omega_z & \omega_y \\ \omega_z & 0 & -\omega_x \\ -\omega_y & \omega_x & 0 \end{bmatrix} \tag{3.53}$$

On the other hand, expression 3.50 is less convenient than expression 3.49. In fact, it should be noted that ω becomes infinite at $\vartheta = \pm(k \cdot 180°)$, with k integer, and, simultaneously, $\mathbf{R}(\omega)$ turns out to be singular.

3.3.2 Exponential form of the rotation matrix and its approximations

Performing the series expansion of $\sin\vartheta/\vartheta$ and $1/2\sin^2(\vartheta/2)/(\vartheta/2)^2$ in the Eq. 3.49 yields:

$$\begin{aligned}
\mathbf{R}(\vartheta) = \mathbf{I} &+ \left(1 - \frac{\vartheta^2}{3!} + \frac{\vartheta^4}{5!} - \dots + (-1)^n \frac{\vartheta^{2n}}{(2n+1)!} \pm \dots\right)\mathbf{S} \\
&+ \left(\frac{1}{2!} - \frac{\vartheta^2}{4!} + \frac{\vartheta^4}{6!} - \dots + (-1)^n \frac{\vartheta^{2n}}{(2n+2)!} \pm \dots\right)\mathbf{S}^2
\end{aligned} \tag{3.54}$$

The powers of matrix $\mathbf{S}$ are given by:

$$\mathbf{S}^3 = -\vartheta^2\mathbf{S}; \quad \mathbf{S}^4 = -\vartheta^2\mathbf{S}^2; \quad \mathbf{S}^5 = +\vartheta^4\mathbf{S}; \quad \mathbf{S}^6 = +\vartheta^4\mathbf{S}^2; \text{ etc.} \tag{3.55}$$

and, consequently, the following recurrence formulae can be written:

$$\mathbf{S}^{2n-1} = (-1)^{n-1}\vartheta^{2(n-1)}\mathbf{S}; \qquad \mathbf{S}^{2n} = (-1)^{n-1}\vartheta^{2(n-1)}\mathbf{S}^2 \tag{3.56}$$

If Eq. 3.54 is re-written by taking Eqs. 3.56 into account, the expansion of matrix $\mathbf{R}(\vartheta)$ is obtained:

$$\mathbf{R}(\vartheta) = \mathbf{I} + \mathbf{S} + \frac{1}{2!}\mathbf{S}^2 + \frac{1}{3!}\mathbf{S}^3 + \dots = \exp\mathbf{S} \tag{3.57}$$

The lowest-order approximation to $\mathbf{R}(\vartheta)$ is the well known matrix of infinitesimal rotation:

$$\mathbf{R}^{(1)}(\vartheta) = \mathbf{I} + \mathbf{S} \tag{3.58}$$

The second-order approximation to $\mathbf{R}(\vartheta)$:

$$\mathbf{R}^{(2)}(\vartheta) = \mathbf{I} + \mathbf{S} + \frac{1}{2}\mathbf{S}^2 \tag{3.59}$$

can be also obtained replacing $\sin\vartheta$ by ϑ and $\sin^2(\vartheta/2)$ by $\vartheta^2/4$ in Eq. 3.49, i.e. assuming *moderately* large rotations.

3.3.3 Rotation matrix corresponding to a sequence of infinitesimal rotations

A finite rotation $\vartheta = \{\varphi, \chi, \psi\}^T$ with an associated auxiliary matrix $\mathbf{S}(\vartheta)$ Eq. 3.46 is considered. Following Argyris *et al.* (1981) and Argyris (1982), such rotation is assumed to be composed of a number $n \to \infty$ of infinitesimal rotations each characterized by an auxiliary matrix of the form:

$$\mathbf{S}_i = \lim_{n\to\infty}\left[\frac{1}{n}\mathbf{S}\right] \tag{3.60}$$

and by a corresponding rotation matrix given by (see Eq. 3.58):

$$\mathbf{R}_i = \lim_{n\to\infty}\left[\mathbf{I} + \frac{1}{n}\mathbf{S}\right] \tag{3.61}$$

where $i, n \in \mathbb{N}$. The rotation matrix corresponding to a sequence of n successive rotations ϑ_i about axes fixed in space is given by the product (Rosenberg 1980):

$$\mathbf{R} = \mathbf{R}_n\mathbf{R}_{n-1}\cdots\mathbf{R}_i\cdots\mathbf{R}_2\mathbf{R}_1 \tag{3.62}$$

where the transformations $\mathbf{R}_i$ take place in the inverse order of application of the rotations ϑ_i. Hence, for a sequence of $n \to \infty$ infinitesimal rotations of the form 3.61 the following relation holds:

$$\mathbf{R} = \lim_{n\to\infty}\left[\mathbf{I} + \frac{1}{n}\mathbf{S}\right]^n \tag{3.63}$$

Developing the right-hand side term of Eq. 3.63 by the binomial theorem leads to the exponential form 3.57.

3.4 Second-order displacement field for shear-deformable beams

A prismatic thin-walled beam with open-section is shown in Figure 3.2. Longitudinal axis z passes through the cross-section centroids C, axes x and y are the principal axes of inertia, whereas S stands for the cross-section shear center defined by the Vlasov theory. The cross-section is assumed to be rigid in its own plane and, by virtue of the small thickness, the beam is reduced to its middle surface described by the curvilinear abscissa s.

3.4.1 Position vector of an arbitrary point after a finite rotation

The movements of a generic point P_0 (Fig. 3.2) lying on the cross-section contour at $z = 0$ and identified by the initial position vector $\mathbf{r}_0 = \{x, y, 0\}^T$ will be determined by using a finite rotation approach based on a sequence of $n \to \infty$ infinitesimal rotations. An infinitesimal rotation $\boldsymbol{\vartheta}_1 = 1/n\{\varphi, \chi, \psi\}^T$ ($n \to \infty$) is considered first, with components φ/n and χ/n referred to axes x and y, respectively, and component ψ/n referred to the axis parallel to z direction and passing through the shear centres. By virtue of such rotation, remembering Eq. 3.61, the position vector $\mathbf{r}_0$ is transformed into vector $\mathbf{r}_1$ as follows (Kim $et\ al.$ 1996):

$$\mathbf{r}_1 = \lim_{n \to \infty} \left[\left(\mathbf{I} + \frac{1}{n}\mathbf{S} \right)\mathbf{r}_0 - \frac{1}{n}\mathbf{As} \right] \tag{3.64}$$

where

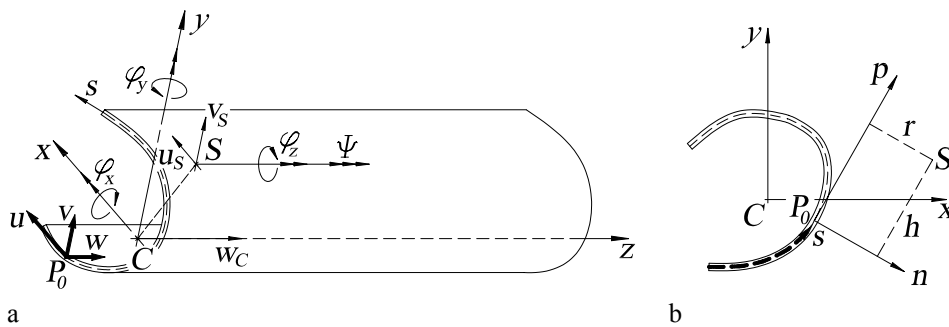$$\mathbf{A} = \begin{bmatrix} 0 & -\psi & 0 \\ \psi & 0 & 0 \\ 0 & 0 & 0 \end{bmatrix} \tag{3.65}$$

Figure 3.2. Global (a) and local (b) reference systems.

and vector $\mathbf{s}^T = \{x_S, y_S, 0\}$ collects the coordinates of point S at $z = 0$. The term $-1/n\,\mathbf{As}$ in Eq. 3.64 operates the shift from axis z to the shear center axis. Since rotation ϑ_1 goes with a shift, a sequence ϑ of n infinitesimal rotations ϑ_i ($i \in \mathbb{N}$) of the same form as ϑ_1 cannot be represented directly using matrix $\mathbf{R}$ in the form 3.62. On the other hand, an infinitesimal rotation ϑ_2 acting on the transformed vector $\mathbf{r}_1$ provides the vector:

$$\mathbf{r}_2 = \lim_{n\to\infty}\left[\left(\mathbf{I} + \frac{1}{n}\mathbf{S}\right)\mathbf{r}_1 - \frac{1}{n}\mathbf{As}\right] = \lim_{n\to\infty}\left[\left(\mathbf{I} + \frac{1}{n}\mathbf{S}\right)^2\mathbf{r}_0 - \frac{1}{n}\left(\mathbf{I} + \frac{1}{n}\mathbf{S}\right)\mathbf{As} - \frac{1}{n}\mathbf{As}\right] \tag{3.66}$$

Repeating such transformation for $n \to \infty$ yields the position vector after the finite rotation ϑ:

$$\mathbf{r} = \lim_{n\to\infty}\left[\left(\mathbf{I} + \frac{1}{n}\mathbf{S}\right)^n\mathbf{r}_0 - \frac{1}{n}\left(\mathbf{I} + \frac{1}{n}\mathbf{S}\right)^{n-1}\mathbf{As} - ... - \frac{1}{n}\left(\mathbf{I} + \frac{1}{n}\mathbf{S}\right)\mathbf{As} - \frac{1}{n}\mathbf{As}\right] \tag{3.67}$$

3.4.2 Second-order approximation

Assuming *moderately* large rotations, vector $\mathbf{r}$ provided by Eq. 3.67 can be approximated up to the second-order and components φ, χ and ψ of finite rotation ϑ can be identified with rotations φ_x, φ_y and φ_z about axes x, y and the shear center axis, respectively. Developing Eq. 3.67 by the binomial theorem and neglecting higher-order terms than the second-order yield the following approximation of the transformed position vector:

$$\mathbf{r} \cong \left(\mathbf{I} + \mathbf{S} + \frac{1}{2}\mathbf{S}^2\right)\mathbf{r}_0 - \left(\mathbf{I} + \frac{1}{2}\mathbf{S}\right)\mathbf{As} \tag{3.68}$$

where

$$\mathbf{S} \cong \begin{bmatrix} 0 & -\varphi_z & \varphi_y \\ \varphi_z & 0 & -\varphi_x \\ -\varphi_y & \varphi_x & 0 \end{bmatrix}; \qquad \mathbf{A} \cong \begin{bmatrix} 0 & -\varphi_z & 0 \\ \varphi_z & 0 & 0 \\ 0 & 0 & 0 \end{bmatrix} \tag{3.69}$$

and term $\left(\mathbf{I} + \mathbf{S} + 1/2\,\mathbf{S}^2\right)$ coincides with the second-order approximation 3.59 of the Rodriguez matrix 3.49.

3.4.3 Total displacement components

The vector of total displacements moving point P_0 into the final position P may be written in the following form:

$$\mathbf{u} = (P - P_0) = \mathbf{u}_0 + (\mathbf{r} - \mathbf{r}_0) \tag{3.70}$$

where $\mathbf{u}_0$ and $(\mathbf{r} - \mathbf{r}_0)$ represent the vectors of translational and rotational displacements, respectively. In particular, with reference to symbols of Figure 3.2a, vector $\mathbf{u}_0$ is defined as:

$$\mathbf{u}_0^T (z,s) = \{u_S(z), v_S(z), w_C(z) + \omega(s)\Psi(z)\} \tag{3.71}$$

where $u_S(z)$ and $v_S(z)$ are the shear center displacements in x and y directions, respectively; $w_C(z)$ is the cross-section mean axial translation; function $\omega(s)$ is the warping function defined in Chapter 1 (§ 1.2.1) and, finally, $\Psi(z)$ represents the cross-section warping amplitude. Now substituting Eq. 3.71 and second-order approximation 3.68 into Eq. 3.70, the displacement field turns out to be given by (Chang *et al.* 1996, Minghini *et al.* 2008b):

$$\mathbf{u} = \mathbf{u}_0 + \left(\mathbf{S} + \frac{1}{2}\mathbf{S}^2\right)\mathbf{r}_0 - \left(\mathbf{I} + \frac{1}{2}\mathbf{S}\right)\mathbf{As} = \mathbf{u}^{(1)} + \mathbf{u}^{(2)} \tag{3.72}$$

where vectors $\mathbf{u}^{(1)}$ and $\mathbf{u}^{(2)}$, respectively collecting first- and second-order displacement components, take, by the way of Eqs. 3.69, the following expressions:

$$\mathbf{u}^{(1)}(z,s) = \begin{Bmatrix} u^{(1)}(z,s) \\ v^{(1)}(z,s) \\ w^{(1)}(z,s) \end{Bmatrix} = \begin{Bmatrix} u_S(z) - \varphi_z(z)(y - y_S) \\ v_S(z) + \varphi_z(z)(x - x_S) \\ w_C(z) - x\varphi_y(z) + y\varphi_x(z) + \omega(s)\Psi(z) \end{Bmatrix} \tag{3.73}$$

$$\mathbf{u}^{(2)}(z,s) = \begin{Bmatrix} u^{(2)}(z,s) \\ v^{(2)}(z,s) \\ w^{(2)}(z,s) \end{Bmatrix} = \frac{1}{2}\begin{Bmatrix} -\left(\varphi_y^2(z) + \varphi_z^2(z)\right)x + \varphi_x(z)\varphi_y(z)y + \varphi_z^2(z)x_S \\ \varphi_x(z)\varphi_y(z)x - \left(\varphi_x^2(z) + \varphi_z^2(z)\right)y + \varphi_z^2(z)y_S \\ \varphi_x(z)\varphi_z(z)(x - x_S) + \varphi_y(z)\varphi_z(z)(y - y_S) \end{Bmatrix} \tag{3.74}$$

The displacement field presented, based on the second-order approximation of the Rodriguez matrix of finite rotation, accounts for the shear strain effects due to nonuniform bending and torsion, since, in general, $\varphi_x \neq -\partial v_S/\partial z$, $\varphi_y \neq \partial u_S/\partial z$ and $\Psi \neq -\partial \varphi_z/\partial z$. In particular, it should be recognized that linear displacements in Eq. 3.73 coincide with Timoshenko-Reissner's kinematical model 1.3–1.5. If the translation given by term $\left[\mathbf{I} + (1/2)\mathbf{S}\right]\mathbf{As}$ is not performed in Eq. 3.68, the kinematical model adopted by Cortínez & Piovan (2006), where the shear center co-ordinates do not appear explicitly, is re-obtained.

3.5 Strain components and stress resultants

By adopting the usual Lagrangian formulation and neglecting higher-order terms than the second-order, the strain components may be expressed in terms of the Green-Lagrange strain tensor **E** in the form:

$$\varepsilon_{ij} = \varepsilon_{ij}^{(1)} + \varepsilon_{ij}^{(2)} \tag{3.75}$$

where $(i, j = x, y, z)$

$$\varepsilon_{ij}^{(1)} = \frac{1}{2}\left(u_{i,j}^{(1)} + u_{j,i}^{(1)}\right); \qquad \varepsilon_{ij}^{(2)} = \frac{1}{2}\left(u_{k,i}^{(1)}u_{k,j}^{(1)} + u_{i,j}^{(2)} + u_{j,i}^{(2)}\right) \tag{3.76}$$

and comma indicates partial differentiation with respect to Lagrangian co-ordinates (x, y, z).

Due to the assumption of cross-section in-plane undeformability, the non-vanishing strain components reduce to the axial strain ε_z and the shear strains $\gamma_{zx} = 2\varepsilon_{zx}$ and $\gamma_{zy} = 2\varepsilon_{zy}$. By using Eqs. 3.76, linear and nonlinear parts of the strain field can respectively be written as:

$$\varepsilon_z^{(1)} = w_C' - x\varphi_y' + y\varphi_x' + \omega\Psi' \tag{3.77}$$

$$\gamma_{zx}^{(1)} = \left(u_S' - \varphi_y\right) + \frac{\partial\omega}{\partial x}\Psi - \varphi_z'\left(y - y_S\right) \tag{3.78}$$

$$\gamma_{zy}^{(1)} = \left(v_S' + \varphi_x\right) + \frac{\partial\omega}{\partial y}\Psi + \varphi_z'\left(x - x_S\right) \tag{3.79}$$

$$\varepsilon_z^{(2)} = \frac{1}{2}\left\{\left[u_S' - \varphi_z'\left(y - y_S\right)\right]^2 + \left[v_S' + \varphi_z'\left(x - x_S\right)\right]^2 \right. \\ \left. + \left(x - x_S\right)\left(\varphi_x\varphi_z\right)' + \left(y - y_S\right)\left(\varphi_y\varphi_z\right)'\right\} \tag{3.80}$$

$$\gamma_{zx}^{(2)} = \varphi_z\left[v_S' + \varphi_z'\left(x - x_S\right)\right] + \frac{1}{2}\varphi_x\varphi_z - \left(\varphi_y\varphi_y' + \varphi_z\varphi_z'\right)x \\ + \frac{1}{2}\left(\varphi_x'\varphi_y + \varphi_x\varphi_y'\right)y + \varphi_z\varphi_z'x_S \tag{3.81}$$

$$\gamma_{zy}^{(2)} = -\varphi_z\left[u_S' - \varphi_z'\left(y - y_S\right)\right] + \frac{1}{2}\varphi_y\varphi_z + \frac{1}{2}\left(\varphi_x'\varphi_y + \varphi_x\varphi_y'\right)x \\ - \left(\varphi_x\varphi_x' + \varphi_z\varphi_z'\right)y + \varphi_z\varphi_z'y_S \tag{3.82}$$

where prime denotes derivative with respect to z. Due to the assumption of small strains involving derivative of axial displacement w, terms $\left(\partial w/\partial x\right)\left(\partial w/\partial z\right)$, $\left(\partial w/\partial y\right)\left(\partial w/\partial z\right)$

and $\left(\partial w/\partial z\right)^2$ provided by Eq. 3.76b were ignored in evaluating the nonlinear components 3.80–3.82 of the strain field (Pignataro *et al.* 1983, Kim *et al.* 1996).

The first-order non-zero components of the stress tensor are the normal stress σ_z and the tangential stresses τ_{zx} and τ_{zy} giving the internal stress resultants (see § 1.2.2):

$$N = \int_A \sigma_z dA; \qquad V_x = \int_A \tau_{xz} dA; \qquad V_y = \int_A \tau_{yz} dA \tag{3.83}$$

$$M_x = \int_A \sigma_z y dA; \qquad M_y = -\int_A \sigma_z x dA; \qquad M_\omega = \int_A \sigma_z \omega dA \tag{3.84}$$

$$M_z = \int_A \left(\tau_{yz} x - \tau_{xz} y\right) dA - V_x y_S + V_y x_S; \qquad M_z^\omega = \int_A \left(\tau_{xz} \frac{\partial \omega}{\partial x} + \tau_{yz} \frac{\partial \omega}{\partial y}\right) dA \tag{3.85}$$

3.6 Constitutive laws

Indicating with E and G longitudinal and transverse elastic moduli and remembering Eqs. 3.77–3.79 of linear strains, substitution of first-order components $\sigma_z = E\varepsilon_z^{(1)}$, $\tau_{zx} = G\gamma_{zx}^{(1)}$ and $\tau_{zy} = G\gamma_{zy}^{(1)}$ of the stress tensor into Eqs. 3.83, 3.84 and 3.85b yields the constitutive relations reported in Chapter 1 (§ 1.2.3):

$$\begin{Bmatrix} N \\ M_x \\ M_y \\ M_\omega \end{Bmatrix} = E \begin{bmatrix} A & 0 & 0 & 0 \\ & J_x & 0 & 0 \\ & & J_y & 0 \\ \text{Sym} & & & J_\omega \end{bmatrix} \begin{Bmatrix} w_C' \\ \varphi_x' \\ \varphi_y' \\ \Psi' \end{Bmatrix} \tag{3.86}$$

$$\begin{Bmatrix} V_x \\ V_y \\ M_z^\omega \end{Bmatrix} = G \begin{bmatrix} D_x & D_{xy} & D_{x\omega} \\ & D_y & D_{y\omega} \\ \text{Sym} & & D_\omega \end{bmatrix} \begin{Bmatrix} \left(u_S' - \varphi_y\right) \\ \left(v_S' + \varphi_x\right) \\ \left(\varphi_z' + \Psi\right) \end{Bmatrix} \tag{3.87}$$

where shear rigidities D_{ij} in Eq. 3.87 are to be evaluated by means of the post-processing procedure developed in Section 1.3.1.

3.7 Formulation of the linearized stability problem

Critical loads are detected by imposing the stationarity condition 3.34 in which functionals $1/2\,\delta^2\Pi_E$ and $1/2\,\delta^2\Pi_G$ are expressed by Eqs. 3.32–3.33. In particular, bearing in mind the expressions of the internal stress resultants 3.83–3.85, the first-order strains 3.77–3.79 and the constitutive relations 3.86–3.87, and dropping symbol δ

on the right-hand side, the elastic strain energy 3.32 for a beam of length L may be written as follows (see § 1.3.1):

$$\frac{1}{2}\delta^2\Pi_E = \frac{1}{2}\int_V C_{ijhk}\varepsilon_{ij}^{(1)}\varepsilon_{hk}^{(1)}dV$$

$$= \frac{1}{2}\int_L E\left(Aw_C'^2 + J_x\varphi_x'^2 + J_y\varphi_y'^2 + J_\omega\Psi'^2\right)dz$$

$$+ \frac{1}{2}\int_L G\left[J_t\varphi_z'^2 + D_x\left(u_S'-\varphi_y\right)^2 + D_y\left(v_S'+\varphi_x\right)^2 + D_\omega\left(\varphi_z'+\Psi\right)^2\right.$$

$$+ 2D_{xy}\left(u_S'-\varphi_y\right)\left(v_S'+\varphi_x\right) + 2D_{x\omega}\left(u_S'-\varphi_y\right)\left(\varphi_z'+\Psi\right)$$

$$\left.+ 2D_{y\omega}\left(v_S'+\varphi_x\right)\left(\varphi_z'+\Psi\right)\right]dz \tag{3.88}$$

where the term $1/2\int_L GJ_t\varphi_z'^2 dz$ was included *a posteriori* to take the contribution of De Saint Venànt torsion into account. Now in Eq. 3.33 the second variation of the displacement field $1/2\,\delta^2\mathbf{u}$ is to be identified with second-order components 3.74. Then, remembering the expressions 3.80–3.82 of second-order strains, indicating with $\mathbf{q}_0 = \int_A \mathbf{f}_0 dA$ and $\mathbf{P}_0^T = \left[\left\{V_x^0, V_y^0, N^0\right\}\right]_0^L$ the vectors of distributed loads per unit length and beam end forces, respectively, and rewriting the pre-critical normal stress in the form

$$\sigma_z^0 = \frac{N^0}{A} + \frac{M_x^0}{J_x}y - \frac{M_y^0}{J_y}x + \frac{M_\omega^0}{J_\omega}\omega \tag{3.89}$$

yield the second-order work 3.33 of initial stresses and external loads to be wri3tten, after some manipulation, as follows:

$$\frac{1}{2}\delta^2\Pi_G = \int_{V_0}\sigma_{ij}^0\varepsilon_{ij}^{(2)}dV_0 - \frac{1}{2}\int_{\partial V_0}p_i^0\delta^2u_i dA_0 - \frac{1}{2}\int_{V_0}f_i^0\delta^2u_i dV_0$$

$$= \int_L\int_A\sigma_{ij}^0\varepsilon_{ij}^{(2)}dAdz - \left[P_i^0 u_i^{(2)}\right]_0^L - \int_L q_i^0 u_i^{(2)}dz$$

$$= \frac{1}{2}\int_L\left\{N^0\left[u_S'^2 + v_S'^2 - x_S\left(2v_S'\varphi_z' + \varphi_x\varphi_z' + \varphi_x'\varphi_z\right) + y_S\left(2u_S'\varphi_z' - \varphi_y\varphi_z' - \varphi_y'\varphi_z\right)\right.\right.$$

$$\left.+ C_N\varphi_z'^2\right] + M_x^0\left(\varphi_y'\varphi_z + \varphi_y\varphi_z' - 2u_S'\varphi_z' + C_x\varphi_z'^2\right) - M_y^0\left(\varphi_x'\varphi_z + \varphi_x\varphi_z' + 2v_S'\varphi_z' + C_y\varphi_z'^2\right)$$

$$- V_y^0\left[2u_S'\varphi_z - \varphi_y\varphi_z - x_S\left(\varphi_x'\varphi_y - \varphi_x\varphi_y'\right)\right] + V_x^0\left[2v_S'\varphi_z + \varphi_x\varphi_z - y_S\left(\varphi_x'\varphi_y - \varphi_x\varphi_y'\right)\right]$$

$$+ M_z^0\left(\varphi_x'\varphi_y - \varphi_x\varphi_y'\right) + M_\omega^0 C_\omega\varphi_z'^2\right\}dz$$

$$+ \frac{1}{2}\left[V_x^0 x\varphi_y^2\right]_0^L + \frac{1}{2}\left[V_x^0\left(x-x_S\right)\varphi_z^2\right]_0^L - \frac{1}{2}\left[V_x^0 y\varphi_x\varphi_y\right]_0^L$$

$$+ \frac{1}{2}\left[V_y^0 y\varphi_x^2\right]_0^L + \frac{1}{2}\left[V_y^0\left(y-y_S\right)\varphi_z^2\right]_0^L - \frac{1}{2}\left[V_y^0 x\varphi_x\varphi_y\right]_0^L$$

$$-\frac{1}{2}\Big[N^0\left(x-x_S\right)\varphi_x\varphi_z\Big]_0^L-\frac{1}{2}\Big[N^0\left(y-y_S\right)\varphi_y\varphi_z\Big]_0^L$$

$$+\frac{1}{2}\int_L\Big\{q_x^0\Big[x\varphi_y^2-y\varphi_x\varphi_y+\left(x-x_S\right)\varphi_z^2\Big]+q_y^0\Big[y\varphi_x^2-x\varphi_x\varphi_y+\left(y-y_S\right)\varphi_z^2\Big]$$

$$-q_z^0\Big[\left(x-x_S\right)\varphi_x\varphi_z+\left(y-y_S\right)\varphi_y\varphi_z\Big]\Big\}dz \tag{3.90}$$

where coefficients C_i ($i = N, x, y, \omega$), representing the so called "Wagner effect", are given by (Laudiero & Zaccaria 1988a, Kim *et al.* 1996, Kim & Kim 2000):

$$C_N=\frac{1}{A}\int_A\left(x^2+y^2\right)dA+x_S^2+y_S^2\ ; \qquad C_x=\frac{1}{J_x}\int_A y\left(x^2+y^2\right)dA-2y_S$$

$$C_y=-\frac{1}{J_y}\int_A x\left(x^2+y^2\right)dA+2x_S\ ; \qquad C_\omega=\frac{1}{J_\omega}\int_A \omega\left(x^2+y^2\right)dA \tag{3.91}$$

3.7.1 Further considerations

The present model allows for the stability analysis of beams with any given cross-section and is particularly tailored to pultruded (FRP) or multi-layered orthotropic profiles having the longitudinal axis coinciding with an orthotropy axis. In the latter case, equivalent rigidities $\overline{EA}$, $\overline{EJ_i}$, $\overline{GJ_t}$, $\overline{GD_i}$, $\overline{GD_{ij}}$ ($i, j = x, y, \omega$, see § 1.4.3) are to be used in the strain energy expression 3.88.

Equation 3.90 represents the extension of the geometrical effects considered by Chang *et al.* (1996) and Kim *et al.* (2001) to the case of a generic surface load. It has to be underlined that second-order contributions related to a possible eccentricity between the applied loads and the shear center are taken into account. An expression similar to functional 3.90 has recently been given by Cortínez & Piovan (2006) and Piovan & Cortínez (2007) for FRP beams with symmetric or generic lay-up. Neglecting shear deformations and assuming surface loads linearly varying along the beam, the functional reported by Kim & Kim (2000) is re-obtained. Thanks to the kinematical field adopted, second-order work expressed by Eq. 3.90 follows the rule of *semitangential* rotations[•] and moments conceived by Ziegler (1977) and later proposed by Argyris *et al.* (1978, 1979) to overcome the drawbacks related to rotations and moments about fixed axes. In fact, Kim *et al.* (2001) demonstrated that the approach based on Rodriguez's matrix of finite rotation (Eq. 3.49) coincides, up to the second-order of approximation, with the approach based on *semitangential* rotations.

The need for adopting a second-order displacement field in formulating finite element models for the flexural-torsional buckling analysis was also highlighted by Pi & Bradford (2001) with reference to doubly-symmetric open section beams. In particular,

---

[•] The rotational *pseudo-vector* of a semitangential rotation is defined as the mean vectorial value of the *pseudo-vectors* about a fixed and a follower axis (Argyris 1982). In the mentioned works it was proved that, differently from rotations about fixed or follower axes, semitangential finite rotations are commutative and, in nonlinear finite element analyses, assure the symmetry of the element tangent stiffness matrix.

for the case of shear-undeformable profiles, they showed that, a linear displacement field frequently yields to unacceptable over-predictions of the lateral buckling load. As will be specified in the following, finite element analyses based on a linear approximation provide critical loads converging to the theoretic values in the case of axially loaded or uniformly bent profiles only.

For shear-undeformable doubly-symmetric cross-section beams, Eqs. 3.88 and 3.90 reduce to the functional introduced by Barsoum & Gallagher (1970), provided that second-order in-plane displacements $u^{(2)}$ and $v^{(2)}$ of Eq. 3.74 are ignored and pre-buckling bending moments are constant, linear, or quadratic at most.

3.8 Analytical solutions

Analytical expressions of the buckling load descending from Eq. 3.34 or reported in literature for isotropic or orthotropic profiles subjected to axial or lateral forces will be presented in the following. Such expressions will be adopted as reference solutions for the finite element buckling analyses developed in Section 3.10.

3.8.1 Centroidal axial load

For an axially-loaded beam with $P_z^0 = N^0$ acting at the end section centroids ($x = y = 0$), functional 3.90 turns out to be given by:

$$\frac{1}{2}\delta^2\Pi_G = \frac{1}{2}\int_L \left\{ N^0 \left[u_S'^2 + v_S'^2 - x_S \left(2v_S'\varphi_z' + \varphi_x\varphi_z' + \varphi_x'\varphi_z \right) + y_S \left(2u_S'\varphi_z' - \varphi_y\varphi_z' - \varphi_y'\varphi_z \right) \right. \right.$$
$$\left. \left. + C_N\varphi_z'^2 \right] \right\} dz + \frac{1}{2}\left[N^0 x_S \varphi_x \varphi_z \right]_0^L + \frac{1}{2}\left[N^0 y_S \varphi_y \varphi_z \right]_0^L \tag{3.92}$$

Since the axial load is constant along the beam, Eq. 3.92 reduces to:

$$\frac{1}{2}\delta^2\Pi_G = \frac{1}{2}\int_L N^0 \left\{ \left[u_S'^2 + v_S'^2 - x_S \left(2v_S'\varphi_z' + \varphi_x\varphi_z' + \varphi_x'\varphi_z \right) + y_S \left(2u_S'\varphi_z' - \varphi_y\varphi_z' - \varphi_y'\varphi_z \right) \right. \right.$$
$$\left. + C_N\varphi_z'^2 \right] + \left(x_S\varphi_x\varphi_z \right)' + \left(y_S\varphi_y\varphi_z \right)' \right\} dz \tag{3.93}$$
$$= \frac{1}{2}N^0\int_L \left(u_S'^2 + v_S'^2 - 2x_S v_S'\varphi_z' + 2y_S u_S'\varphi_z' + C_N\varphi_z'^2 \right) dz$$

which coincides with the expression deriving by adopting linear displacement components 3.73 only (Kim *et al.* 1994). The critical axial load must satisfy the variational equation:

$$
\frac{1}{2}\delta^2\Pi = \Bigg\{ \int_L E\left(J_x \varphi_x'^2 + J_y \varphi_y'^2 + J_\omega \Psi'^2 \right) dz
$$

$$
+ G\Bigg[J_t \varphi_z'^2 + D_x \left(u_S' - \varphi_y \right)^2 + D_y \left(v_S' + \varphi_x \right)^2 + D_\omega \left(\varphi_z' + \Psi \right)^2
$$

$$
+ 2D_{xy}\left(u_S' - \varphi_y \right)\left(v_S' + \varphi_x \right) + 2D_{x\omega}\left(u_S' - \varphi_y \right)\left(\varphi_z' + \Psi \right)
$$

$$
+ 2D_{y\omega}\left(v_S' + \varphi_x \right)\left(\varphi_z' + \Psi \right)\Bigg] + N^0\left(u_S'^2 + v_S'^2 - 2x_S v_S' \varphi_z' \right.
$$

$$
+ 2y_S u_S' \varphi_z' + C_N \varphi_z'^2 \Big)\Bigg\} dz = 0 \tag{3.94}
$$

where the term $1/2\int_L EAw_C'^2 dz$ of Eq. 3.88, related to pre-buckling deformations, was omitted. Performing the variation of Eq. 3.94 and integrating by part yield the following equilibrium differential equations:

$$
GD_x \left(u_S'' - \varphi_y' \right) + GD_{xy}\left(v_S'' + \varphi_x' \right) + GD_{x\omega}\left(\varphi_z'' + \Psi' \right) + N^0 u_S'' + N^0 y_S \varphi_z'' = 0 \tag{3.95}
$$

$$
EJ_y \varphi_y'' + GD_x \left(u_S' - \varphi_y \right) + GD_{xy}\left(v_S' + \varphi_x \right) + GD_{x\omega}\left(\varphi_z' + \Psi \right) = 0 \tag{3.96}
$$

$$
GD_{xy}\left(u_S'' - \varphi_y' \right) + GD_y \left(v_S'' + \varphi_x' \right) + GD_{y\omega}\left(\varphi_z'' + \Psi' \right) + N^0 v_S'' - N^0 x_S \varphi_z'' = 0 \tag{3.97}
$$

$$
EJ_x \varphi_x'' - GD_{xy}\left(u_S' - \varphi_y \right) - GD_y \left(v_S' + \varphi_x \right) - GD_{y\omega}\left(\varphi_z' + \Psi \right) = 0 \tag{3.98}
$$

$$
GJ\varphi_z'' + GD_{x\omega}\left(u_S'' - \varphi_y' \right) + GD_{y\omega}\left(v_S'' + \varphi_x' \right) + GD_\omega \left(\varphi_z'' + \Psi' \right)
$$

$$
+ N^0 C_N \varphi_z'' - N^0 x_S v_S'' + N^0 y_S u_S'' = 0 \tag{3.99}
$$

$$
EJ_\omega \Psi'' - GD_{x\omega}\left(u_S' - \varphi_y \right) - GD_{y\omega}\left(v_S' + \varphi_x \right) - GD_\omega \left(\varphi_z' + \Psi \right) = 0 \tag{3.100}
$$

with the relevant boundary conditions:

$$
\Big[GD_x \left(u_S' - \varphi_y \right) + GD_{xy}\left(v_S' + \varphi_x \right) + GD_{x\omega}\left(\varphi_z' + \Psi \right)
$$

$$
+ N^0 u_S' + N^0 y_S \varphi_z' - V_x \Big]\delta u_S \Big|_0^L = 0 \tag{3.101}
$$

$$
\left(EJ_y \varphi_y' - M_y \right)\delta \varphi_y \Big|_0^L = 0 \tag{3.102}
$$

$$
\Big[GD_{xy}\left(u_S' - \varphi_y \right) + GD_y \left(v_S' + \varphi_x \right) + GD_{y\omega}\left(\varphi_z' + \Psi \right)
$$

$$
+ N^0 v_S' - N^0 x_S \varphi_z' - V_y \Big]\delta v_S \Big|_0^L = 0 \tag{3.103}
$$

$$
\left(EJ_x \varphi_x' - M_x \right)\delta \varphi_x \Big|_0^L = 0 \tag{3.104}
$$

$$
\Big[GJ\varphi_z' + GD_{x\omega}\left(u_S' - \varphi_y \right) + GD_{y\omega}\left(v_S' + \varphi_x \right) + GD_\omega \left(\varphi_z' + \Psi \right)
$$

$$
+ N^0 C_N \varphi_z' - N^0 x_S v_S' + N^0 y_S u_S' - M_z \Big]\delta \varphi_z \Big|_0^L = 0 \tag{3.105}
$$

$$
\left(EJ_\omega \Psi' - M_\omega \right)\delta \Psi \Big|_0^L = 0 \tag{3.106}
$$

3.8.1.1 Beams with doubly-symmetric cross-section

If axes x and y coincide with the symmetry axes, $x_S = y_S = D_{xy} = D_{x\omega} = D_{y\omega} = 0$, $C_N = (J_x + J_y)/A$ and equilibrium equations 3.95–3.100 take the following uncoupled form:

$$GD_x\left(u_S'' - \varphi_y'\right) + N^0 u_S'' = 0 \tag{3.107}$$

$$EJ_y\varphi_y'' + GD_x\left(u_S' - \varphi_y\right) = 0 \tag{3.108}$$

$$GD_y\left(v_S'' + \varphi_x'\right) + N^0 v_S'' = 0 \tag{3.109}$$

$$EJ_x\varphi_x'' - GD_y\left(v_S' + \varphi_x\right) = 0 \tag{3.110}$$

$$GJ\varphi_z'' + GD_\omega\left(\varphi_z'' + \Psi'\right) + N^0\varphi_z''\left(J_x + J_y\right)\Big/A = 0 \tag{3.111}$$

$$EJ_\omega\Psi'' - GD_\omega\left(\varphi_z' + \Psi\right) = 0 \tag{3.112}$$

In particular, Eqs. 3.107–3.108 and Eqs. 3.109–3.110 respectively represent the equilibrium equations into x-z and y-z plane for an axially-loaded Timoshenko beam, whereas Eqs. 3.111–3.112 rule the torsional behaviour according to Reissner's torsion theory. These three uncoupled problems attain a solution in correspondence of the following compressive loads:

$$\left|N^0_{cr,x-z}\right| = \frac{\pi^2 EJ_y}{L_0^2}\left[\frac{1}{1 + \left(\pi^2 EJ_y\right)\big/\left(L_0^2 GD_x\right)}\right] \tag{3.113}$$

$$\left|N^0_{cr,y-z}\right| = \frac{\pi^2 EJ_x}{L_0^2}\left[\frac{1}{1 + \left(\pi^2 EJ_x\right)\big/\left(L_0^2 GD_y\right)}\right] \tag{3.114}$$

$$\left|N^0_{cr,torsion}\right| = \frac{A}{J_x + J_y}\frac{\pi^2 EJ_\omega}{L_0^2}\left[\frac{1}{1 + \left(\pi^2 EJ_\omega\right)\big/\left(L_0^2 GD_\omega\right)} + GJ_t\right] \tag{3.115}$$

where L_0 represents the effective length depending on the constraint conditions on flexural rotations and lateral displacements in Eqs. 3.113–3.114 and on torsional rotation end cross-section warping in Eq. 3.115. Equations 3.113 and 3.114, providing the axial load causing flexural instability into x-z and y-z plane, respectively, coincide with the expression given by Bazant & Cedolin (1991). Neglecting shear deformations they reduce to the buckling loads of classical Euler-Bernoulli's theory. Equation 3.115, providing the pure torsional buckling load, was reported also by Kim *et al.* (1994). If shear deformations are neglected, the buckling load corresponding to Vlasov's model (Corradi Dell'Acqua 1994) is re-obtained. In the case of FRP orthotropic multi-layered profiles, the equivalent rigidities $\overline{EJ_y}$, $\overline{GD_x}$, $\overline{EJ_x}$, $\overline{GD_y}$, $\overline{EJ_\omega}$, $\overline{GD_\omega}$, $\overline{GJ_t}$ are to be used in the above equations (Kollár 2001a).

Figure 3.3. Pure flexural and torsional buckling loads of an I-section GFRP pultruded column ($E = 25$ GPa, $G = E/10$) vs. column height. Analytical solutions by Eqs. 3.113–3.114 for $L_0 = h/2$ (dotted and dash-dot lines) and by Eq. 3.115 for three different warping restraint conditions (solid lines).
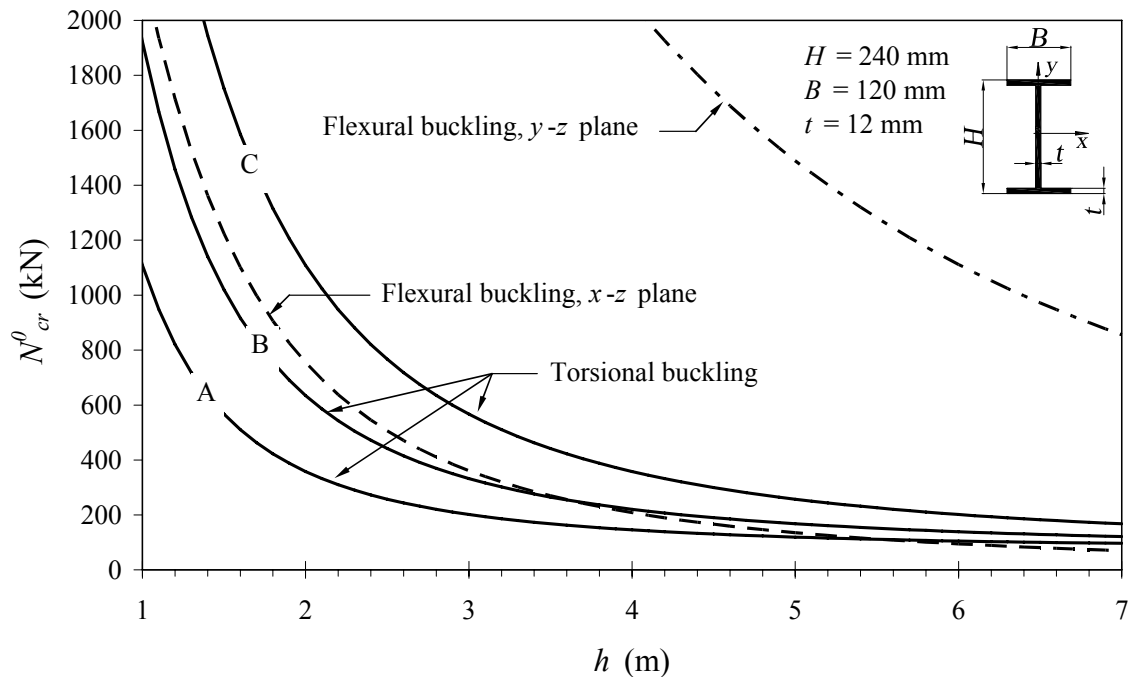
End rotations $\varphi_x, \varphi_y, \varphi_z$	End warping displacements		
	Curve A	Curve B	Curve C
fixed-fixed	free-free ($L_0 = h$)	fixed-free ($L_0 = 2h/3$)	fixed-fixed ($L_0 = h/2$)

For example purposes, an I-section pultruded column (Fig. 3.3) with elastic moduli $E = 25$ GPa, $G = E/10$ is considered. Cross-section properties were evaluated by using the relations reported in Chapter 1. The analytical (global) buckling loads were determined assuming fixed end flexural and torsional rotations for three different constraint conditions on the end cross-section warping. The results are plotted in Figure 3.3 versus the column height h. It should be noted that flexural buckling in the weak plane prevails only when end warping displacements are fixed. Therefore, in FRP pultruded structures, where warping displacements at the beam ends cannot be easily prevented, pure torsional buckling of columns may occur provided that local instability is avoided.

3.8.1.2 Beams with monosymmetric cross-section

A C-shaped profile under axial compression is now considered. Identifying principal plane x-z with the plane of symmetry ($y_S = 0$), Eqs. 3.95–3.100 reduce to:
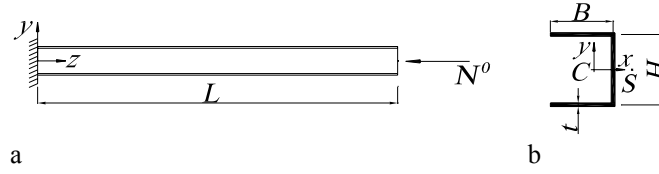
Figure 3.4. a: cantilever CFRP profile subjected to a centroidal axial load. b: C-shaped cross-section with $H = B = 600$ mm, $t = 30$ mm.

Table 3.I. Properties of the C-shaped FRP profile analyzed (material properties and cross-section dimensions by Cortínez & Piovan 2002).

E	G	A	x_S	J_x	J_y	J_t	J_ω
kNmm^{-2}	kNmm^{-2}	mm^2	mm	mm^4	mm^4	mm^4	mm^6
1.44E+2	4.14	5.40E+4	4.57E+2	3.78E+9	2.16E+9	1.62E+7	1.39E+14

C_N	D_x	D_y	D_ω	$D_{y\omega}$
mm^2	mm^2	mm^2	mm^4	mm^3
3.19E+5	2.77E+4	1.62E+4	3.74E+9	−3.95E+6

$$GD_x \left(u_S'' - \varphi_y' \right) + N^0 u_S'' = 0 \tag{3.116}$$

$$EJ_y \varphi_y'' + GD_x \left(u_S' - \varphi_y \right) = 0 \tag{3.117}$$

$$GD_y \left(v_S'' + \varphi_x' \right) + GD_{y\omega} \left(\varphi_z'' + \Psi' \right) + N^0 v_S'' - N^0 x_S \varphi_z'' = 0 \tag{3.118}$$

$$EJ_x \varphi_x'' - GD_y \left(v_S' + \varphi_x \right) - GD_{y\omega} \left(\varphi_z' + \Psi \right) = 0 \tag{3.119}$$

$$GJ \varphi_z'' + GD_{y\omega} \left(v_S'' + \varphi_x' \right) + GD_\omega \left(\varphi_z'' + \Psi' \right) + N^0 C_N \varphi_z'' - N^0 x_S v_S'' = 0 \tag{3.120}$$

$$EJ_\omega \Psi'' - GD_{y\omega} \left(v_S' + \varphi_x \right) - GD_\omega \left(\varphi_z' + \Psi \right) = 0 \tag{3.121}$$

Equations 3.116–3.117, coinciding with Eqs. 3.107–3.108, rule the flexural buckling behaviour into x-z plane examined in the previous paragraph. The remaining four equations 3.118–3.121 rule another form of instability, characterized by bending into y-z plane coupled with torsion. The displacement functions $v_S(z)$, $\varphi_x(z)$, $\varphi_z(z)$ and $\Psi(z)$ can be expressed in terms of four different sets of constants. It is possible to demonstrate that only six of these constants are independent. Hence, a system of six linear homogeneous algebraic equations with constant coefficients is obtained, which is to be solved by introducing the boundary conditions. In particular, since non-trivial solutions are searched for, the flexural-torsional ("FT") buckling load $\left| N_{FT}^0 \right|$ is obtained by vanishing the determinant of the coefficient matrix. For example purposes, a cantilever composite beam made of unidirectional graphite epoxy is analyzed (Fig. 3.4, Table 3.I). Due to the cross-section shape, flexural-torsional buckling prevails on the flexural buckling into the symmetry plane. In particular, for slenderness ratios $L/H = 3.5$ and 5.0, vanishing the determinant of the coefficient matrix yields the analytical buckling loads

$\left|N_{FT}^0\right|$ = 19.2 × 10^3 kN and 12.0 × 10^3 kN, respectively. The same results may be obtained implementing the exact finite element proposed by Kim *et al.* (2004), which is based on the linear displacement field 3.73.

3.8.2 Lateral loads

By adopting a linear displacement field to predict the lateral buckling load, accurate solutions may be obtained in the case of uniform bending only (Pi & Bradford 2001). In all other cases, second-order displacement components 3.74 are needed.

Sapkás & Kollár (2002) analyzed the lateral-torsional buckling behaviour of FRP composite beams with orthotropic lay-up presenting doubly- or monosymmetric cross-section. In order to take shear deformations into account, they modified the formula proposed by Clark & Hill (1960) for isotropic material. In particular, assuming that pre-buckling bending occurs in the *y-z* symmetry plane (Fig. 3.5), the buckling moment provided by Sapkás and Kollár for cantilever or simply-supported beams can be written as:

$$M_{x,cr} = C_1 \frac{\pi^2}{L_0^2}\left(\frac{1}{\overline{EJ_y}}+\frac{\pi^2}{L_0^2\overline{GD_x}}\right)^{-1}\left\{-C_2\left(y_P-y_S\right)+C_3 C_x\right.$$

$$\left.+\sqrt{\left[C_2\left(y_P-y_S\right)+C_3 C_x\right]^2+\frac{\left(1/\overline{EJ_\omega}+\pi^2/L_0^2\overline{GD_\omega}\right)^{-1}}{\left(1/\overline{EJ_y}+\pi^2/L_0^2\overline{GD_x}\right)^{-1}}\left[1+\frac{L_0^2\overline{GJ_t}}{\pi^2\left(1/\overline{EJ_\omega}+\pi^2/L_0^2\overline{GD_\omega}\right)^{-1}}\right]}\right\}$$

(3.122)

where L_0 is the effective length, y_P–y_S is the distance between the load location and the shear center, C_x is the cross-section parameter defined by Eq. 3.91b and C_i (i = 1, 2, 3) are constants reported in Table 3.II for simply-supported beams (L_0 = L) subjected to three different load conditions. Equation 3.122 generally provides good approximations of the buckling load, especially for doubly-symmetric cross-section.
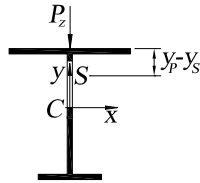

Figure 3.5. Monosymmetric thin-walled profile under lateral load.

Table 3.II. Coefficients of Eq. 3.122 for simply-supported profiles (Sapkás & Kollár 2002).

Load condition	C_1	C_2	C_3
Uniform bending	1.00	0.00	0.50
Uniformly distributed load ($M_{x,cr} = q_{z,cr}\,L^2/8$)	1.13	0.45	0.27
Concentrated force at mid-span ($M_{x,cr} = P_{z,cr}\,L$)/4	1.35	0.55	0.21

In fact, the contribution of the shear stiffness $\overline{GD_{x\omega}}$, not null for monosymmetric beams, is neglected in Eq. 3.122. Moreover, for doubly-symmetric simply-supported profiles in uniform bending, Eq. 3.122 gives the exact solution with respect to the beam model presented in Sections 3.4–3.7. Machado & Cortínez (2005) proposed a closed-form expression for the lateral-torsional buckling load of FRP doubly-symmetric beams taking pre-buckling deflections into account. On the other hand, when pre-buckling deflections are neglected their expression coincides with Eq. 3.122.

3.9 Finite element formulation

Figure 3.6 shows a typical two-node beam element, nodal displacements and forces, and external (distributed) loads. The displacement field 3.73–3.74 is approximated in the usual form:

$$\mathbf{d} = \mathbf{N}\mathbf{q} \tag{3.123}$$

where $\mathbf{d}$ and $\mathbf{q}$ are given by:

$$\mathbf{d}_e^T = \left\{ w_C(z), u_S(z), \varphi_y(z), v_S(z), \varphi_x(z), \varphi_z(z), \Psi(z) \right\} \tag{3.124}$$

$$\mathbf{q}_e^T = \left\{ w_{C1}, w_{C2}, u_{S1}, \varphi_{y1}, u_{S2}, \varphi_{y2}, v_{S1}, \varphi_{x1}, v_{S2}, \varphi_{x2}, \varphi_{z1}, \Psi_1, \varphi_{z2}, \Psi_2 \right\} \tag{3.125}$$

and matrix $\mathbf{N}$ collects a proper set of shape functions in the form:

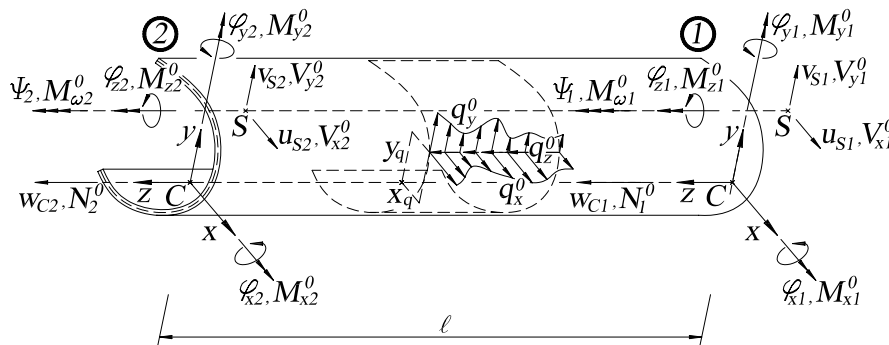$$\mathbf{N} = diag\left[\mathbf{N}^z, \mathbf{N}^x, \mathbf{N}^y, \mathbf{N}^\omega \right] \tag{3.126}$$

Figure 3.6. Free-body force distribution and nodal displacements of the element.

Substituting Eq. 3.123 into the second variation $1/2\,\delta^2\Pi$ of the total potential energy yields the element stiffness matrix. It should be recognized that, before assembling the global matrix of a structure, the nodal displacements should be referred to a single reference point (see Appendix 2.C). Then, the usual assemblage technique yields:

$$\frac{1}{2}\delta^2\Pi\bigg|_{structure} = \frac{1}{2}\mathbf{q}^T\mathbf{K}\mathbf{q} \tag{3.127}$$

where $\mathbf{K}$ represents the global stiffness matrix. It should be underlined that, as usual in linearized stability problems, the internal forces are assumed to be linear functions of the external loads. Hence, matrix $\mathbf{K}$ can be written as follows:

$$\mathbf{K} = \mathbf{K}_E + \lambda\mathbf{K}_G \tag{3.128}$$

where $\mathbf{K}_E$ and $\lambda\mathbf{K}_G$, which approximate functionals $1/2\,\delta^2\Pi_E$ and $1/2\,\delta^2\Pi_G$, are the elastic and geometric stiffness matrix of the structure, respectively. The critical loads are given by the roots of the equation $\det(\mathbf{K})=0$ which can be suitably reduced to a standard eigenvalue problem.

In the presence of off-axis loadings, the contributions due to possible distributed forces q_i^0 ($i = x, y, z$) may be obtained for each element in its local reference system, whereas the terms related to concentrated forces should be defined directly in the global reference of the assembled structure.

With the exception of w_C, described by linear shape functions, the unknown displacements 3.124 were interpolated resorting to the "modified" Hermitian element $H32$ (§ 2.2.1, see Appendix 2.B for $\mathbf{K}_E$), which does not require static condensation and showed good convergence rate in static analyses of shear-deformable isotropic and FRP beams. These *locking-free* shape functions were also adopted by Chang *et al.* (1996) for flexural-torsional buckling analyses of isotropic beams with a generic cross-section. However, in that work the nonuniform torsion-shear coupling terms (D_{ij}, $i, j = x, y, \omega, i \neq j$) introduced in Chapter 1 were ignored in the elastic strain energy expression and geometrical effects due to surface loads were not considered. In the following section, it will be shown that finite element $H32$ gives accurate results in the stability analysis of FRP orthotropic profiles subjected to both axial and lateral concentrated or distributed loads, also in the presence of shear strain coupling terms. Consequently, it was applied to the buckling analysis of portal frames made of FRP pultruded composite profiles. The more significant results will be discussed, with particular attention to the influence of shear deformations, base warping restraints and lateral bracing.

The geometric stiffness matrix $\mathbf{K}_G$ of element $H32$ is reported in Appendix 3.A for axial and uniformly distributed transversal load.

3.10 Buckling analysis of FRP composite beams

3.10.1 C-shaped FRP profile under axial load

The first example is intended to represent a convergence test for the numerical model adopted. To this purpose, a C-shaped CFRP profile (properties in Table 3.I) was considered. The global buckling load was determined for three different constraint conditions. The beam was subjected to a constant compressive axial load acting at the centroid. As a matter of fact, for the wide-flange C-shaped profile investigated, the axial load is limited by local buckling; yet, to perform the convergence test, global buckling loads only were evaluated.

In Figure 3.7, the analytical buckling load evaluated by solving Eqs. 3.118–3.121 is reported versus the beam slenderness for the case of a cantilever profile. The analytical solutions corresponding to the Euler-Bernoulli-Vlasov theory, obtained by neglecting shear deformations ($\varphi_x = -\partial v_S/\partial z$, $\Psi = -\partial \varphi_z/\partial z$), are also reported. Moreover, solutions corresponding to the numerical model $H32$ are reported for 1 and 2 finite elements.

It is quite evident that ignoring shear deformations (S.D.) implies a strong overestimate of the buckling load for the entire slenderness range going from 2 to 10 (+ 33% for $L/H = 5$). Also, it can be observed that one element always gives accurate results (the error is of about 4.6% for $L/H = 2$). Finally, if coefficients ϕ_y and ϕ_ω defined by Eqs. 2.14 and 2.20 are set equal to zero, the solution to the classical beam theory is substantially re-obtained using one finite element only.
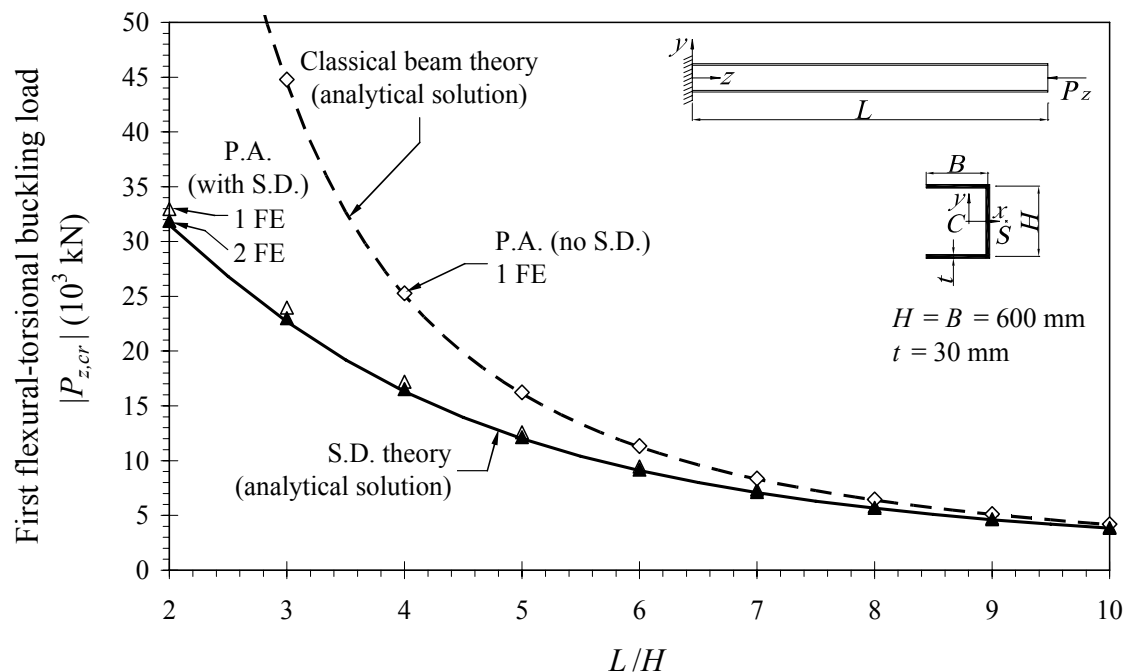

Figure 3.7. Flexural-torsional buckling load vs. beam slenderness for an FRP C-shaped cantilever profile subjected to a centroidal axial force. Comparison between present analysis (P.A., ▲, Δ, ◊) and analytical solutions (solid and dotted lines). Material strength limit: 300 MPa ($P_{z,res} = 16.2 \cdot 10^3$ kN).
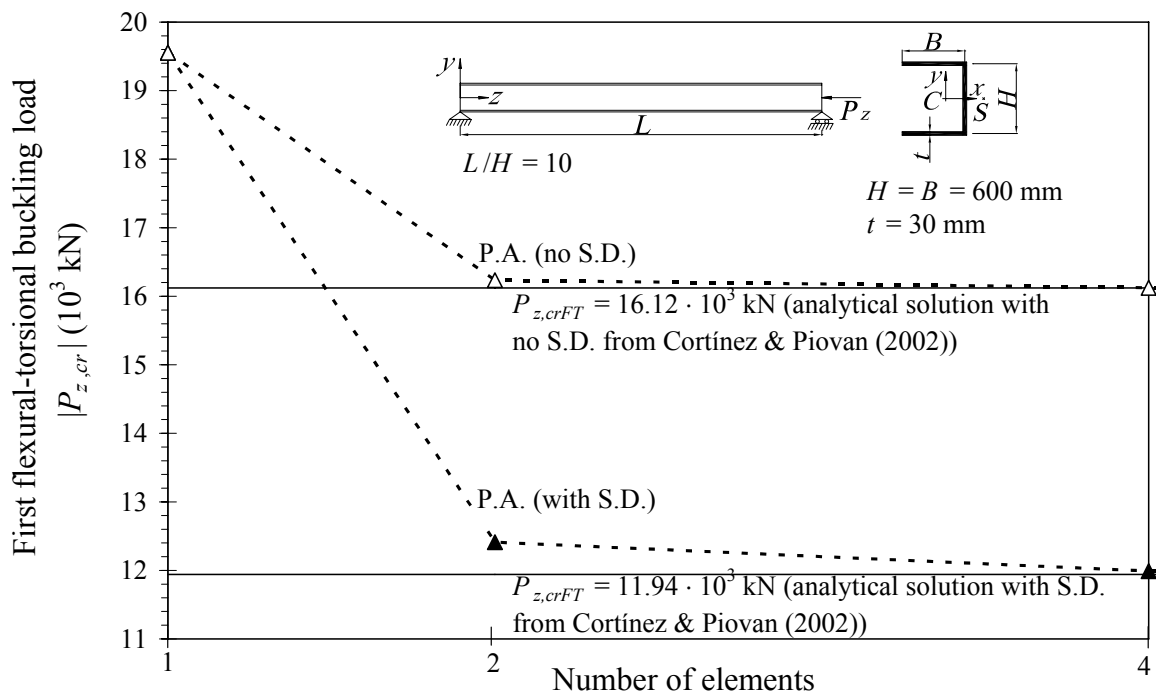
Figure 3.8. Flexural-torsional buckling load for a simply supported C-shaped FRP profile subjected to a centroidal axial force. Convergence rate of the proposed FE formulation considering (--▲--) and neglecting (--△--) shear deformations (S.D.).

Table 3.III. Buckling load (10^3 kN) for a fully clamped C-shaped FRP beam with unidirectional reinforcement. Comparison between present analysis (P.A.) and the FE model proposed by Cortínez & Piovan (2006).

		L/H	20	10	5
no S.D.	Cortínez & Piovan (30 FE)		9.5	36.6	141.8
	P.A. (4 FE)		9.6	36.9	142.8
with S.D.	Cortínez & Piovan (30 FE)		7.5	16.9	25.0
	P.A. (4 FE)		7.7	17.4	26.2

Figure 3.8 highlights the convergence rate of the proposed formulation for the case of a simply supported beam ($L/H = 10$). It is well known that, when no relative displacement between the end sections is allowed, one beam element gives unacceptable errors. In the present case, the error is additionally increased due to the structure of polynomials 2.12–2.13. In fact, when one element is adopted to describe a simply supported beam, the constraint conditions cancel some rows and columns of the stiffness matrix which take the shear deformations into account. As a matter of fact, when 2 finite elements are adopted, the error with respect to the analytical solution, reported for this case also by Cortínez & Piovan (2002), reduces from 63% to about 3%.

In Table 3.III, the buckling load for a fully clamped monosymmetric profile ($H = B$ = 100 mm, t = 10 mm) made of graphite-epoxy (AS4/3501) is reported for different slenderness ratios. The present model is in a very good agreement with the numerical model by Cortínez & Piovan (2006), giving almost coincident results when the same number of elements is adopted.

3.10.2 Simply supported I-beam under axial load

An orthotropic I-beam simply supported at both ends was considered (Kollár 2001b, see Table 3.IV). The beam is subjected to a centroidal axial load. Due to double symmetry, flexural and torsional buckling are independent of each other. The accuracy of the adopted numerical model was verified with reference to the pure torsional buckling load versus the beam slenderness (Fig. 3.9).

Table 3.IV. Properties of the I-beam analyzed in Figs. 3.9 and 3.10 (from Kollár 2001b).

$\overline{EJ}_x$	$\overline{EJ}_y$	$\overline{EJ}_\omega$	$\overline{GJ}_t$	$\overline{GD}_x$	$\overline{GD}_y$	$\overline{GD}_\omega$	C_N
kNmm^2	kNmm^2	kNmm^4	kNmm^2	kN	kN	kNmm^2	mm^2
9.20E+8	4.85E+8	2.55E+12	1.21E+5	7.56E+3	3.25E+3	3.92E+7	3.81E+3
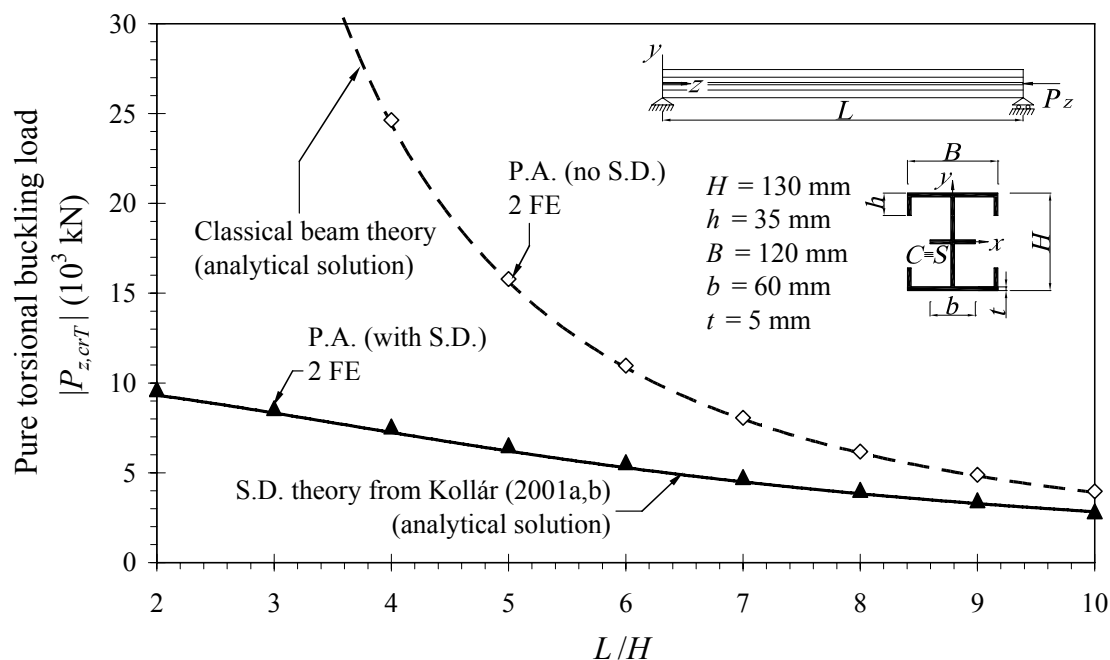
Figure 3.9. Pure torsional buckling load vs. beam slenderness for a simply supported FRP (stiffened) I-profile (Kollár 2001b) subjected to a centroidal compression force. Comparison between the present analysis (P.A., ▲, ◊) and analytical solutions (solid and dotted lines).
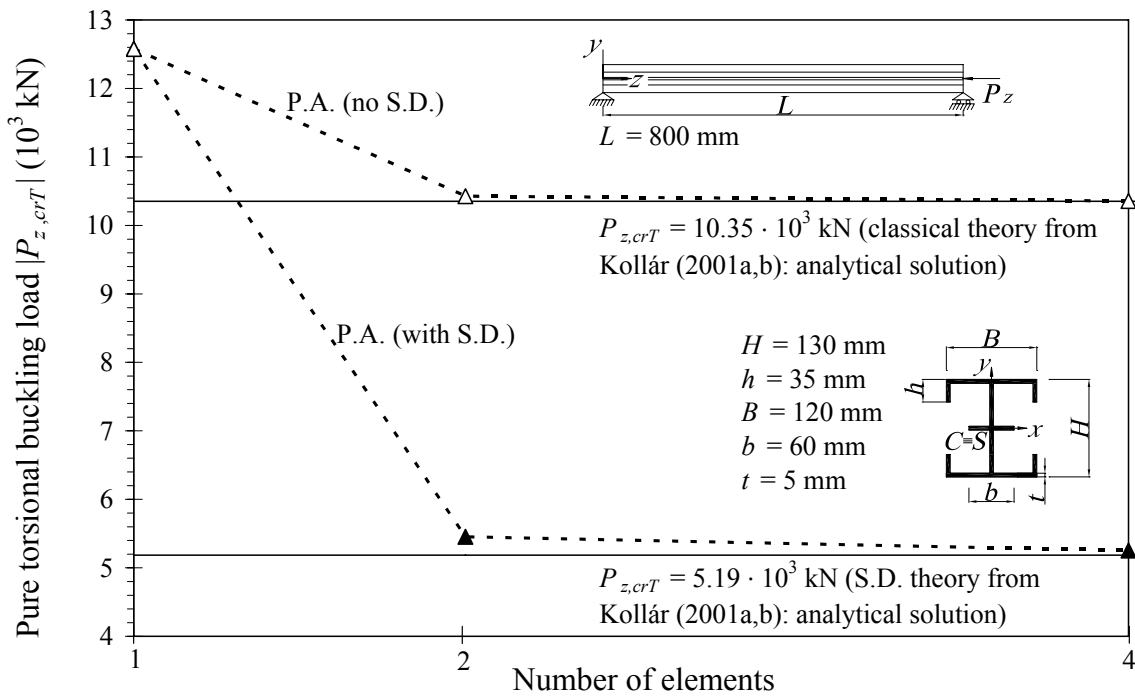
Figure 3.10. Pure torsional buckling load for a simply supported FRP (stiffened) I-profile (Kollár 2001b) subjected to a centroidal compression force. Convergence rate of the proposed FE formulation including (--▲--) and neglecting (--△--) shear deformations (S.D.).

The solid line refers to the closed-form solution 3.115, in which the shear strain effects on nonuniform torsion are included, whereas the dotted line represents the classical Vlasov solution. Two finite elements of the proposed model give a good approximation of the buckling load (error ≤3.8%) for slenderness ranging between 2 and 10. The convergence rate for $L/H \cong 6$ is illustrated in Figure 3.10. Once again, neglecting shear deformations, the numerical solution rapidly converges to the pure torsional buckling load given by Vlasov's theory.

3.10.3 Simply supported I-beam under lateral loads

The proposed model was then applied to the buckling analysis of a simply supported orthotropic I-profile (properties by Sapkás & Kollár 2002, see Table 3.V) subjected to end concentrated moments (Fig. 3.11), to a concentrated force acting at mid-span (Fig. 3.12) and, finally, to a uniformly distributed load (Fig. 3.13). For the last two cases, it is mandatory to consider a second-order approximation of the displacement field.

Table 3.V. Properties of the I-beam analyzed in Figs. 3.11−3.13 (from Sapkás & Kollár 2002).

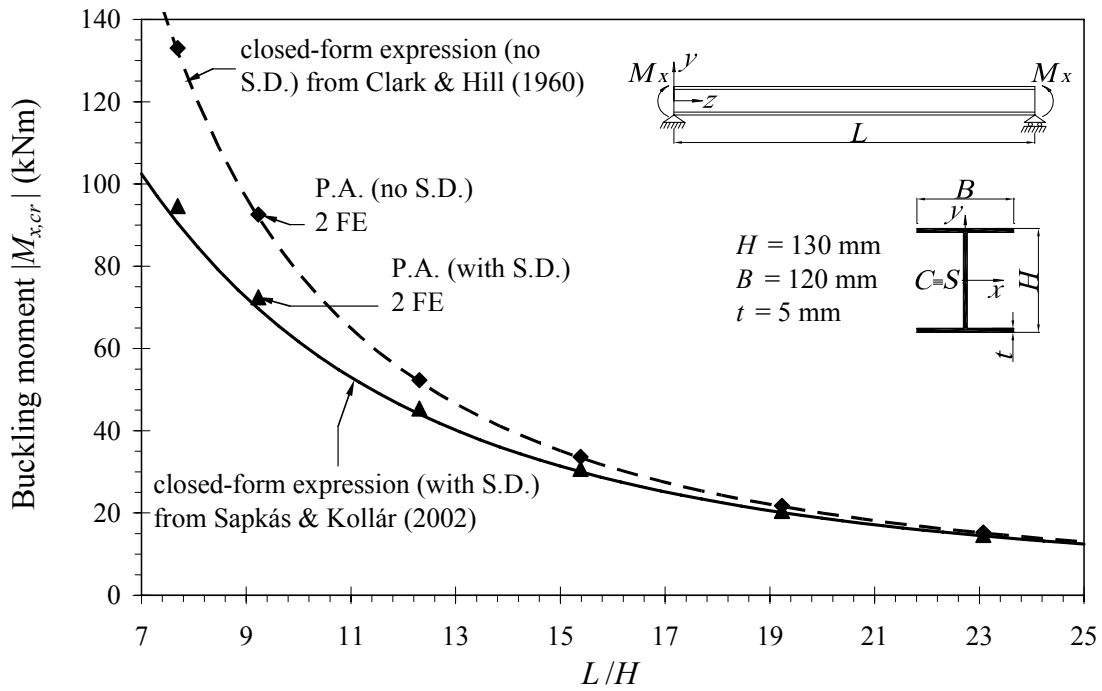| $\overline{EJ_y}$	$\overline{EJ_\omega}$	$\overline{GJ_t}$	$\overline{GD_x}$	$\overline{GD_\omega}$	C_N
kNmm^2	kNmm^4	kNmm^2	kN	kNmm^2	mm^2
2.13E+8	8.33E+11	6.80E+4	4.55E+3	1.78E+7	3.81E+3

Figure 3.11. Lateral-torsional buckling load vs. beam slenderness for an orthotropic I-profile subjected to end concentrated bending moments. Comparison between the proposed FE formulation (▲, ♦) and the expressions reported by Sapkás & Kollár and by Clark & Hill (solid and dotted lines).
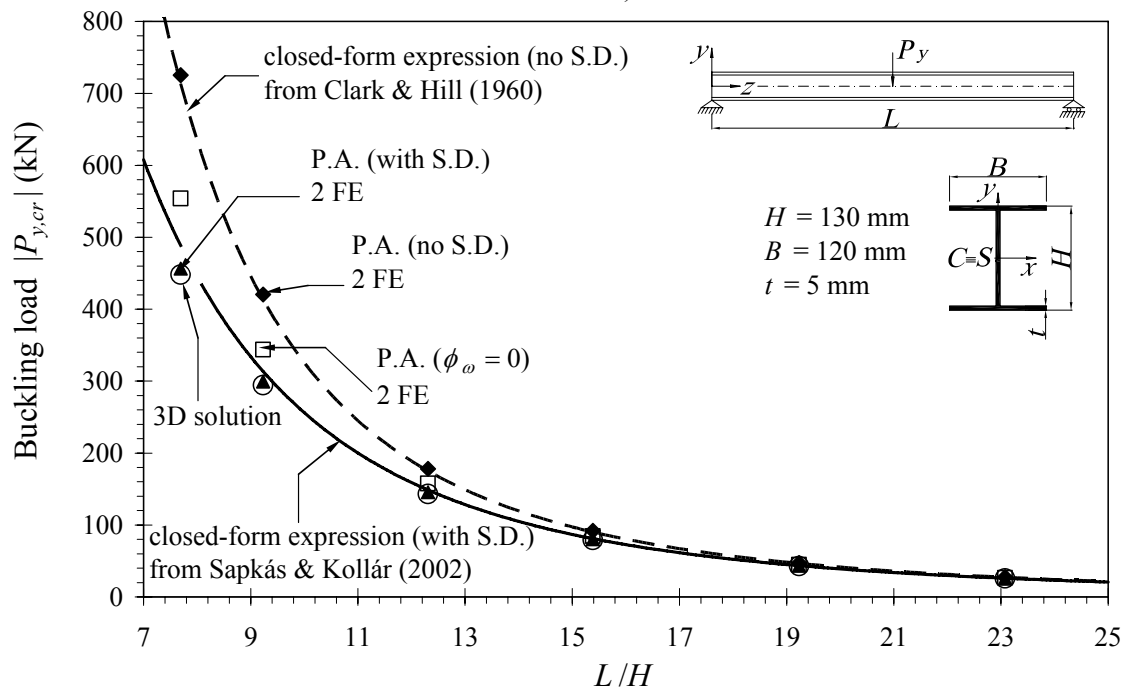
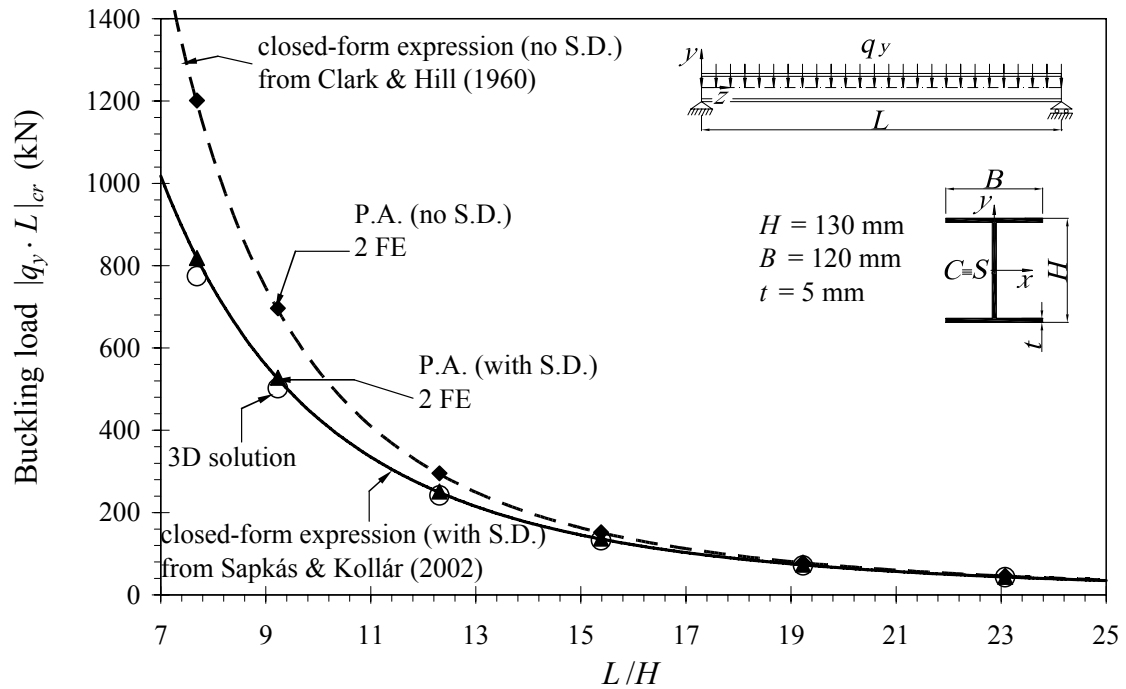

Figure 3.12. Lateral-torsional buckling load vs. beam slenderness for an orthotropic I-profile subjected to a centroidal lateral force at mid-span. Comparison between the proposed FE formulation including shear deformations (▲), neglecting shear deformations (♦), and neglecting warping shear deformations only (□); the expressions reported by Sapkás & Kollár and by Clark & Hill (solid and dotted lines) and the 3D-model results (○).

Closed-form solutions in the presence and in the absence of shear deformations were found using Eq. 3.122 and formula of Clark and Hill (1960), respectively, with coefficients of Table 3.II. In the last two examples (Figs. 3.12 and 3.13), the buckling loads were also calculated by implementing a 3D numerical model (Fig. 3.14), and making use of 4-node orthotropic shell elements (STRAUS7® 2004). To avoid local buckling phenomena, rigid links were introduced making the cross-section rigid in its own plane only.

Figure 3.13. Lateral-torsional buckling load vs. beam slenderness for an orthotropic I-profile subjected to a uniformly distributed load acting at the (b.d.) shear centre. Comparison between the proposed FE formulation (▲, ♦), the expressions reported by Sapkás & Kollár and by Clark & Hill (solid and dotted lines) and the 3D-model results (○).
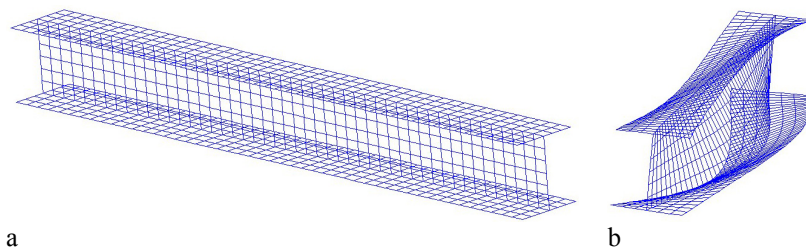

Figure 3.14. CFRP profile of § 3.10.3. a: 3D numerical model (shell elements 20 mm × 20 mm). b: typical flexural-torsional buckling shape.

Due to the constitutive relation 1.118 and the interpolating polynomials N_{2i}^y ($i = 1,\dots,4$) of Eq. 2.13, the pre-buckling bending moments can be represented by constant or linear functions at most. Consequently, in the presence of lateral distributed forces, the monotonic convergence to critical loads from above is lost (Laudiero & Zaccaria 1988b) because of the dependence of the pre-buckling stresses on the assumed discretization. For this reason, in evaluating the geometrical effects of a constant distributed load (see Fig. 3.13), a quadratic expression for the pre-buckling moment was substituted into functional 3.90. Two finite elements were sufficient to provide very accurate results (Figs. 3.11–3.13). The solutions given by the formula of Clark and Hill were readily re-obtained by ignoring the shear strain influence. For the case of a simply supported beam loaded at midspan (Fig. 3.12), numerical results obtained in the absence of warping shear deformations ($\phi_\omega = 0$, see Eq. 2.20) were also reported. In this case, for $L/H = 7.5$, the overestimate of the lateral buckling load is of about 22%.

Table 3.VI. Properties of the monosymmetric I-beam analyzed in Fig. 3.15 (from Sapkás & Kollár 2002).

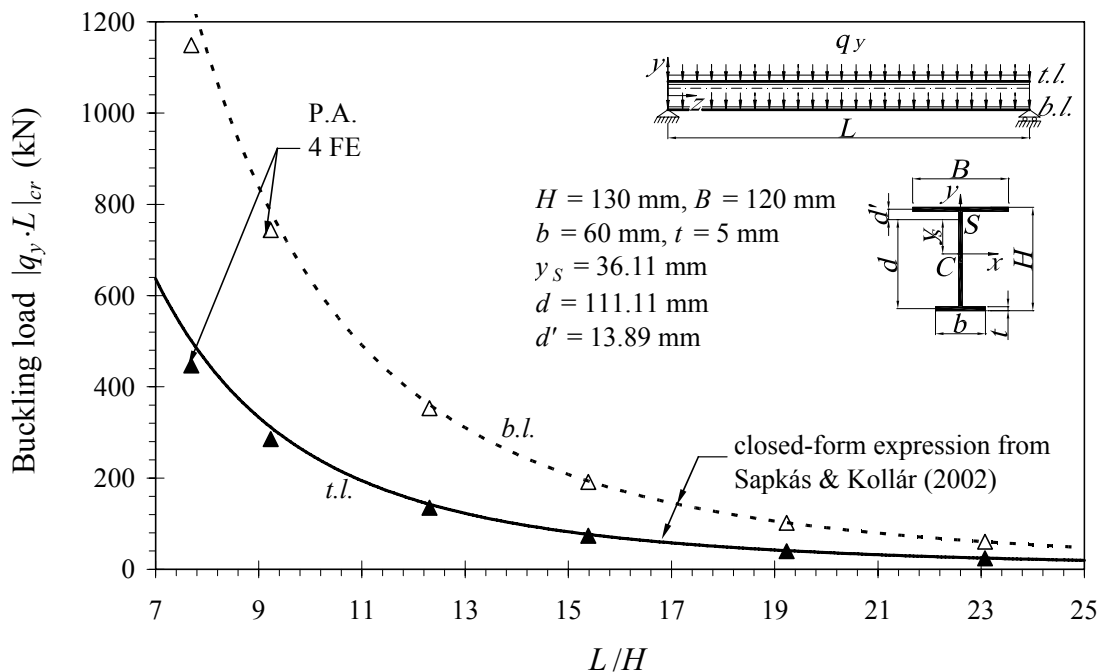| $\overline{EJ_y}$	$\overline{EJ_\omega}$	$\overline{GJ_t}$	$\overline{GD_x}$	$\overline{GD_\omega}$	$\overline{GD_{x\omega}}$	y_S	C_N	C_x
kNmm^2	kNmm^4	kNmm^2	kN	kNmm^2	kNmm	mm	mm^2	mm
1.20e8	1.85e11	5.70e4	3.41e3	1.45e7	−9.48e4	3.61e1	4.51e3	8.48e1

Figure 3.15. Lateral-torsional buckling load vs. beam slenderness (with S.D.) for an orthotropic monosymmetric I-profile subjected to an uniformly distributed vertical load. Solid and dotted lines correspond to the approximate expressions reported by Sapkás & Kollár. In the present analysis, symbols ▲ and △ stand for top loading and bottom loading respectively.

3.10.4 Simply-supported monosymmetric I-beam under uniformly distributed lateral load

In this example, the influence of the load location on lateral-torsional buckling was investigated for a monosymmetric orthotropic I-beam subjected to a uniformly distributed load q_y. The beam properties are reported in Table 3.VI. In particular, top and bottom loads were considered adopting 4 finite elements. Figure 3.15 also shows the approximate solution given by Sapkás and Kollár (Eq. 3.122) which ignores non uniform bending-torsion coupling ($\overline{GD_{x\omega}} = 0$). It should be noted that, for $L/H = 7.5$, the critical value of q_y for the bottom load is 2.6 times the corresponding value for the top load. For the same slenderness, the values given by Eq. 3.122 overestimate the buckling load by about 8.6% and 12% respectively.

3.11 Buckling analysis of FRP pultruded portal frames

3.11.1 Portal frame under in-plane horizontal nodal forces

In the following examples, the buckling analysis of a plane frame subjected to horizontal load concentrated at the beam-column joints is presented. Particular attention was paid to the influence of beam slenderness, to the shear strain effects and, furthermore, to the role of out-of-plane restraints. Four finite elements per member were adopted.

3.11.1.1 Critical load for increasing beam length

The portal frame shown in Figure 3.16 was analyzed for the beam length l ranging from 1.5 m to 5.0 m. All members, showing $E = 25$ GPa and $G = E/10$, are GFRP-pultruded I-section profiles having the major axis parallel to the global axis y. The cross-section dimensions are: $H = 240.0$ mm, $B = 120.0$ mm, $t = 12.0$ mm. Full displacement and rotation continuity, and no warping restraint were assumed at the column-beam joints.

    The pre-buckling state is characterized by a plane antisymmetrical deflection, and, in particular, column A-B is in tension and column C-D in compression. Possible warping restraints at the column bases were considered.
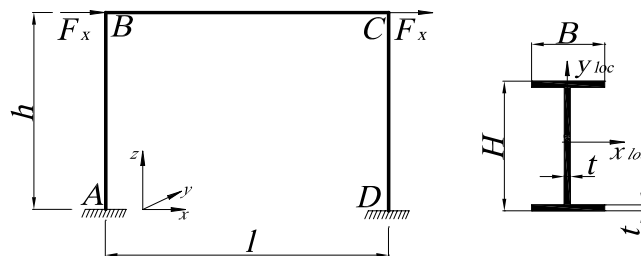

Figure 3.16. FRP portal frame subjected to two equal horizontal forces at nodes B and C; $h = 3.0$ m, l ranges between 1.5 and 5.0 m. Examples 4.5.1, 4.5.3: $H = 240.0$ mm, $B = 120.0$ mm, $t = 12.0$ mm. Examples 4.5.2, 4.6.1, 4.6.2: $H = B = 203.2$ mm, $t = 9.5$ mm. All members have the major axis x_{loc} parallel to the global axis y.

To highlight the bracing influence on the frame response, three constraint conditions were analyzed: preventing lateral displacements along columns, along the beam, or at nodes B and C only, respectively (Fig. 3.17).

The dashed curve in Figure 3.17 indicates restraints on column lateral displacements. In the corresponding buckling mode (Fig. 3.18a), the beam shows antisymmetrical lateral displacements and symmetrical torsional rotations (Pi & Bradford 2001), whereas the columns present same torsional rotations. In the case under examination, restraining the column base warping gives insignificant variations of the frame response.

The two dash-dot curves of Figure 3.17 indicate restraints on beam lateral displacements. In particular, the lower curve corresponds to the case of free warping at the column bases, whereas the upper curve refers to the case of totally restrained warping. It should be noted that, as the beam length increases, the axial compressive force in column C-D lowers so as to increase the frame buckling load. In the corresponding buckling mode (Fig. 3.18b), the beam is subjected to pure torsional rotation, whereas the compressed column shows lateral deflections coupled with torsion. In particular, restraining warping at the column base implies a strong increase (40%) of the buckling load.

Another significant solution is obtained when the out-of-plane displacements of joints B and C are prevented. In this case (thick solid lines of Fig. 3.17), the frame response borders the two limit cases described above. In fact, for $l/h \leq 0.8$ and for $l/h \geq 1.1$, the solid lines substantially coincide with the cases of lateral restraints on beam and columns respectively. Moreover, the two curves reach a maximum for $l \cong h$ and, as the beam length increases, they quickly tend to coincide.
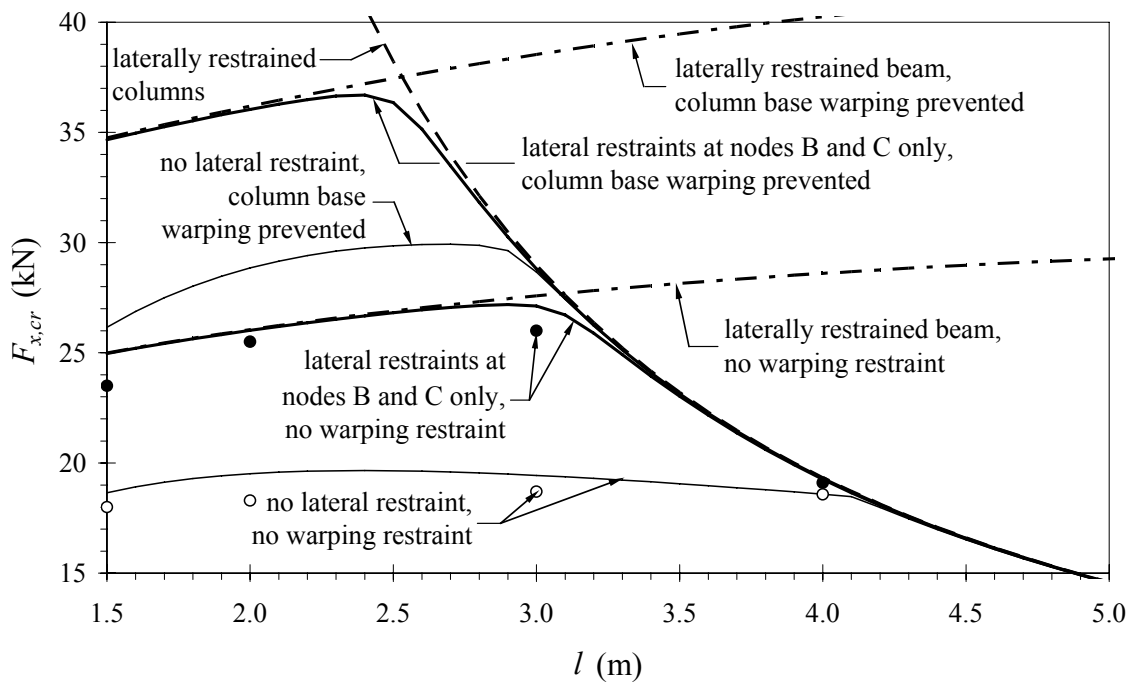

Figure 3.17. Critical horizontal forces for increasing beam length, under different lateral restraint conditions. Symbols (●, ○) refer to the 3D FEM solutions.
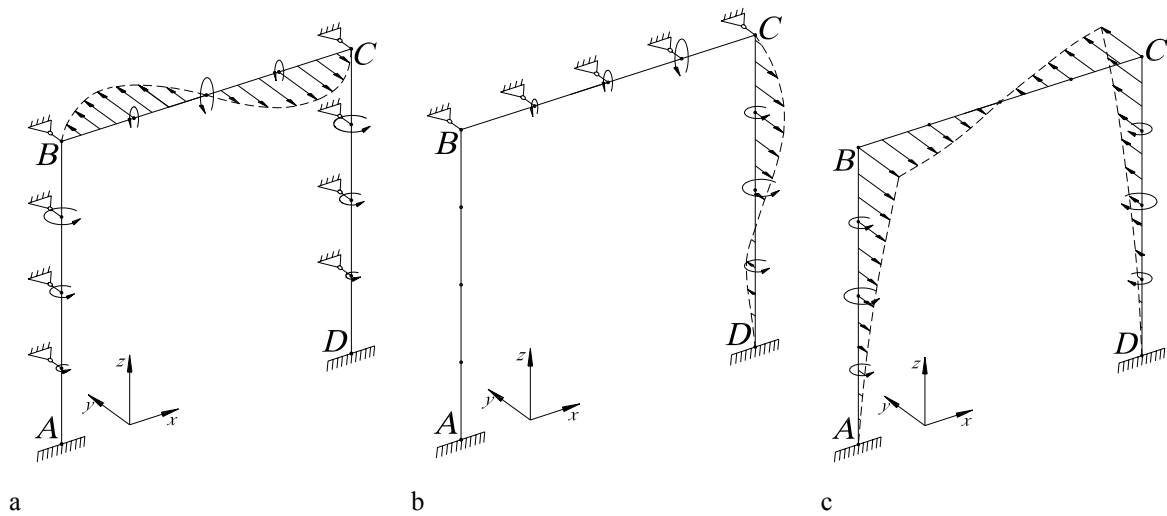
Figure 3.18. Mode shapes of the portal frame of Fig. 3.16 for different out-of-plane restraint conditions. Straight and circular arrows indicate lateral displacements (*y* direction) and torsional rotations, respectively. a: laterally restrained columns; b: laterally restrained beam; c: no lateral restraint.
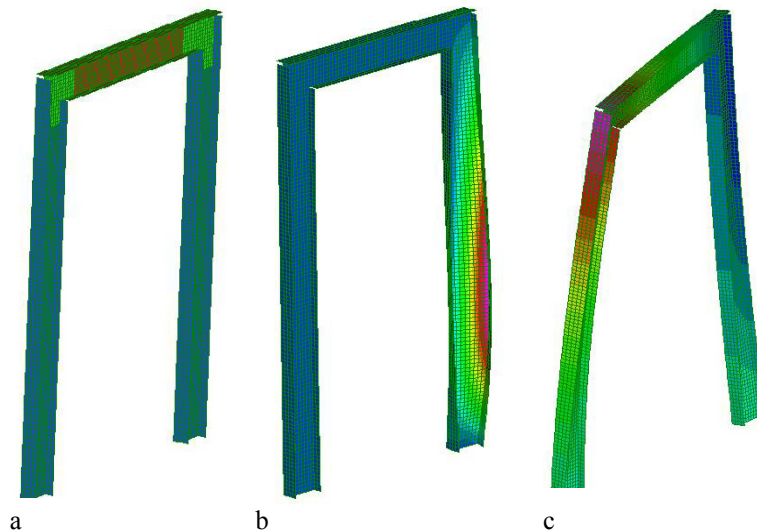

Figure 3.19. GFRP portal frame of Fig. 3.16 with *l* = 1.5 m and *h* = 3.0 m. a: 3D numerical model (shell elements 60 mm × 60 mm). b: buckling shape in the case of lateral restraints at the beam-column nodes: prevailing flexural (2 half waves)-torsional (1 half wave) instability of compressed column (see Fig. 3.18b). c: buckling shape in the absence of lateral restraints: antisymmetrical out-of-plane deflection (see Fig. 3.18c).

Finally, the two thin solid curves refer to the case of free lateral displacements, in the presence of restraints on column base warping or not. In both cases, for relatively short beams, the (antisymmetrical) critical shape (Fig. 3.18c) is influenced by the flexural-torsional column displacements and, consequently, by the presence of base

warping restraints. Nevertheless, as the beam length increases, both curves tend to reduce to the case of laterally restrained columns.

The two cases of frames with no lateral restraints or with restraints at beam-column nodes only (with column bases free to warp) were re-analyzed by developing a 3-D plate-shell FE model (STRAUS7® 2004, Fig. 3.19). The two nodal forces were applied as uniform stress distributions at the beam end sections. As a matter of fact, the 3-D model was able to capture local instability at the column bases and in the proximity of the beam ends. Hence, the buckling load estimate was slightly lower (≤ 5%) than the corresponding beam solution.

3.11.1.2 Influence of shear deformations

The portal frame of Figure 3.16 was again analyzed, for an increasing beam length, adopting a wide-flange pultruded profile with cross-section dimensions: $H = B = 203.2$ mm, $t = 9.5$ mm. Lateral restraints were placed at the beam-column joints only and no warping restraint was introduced at all. In order to put in evidence the influence of shear deformations, the critical load was evaluated in both cases (Fig. 3.20) of glass-FRP profiles ($E = 25$ GPa, $G = E/10$) and carbon-FRP profiles ($E = 144$ GPa, $G = E/35$). It can be noted that, for $l = h = 3$ m, neglecting shear deformations overestimates the buckling load by about 10% for GFRP profiles and by about 44% for CFRP profiles.

3.11.1.3 Influence of the out-of-plane bracing systems at the beam-column nodes

The role of the out-of-plane bracing systems is simulated by two springs of variable stiffness located at nodes B and C of the portal frame of Figure 3.16.
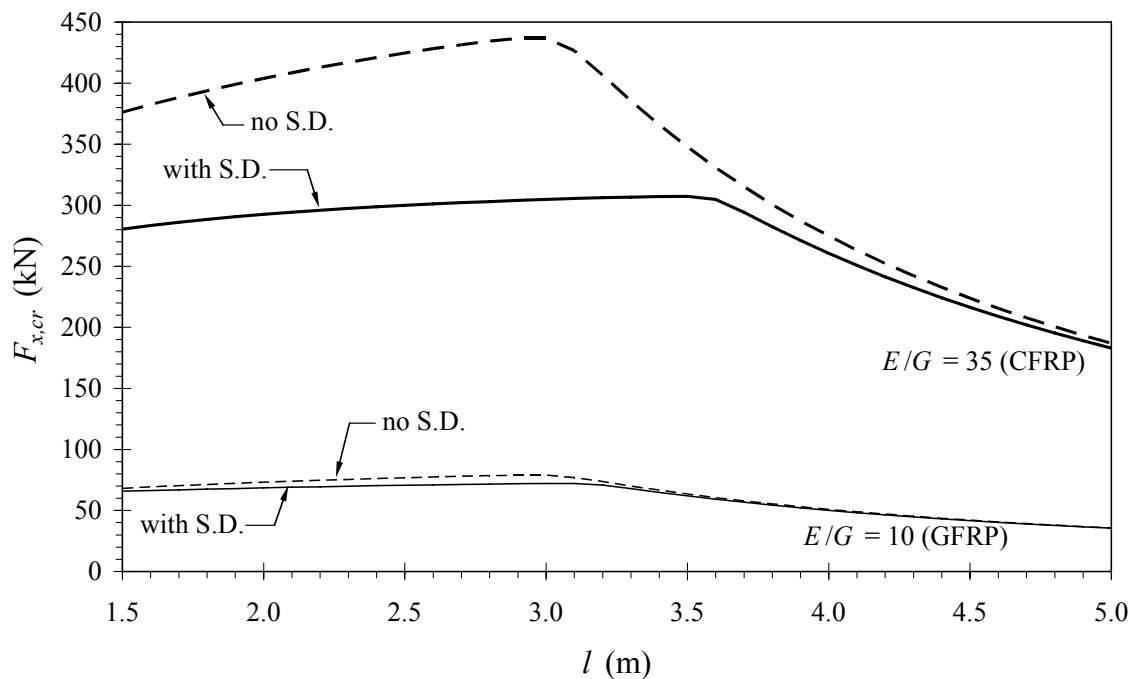

Figure 3.20. Portal frame of Fig. 3.16 adopting wide-flange GFRP and CFRP I-profiles. Critical horizontal forces vs. beam length. Results with or without shear deformations (S.D.).
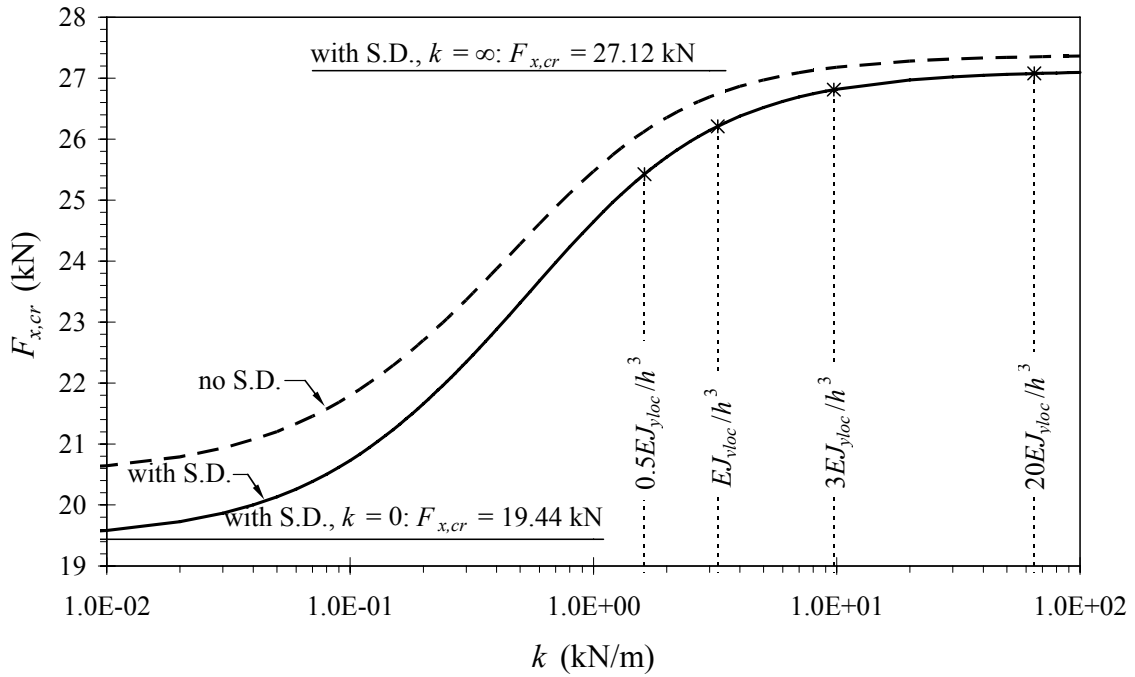
Figure 3.21. Critical horizontal forces of the portal frame of Fig. 3.16, for the
case $l = h = 3$ m, vs. stiffness of out-of-plane springs acting at the beam-column joints.
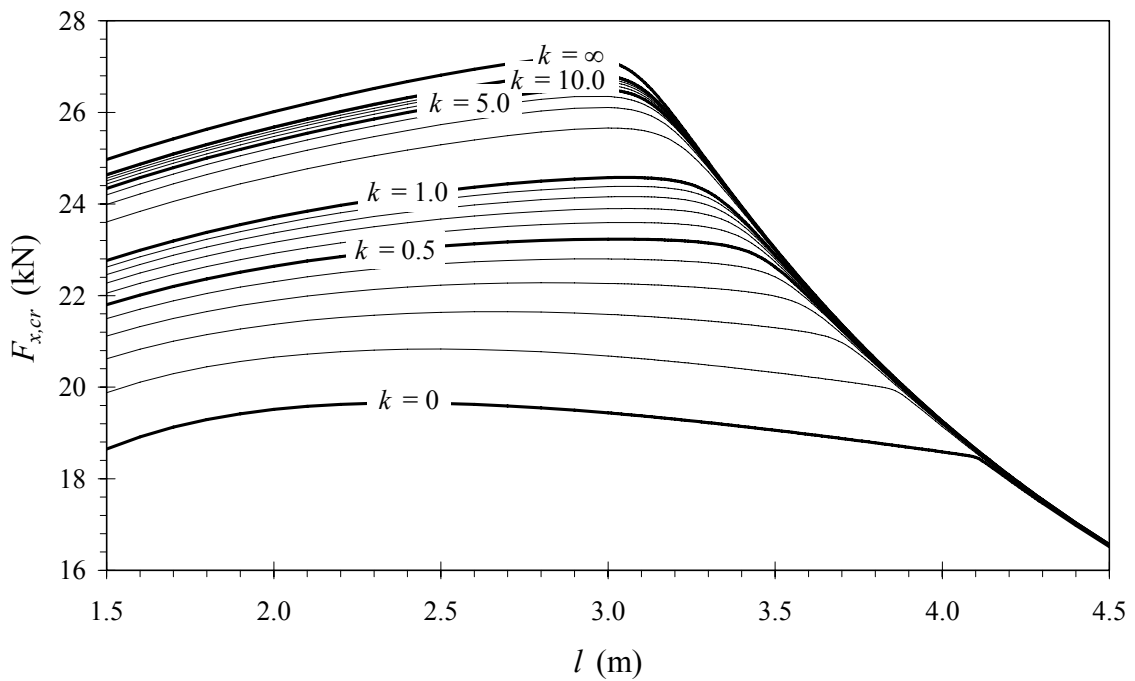

Figure 3.22. Critical horizontal forces vs. beam length for many values
of stiffness k (kN/m) of the out-of-plane springs acting at the beam-column joints.

GFRP I-profiles (E/G = 10) with cross-section dimensions: H = 240.0 mm, B = 120.0 mm, t = 12.0 mm were adopted. Again, no warping restraint was introduced. In Figure 3.21, critical horizontal forces for $l = h$ = 3 m are reported versus the spring stiffness k (logarithmic scale). The buckling load ranges from F_x = 19.44 kN (unbraced frame) to F_x = 27.12 kN (rigidly braced frame), corresponding to an increment of about 40%. It can be seen that, for $k > 3\,EJ_{yloc}\big/h^3$, lateral restraints substantially act as if they were rigid supports.

Figure 3.22 shows the frame buckling loads versus the beam length, for different values of the out-of-plane spring stiffness. The curves corresponding to $k = 0$ and $k = \infty$ can be easily found in Figure 3.17.

3.11.2 Portal frame subjected to horizontal and vertical loads uniformly distributed along the beam

The critical interaction curves of a portal frame subjected to horizontal and vertical loads (Fig. 3.23), under different constraint conditions, are presented. GFRP-pultruded wide-flange profiles (E = 25 GPa, $G = E$/10) were adopted, having cross-section dimensions: $H = B$ = 203.2 mm, t = 9.5 mm. Again, the major inertia axis was assumed to be orthogonal to the frame plane and no warping restraint was introduced. The vertical load was applied at the top flange of the beam. Two span/height ratios: l/h = 2/3 and l/h = 3/2, and four different lateral restraint conditions were considered. Four beam finite elements for each member were adopted.

3.11.2.1 Interaction curves for l = 2 m, h = 3 m

Thin dashed curve of Figure 3.24 represents buckling interaction between horizontal and vertical loads when lateral column displacements are prevented. Because of the constraint conditions, instability is mainly governed by the vertical load and, consequently, the frame buckles with a torsional-flexural (one half wave) mode of the beam (Fig. 3.25a).

The dash-dot curve of Figure 3.24 represents buckling interaction when the beam lateral displacements are prevented. In this case, high vertical loads cause columns symmetrical buckling (Fig. 3.25b1), whereas, prevailing horizontal loads give a mode shape ruled by the flexural-torsional buckling of the compressed column only (Fig. 3.25b2).
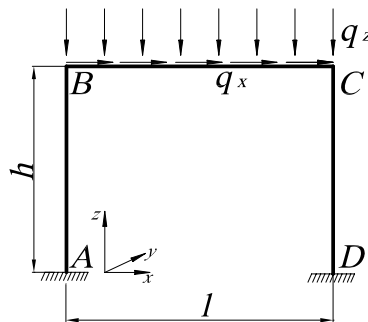

Figure 3.23. Portal frame subjected to horizontal and vertical loads distributed along the beam. l = 2 m, h = 3 m (§ 3.11.1.1); l = 3 m, h = 2 m (§ 3.11.1.2).
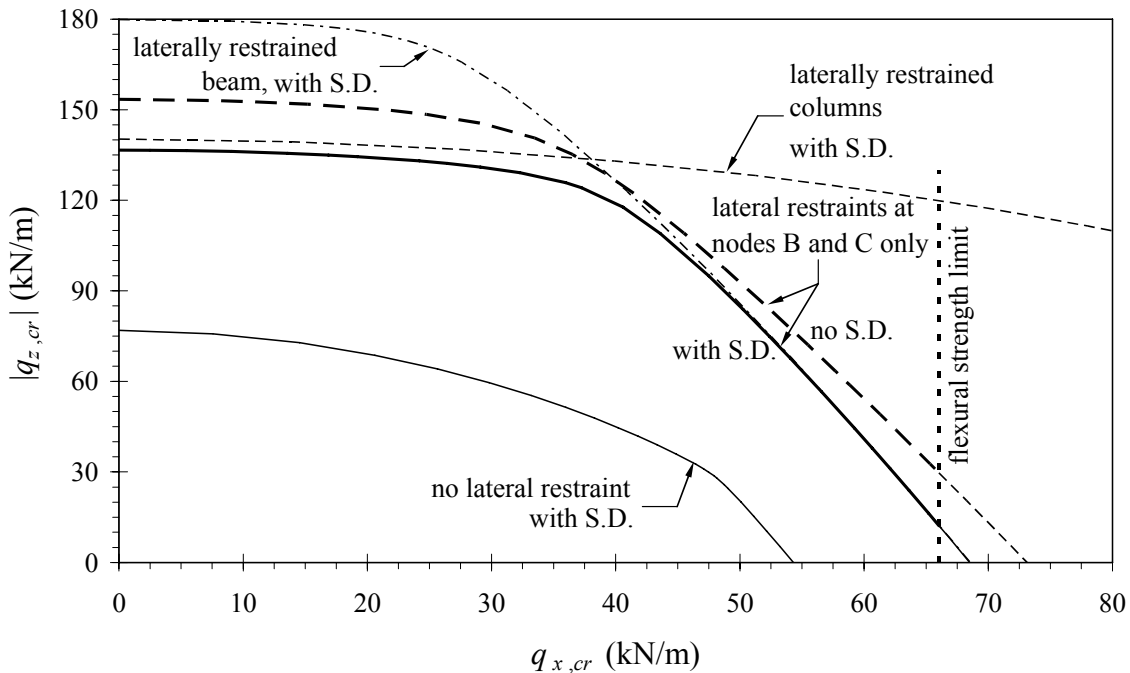
Figure 3.24. Portal frame of Fig. 3.23, with l = 2 m and h = 3 m. Critical interaction between vertical and horizontal loads. Comparison between different lateral restraint conditions. Influence of shear deformations is evaluated for the case of lateral restraints at nodes B and C only. Material strength limit: 250 MPa.

The third case illustrates the frame buckling when lateral restraints are acting at the beam-column joints only. Thick solid and dashed curves of Figure 3.24 refer to cases accounting for shear deformations or not.

Finally, removing the lateral restraints at the beam-column joints decreases the buckling load of about 45% for q_x = 0 and of about 22% for q_z = 0 (thin solid curve of Fig. 3.24). In this case, prevailing vertical or horizontal loads give symmetrical (Fig. 3.25c1) and antisymmetrical (Fig. 3.25c2) mode shapes, respectively. Vertical dotted line (Fig. 3.24) indicates the flexural limit corresponding to material strength of 250 MPa.

3.11.2.2 Interaction curves for l = 3 m, h = 2 m

With the exception of the case with laterally restrained beam, all curves are close to each other (Fig. 3.26). In particular, if the beam lateral displacements are not totally restrained, the buckling mode essentially involves lateral-torsional displacements of the beam itself, associated with column torsional rotations. Prevailing vertical or horizontal loads give symmetrical (Fig. 3.27a) or antisymmetrical (Fig. 3.27b) beam buckling shape. The vertical dotted line of Figure 3.26 indicates the flexural strength limit (250 MPa).
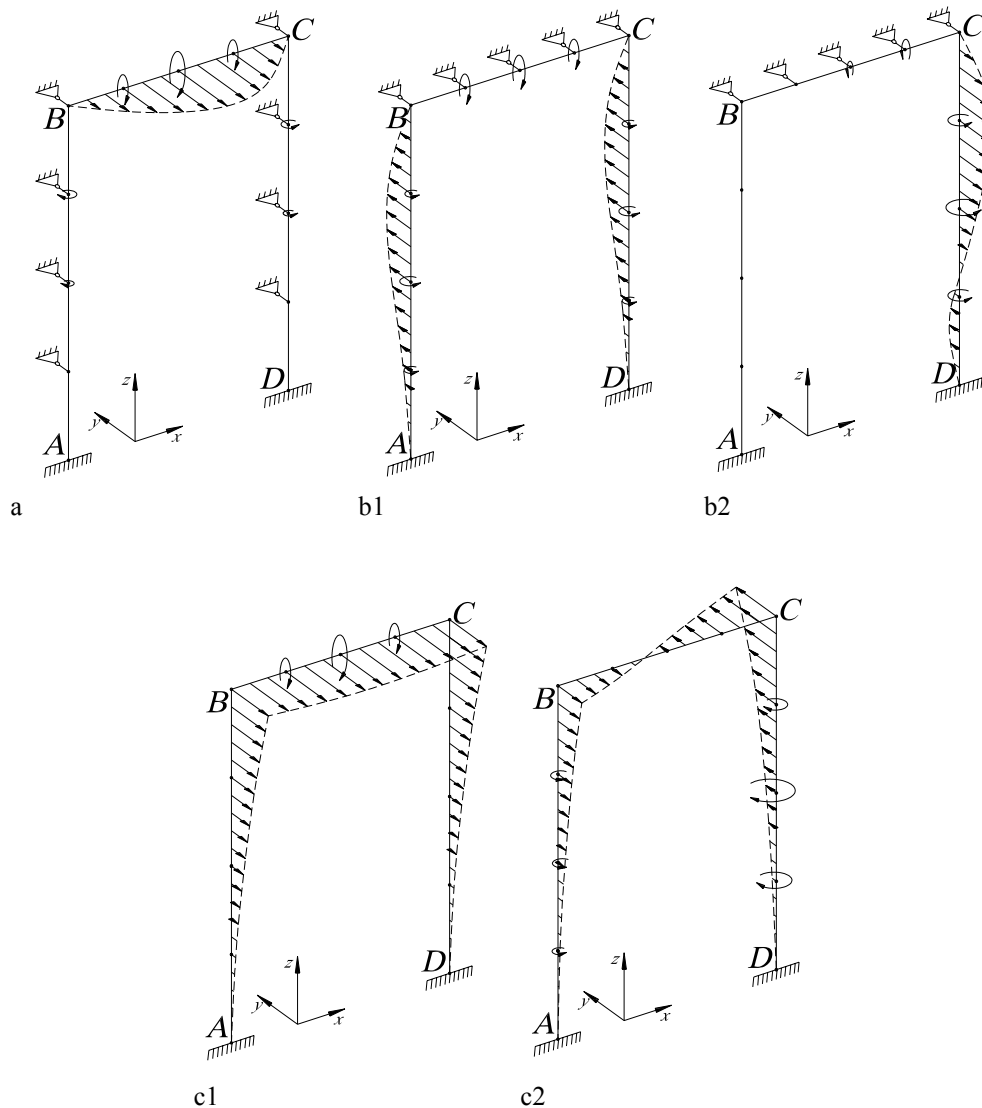
Figure 3.25. Mode shapes of the portal frame of Fig. 3.23 ($l = 2$ m, $h = 3$ m) for different out-of-plane restraint conditions. Straight and circular arrows indicate lateral displacements (y direction) and torsional rotations, respectively. a: laterally restrained columns; b1: laterally restrained beam (predominance of vertical load); b2: laterally restrained beam (predominance of horizontal load); c1: no lateral restraint (predominance of vertical load); c2: no lateral restraint (predominance of horizontal load).

3.11.3 Three-bay frame subjected to a uniformly distributed (wind-type) lateral load and to a vertical load uniformly distributed along the beam

A three-bay, cable-carrying, pultruded frame is finally presented. The beam has a C-shaped cross-section, whereas columns are wide-flange I-profiles (Fig. 3.28). Both columns and beam are bent in the weak plane when subjected to in-plane loads (y_{loc} axis is parallel to y global axis). Columns are fully clamped at the base and free to warp at

both ends. At nodes E, F, G and H, full continuity of rotations and displacements is imposed between beams and columns. The out-of-plane displacements are prevented at joints E and H only.
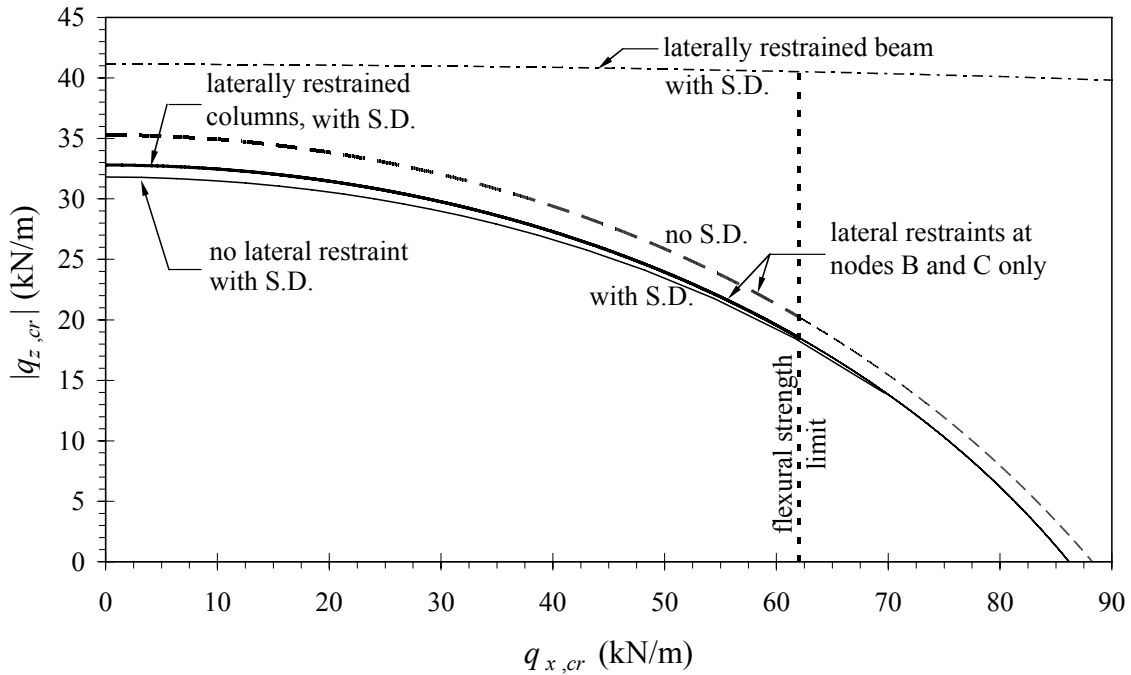

Figure 3.26. Portal frame of Fig. 3.23 with $l = 3$ m and $h = 2$ m. Critical interaction between vertical and horizontal loads. Comparison between different lateral restraint conditions. Influence of shear deformations is evaluated for the case of lateral restraints at nodes B and C only. Material strength limit: 250 MPa.
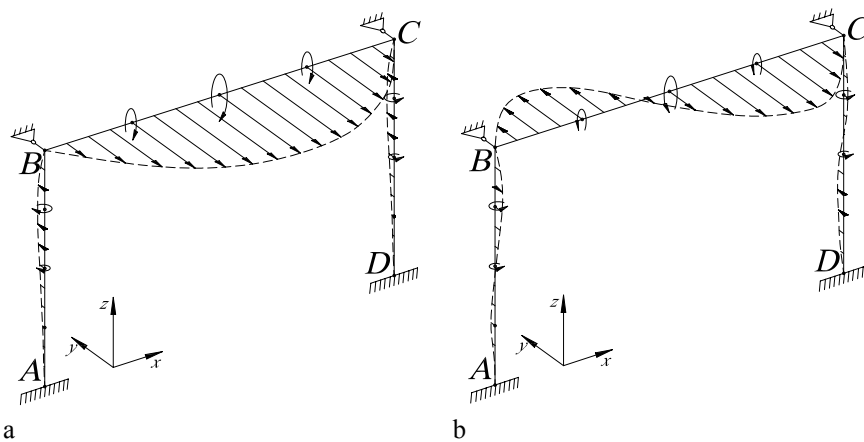

Figure 3.27. Mode shapes of the portal frame of Fig. 3.23 ($l = 3$ m, $h = 2$ m) with constraints acting at column-beam nodes only. Straight and circular arrows indicate lateral displacements (y direction) and torsional rotations, respectively. a: predominance of vertical load; b: predominance of horizontal load.

a: no stiffeners, uniformly distributed vertical and lateral loads.

b: stiffeners at the central bay, same loads as in Fig. 3.28a.
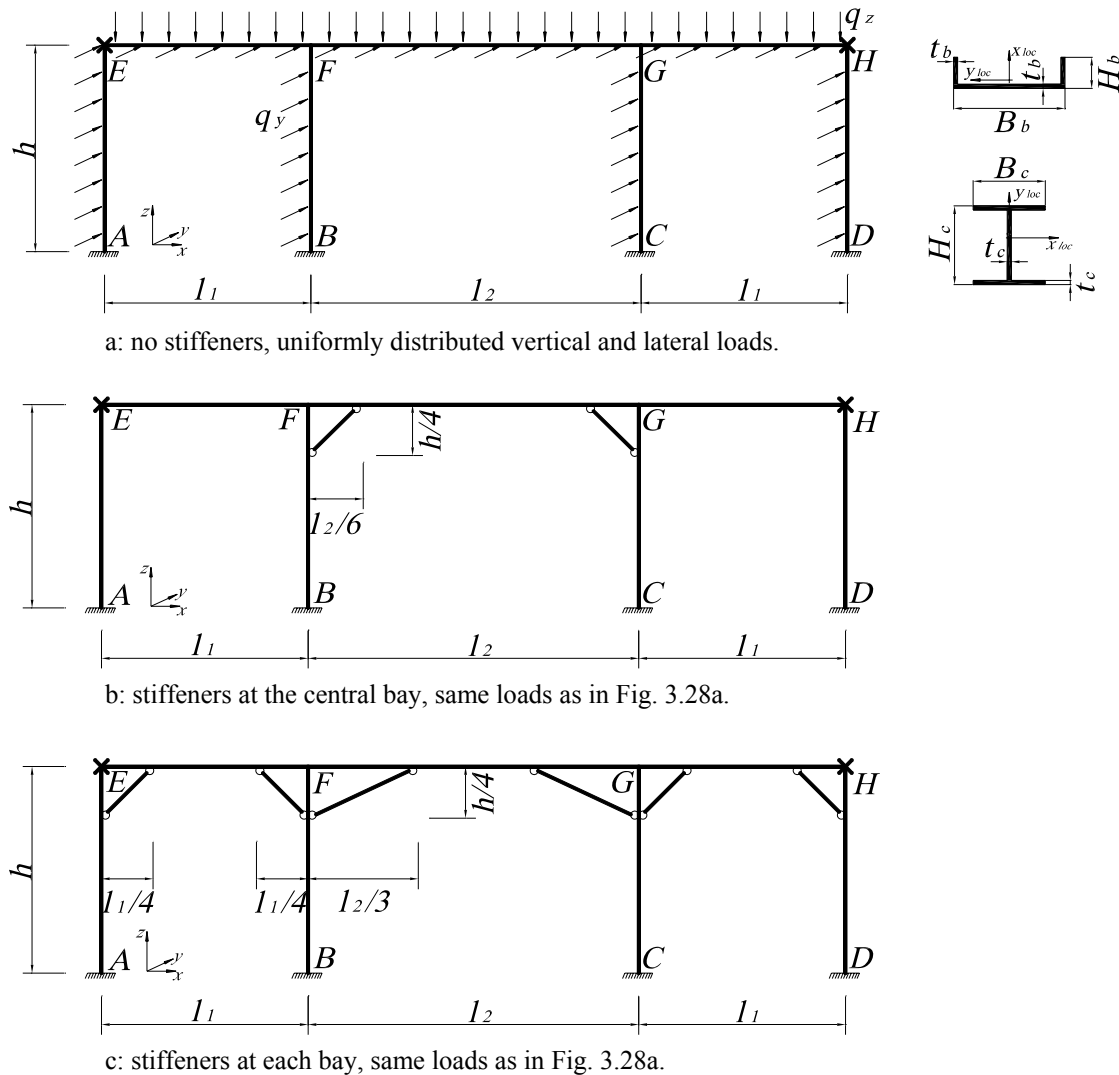

c: stiffeners at each bay, same loads as in Fig. 3.28a.

Figure 3.28. Three-bay frame ($h = l_1 = 2.5$ m, $l_2 = 4.0$ m) subjected to a uniformly distributed lateral load and to a vertical load acting along the beam. C-shaped beam cross-section: $B_b = 300$ mm, $H_b = 80$ mm, $t_b = 10$ mm. Wide-flange I-shaped column cross-section: $B_c = 203.2$ mm, $H_c = 203.2$ mm, $t_c = 9.5$ mm. Stiffener cross-section: hollow square tubes 101.6–101.6–6.4 mm.

A uniform lateral load acting on the whole frame was considered. Moreover, a vertical load was uniformly applied along the beam EH. The frame buckling was analyzed for the three cases shown in Figure 3.28. Four beam finite elements were adopted for beams EF and GH, and for columns, whereas six elements were used for beam FG. The stiffeners, having hollow square section, were modelled using truss-type elements.

The critical load interaction curves for the three configurations are summarized in Figure 3.29. In all cases, for predominant lateral loads, buckling is governed by beam flexural-torsional instability, i.e.: beam deflection into the vertical (weak) plane coupled with torsion. In turn, due to the presence of one single symmetry axis, torsion is

necessarily coupled with flexure into the plane of major stiffness (*x*-*y*). Viceversa, when the vertical load prevails, columns BF and CG tend to buckle out of the frame plane taking the beam along.

Figure 3.29 shows that the stiffeners significantly increase the buckling load only in the case of predominant lateral forces. It should be remembered that the members present the minimum second moment of area into the frame plane and, consequently, in the presence of vertical loads, the beam can reach the flexural strength limit before buckling takes place. Horizontal lines of Figure 3.29 indicate, for the three configurations of Figure 3.28, the flexural collapse ruled by material strength.
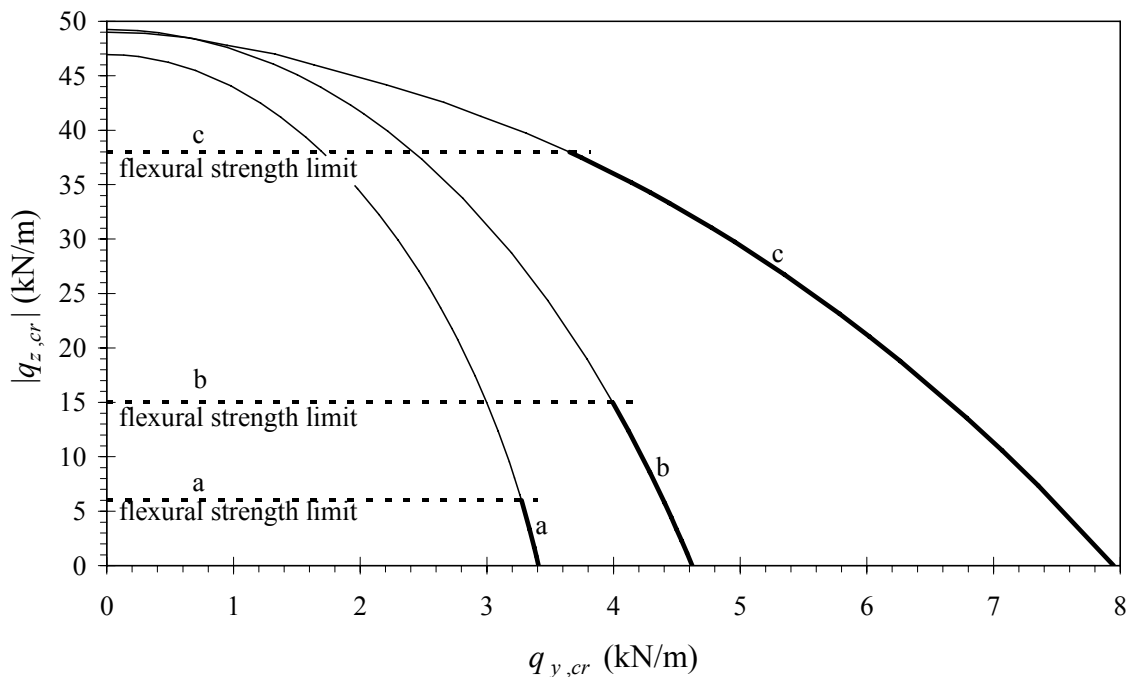

Figure 3.29. Critical load interaction for the three-bay pultruded frame of Fig. 3.28 ($E/G = 10$). Horizontal dashed lines correspond to material strength limit (250 MPa).

3.12 Conclusions

A simple and effective thin-walled beam model for buckling analysis of FRP structures was proposed. The beam kinematics is based on a second-order approximation of the displacement field, accounting for the shear strain effects on both nonuniform bending and torsion. A proper coordinate transformation is adopted in deriving the finite rotation tensor so as to make the bending deformation shear centre coordinates explicit and, consequently, to allow for the analysis of beams with any given cross-section. The linear part of the kinematics adopted coincides with Timoshenko-Reissner's beam theory.

The energy criterion was based on the positive definiteness of the second variation of the total potential energy. The adopted expression for the second-order work of

external forces holds for generic surface loads and accounts for the actual load position with respect to the shear centre.

The displacement field was interpolated by means of two-node *locking-free* finite elements of the Hermitian family (*H*32, see § 2.2.1). Such numerical formulation does not contain inner nodes and, consequently, offers computational advantages with respect to the numerical models adopting cubic and quadratic Lagrangian shape functions (see § 2.2.2). Moreover, for buckling analysis in the absence of shear deformations, the elastic and geometric stiffness matrices may be reduced to those of a classical Bernoulli-Euler-Vlasov model. The element geometric stiffness matrix for two particular load conditions is reported in Appendix 3.A.

Convergence rate and accuracy of the formulation adopted were analyzed with reference to thin-walled composite profiles under different load and restraint conditions. It was observed that one single finite element yields very accurate estimates of the flexural-torsional buckling load of an orthotropic cantilever C-shaped FRP profile subjected to an axial load. Furthermore, two elements proved to give very accurate estimates of the buckling load for shear-flexible beams under lateral loads over a wide range of beam slenderness. The model proposed was then applied to the stability analysis of pultruded frames. The occurrence of different buckling modes, depending on span to height ratio and to lateral restraint conditions, was also discussed. The influence of shear deformations was then pointed out and, in the case of carbon profiles, reductions of the buckling load up to 45% were obtained. It was also shown that, in the case of horizontally loaded GFRP frames, restraining warping at the column base can significantly increase (+ 40%) the critical load.

Appendix 3.A – Geometric stiffness matrix of element *H*32

The 14×14 geometric stiffness matrix of *H*32 element (see § 2.2.1) can be posed in the following form:

$$
\mathbf{K}_G^{H32} = \begin{bmatrix} \mathbf{0} & \mathbf{0} & \mathbf{0} & \mathbf{0} \\ & \mathbf{K}_G^{u} & \mathbf{K}_G^{uv} & \mathbf{K}_G^{u\omega} \\ & & \mathbf{K}_G^{v} & \mathbf{K}_G^{v\omega} \\ \text{Sym} & & & \mathbf{K}_G^{\omega} \end{bmatrix}
\tag{3.A.1}
$$

in which the submatrices lying on the main diagonal are obviously symmetrical.

3.A.1 Axial load

In the presence of a centroidal axial load N^0, submatrix $\mathbf{K}_G^{u}$ appearing in Eq. (3.A.1) is given by:

$$K_{G,11}^{u} = K_{G,33}^{u} = -K_{G,13}^{u} = -N^0 \frac{\left(5\phi_x^2 + 10\phi_x + 6\right)}{5l\left(1+\phi_x\right)^2} \tag{3.A.2}$$

$$K_{G,12}^{u} = K_{G,14}^{u} = -K_{G,23}^{u} = -K_{G,34}^{u} = -N^0 \frac{1}{10\left(1+\phi_x\right)^2} \tag{3.A.3}$$

$$K_{G,22}^{u} = K_{G,44}^{u} = -N^0 \frac{l\left(5\phi_x^2 + 10\phi_x + 8\right)}{60\left(1+\phi_x\right)^2} \tag{3.A.4}$$

$$K_{G,24}^{u} = N^0 \frac{l\left(5\phi_x^2 + 10\phi_x + 2\right)}{60\left(1+\phi_x\right)^2} \tag{3.A.5}$$

Moreover, $\mathbf{K}_G^{uv} = \mathbf{0}$ whereas matrix $\mathbf{K}_G^{u\omega}$ is given by:

$$K_{G,11}^{u\omega} = K_{G,33}^{u\omega} = -K_{G,13}^{u\omega} = -K_{G,31}^{u\omega} = -N^0 \frac{y_S\left(5\phi_x\phi_\omega + 5\phi_x + 5\phi_\omega + 6\right)}{5l\left(1+\phi_x\right)\left(1+\phi_\omega\right)} \tag{3.A.6}$$

$$\begin{aligned}
K_{G,12}^{u\omega} = -K_{G,21}^{u\omega} &= K_{G,14}^{u\omega} = -K_{G,41}^{u\omega} = K_{G,23}^{u\omega} \\
&= -K_{G,32}^{u\omega} = -K_{G,34}^{u\omega} = K_{G,43}^{u\omega} = N^0 \frac{y_S}{10\left(1+\phi_x\right)\left(1+\phi_\omega\right)}
\end{aligned} \tag{3.A.7}$$

$$K_{G,22}^{u\omega} = K_{G,44}^{u\omega} = N^0 \frac{y_S l\left(5\phi_x\phi_\omega + 5\phi_x + 5\phi_\omega + 8\right)}{60\left(1+\phi_x\right)\left(1+\phi_\omega\right)} \tag{3.A.8}$$

$$K_{G,24}^{u\omega} = K_{G,42}^{u\omega} = -N^0 \frac{y_S l\left(5\phi_x\phi_\omega + 5\phi_x + 5\phi_\omega + 2\right)}{60\left(1+\phi_x\right)\left(1+\phi_\omega\right)} \tag{3.A.9}$$

Matrix $\mathbf{K}_G^v$ is obtained from $\mathbf{K}_G^u$ replacing ϕ_x with ϕ_y and changing the sign of the terms whose indices give an odd summation integer. Matrix $\mathbf{K}_G^{v\omega}$ is obtained from $\mathbf{K}_G^{u\omega}$ changing the sign of the first and third row and replacing ϕ_x with ϕ_y, and y_S with x_S. Finally, $\mathbf{K}_G^\omega$ is obtained from $\mathbf{K}_G^u$ multiplying by C_N, replacing ϕ_x with ϕ_ω and changing the sign of the terms with an odd summation of indices.

In the absence of shear deformations $\phi_x = \phi_y = \phi_\omega = 0$ and, consequently, $\mathbf{K}_G$ reduces to the geometric stiffness matrix commonly used for detecting the buckling axial load of Euler-Bernoulli-Vlasov's element (Barsoum & Gallagher 1970).

3.A.2 Uniformly distributed lateral load

When pre-critical conditions are ruled by bending in the *y-z* (principal) plane caused by an external load q_y uniformly distributed along the element, $\mathbf{K}_G^u = \mathbf{K}_G^{v\omega} = \mathbf{0}$. Moreover, referring the internal stress resultants to node 1 of the finite element (i.e.: M_{x1}^0, V_{y1}^0), matrix $\mathbf{K}_G^{uv}$ is given by:

$$K_{G,11}^{uv} = K_{G,33}^{uv} = -K_{G,13}^{uv} = -K_{G,31}^{uv} = \frac{6q_y x_S}{5l\left(1+\phi_x\right)\left(1+\phi_y\right)} \tag{3.A.10}$$

$$K_{G,12}^{uv} = -K_{G,32}^{uv} = \frac{\left[q_y l\left(5\phi_y - 7\right) - 20\left(1+\phi_y\right)V_{y1}^0\right]x_S}{20l\left(1+\phi_x\right)\left(1+\phi_y\right)} \tag{3.A.11}$$

$$K_{G,14}^{uv} = -K_{G,34}^{uv} = \frac{\left[q_y l\left(25\phi_y + 13\right) + 20\left(1+\phi_y\right)V_{y1}^0\right]x_S}{20l\left(1+\phi_x\right)\left(1+\phi_y\right)} \tag{3.A.12}$$

$$K_{G,21}^{uv} = -K_{G,23}^{uv} = -\frac{\left[3q_y l\left(5\phi_x + 1\right) + 20\left(1+\phi_x\right)V_{y1}^0\right]x_S}{20l\left(1+\phi_x\right)\left(1+\phi_y\right)} \tag{3.A.13}$$

$$K_{G,22}^{uv} = -\frac{\left[q_y l\left(40\phi_x\phi_y - 5\phi_x + 25\phi_y + 16\right) + 60\left(1+\phi_x\phi_y + 2\phi_y\right)V_{y1}^0\right]x_S}{120\left(1+\phi_x\right)\left(1+\phi_y\right)} \tag{3.A.14}$$

$$K_{G,24}^{uv} = \frac{\left[q_y l\left(-50\phi_x\phi_y - 5\phi_x + 25\phi_y + 34\right) - 60\left(\phi_x\phi_y - 1\right)V_{y1}^0\right]x_S}{120\left(1+\phi_x\right)\left(1+\phi_y\right)} \tag{3.A.15}$$

$$K_{G,41}^{uv} = -K_{G,43}^{uv} = \frac{\left[q_y l\left(5\phi_x + 17\right) + 20\left(1+\phi_x\right)V_{y1}^0\right]x_S}{20l\left(1+\phi_x\right)\left(1+\phi_y\right)} \tag{3.A.16}$$

$$K_{G,42}^{uv} = \frac{\left[q_y l\left(10\phi_x\phi_y - 5\phi_x + 25\phi_y - 26\right) + 60\left(\phi_x\phi_y - 1\right)V_{y1}^0\right]x_S}{120\left(1+\phi_x\right)\left(1+\phi_y\right)} \tag{3.A.17}$$

$$K_{G,44}^{uv} = \frac{\left[q_y l\left(20\phi_x\phi_y + 5\phi_x + 95\phi_y + 44\right) + 60\left(\phi_x\phi_y + 2\phi_y + 1\right)V_{y1}^0\right]x_S}{120\left(1+\phi_x\right)\left(1+\phi_y\right)} \tag{3.A.18}$$

Matrix $\mathbf{K}_G^{u\omega}$ is given by:

$$K_{G,11}^{u\omega} = K_{G,33}^{u\omega} = -K_{G,13}^{u\omega} = -K_{G,31}^{u\omega}$$

$$= \frac{28M_{x1}^0\left(5\phi_x\phi_\omega + 5\phi_x + 5\phi_\omega + 6\right) + l\left[14V_{y1}^0 - q_y l\left(7\phi_\omega + 2\right)\right]}{140l\left(1+\phi_x\right)\left(1+\phi_\omega\right)} \tag{3.A.19}$$

$$K_{G,12}^{u\omega} = -K_{G,32}^{u\omega} = \frac{-28M_{x1}^0 + l\left[14V_{y1}^0\phi_\omega + q_y l\left(7\phi_\omega + 2\right)\right]}{280\left(1+\phi_x\right)\left(1+\phi_\omega\right)} \tag{3.A.20}$$

$$K_{G,13}^{u\omega} = -\frac{1}{140l\left(1+\phi_x\right)\left(1+\phi_\omega\right)}\Big[28M_{x1}^0\left(5\phi_x\phi_\omega + 5\phi_x + 5\phi_\omega + 6\right)$$
$$+14V_{y1}^0 l\left(10\phi_x\phi_\omega + 10\phi_x + 10\phi_\omega + 11\right) + q_y l^2\left(70\phi_x\phi_\omega + 70\phi_x + 63\phi_\omega + 68\right)\Big] \tag{3.A.21}$$

$$K_{G,14}^{u\omega} = -K_{G,34}^{u\omega} = -\frac{28M_{x1}^0 + l\left[14V_{y1}^0\left(\phi_\omega + 2\right) + q_y l\left(7\phi_\omega + 12\right)\right]}{280\left(1+\phi_x\right)\left(1+\phi_\omega\right)} \tag{3.A.22}$$

$$K_{G,21}^{u\omega} = \frac{1}{840\left(1+\phi_x\right)\left(1+\phi_\omega\right)}\Big[84M_{x1}^0\left(5\phi_x\phi_\omega + 5\phi_x + 5\phi_\omega + 6\right)$$
$$+14V_{y1}^0 l\left(10\phi_x\phi_\omega + 9\phi_x + 10\phi_\omega + 12\right) + q_y l^2\left(35\phi_x\phi_\omega + 28\phi_x + 14\phi_\omega + 22\right)\Big] \tag{3.A.23}$$

$$K_{G,22}^{u\omega} = -\frac{l}{1680\left(1+\phi_x\right)\left(1+\phi_\omega\right)}\Big[28M_{x1}^0\left(5\phi_x\phi_\omega + 5\phi_x + 5\phi_\omega + 8\right)$$
$$+14V_{y1}^0 l\left(5\phi_x\phi_\omega + 4\phi_x + 2\phi_\omega + 4\right) + q_y l^2\left(21\phi_x\phi_\omega + 14\phi_x + 8\right)\Big] \tag{3.A.24}$$

$$K_{G,23}^{u\omega} = -\frac{1}{840\left(1+\phi_x\right)\left(1+\phi_\omega\right)}\Big[84M_{x1}^0 + 14V_{y1}^0 l\left(10\phi_x\phi_\omega + 9\phi_x + 10\phi_\omega + 12\right)$$
$$+ q_y l^2\left(105\phi_x\phi_\omega + 98\phi_x + 84\phi_\omega + 92\right)\Big] \tag{3.A.25}$$

$$K_{G,24}^{u\omega} = \frac{l}{1680\left(1+\phi_x\right)\left(1+\phi_\omega\right)}\Big[28M_{x1}^0\left(5\phi_x\phi_\omega + 5\phi_x + 5\phi_\omega + 2\right)$$
$$+14V_{y1}^0 l\left(5\phi_x\phi_\omega + 6\phi_x + 2\phi_\omega\right) + q_y l^2\left(21\phi_x\phi_\omega + 28\phi_x - 8\right)\Big] \tag{3.A.26}$$

$$K_{G,41}^{u\omega} = \frac{1}{840\left(1+\phi_x\right)\left(1+\phi_\omega\right)}\Big[84M_{x1}^0 - 14V_{y1}^0 l\left(10\phi_x\phi_\omega + 9\phi_x + 10\phi_\omega + 6\right)$$
$$+ q_y l^2\left(35\phi_x\phi_\omega + 28\phi_x + 56\phi_\omega + 34\right)\Big] \tag{3.A.27}$$

$$K_{G,42}^{u\omega} = \frac{l}{1680(1+\phi_x)(1+\phi_\omega)}\Big[28M_{x1}^0\left(5\phi_x\phi_\omega + 5\phi_x + 5\phi_\omega + 2\right)$$
$$+14V_{y1}^0 l\left(5\phi_x\phi_\omega + 4\phi_x + 8\phi_\omega + 4\right) + q_y l^2\left(21\phi_x\phi_\omega + 14\phi_x + 42\phi_\omega + 20\right)\Big] \tag{3.A.28}$$

$$K_{G,43}^{u\omega} = -\frac{1}{840(1+\phi_x)(1+\phi_\omega)}\Big[84M_{x1}^0\left(5\phi_x\phi_\omega + 5\phi_x + 5\phi_\omega + 6\right)$$
$$+14V_{y1}^0 l\left(20\phi_x\phi_\omega + 21\phi_x + 20\phi_\omega + 24\right) + q_y l^2\left(105\phi_x\phi_\omega + 112\phi_x + 84\phi_\omega + 106\right)\Big] \tag{3.A.29}$$

$$K_{G,44}^{u\omega} = -\frac{l}{1680(1+\phi_x)(1+\phi_\omega)}\Big[28M_{x1}^0\left(5\phi_x\phi_\omega + 5\phi_x + 5\phi_\omega + 8\right)$$
$$+14V_{y1}^0 l\left(5\phi_x\phi_\omega + 6\phi_x + 8\phi_\omega + 12\right) + q_y l^2\left(21\phi_x\phi_\omega + 28\phi_x + 42\phi_\omega + 64\right)\Big] \tag{3.A.30}$$

Matrix $\mathbf{K}_G^v$ is given by:

$$K_{G,11}^v = K_{G,33}^v = -K_{G,13}^v = \frac{12 y_S q_y}{5l\left(1+\phi_y\right)^2} \tag{3.A.31}$$

$$K_{G,12}^v = K_{G,14}^v = -K_{G,23}^v = -K_{G,34}^v = \frac{y_S q_y\left(5\phi_y - 1\right)}{5l\left(1+\phi_y\right)^2} \tag{3.A.32}$$

$$K_{G,22}^v = \frac{y_S\left[15V_{y1}^0\left(1+\phi_y\right)^2 + q_y l\left(10\phi_y^2 + 5\phi_y + 4\right)\right]}{15\left(1+\phi_y\right)^2} \tag{3.A.33}$$

$$K_{G,24}^v = \frac{y_S q_y l\left(5\phi_y^2 - 5\phi_y - 1\right)}{15\left(1+\phi_y\right)^2} \tag{3.A.34}$$

$$K_{G,44}^v = -\frac{y_S\left[15V_{y1}^0\left(1+\phi_y\right)^2 + q_y l\left(5\phi_y^2 + 25\phi_y + 11\right)\right]}{15\left(1+\phi_y\right)^2} \tag{3.A.35}$$

Matrix $\mathbf{K}_G^\omega$ is given by:

$$K_{G,11}^{\omega} = K_{G,33}^{\omega} = -K_{G,13}^{\omega} = -\frac{C_x}{210l(1+\phi_\omega)^2}\Big[42M_{x1}^0\left(5\phi_\omega^2+10\phi_\omega+6\right)$$
$$+21V_{y1}^0l\left(5\phi_\omega^2+10\phi_\omega+6\right)+q_yl^2\left(35\phi_\omega^2+63\phi_\omega+36\right)\Big] \tag{3.A.36}$$

$$K_{G,12}^{\omega} = -K_{G,23}^{\omega} = \frac{C_x\Big[84M_{x1}^0+14V_{y1}^0l\left(5\phi_\omega^2+8\phi_\omega+6\right)+q_yl^2\left(35\phi_\omega^2+49\phi_\omega+30\right)\Big]}{840(1+\phi_\omega)^2} \tag{3.A.37}$$

$$K_{G,14}^{\omega} = -K_{G,34}^{\omega} = -\frac{C_x\Big[-84M_{x1}^0+14V_{y1}^0l\left(5\phi_\omega^2+8\phi_\omega\right)+q_yl^2\left(35\phi_\omega^2+63\phi_\omega+12\right)\Big]}{840(1+\phi_\omega)^2} \tag{3.A.38}$$

$$K_{G,22}^{\omega} = -\frac{C_xl}{840(1+\phi_\omega)^2}\Big[14M_{x1}^0\left(5\phi_\omega^2+10\phi_\omega+8\right)$$
$$+7V_{y1}^0l\left(5\phi_\omega^2+6\phi_\omega+4\right)+2q_yl^2\left(7\phi_\omega^2+7\phi_\omega+4\right)\Big] \tag{3.A.39}$$

$$K_{G,24}^{\omega} = \frac{C_xl}{840(1+\phi_\omega)^2}\Big[14M_{x1}^0\left(5\phi_\omega^2+10\phi_\omega+2\right)$$
$$+7V_{y1}^0l\left(5\phi_\omega^2+10\phi_\omega+2\right)+2q_yl^2\left(7\phi_\omega^2+14\phi_\omega+3\right)\Big] \tag{3.A.40}$$

$$K_{G,44}^{\omega} = -\frac{C_xl}{840(1+\phi_\omega)^2}\Big[14M_{x1}^0\left(5\phi_\omega^2+10\phi_\omega+8\right)$$
$$+7V_{y1}^0l\left(5\phi_\omega^2+14\phi_\omega+12\right)+2q_yl^2\left(7\phi_\omega^2+21\phi_\omega+18\right)\Big] \tag{3.A.41}$$

In the case of off-axis loading, some further terms are to be introduced. In particular, indicating with $\left(0, y_q\right)$ the coordinates of the point of application of the external load q_y, the following terms are to be added to the corresponding coefficients of matrix $\mathbf{K}_G^v$ (see Eqs. 3.A.31–3.A.35):

$$K_{G,11}^{v,off} = K_{G,33}^{v,off} = -K_{G,13}^{v,off} = \frac{6q_y\left(y_q-y_S\right)}{5l(1+\phi_y)^2} \tag{3.A.42}$$

$$K_{G,12}^{v,off} = K_{G,14}^{v,off} = -K_{G,23}^{v,off} = -K_{G,34}^{v,off} = \frac{q_y\left(y_q-y_S\right)\left(5\phi_y-1\right)}{10l(1+\phi_y)^2} \tag{3.A.43}$$

$$K_{G,22}^{v,off} = K_{G,44}^{v,off} = \frac{q_y l \left(y_q - y_S\right)\left(10\phi_y^2 + 5\phi_y + 4\right)}{30\left(1 + \phi_y\right)^2} \tag{3.A.44}$$

$$K_{G,24}^{v,off} = \frac{q_y l \left(y_q - y_S\right)\left(5\phi_y^2 - 5\phi_y - 1\right)}{30\left(1 + \phi_y\right)^2} \tag{3.A.45}$$

Finally, the following terms are to be added to the corresponding coefficients of matrix $\mathbf{K}_G^\omega$ (see Eqs. 3.A.36–3.A.41):

$$K_{G,11}^{\omega,off} = K_{G,33}^{\omega,off} = \frac{q_y l \left(y_q - y_S\right)\left(70\phi_\omega^2 + 147\phi_\omega + 78\right)}{210\left(1 + \phi_\omega\right)^2} \tag{3.A.46}$$

$$K_{G,12}^{\omega,off} = -K_{G,34}^{\omega,off} = -\frac{q_y l^2 \left(y_q - y_S\right)\left(35\phi_\omega^2 + 77\phi_\omega + 44\right)}{840\left(1 + \phi_\omega\right)^2} \tag{3.A.47}$$

$$K_{G,13}^{\omega,off} = \frac{q_y l \left(y_q - y_S\right)\left(35\phi_\omega^2 + 63\phi_\omega + 27\right)}{210\left(1 + \phi_\omega\right)^2} \tag{3.A.48}$$

$$K_{G,14}^{\omega,off} = -K_{G,23}^{\omega,off} = \frac{q_y l^2 \left(y_q - y_S\right)\left(35\phi_\omega^2 + 63\phi_\omega + 26\right)}{840\left(1 + \phi_\omega\right)^2} \tag{3.A.49}$$

$$K_{G,22}^{\omega,off} = K_{G,44}^{\omega,off} = \frac{q_y l^3 \left(y_q - y_S\right)\left(7\phi_\omega^2 + 14\phi_\omega + 8\right)}{840\left(1 + \phi_\omega\right)^2} \tag{3.A.50}$$

$$K_{G,24}^{\omega,off} = -\frac{q_y l^3 \left(y_q - y_S\right)\left(7\phi_\omega^2 + 14\phi_\omega + 6\right)}{840\left(1 + \phi_\omega\right)^2} \tag{3.A.51}$$

If shear deformations and displacement components $u^{(2)}$ and $v^{(2)}$ in Eq. 3.74 are neglected, the stiffness matrix $\mathbf{K}_G$ reduces to the geometric matrix reported by Barsoum & Gallagher (1970) as well.

Chapter 4

Vibration analysis including second-order effects

4.1 Introduction

The influence of initial stresses on the dynamic response of structural systems may be of great importance. To evaluate natural frequencies of axially-loaded beams with various constraint conditions, Euler-Bernoulli and Timoshenko beam theories were widely used to determine closed-form solutions (Bokaian 1988, Bokaian 1990, Abramovich 1992, Farchaly & Shebl 1995) or to formulate numerical models (Kosmatka 1995). The effects of rotatory inertia and shear deformations on bending natural frequencies and the corresponding mode shapes were extensively investigated and the discrepancies between the two mentioned theories were emphasized especially for higher modes (Abramovich & Ekishakoff 1990, Kosmatka 1995, Han *et al.* 1999, Renton 2001). For laminated composite beams, higher-order models (Ghugal & Shimpi 2001) are needed to predict local effects, but they do not show significant improvements, with respect to the classical Timoshenko theory, when global effects are to be evaluated, like buckling loads and natural vibration frequencies (Song & Waas 1997, Eisenberger 2003).

Present symbolic computing packages enabled several authors (Banerjee *et al.* 1996, Tanaka & Bercin 1999, Banerjee 2000) to obtain important closed-form solutions in terms of vibration frequencies and mode shapes, even for thin-walled beams with monosymmetric or nonsymmetric cross-sections. However, Euler-Bernoulli-Vlasov's beam theory was generally adopted and shear strain effects were consequently neglected. Furthermore, only geometrical effects due to axial loads were generally considered. In recent years, many researchers, already mentioned in the previous chapter, developed accurate beam models for dynamic and buckling analysis of FRP profiles with symmetrical (Cortínez & Piovan 2006) or generic lay-up (Piovan & Cortínez 2007, Kim *et al.* 2007a,b). Howson & Williams (1973) presented in-plane vibration analyses of frames with axially loaded columns by making use of Timoshenko beam model. Yet, to the author's knowledge, no works were specifically oriented into flexural-torsional vibration analyses of FRP beam assemblages, where the high ratio between longitudinal and transverse elastic moduli makes shear strain influence particularly significant and additional masses produce strong reductions of vibration frequencies.

In this chapter, an extensive vibration analysis of FRP (thin-walled) beam assemblages is presented. As for the beam model, the quadratic displacement field presented in Chapter 3 (Chang *et al.* 1996, Cortínez & Piovan 2006, Minghini *et al.* 2008a) is adopted. Shear strain effects due to both nonuniform bending and torsion are consequently accounted for. The motion equations are derived from Hamilton's principle where second-order effects due to axial and lateral concentrated or distributed surface loads are considered. Stiffness and mass matrices are consistently derived interpolating the displacement field by means of the *locking-free* Hermitian polynomials presented in Chapter 2 (element *H*32, Minghini *et al.* 2007). As for plane problems, Kosmatka (1995) showed the high performances of these shape functions in flexural vibration analyses. On the other hand, element *H*32 has not previously been tested for flexural-torsional vibrations. Hence, the first goal of the present chapter is to emphasize convergence rate and accuracy of the *locking-free* Hermitian element *H*32 in vibration analysis of FRP composite profiles with nonsymmetric cross-section, for which coupling between shear and nonuniform torsion arises due to shear deformations (see Chapter 1). The second goal of this chapter is to analyse vibration frequencies and mode shapes of FRP pultruded portal frames. The plots of the natural frequencies versus the external load uniformly distributed along the beam reveal a frequency crossing between first and second vibration modes. This phenomenon is shown to be ruled by frame span-to-height ratios, beam cross-section shapes and participating additional masses. Particular attention is paid to the influence of shear deformations and to geometric nonlinearities arising from distributed surface loads.

Finally, the vibration analysis of a footbridge with GFRP truss structure is presented, showing the influence of the masses associated to pedestrian traffic on the first two natural frequencies. Once again, the corresponding mode shapes are reported and commented.

The analyses presented in the following has been recently reported in two papers of Minghini *et al.* (2008b,c).

4.2 Problem statement

The beam kinematical model adopted is the same as in the previous chapter and, omitting basic assumptions and significance of symbols, is reported in the following for sake of clarity (quadratic terms in square brackets):

$$u(z,s) = u^{(1)} + u^{(2)}$$

$$= u_S(z) - \varphi_z(z)(y - y_S) \tag{4.1}$$

$$+ \frac{1}{2}\left[-\left(\varphi_y^2(z) + \varphi_z^2(z)\right)x + \varphi_x(z)\varphi_y(z)y + \varphi_z^2(z)x_S \right]$$

$$
\begin{aligned}
v(z,s) &= v^{(1)} + v^{(2)} \\
&= v_S(z) + \varphi_z(z)(x - x_S) \\
&\quad + \frac{1}{2}\Big[\varphi_x(z)\varphi_y(z)x - \big(\varphi_x^2(z) + \varphi_z^2(z)\big)y + \varphi_z^2(z)y_S\Big]
\end{aligned}
\tag{4.2}
$$

$$
\begin{aligned}
w(z,s) &= w^{(1)} + w^{(2)} \\
&= w_C(z) - x\varphi_y(z) + y\varphi_x(z) + \omega(s)\Psi(z) \\
&\quad + \frac{1}{2}\Big[\varphi_x(z)\varphi_z(z)(x - x_S) + \varphi_y(z)\varphi_z(z)(y - y_S)\Big]
\end{aligned}
\tag{4.3}
$$

Due to in-plane cross-section undeformability and small thickness, ε_z and $\gamma_{zs} = 2\varepsilon_{zs}$ turn out to be the only non-vanishing components of Green's strain tensor:

$$
\varepsilon_{ij} = \varepsilon_{ij}^{(1)} + \varepsilon_{ij}^{(2)} = \frac{1}{2}\big(u_{i,j}^{(1)} + u_{j,i}^{(1)}\big) + \frac{1}{2}\big(u_{k,i}^{(1)}u_{k,j}^{(1)} + u_{i,j}^{(2)} + u_{j,i}^{(2)}\big)
\tag{4.4}
$$

In evaluating analytically flexural-torsional vibrations of FRP composite beams, Piovan and Cortínez (2005) also considered the in-thickness shear strain γ_{zn}, stating that such contribution leads to very accurate frequency values provided that Hellinger-Reissner's variational principle is adopted to devise the problem governing equations. In fact, they observed that using the virtual work theorem gives rise to an overprediction of the frequency values if shear strain component γ_{zn} is included, whereas acceptable results are obtained in the absence of γ_{zn}. On the other hand, in the approach based on the virtual work theorem, they had not introduced shear correction factors in the evaluation of the shear flows, and this seems to be the main reason of the inadequate beam stiffness observed. Even if the model adopted in the present work neglects the contribution of γ_{zn}, it will be shown (see § 4.3) that accurate frequency values are obtained when shear correction factors (contained in coefficients D_{ij} of Eq. 1.51) are introduced, revealing that the in-thickness shear strain does not play a significant role in global vibration analysis.

4.2.1 Variational formulation

The equation of motion is obtained using Hamilton's principle which, for a vibrating system subjected to conservative loads, can be written in the form:

$$
\delta H = \int_{t_1}^{t_2} \big(\delta U + \delta V^0 - \delta T - \delta W_e\big)dt = 0
\tag{4.5}
$$

where U, V^0, T and W_e respectively represent the strain energy, the potential energy associated to initial stresses and external loads, the kinetic energy and, finally, the work done by external incremental loads. In particular, functionals U and V^0 for a shear-deformable thin-walled beam, respectively derived in Chapter 3 (Eqs. 3.88, 3.90), are reported in the following without further explanations:

$$U = \frac{1}{2} \int_L E \left(A w_C'^2 + J_x \varphi_x'^2 + J_y \varphi_y'^2 + J_\omega \Psi'^2 \right) dz$$

$$+ \frac{1}{2} \int_L G \left[J_t \varphi_z'^2 + D_x \left(u_S' - \varphi_y \right)^2 + D_y \left(v_S' + \varphi_x \right)^2 + D_\omega \left(\varphi_z' + \Psi \right)^2 \right.$$

$$\left. + 2 D_{xy} \left(u_S' - \varphi_y \right) \left(v_S' + \varphi_x \right) + 2 D_{x\omega} \left(u_S' - \varphi_y \right) \left(\varphi_z' + \Psi \right) + 2 D_{y\omega} \left(v_S' + \varphi_x \right) \left(\varphi_z' + \Psi \right) \right] dz$$

(4.6)

$$V^0 = \frac{1}{2} \delta^2 \Pi_G = \frac{1}{2} \int_L \left\{ N^0 \left[u_S'^2 + v_S'^2 - x_S \left(2 v_S' \varphi_z' + \varphi_x \varphi_z' + \varphi_x' \varphi_z \right) \right. \right.$$

$$+ y_S \left(2 u_S' \varphi_z' - \varphi_y \varphi_z' - \varphi_y' \varphi_z \right) + C_N \varphi_z'^2 \right] + M_x^0 \left(\varphi_y' \varphi_z + \varphi_y \varphi_z' - 2 u_S' \varphi_z' + C_x \varphi_z'^2 \right)$$

$$- M_y^0 \left(\varphi_x' \varphi_z + \varphi_x \varphi_z' + 2 v_S' \varphi_z' + C_y \varphi_z'^2 \right) - V_y^0 \left[2 u_S' \varphi_z - \varphi_y \varphi_z - x_S \left(\varphi_x' \varphi_y - \varphi_x \varphi_y' \right) \right]$$

$$+ V_x^0 \left[2 v_S' \varphi_z + \varphi_x \varphi_z - y_S \left(\varphi_x' \varphi_y - \varphi_x \varphi_y' \right) \right] + M_z^0 \left(\varphi_x' \varphi_y - \varphi_x \varphi_y' \right) + M_\omega^0 C_\omega \varphi_z'^2 \right\} dz$$

$$+ \frac{1}{2} \left[V_x^0 x \varphi_y^2 \right]_0^L + \frac{1}{2} \left[V_x^0 \left(x - x_S \right) \varphi_z^2 \right]_0^L - \frac{1}{2} \left[V_x^0 y \varphi_x \varphi_y \right]_0^L$$

$$+ \frac{1}{2} \left[V_y^0 y \varphi_x^2 \right]_0^L + \frac{1}{2} \left[V_y^0 \left(y - y_S \right) \varphi_z^2 \right]_0^L - \frac{1}{2} \left[V_y^0 x \varphi_x \varphi_y \right]_0^L$$

$$- \frac{1}{2} \left[N^0 \left(x - x_S \right) \varphi_x \varphi_z \right]_0^L - \frac{1}{2} \left[N^0 \left(y - y_S \right) \varphi_y \varphi_z \right]_0^L$$

$$+ \frac{1}{2} \int_L \left\{ q_x^0 \left[x \varphi_y^2 - y \varphi_x \varphi_y + \left(x - x_S \right) \varphi_z^2 \right] + q_y^0 \left[y \varphi_x^2 - x \varphi_x \varphi_y + \left(y - y_S \right) \varphi_z^2 \right] \right.$$

$$\left. - q_z^0 \left[\left(x - x_S \right) \varphi_x \varphi_z + \left(y - y_S \right) \varphi_y \varphi_z \right] \right\} dz$$

(4.7)

Making use of linear displacement components $u_i^{(1)}$ (see Eqs. 4.1–4.3), the kinetic energy of the beam can be written as:

$$T = \frac{1}{2} \int_L \left(\int_A \rho \dot{u}_i^{(1)2} dA \right) dz$$

$$= \frac{1}{2} \rho \int_0^L \left[A \left(\dot{u}_S^2 + \dot{v}_S^2 + \dot{w}_C^2 \right) + \left(J_x + J_y + A x_S^2 + A y_S^2 \right) \dot{\varphi}_z^2 \right.$$

$$+ J_x \dot{\varphi}_x^2 + J_y \dot{\varphi}_y^2 + J_\omega \dot{\Psi}^2 + 2 A \dot{\varphi}_z \left(y_S \dot{u}_S - x_S \dot{v}_S \right) \right] dz$$

(4.8)

where ρ is the mass per unit volume and over dot indicates time derivative; the terms $1/2 \rho \int_0^L \left(J_x \dot{\varphi}_x^2 + J_y \dot{\varphi}_y^2 \right) dz$ and $1/2 \rho \int_0^L \left(J_\omega \dot{\Psi}^2 \right) dz$ represent rotary and warping inertia, respectively, and are commonly disregarded in vibration analysis resorting to Euler-Bernoulli-Vlasov's beam model; finally, the last two terms on the right-hand side of Eq. 4.8 give rise to flexural-torsional coupling and vanish for doubly-symmetric cross-sections only.

Functional $W_e = \int_S p_i u_i^{(1)} dS$ of Eq. 4.5 represents the (first-order) work of the external incremental loads p_i ($i = x, y, z$) and vanishes for free vibrating systems.

By means of the formulation presented, dynamic analyses of shear-deformable thin-walled beams with any given cross-section can be performed, also in the presence of geometrical nonlinearities due to conservative external loads. In particular, multilayered orthotropic profiles having the longitudinal axis coinciding with an orthotropy axis (see § 1.4) may be analyzed.

It is worthwhile to remember that expression 4.7 of second-order work holds for generic surface loads and includes the second-order terms accounting for the actual location of the applied loads with respect to the shear centre. If shear deformations are neglected, the functionals 4.6–4.8 reduce to those reported by Kim & Kim (2000).

4.2.2 Finite element formulation

Once again, with reference to a typical two-node finite element, the seven kinematical fields unknown are represented in the approximated form:

$$\mathbf{d}_e = \mathbf{N}\mathbf{q}_e \tag{4.9}$$

where vectors $\mathbf{d}_e$ and $\mathbf{q}_e$ are given by:

$$\mathbf{d}_e^T = \left\{ w_C(z), u_S(z), \varphi_y(z), v_S(z), \varphi_x(z), \varphi_z(z), \Psi(z) \right\} \tag{4.10}$$

$$\mathbf{q}_e^T = \left\{ w_{C1}, w_{C2}, u_{S1}, \varphi_{y1}, u_{S2}, \varphi_{y2}, v_{S1}, \varphi_{x1}, v_{S2}, \varphi_{x2}, \varphi_{z1}, \Psi_1, \varphi_{z2}, \Psi_2 \right\} \tag{4.11}$$

matrix $\mathbf{N}$ collects the selected shape functions in the form:

$$\mathbf{N} = \mathrm{diag}\left[\mathbf{N}^z, \mathbf{N}^x, \mathbf{N}^y, \mathbf{N}^\omega \right] \tag{4.12}$$

and indices "1" and "2" refer to first and second element node, respectively. Under the assumptions of small oscillations, the solution to the free vibration problem can be postulated to be of the form:

$$\mathbf{q} = \overline{\mathbf{q}} e^{i\Omega t} \tag{4.13}$$

where Ω indicates the unknown circular frequency. Taking Eq. 4.13 into account, substituting Eq. 4.9 into Eqs. 4.6–4.8, and the resulting expressions into Eq. 4.5 of Hamilton's principle yield the well known eigenvalue problem:

$$\left(\mathbf{K} - \Omega^2 \mathbf{M} \right) \overline{\mathbf{q}} = \mathbf{0} \tag{4.14}$$

where $\mathbf{M}$ and $\mathbf{K}$ represent the mass and stiffness matrix of the assembled structure, respectively. In particular, if the initial stress state is assumed to be a linear function of applied loads, matrix $\mathbf{K}$ can be written as follows:

$$\mathbf{K} = \mathbf{K}_E + \lambda \mathbf{K}_G \qquad\qquad (4.15)$$

where $\mathbf{K}_E$ and $\lambda \mathbf{K}_G$ are the elastic and geometric stiffness matrix, respectively. The values of Ω satisfying the equation

$$\det(\mathbf{K} - \Omega^2 \mathbf{M}) = 0 \qquad\qquad (4.16)$$

represent the natural (circular) frequencies of the vibrating system.

As in Chapter 2 and 3, polynomial interpolation of the displacement fields unknown is adopted here. In particular, with the exception of the axial displacement w_C, interpolated by means of linear functions, "modified" cubic and quadratic Hermitian polynomials are used (element H32, Section § 2.2.1). Element mass and stiffness matrices are evaluated by means of exact integration so as to obtain a consistent mass matrix $\mathbf{M}$ reported in Appendix 4.A. The consistent mass matrix of the Euler-Bernoulli-Vlasov element is re-obtained by neglecting both shear deformations and rotary inertia terms. Stiffness matrices $\mathbf{K}_E$ and $\mathbf{K}_G$ (for axial and uniformly distributed transversal load) of element H32 are reported in the Appendix 2.A and 3.A, respectively.

As for the external (additional) masses, a lumped formulation is adopted. For example, in the case of an external mass m uniformly distributed along the element, the lumped mass matrix is assumed to be of the form (Kollár 2001b):

$$\mathbf{M}_{lump} = m \begin{bmatrix} \mathbf{M}_{lump}^w & \mathbf{0} & \mathbf{0} & \mathbf{0} \\ & \mathbf{M}_{lump}^u & \mathbf{0} & \mathbf{M}_{lump}^{u\omega} \\ & & \mathbf{M}_{lump}^v & \mathbf{M}_{lump}^{v\omega} \\ \text{Sym} & & & \mathbf{M}_{lump}^\omega \end{bmatrix} \qquad (4.17)$$

where:

$$\mathbf{M}_{lump}^u = \mathbf{M}_{lump}^v = \mathbf{M}_{lump}^w = \operatorname{diag}\{1,0,1,0\}; \qquad \mathbf{M}_{lump}^\omega = J_{m,S}\mathbf{M}_{lump}^u \qquad (4.18)$$

$$\mathbf{M}_{lump}^{u\omega} = (y_m - y_S)\mathbf{M}_{lump}^u; \qquad\qquad \mathbf{M}_{lump}^{v\omega} = -(x_m - x_S)\mathbf{M}_{lump}^u \qquad (4.19)$$

In the previous equations $J_{m,S} = (x_m - x_S)^2 + (y_m - y_S)^2$, whereas coordinates x_m, y_m indicate the line of mass centroids with respect to the principal axes of the beam cross-section. Hence, the inertial contributions associated to the mass position with respect to the shear center are accounted for in mass matrix 4.17.

4.3 Flexural-torsional frequencies of FRP beams

To highlight the role of the shear strains, frequency analyses of orthotropic profiles reinforced by longitudinal carbon fibres were considered first. In particular, a convergence rate test is reported in example 4.3.1 for a C-shaped beam subjected to self weight only. In examples 4.3.2 and 4.3.3 the FEM results (with no geometrical effects) are compared with numerical shell solutions and with analytical results. Finally, examples 4.3.4 and 4.3.5 are intended to underline the role of geometrical effects. Obviously, the vibration frequency plots locate the Eulerian buckling load as the first frequency attains a null value (Corradi Dell'Acqua 1994).

4.3.1 Convergence rate test

A simply-supported C-shaped carbon-epoxy beam (Fig. 4.1) was analysed for slenderness ratios L/H = 20, 10, 6.67. The beam properties are reported in Table 4.I. The analytical solutions by Cortínez and Piovan (2002) were assumed as reference solutions. Figure 4.2 shows the first five vibration mode shapes. The first mode (Fig. 4.2a) presents y-direction displacements and torsional rotations modulated by a single half wave. One half wave is still present in the second mode (Fig. 4.2b), representing the displacement field in the symmetry plane (x-direction). Vice versa, the third mode (Fig. 4.2c) is characterized by two half waves modulating y-direction displacements and torsional rotations for both slenderness ratios L/H = 20 and 10. Still for L/H = 20 and 10
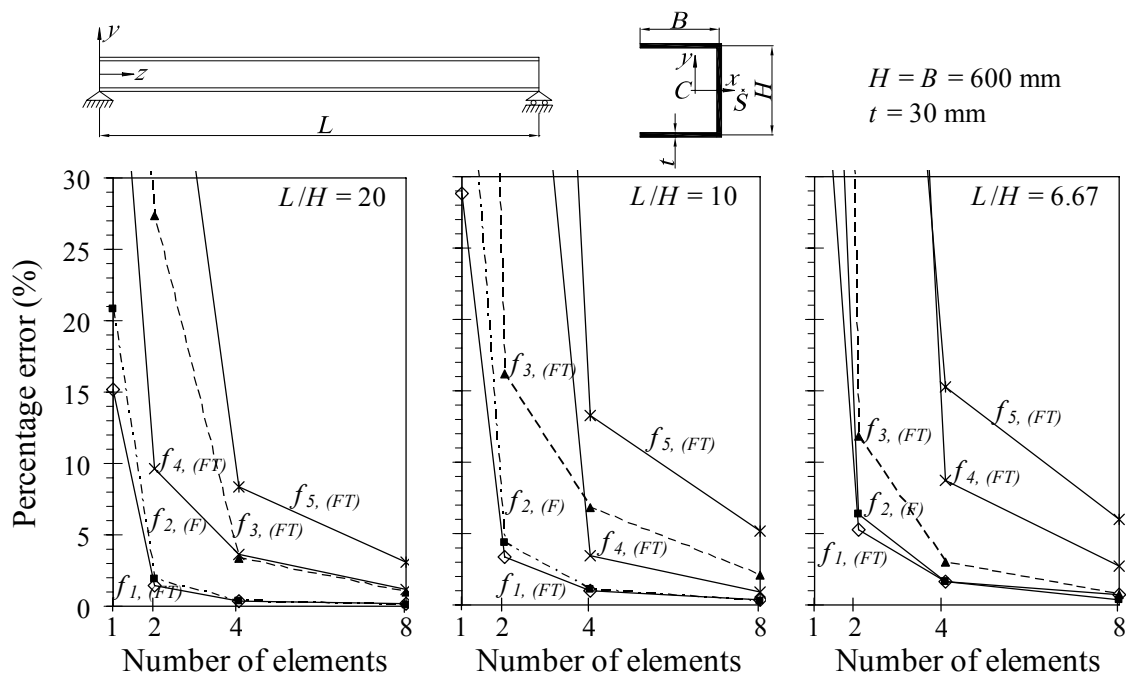
Figure 4.1. Natural frequencies of a simply-supported C-shaped CFRP profile for three different slenderness ratios (*FT*: flexural-torsional mode; *F*: flexural mode). Convergence rate of the formulation adopted with respect to the analytical solutions given by Cortínez and Piovan (2002).

Table 4.I. Properties of the C-shaped CFRP profile
considered in examples 4.3.1, 4.3.2 and 4.3.4.

$\overline{EA}$	$\overline{EJ_x}$	$\overline{EJ_y}$	$\overline{EJ_\omega}$	$\overline{GJ_t}$
kN	kNmm^2	kNmm^2	kNmm^4	kNmm^2
7.78E+6	5.44E+11	3.11E+11	2.00E+16	6.71E+7
$\overline{GD_x}$	$\overline{GD_y}$	$\overline{GD_\omega}$	$\overline{GD_{y\omega}}$	C_N
kN	kN	kNmm^2	kNmm	mm^2
1.15E+5	6.71E+4	1.55E+10	−1.64E+7	3.19E+5
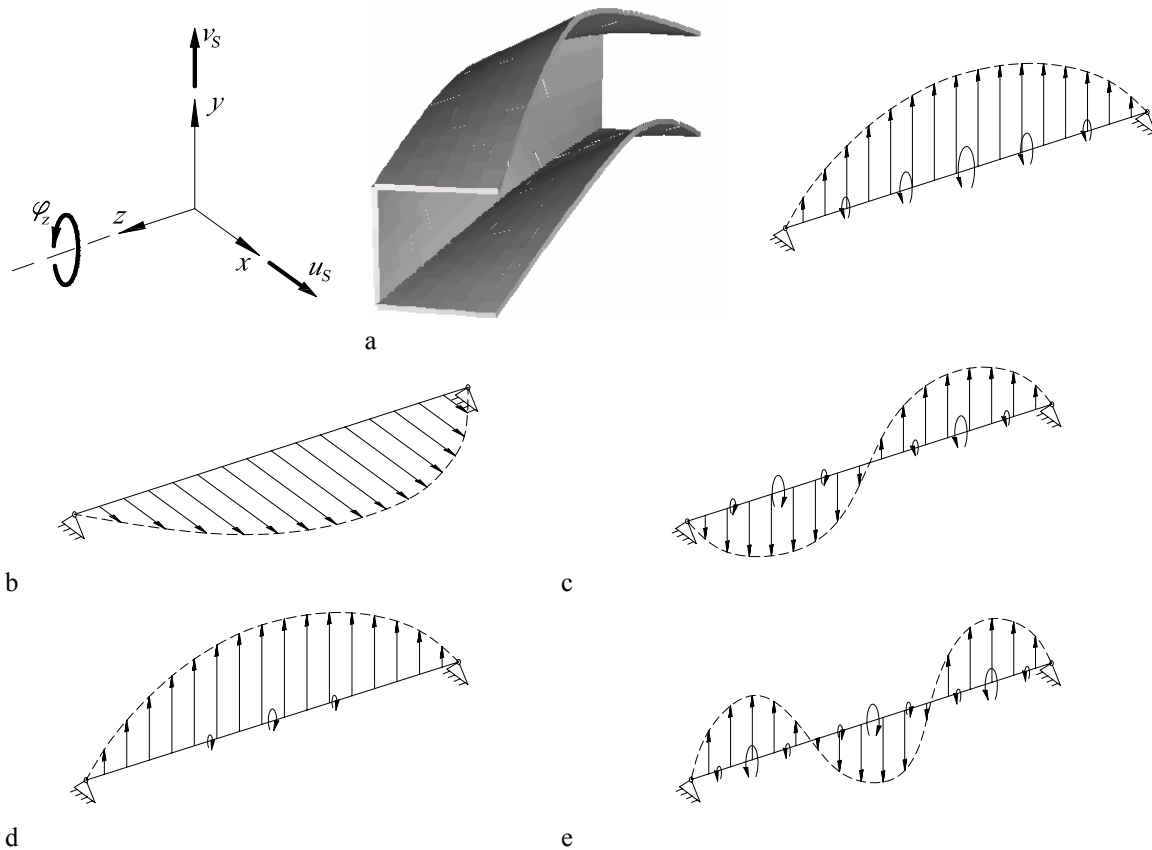
Figure 4.2. First five mode shapes of the C-shaped CFRP profile of example 4.3.1 for L/H = 20, 10, 6.67. Straight and circular arrows indicate direction and amplitude of lateral displacements and torsional rotations, respectively.

the fourth mode (Fig. 4.2d) is similar to the first mode but they present torsional rotations of opposite sign. For L/H = 6.67, third and fourth mode shape exchange with each other. Finally, in the fifth mode (Fig. 4.2e) y-direction displacements and torsional rotations present three half waves. Observation of numerical results indicates that, for

each half wave of the mode shapes, limiting errors on the frequency values to 3.5% would require four finite elements. In particular, adopting four elements, the first two frequencies (Fig. 4.2a,b) show an error not larger than 1.6%. Viceversa, using two finite elements for each half wave, leads to an error up to 6.4% for the first two frequencies and up to 16.2% for the following three.

4.3.2 Frequency analysis for increasing slenderness of a C-shaped cantilever beam

A cantilever FRP profile with the same cross-section as in the previous example is considered. The first (flexural-torsional) frequency of vibration is reported in Figure 4.3 for increasing slenderness. Solid and dotted lines represent the analytical solutions to the vibration beam problem (evaluated by the authors for the problem at hand). For comparison purposes, a 3D model was implemented making use of 4-node orthotropic shell elements (STRAUS7® Theoretical manual 2004). It can be observed that the first natural frequency (for the whole range $2 \leq L/H \leq 10$ under investigation) is seized by the beam model, even when using one single finite element. If shear deformations (S.D.) related to shear and torsion are neglected ($\phi_i = 0$, $i = y, \omega$, see Section § 2.2.1), the Euler-Bernoulli-Vlasov analytical solution is accurately predicted by one single element. Nevertheless, even for a rather slender cantilever beam ($L/H = 6$), neglecting shear deformations overestimates the first frequency of about 20%. Moreover, if shear
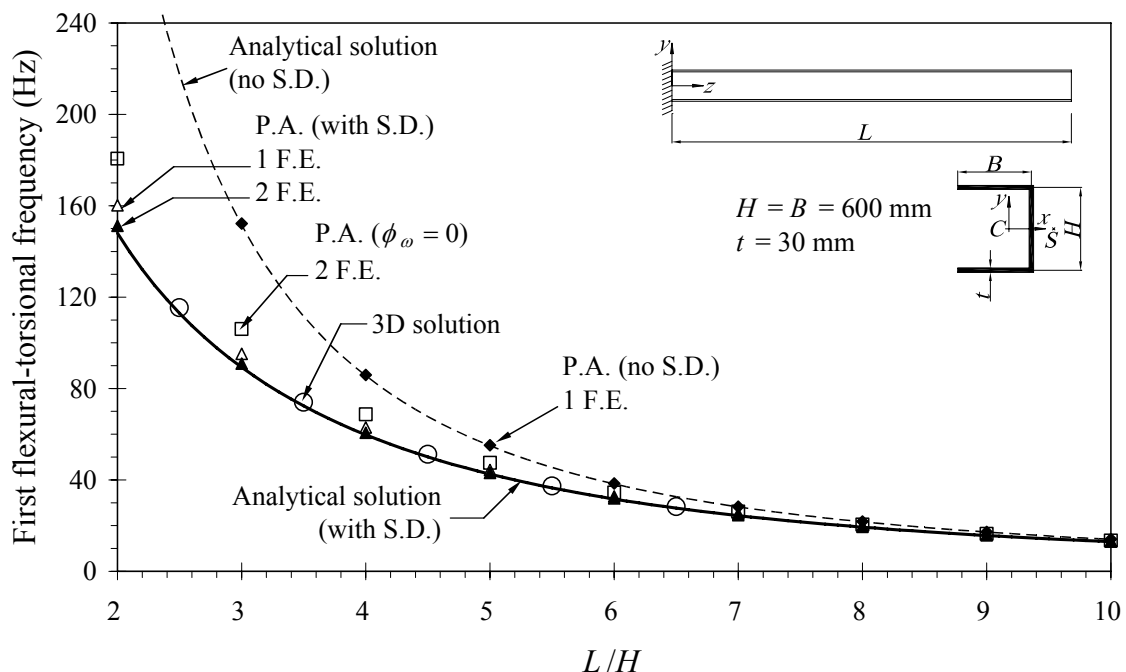
Figure 4.3. First (flexural-torsional) natural frequency vs. beam slenderness for a C-shaped CFRP cantilever profile. Comparison of Present Analysis ($\triangle$, $\blacktriangle$, $\square$, $\blacklozenge$) with beam analytical solutions (solid and dotted lines) and with the results of a 3D shell model ($\circ$). Shell elements 100 mm $\times$ 100 mm.

strain effects due to bending only are considered (setting $\phi_\omega = 0$, see § 2.2.1), the error with respect to Timoshenko-Reissner's model is of about 10%. In fact, it should be recognized that the condition $\phi_\omega = 0$ makes the flexural-torsional coupling terms of matrix $\mathbf{K}_E$ vanish, even for monosymmetric and nonsymmetric cross-sections (see Appendix 2.A).

4.3.3 I-beam with masses attached to the top flange

A simply-supported graphite-epoxy I-profile (Kollár 2001b) with two uniform mass distributions m rigidly attached to the top flange (Fig. 4.4), is considered. The beam properties are reported in Table 4.II, for three different values of the bottom flange width b_2. The location of the mass distribution makes flexural vibrations in x direction and torsional vibrations couple even for $b_1 = b_2$. Neglecting the beam self weight, Kollár determined a closed-form solution for the first three circular frequencies, showing that the first two correspond to flexural-torsional modes (x-z plane), whereas the third one is of purely flexural type (y-z plane). Again, a shell model was implemented to verify the accuracy of the FE beam solutions with reference to the first two circular frequencies. Figure 4.4 shows the good agreement between the model adopted (2 F.E.), and the results given by Kollár and by the shell model, for increasing beam slenderness.
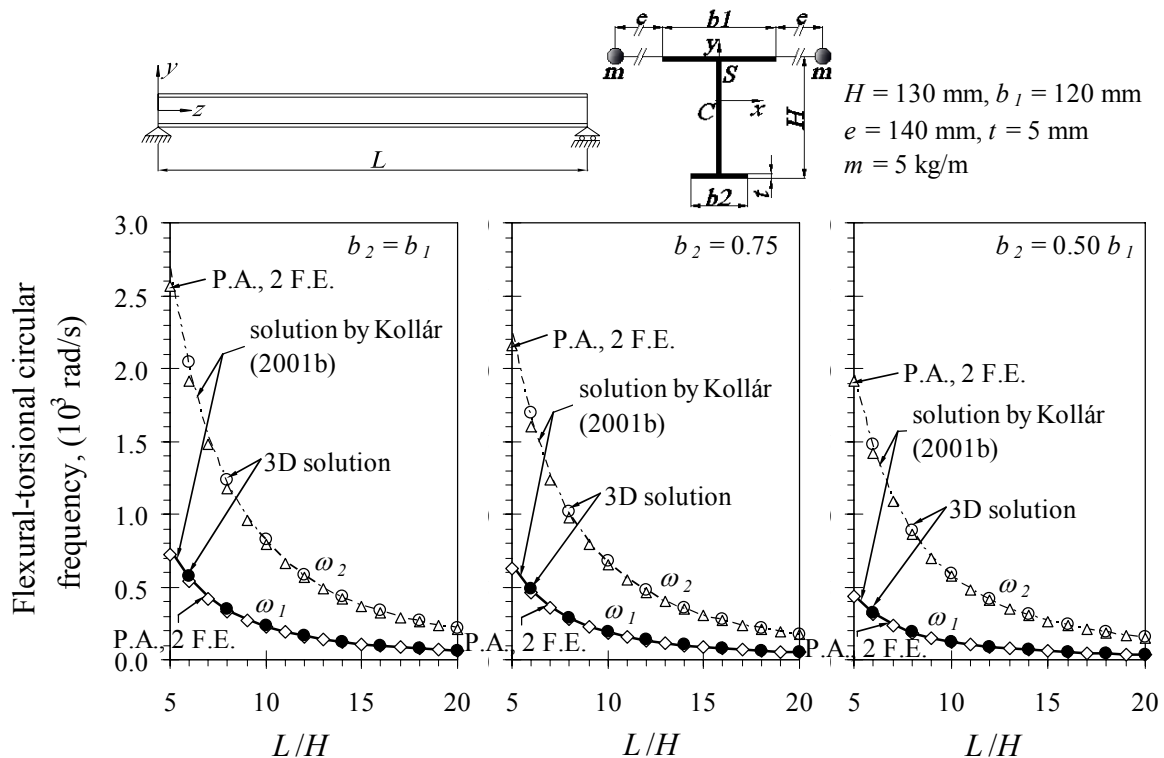
Figure 4.4. Simply-supported CFRP I-profile with uniformly distributed masses attached to the top flange. First and second circular frequency vs. beam slenderness for three different values of the lower flange width. Comparison of the Present Analysis (Δ, $\lozenge$) with the solutions by Kollár (solid and dotted lines) and of a 3D shell model ($\bullet$, $\circ$). Shell elements 15 mm × 15 mm.

Table 4.II. Properties of the FRP I-profile considered in the example of example 4.3.3 (Kollár 2001b).

	$\overline{EJ_x}$ kNmm^2	$\overline{EJ_y}$ kNmm^2	$\overline{EJ_\omega}$ kNmm^4	$\overline{GJ_t}$ kNmm^2
$b_2 = b_1$	7.47E+8	1.99E+8	7.76E+11	1.04E+5
$b_2 = 0.75b_1$	6.58E+8	1.41E+6	4.61E+11	9.49E+4
$b_2 = 0.50b_1$	5.52E+8	1.12E+8	1.73E+11	8.63E+4
	$\overline{GD_x}$ kN	$\overline{GD_y}$ kN	$\overline{GD_\omega}$ kNmm^2	$\overline{GD_{x\omega}}$ kNmm
$b_2 = b_1$	6.90E+3	3.72E+3	2.70E+7	0
$b_2 = 0.75b_1$	6.04E+3	3.78E+3	2.47E+7	9.95E+4
$b_2 = 0.50b_1$	5.18E+3	3.85E+3	2.20E+7	1.44E+5

4.3.4 Monosymmetric beam subjected to compression forces or bending moments acting at the end sections

The example refers to a simply-supported C-shaped FRP beam (Table 4.I) with $L/H =$ 10. In this case, geometrical nonlinearities were considered in the frequency analysis. In Figure 4.5, the first beam frequency for different values of a constant centroidal axial load is reported.
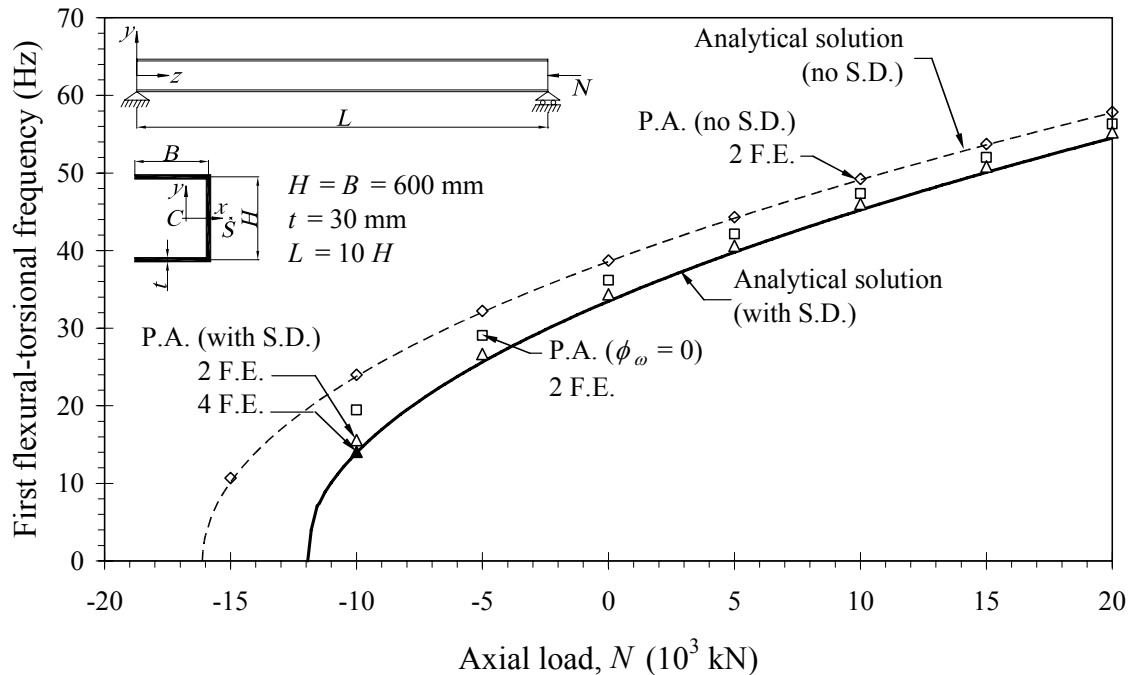
Figure 4.5. First (flexural-torsional) natural frequency for a simply-supported C-shaped CFRP profile subjected to a centroidal axial load. Comparison between Present Analysis (Δ, $\blacktriangle$, $\lozenge$) and analytical solutions of Cortínez & Piovan and of Ghorbanpoor & Omidvar (solid and dotted lines). Flexural-torsional buckling loads: $N_{cr} = -11.94 \cdot 10^3$ kN (with S.D.); $N_{cr} = -16.12 \cdot 10^3$ kN (with no S.D.).
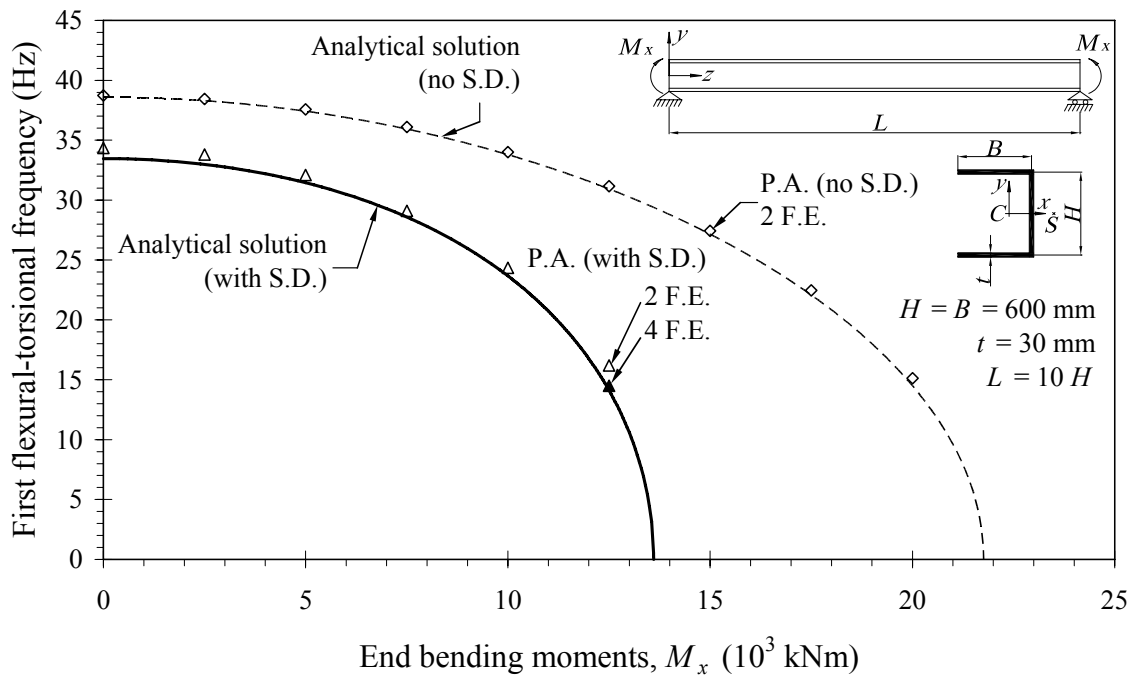
Figure 4.6. First (flexural-torsional) natural frequency for a simply-supported C-shaped CFRP profile subjected to end bending moments acting in the plane orthogonal to the symmetry plane. Comparison between Present Analysis (Δ, $\blacktriangle$, $\Diamond$) and analytical solutions of Cortínez & Piovan and of Ghorbanpoor & Omidvar (solid and dotted lines). Buckling moments: $M_{x,cr} = 13.60 \cdot 10^3$ kNm (with S.D.); $M_{x,cr} = 21.75 \cdot 10^3$ kNm (with no S.D.).

With reference to Euler-Bernoulli-Vlasov's model and to Timoshenko-Reissner's model, analytical solutions were determined by means of the corresponding "exact" stiffness and mass matrices (Cortínez & Piovan 2002, Ghorbanpoor & Omidvar 1996). As is shown in Figure 4.5, two elements are generally sufficient to obtain good results even though a larger number of elements is necessary in the proximity of the buckling load (N_{cr}). Moreover, ignoring shear deformations significantly overestimates the vibration frequencies. For instance, for compressive loads $N = -5 \cdot 10^3$ kN $= 0.42 \cdot N_{cr}$ and $N = -10 \cdot 10^3$ kN $= 0.84 \cdot N_{cr}$, neglecting warping shear deformations only ($\phi_\omega = 0$, see § 2.2.1) overestimates the solution of about 13% and 35% respectively.

Figure 4.6 shows the first (flexural-torsional) vibration frequency of a beam subjected to two bending moments acting at the end sections in the y-z plane (orthogonal to the symmetry plane). It can be seen that two finite elements generally provide very accurate results whereas, when M_x tends to $M_{x,cr}$, a mesh refinement is required.

4.3.5 I-beam with a gravitational load at midspan

The beam is simply-supported and has a doubly-symmetric cross-section (properties in Table 4.III). A gravitational load $M \cdot g$ applied at midspan, alternatively attached to the bottom (Fig. 4.7) or to the top flange (Fig. 4.8) is considered. Making use of two finite elements, the first (flexural-torsional) natural frequency for different values of the
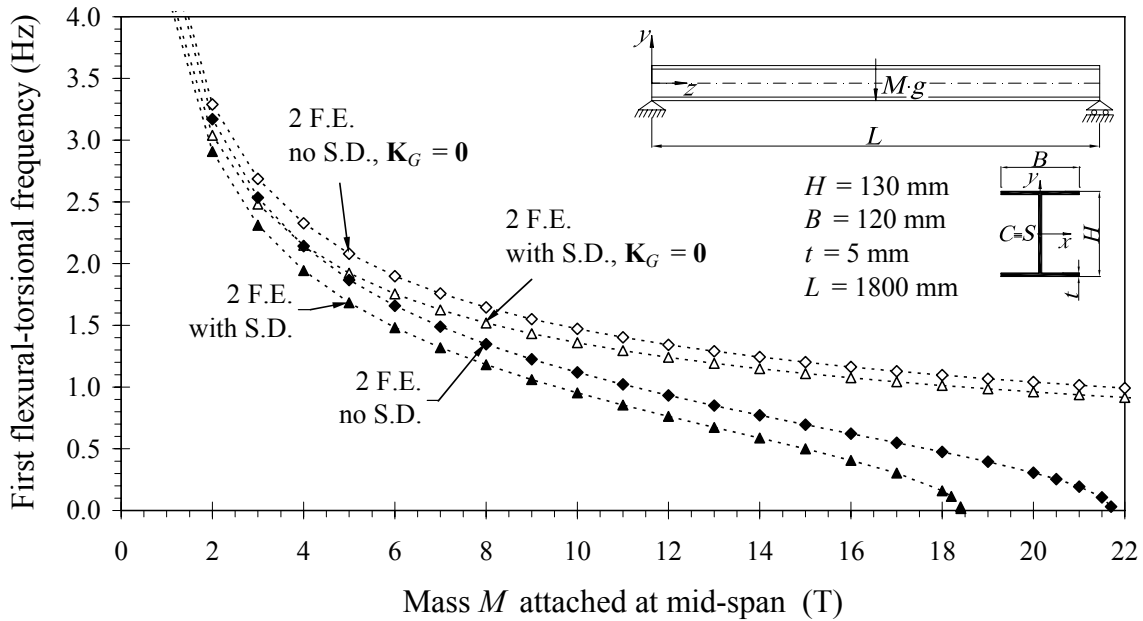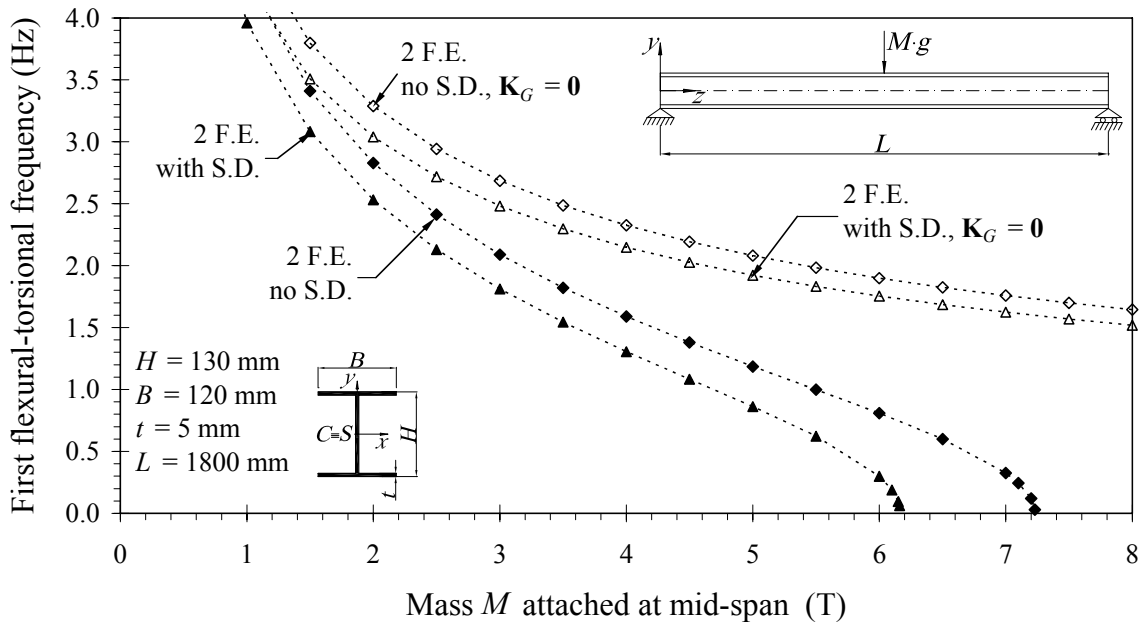
Figure 4.7. Simply-supported CFRP I-profile with a gravitational load attached to the bottom flange of the mid section. First natural frequency for increasing values of mass M. Upper curves obtained ignoring 2nd order effects and including S.D. (Δ) or not ($\Diamond$). Lower curves obtained including 2nd order effects and considering S.D. ($\blacktriangle$) or not ($\blacklozenge$). Lateral buckling load: $(M \cdot g)_{cr} = -184.1$ kN (with S.D.); $(M \cdot g)_{cr} = -217.2$ kN (with no S.D.).

Figure 4.8. Simply-supported CFRP I-profile with a gravitational load attached to the top flange of the mid section. First natural frequency for increasing values of mass M. Upper curves obtained ignoring 2nd order effects and including S.D. (Δ) or not ($\Diamond$). Lower curves obtained including 2nd order effects and considering S.D. ($\blacktriangle$) or not ($\blacklozenge$). Lateral buckling load: $(M \cdot g)_{cr} = -61.7$ kN (with S.D.); $(M \cdot g)_{cr} = -72.3$ kN (with no S.D.).

Table 4.III. Properties of the I-beam of example 4.3.5.

$\overline{EJ}_y$	$\overline{EJ}_\omega$	$\overline{GJ}_t$	$\overline{GD}_x$	$\overline{GD}_\omega$
kNmm^2	kNmm^4	kNmm^2	kN	kNmm^2
2.13E+8	8.33E+11	6.80E+4	4.55E+3	1.78E+7

attached mass was determined. The example is aimed at evaluating second-order effects and influence of shear deformations. In particular, neglecting second-order effects implies an error on the fundamental frequency of about +40% for a gravitational load $M \cdot g = 0.5 \cdot (M \cdot g)_{cr}$, corresponding to $M = 9$ T in Figure 4.7 and $M = 3$ T in Figure 4.8. Moreover, neglecting shear deformations leads to a systematic overestimate of the fundamental frequency and to a significant miscalculation (+18%) of the buckling load. It is noteworthy that, with respect to the top buckling load, the bottom buckling load is approximately three times greater.

4.4 Frequency analysis of pultruded frames

A pultruded (GFRP) portal frame is reported in Figure 4.9. All members have the major axis x_{loc} aligned with the global y-axis and present typical material properties of GFRP profiles: $E = 25$ GPa, $G = E/10$, $\rho = 1.83$ t/m^3. Full displacement and rotation continuity was assumed at the column-beam joints, whereas top and bottom column end-sections were considered free to warp. A uniformly distributed vertical load q_z was applied at the top flange of the beam. For analysis purposes, the corresponding mass per unit length was given the expression $(\alpha \cdot q_z)/g$ and was assumed fully participant ($\alpha = 1$), partly participant ($\alpha = 0.2$), or totally ineffective ($\alpha = 0$).
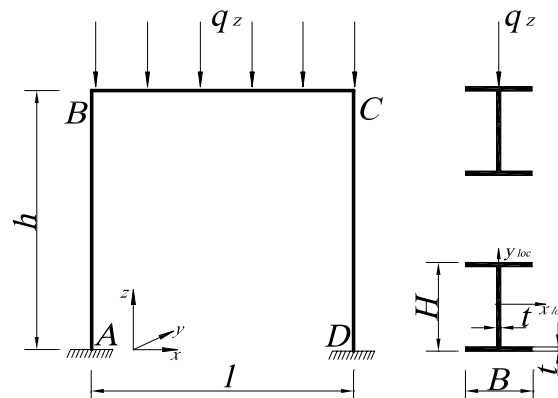
Figure 4.9. GFRP portal frame subjected to a uniform gravitational load acting at the top flange of beam ($E = 25$ GPa, $G = E/10$, $\rho = 1.83$ t/m^3). All members show major inertia in the frame plane. Example 4.4.1: I-section members with $H = 240.0$ mm, $B = 120.0$ mm, $t = 12.0$ mm. Absence of out-of-plane supports. Example 4.4.2: same profiles as in example 4.4.1. Rigid out-of-plane supports acting at joints B and C. Examples 4.4.3–4.4.5: wide-flange profiles with $H = B = 203.2$ mm, $t = 9.5$ mm. Rigid out-of-plane supports acting at joints B and C.

Five cases were considered, in which the influence of geometrical effects, shear deformations, cross-section shape, frame geometry and possible out-of-plane supports was investigated. An accurate solution was searched for adopting four finite elements for each member.

4.4.1 GFRP portal frame (l = 2 m, h = 3 m) with no lateral supports. I-section profiles

In Figure 4.10 the first three natural frequencies are plotted versus the external load q_z, whereas Figure 4.11 shows an enlargement of the first two frequency plots. Independently of the participant masses, the fundamental frequency corresponds to a symmetrical out-of-plane mode shape (Fig. 4.12a), whereas the second frequency is characterized by an antisymmetrical out-of-plane mode shape presenting flexural-torsional column displacements (Fig. 4.12b). Due to the absence of any bracing system, the buckling load $q_{z,cr} = -20.8$ kN/m, corresponding to the first mode shape (Fig. 4.12a), is much lower than the flexural failure load. In the absence of participant masses ($\alpha = 0$) the frequency reduction, as the external load increases, highlights a significant influence of second-order effects. Furthermore, as is typical of pultruded structures, self weight (0.8 kN only) is a small fraction of the global load and additional masses significantly influence the dynamic response. For example (Fig. 4.11), for $q_z/q_{z,cr} = 0.30$, when α changes from 0 to 0.2, the first frequency decreases of about 63%.

In Figure 4.13, the frequency plots for $\alpha = 0.2$ are compared with the results obtained by neglecting second-order effects. In particular, for $q_z/q_{z,cr} = 0.2$ and 0.5,
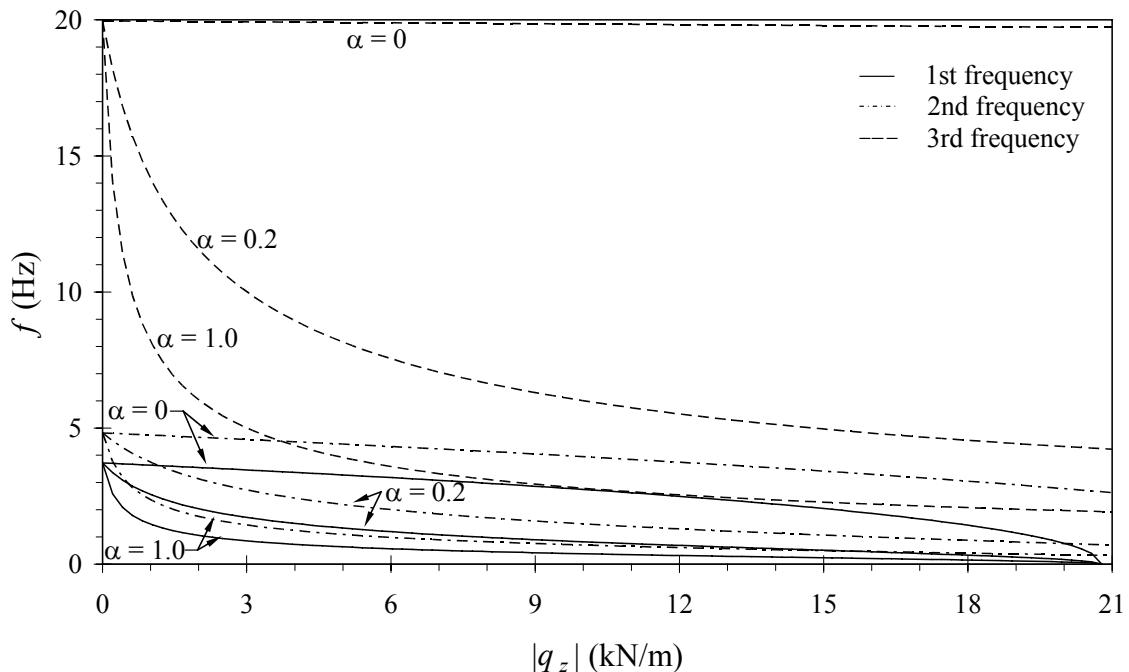
Figure 4.10. Portal frame of Figure 4.9 ($l = 2$ m and $h = 3$, I-section profiles) in the absence of out-of-plane bracing. First three natural frequencies (solid, dash-dot and dotted lines, respectively) vs. vertical load for different participating mass factors α. Buckling load: $q_{z,cr} = -20.80$ kN/m.
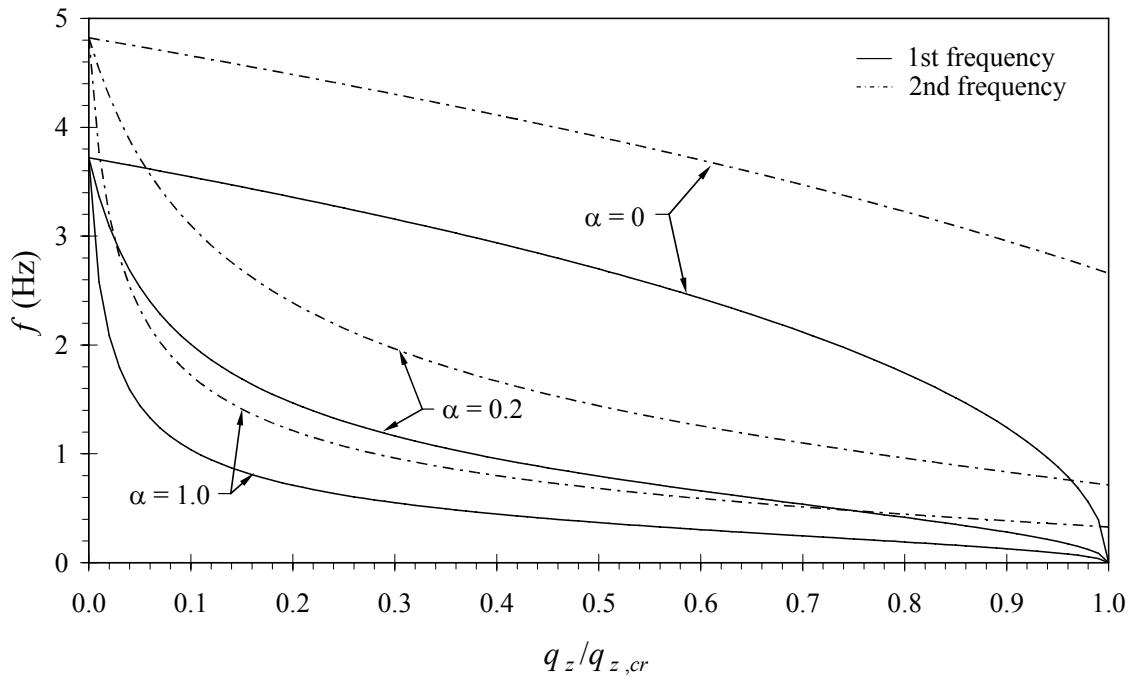
Figure 4.11. Portal frame of Figure 4.9 ($l = 2$ m and $h = 3$, I-section profiles) in the absence of out-of-plane bracing. First two natural frequencies (solid and dash-dot lines, respectively) vs. vertical load for different participating mass factors α.
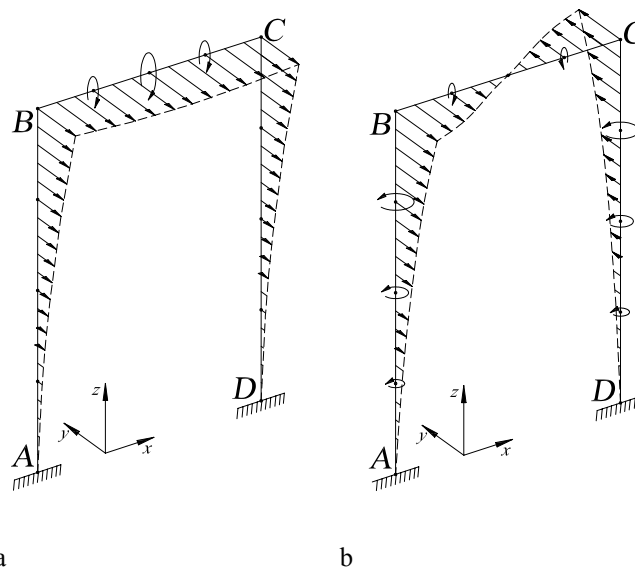

Figure 4.12. First two vibration modes of the frame of example 4.4.1 ($l = 2$ m and $h = 3$ m, I-section profiles). Straight and circular arrows indicate lateral displacements and torsional rotations, respectively. a: symmetrical out-of-plane flexural mode. b: antisymmetrical out-of-plane flexural-torsional mode.
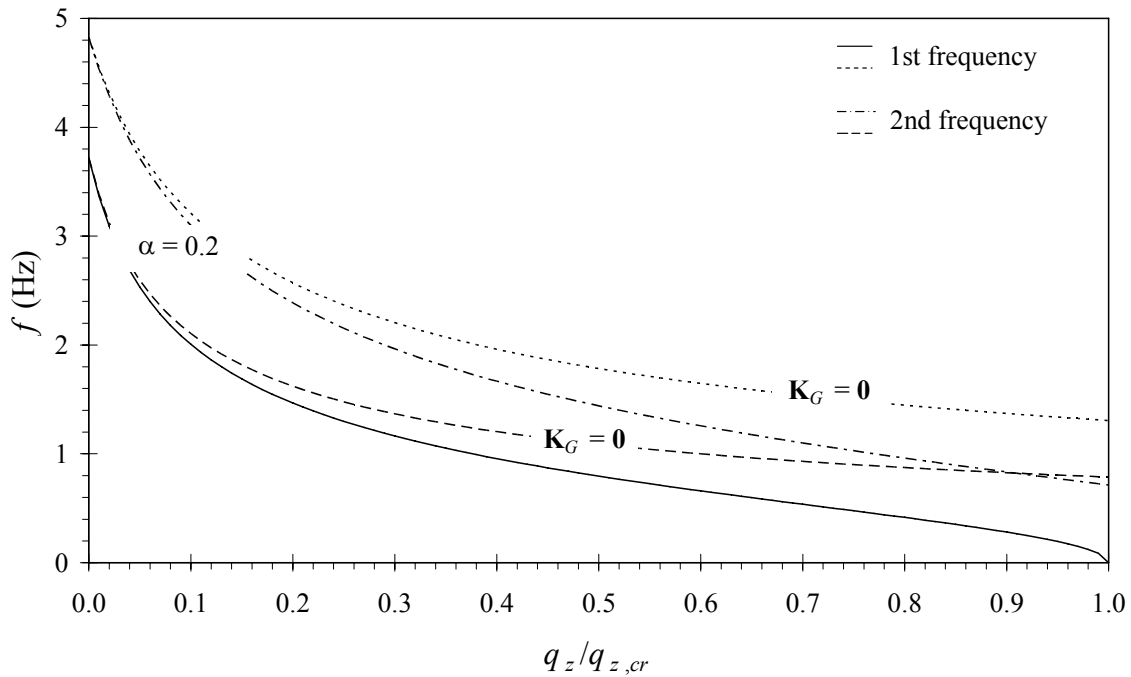
Figure 4.13. Portal frame of example 4.4.1. First and second natural frequencies including or neglecting second-order effects.
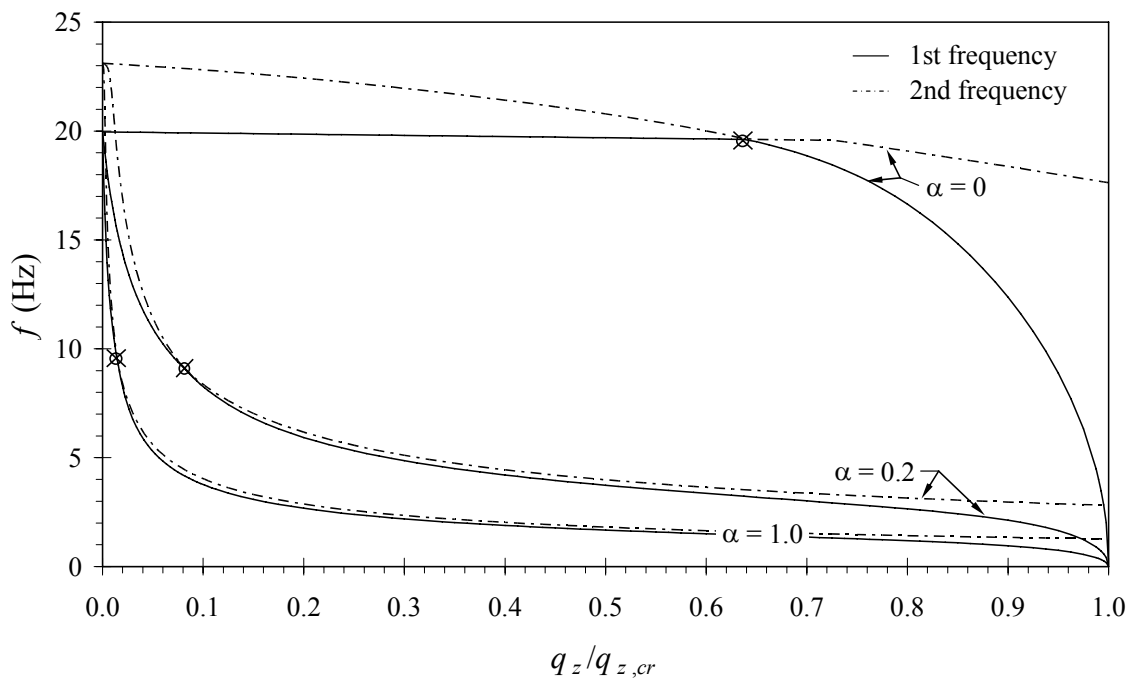
Figure 4.14. Portal frame of Figure 4.9 ($l = 2$ m and $h = 3$ m, I-section profiles) with rigid lateral supports at the beam-column nodes. First and second natural frequencies (solid and dash-dot lines respectively) vs. vertical load for different participating mass factors α. Symbol ⊗ indicates the vertical load at which first (in-plane) and second (out-of-plane) vibration modes exchange with each other. Buckling load: $q_{z,cr} = -47.12$ kN/m.

ignoring geometrical effects leads to overestimates of about 10.5% and 36.8% of the first frequency and of about 8.0% and 23.8% of the second frequency, respectively.

4.4.2. GFRP portal frame (l = 2 m, h = 3 m) with rigid out-of-plane bracings at the beam-column nodes. I-section profiles

The portal frame of example 4.4.1 was re-analysed in the presence of out-of-plane bracings acting at the beam-column nodes. For practical purposes, such supports can be assumed to behave rigidly for very low stiffnesses, approximately larger than $3\,EJ_{yloc}/h^3$ (see § 3.11.1.3).

In this case (Fig. 4.14), in the absence of participant masses ($\alpha = 0$), the first natural frequency remains substantially constant as the external load increases, revealing a rather small influence of second-order effects. Then, for $q_z/q_{z,cr} \cong 0.65$, a frequency crossing is observed. In fact, for $|q_z| \leq 0.65\,|q_{z,cr}|$, the first mode shape is characterized by in-plane frame vibrations (Fig. 4.15a), whereas, for $|q_z| \geq 0.65\,|q_{z,cr}|$, out-of-plane (flexural-torsional) vibrations occur (Fig. 4.15b). Also in this case, participant masses significantly reduce the natural frequencies. For example (Fig. 4.14), for $q_z/q_{z,cr} = 0.06$, when α changes from 0 to 0.2, the first frequency decreases of about 50%. Moreover, the load at frequency crossing drastically reduces.

4.4.3. GFRP portal frame (l = 2 m, h = 3 m) with rigid out-of-plane bracings at the beam-column nodes. Wide-flange profiles

The major moment of inertia is approximately the same as in the previous example whereas the minor moment of inertia is 3.5 times larger. Consequently, the transition of the first mode from in-plane to lateral-torsional vibrations (Fig. 4.16) occurs in proximity of the buckling load ($q_z/q_{z,cr} \cong 0.97$ for the whole range $\alpha = 0\div1$). The frame natural frequencies were then compared with those obtained when shear deformations are neglected (Fig. 4.17, $\alpha = 1$). In particular, ignoring shear deformations implies an overestimate of the first frequency of about 20% before the frequency crossing. Furthermore, when the shear strain effects are not considered, the load at crossing, as well as the buckling load, turn out to be overestimated of about 12%.

4.4.4. GFRP portal frame (l = h = 3 m) with rigid out-of-plane bracings at the beam-column nodes. Wide-flange profiles

With respect to example 4.4.3, the beam has greater slenderness and the exchange between first and second mode shape (Fig. 4.18) occurs for a lower vertical load ($q_z/q_{z,cr} \cong 0.80$ for the whole range $\alpha = 0\div1$).

4.4.5. GFRP portal frame (l = 3 m, h = 2 m) with rigid out-of-plane bracings at the beam-column nodes. Wide-flange profiles

Finally, for $l = 1.5\,h$ (Fig. 4.19), even in the presence of wide-flange cross-sections, a fundamental out-of-plane vibration mode (Fig. 4.20) is determined by quite low values

of the external loads. In this case, neglecting second-order effects overestimates the first frequency of about 15% for $q_z/q_{z,cr} = 0.75$.
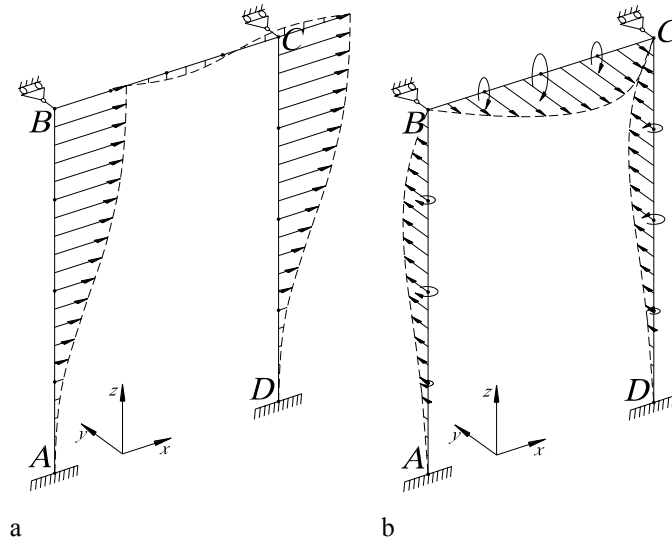

Figure 4.15. First two vibration modes of the frame of example 4.4.2 ($l = 2$ m and $h = 3$ m, I-section profiles) with rigid supports at the beam-column nodes. Straight and circular arrows indicate in-plane or lateral displacements, and torsional rotations, respectively. a: antisymmetrical in-plane flexural mode; b: symmetrical out-of-plane flexural-torsional mode.
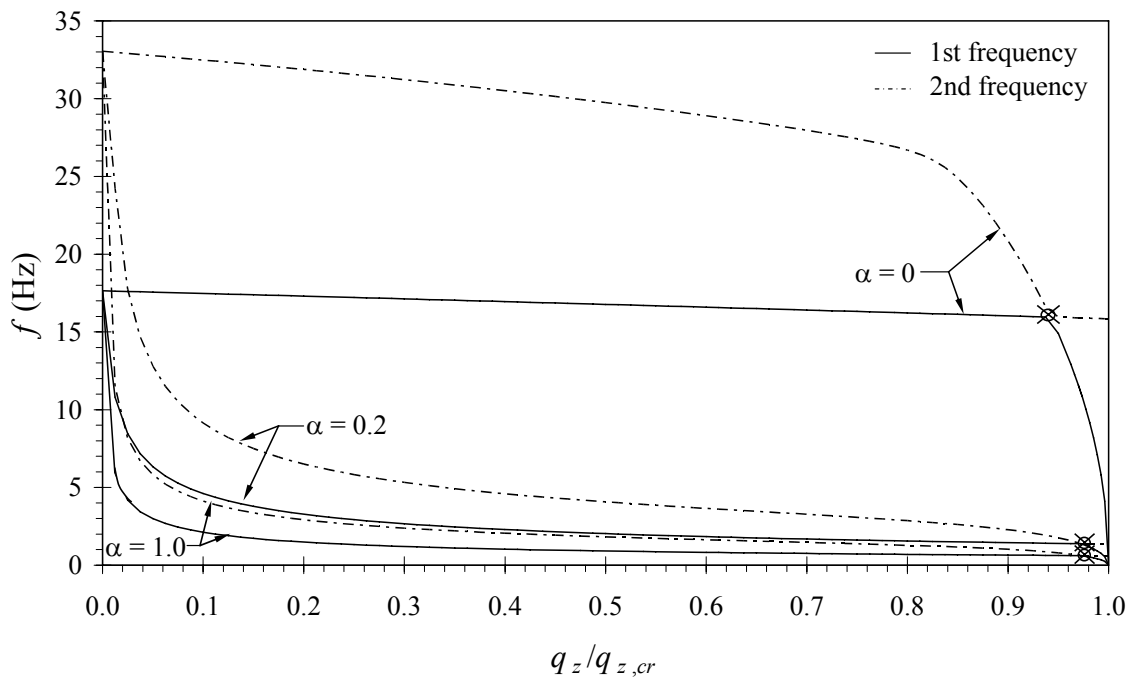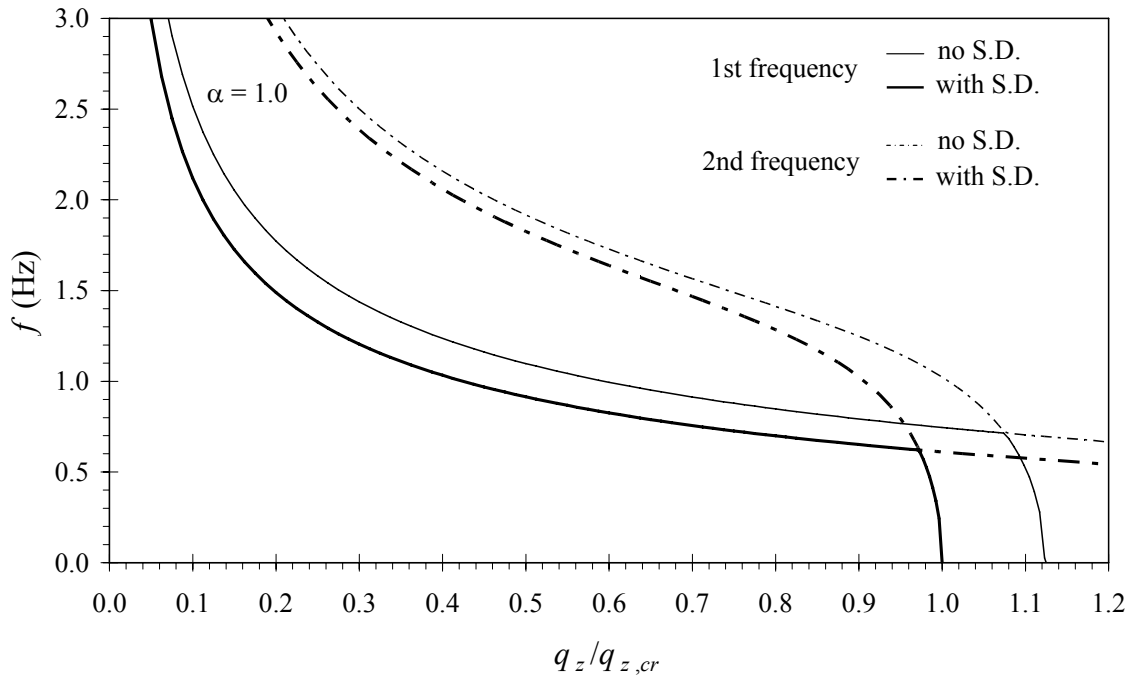

Figure 4.16. Portal frame of Fig. 4.9 ($l = 2$ m and $h = 3$ m, wide-flange profiles) with rigid lateral supports at the beam-column nodes. First and second natural frequencies (solid and dash-dot lines respectively) vs. vertical load for different participating mass factors α. Symbol $\boxtimes$ indicates the vertical load at which first (in-plane) and second (out-of-plane) vibration modes exchange with each other. Buckling load: $q_{z,cr} = -136.47$ kN/m.

Figure 4.17. Portal frame reported in Fig. 4.9 ($l = 2$ m and $h = 3$ m, wide-flange profiles). First and second natural frequencies, including shear deformations (S.D.) or not.
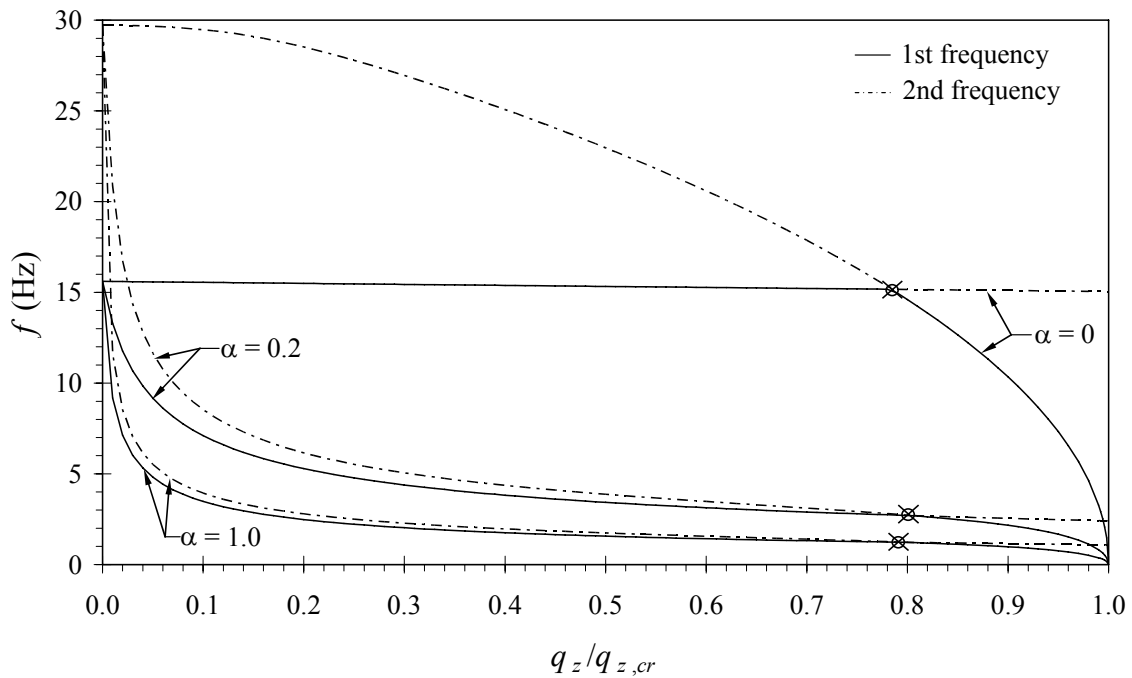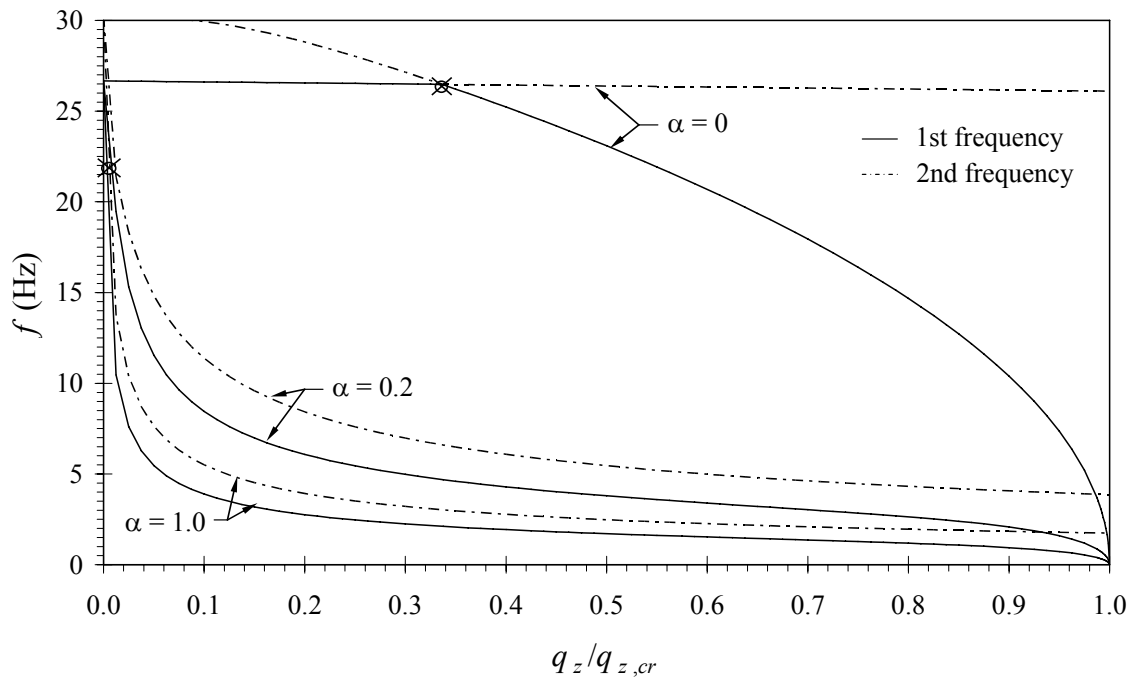

Figure 4.18. Portal frame of Fig. 4.9 ($l = h = 3$ m, wide-flange profiles) with rigid lateral supports at the beam-column nodes. First and second natural frequencies (solid and dash-dot lines respectively) vs. vertical load for different participating mass factors α. Symbol ⊠ indicates the vertical load at which first (in-plane) and second (out-of-plane) vibration modes exchange with each other. Buckling load: $q_{z,cr} = -32.18$ kN/m.
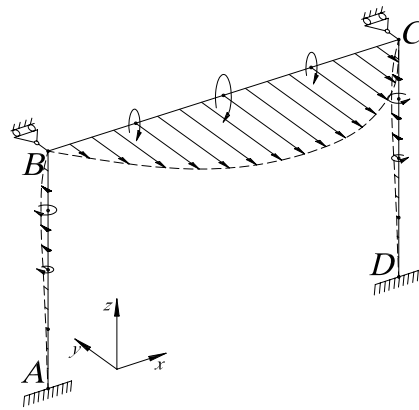
Figure 4.19. Portal frame of Fig. 4.9 (l = 3 m and h = 2 m, wide-flange profiles). First and second natural frequencies (solid and dash-dot lines respectively) vs. vertical load for different participating mass factors α. Symbol ⊠ indicates the vertical load at which first (in-plane) and second (out-of-plane) vibration modes exchange with each other. Buckling load: $q_{z,cr}$ = −32.80 kN/m.

Figure 4.20. Lateral-torsional (out-of-plane) mode shape of the frame of example 4.4.5 (l = 3 m and h = 2 m, wide-flange profiles). Straight and circular arrows indicate lateral displacements (y-direction) and torsional rotations, respectively.

4.5 Dynamic response of a footbridge composed by pultruded profiles

Finally, the finite element formulation $H32$ was applied to the vibration analysis of a footbridge composed by GFRP pultruded profiles with E = 25 MPa, $G = E/8$. The

structure, presenting span length L = 15 m and deck width B = 1.8 m, is shown in Figures 4.21–4.22. Cross-section shapes and dimensions of the pultruded members adopted are reported in Table 4.IV. In particular, (longitudinal) main girders and (transversal) floor beams present wide-flange doubly-symmetric cross-section, whereas diagonal and vertical elements are made of hollow square tubes. As for the connections, resort can be made to the works of Smith *et al.* (1999a) or Sobrino and Pulido (2002). Alternatively, main girders may by realized using two back-to-back C-shaped profiles,
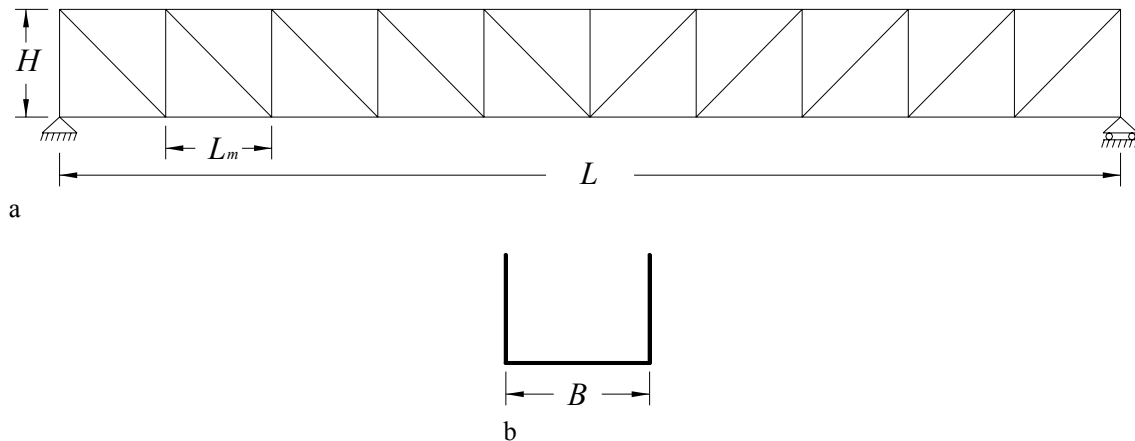

Figure 4.21. a: side view of the footbridge (L = 15.0 m, L_m = H = 1.5 m). b: footbridge cross-section (B = 1.8 m).
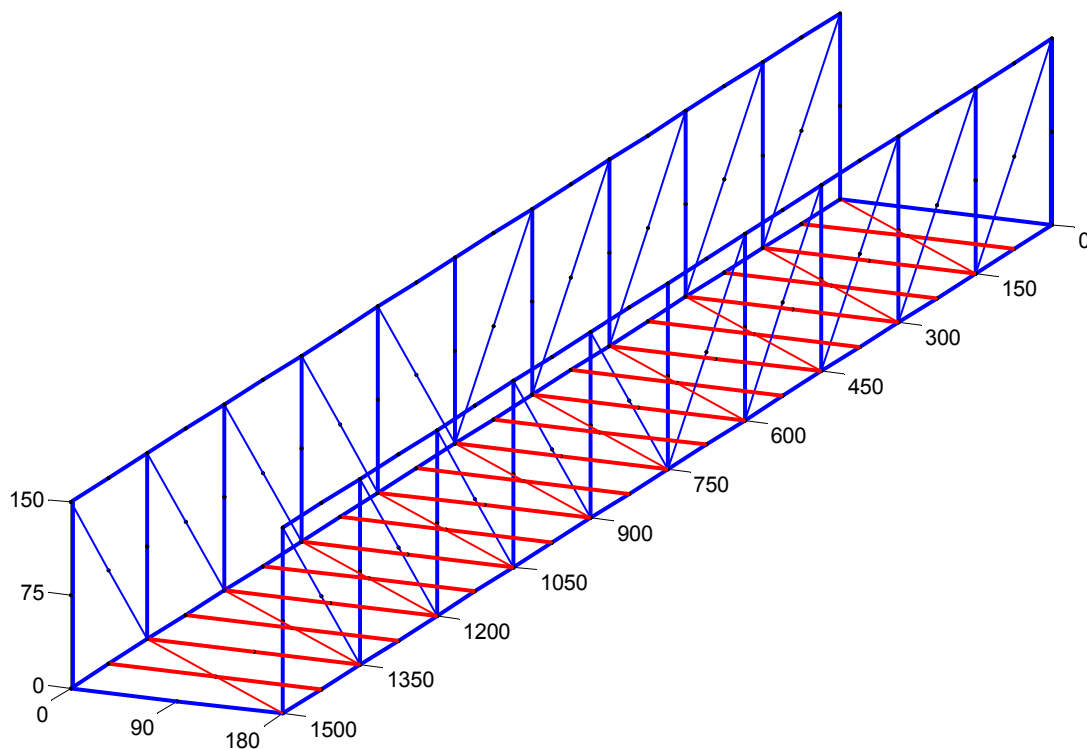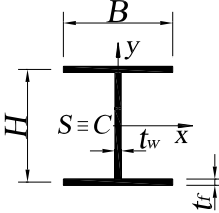

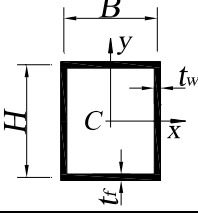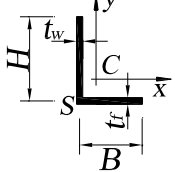Figure 4.22. Assonometric view of the footbridge.

Table 4.IV. Profiles adopted in the footbridge design.

Main girders	Wide-flange I-profiles		$H = B = 152.4$ mm $t_f = t_w = 9.53$ mm
Deck beams			$H = B = 101.6$ mm $t_f = t_w = 6.35$ mm
Vertical elements	Hollow square tubes		$H = B = 101.6$ mm $t_f = t_w = 6.35$ mm
Inclined tension members			
Deck bracing	Equal leg angles		$H = B = 50.8$ mm $t_f = t_w = 6.35$ mm

allowing for connections similar to those adopted in Pontresina bridge (Keller 1999). Vertical members was spaced of $L_m = 1.5$ m (module length). The deck is stiffened by diagonal bracing with L-shaped cross-section.

Assuming for the (timber or FRP) deck panels a mass per unit area of 0.2 kN/m², the self weight of the footbridge turns out to be of about 15 kN (= G_k) only, divided between profiles ($\cong$ 9.5 kN) and floor system ($\cong$ 5.5 kN).

To establish the characteristic value of the (static) vertical distributed load corresponding to the pedestrian action, reference was made to Eurocode 1 (EN 1991-2:2003). For the span length adopted, such value is $Q_k = 4.65$ kN/m². Consequently, the ratio between live loads and dead loads was about 8.

A numerical model of the bridge was implemented discretizing all members of each module with two elements, resulting in 216 finite elements in all.

A linear static analysis was performed first. The live load was applied to the floor beams, uniformly distributed along the top flange. A midspan deflection of about L/650 was obtained under frequent loads ($G_k + 0.50Q_k$, Eurocode 0 − EN 1990:2002). Then, a global buckling analysis of the bridge undergoing the usual Ultimate Limit State load combination $1.35G_k + 1.50Q_k$ was carried out. An overall safety factor of about 1.45 was obtained, corresponding to the critical shape shown in Figure 4.23. It should be noted that instability is governed by flexural-torsional out-of-plane deflections of the top chords, with higher amplitude in the central part of the bridge, where compression is larger.

Finally, a vibration analysis of the structure undergoing the Serviceability Limit State load combination $G_k + Q$, with $Q \leq Q_k$, was performed. The mass associated to the live load was given the expression $(\alpha \cdot Q)/g$ and, for comparison purposes, was assumed

fully ($\alpha = 1$) or partly ($\alpha = 0.2$, $\alpha = 0.6$) participant, or totally ineffective ($\alpha = 0$). Second-order effects due to live load were included.
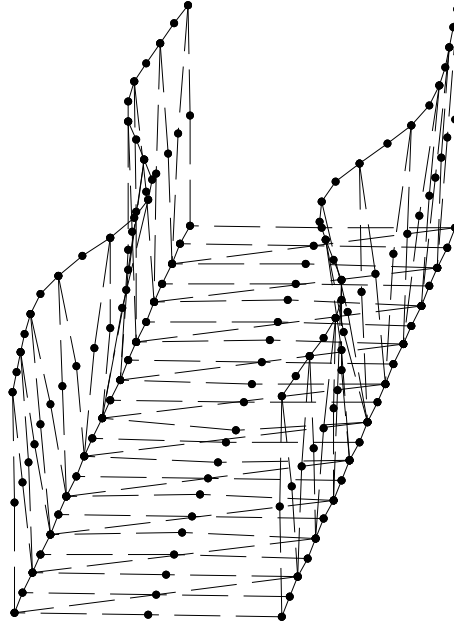

Figure 4.23. Buckling shape obtained for a critical multiplier $\lambda_{cr} = 1.45$ of the ULS load combination.
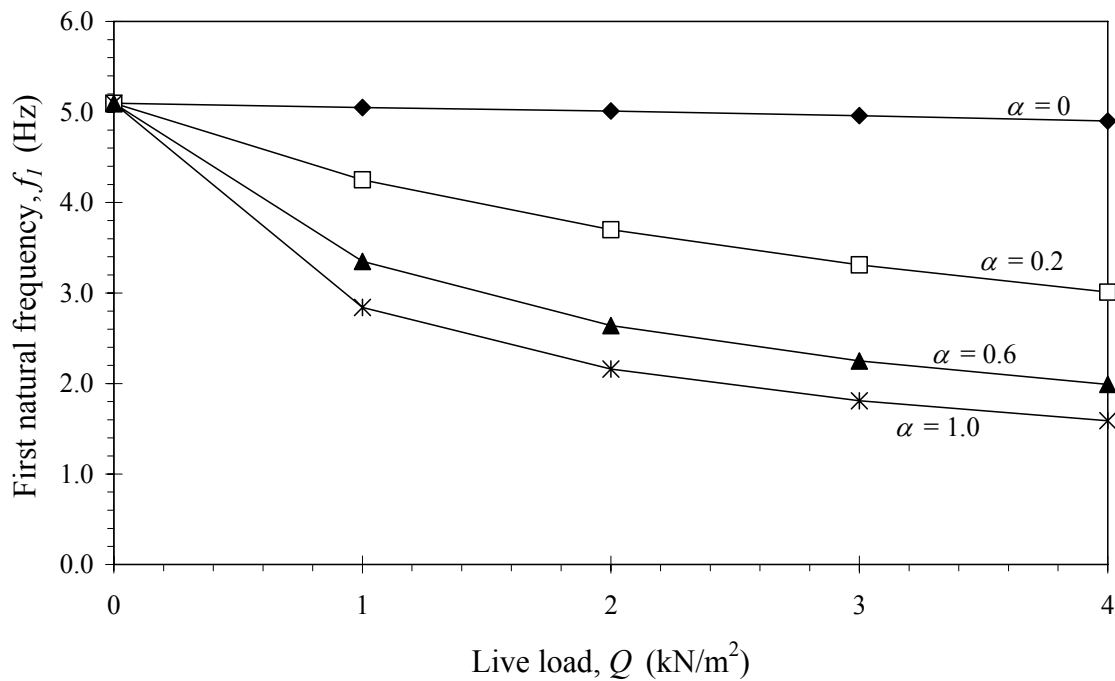

Figure 4.24. Fundamental frequency vs. the applied live load for different participating mass factors.

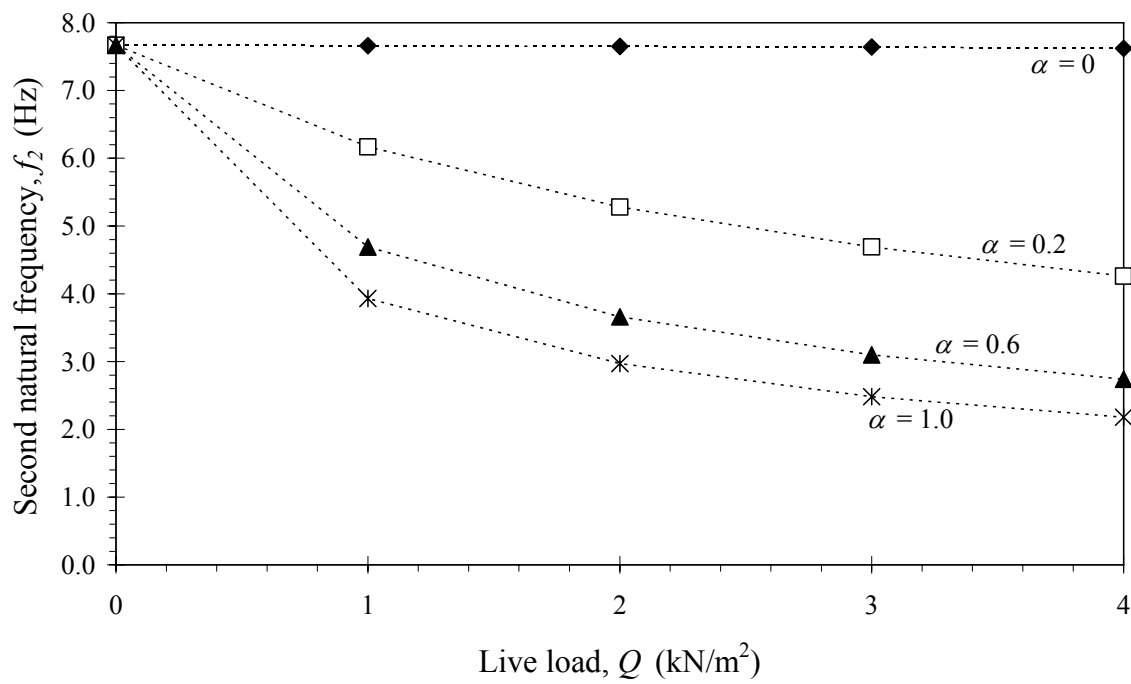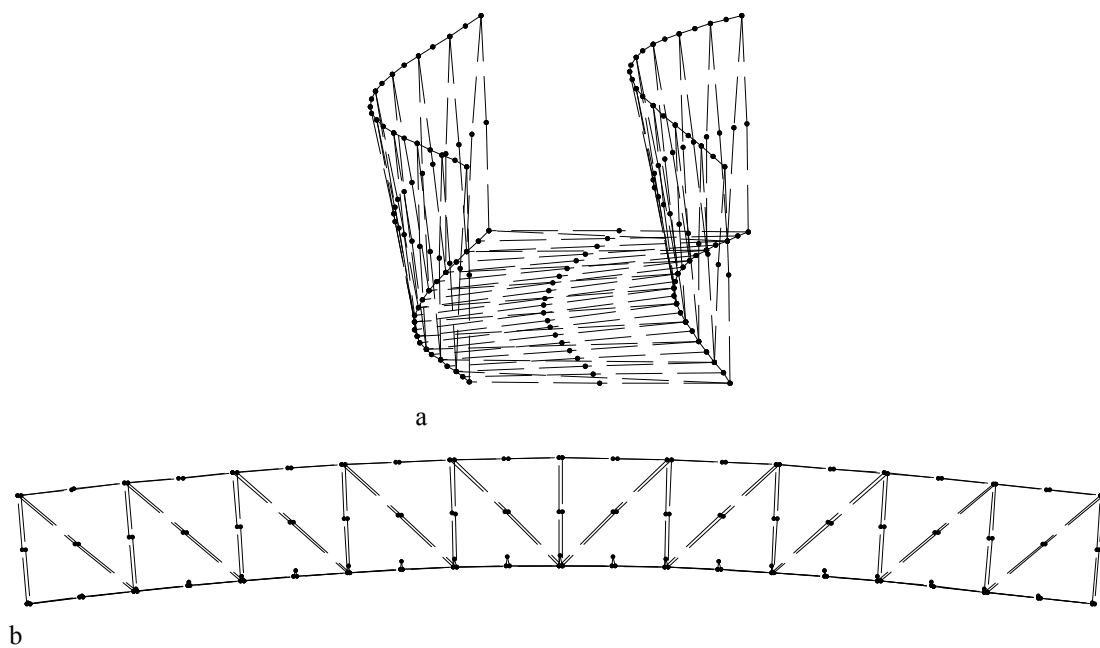Figure 4.25. Second natural frequency vs. the applied live load for different participating mass factors.

Figure 4.26. First two vibration mode shapes of the footbridge for $Q \leq Q_k$. a: lateral mode. b: vertical mode.

Table 4.V. Vertical forcing frequencies of pedestrians (Bachmann 2002).

Walking person	Running person	Jumping person
1.2–2.4 Hz	1.9–3.3 Hz	1.3–3.4 Hz

The values of the first two natural frequencies are reported in Figures 4.24–4.25 versus the pedestrian load ranging from zero up to 4 kN/m². The corresponding mode shapes are shown in Figure 4.26. In particular, the first mode (Fig. 4.26a) is governed by lateral vibrations of the whole structure with flexural-torsional displacements of main girders. The second mode (Fig. 4.26b) is mainly ruled by vertical bridge deflections. The small reduction of the frequency values for a null participating mass factor (Figs. 4.24–4.25) indicates a negligible influence of second-order effects for $Q \leq Q_k$. In fact, a frequency crossing changing the mode shape of Figure 4.26a into the critical shape of Figure 4.23 would be observed for impractical loads, in the proximity of the global buckling load. On the other hand, a remarkable influence of the mass associated to the live load is put in evidence by the frequency plots of Figures 4.24–4.25. In fact, for $Q = 4$ kN/m², when α goes from 0 to 0.2, fundamental and second frequencies decrease of about 39% and 44%, respectively.

As is known, in recent years, the highly publicized closure of the London Millennium Bridge alerted footbridge designers to the dynamic response induced by pedestrians, with particular attention to lateral vibrations. In Table 4.V, the typical frequencies of the pedestrian vertical action are reported (Bachmann 2002). Since alternate footsteps apply forces in opposite lateral directions, the predominant lateral forcing frequencies are half of the values of Table 4.V, so lie in the range 0.6–1.7 Hz. On the other hand, in situations of large crowd density, the typical footfall rate is of about 1.4 steps per second or lower (Dallard *et al*. 2001). Hence, the corresponding forcing frequency lies in the range 0.6–1.1 Hz. From results of Figure 4.24, we can conclude that lateral vibrations of the footbridge will not reasonably be excited. As for the vertical vibrations, the frequency associated to the mode of Figure 4.26b lies in the frequency ranges of running and jumping persons (Table 4.V) for $Q \geq 3$ kN/m² and $\alpha \geq 0.6$. On the other hand, the probability to have crowded running or jumping traffic ($Q \geq 3$ kN/m²) is generally low. Therefore, even if a nonlinear dynamic study is probably required to analyze the pedestrian vertical action, no significant resonance phenomena are expected.

Finally, shear strain effects have been proved to be not significant in this case: if they were neglected, an underestimate of the maximum deflection and overestimates of natural frequencies and buckling load not larger than 5% were observed.

4.6 Conclusions

Vibration frequencies and mode shapes of FRP thin-walled beams and pultruded portal frames were extensively analysed by means of a *locking-free* Hermitian FE formulation. A nonlinear displacement field accounting for shear strain effects due to both nonuniform bending and torsion was adopted. The motion equations were derived from Hamilton's principle. Geometrical effects due to axial and lateral concentrated or distributed surface loads were considered.

Comparisons with results of ad-hoc plate-shell models and beam analytical solutions showed the accuracy of the adopted finite element in capturing flexural-torsional frequencies of monosymmetric cross-section FRP profiles, even for external loads not

far from their critical values. The strong influence of shear deformations (especially due to nonuniform torsion) for Carbon-FRP beams was underlined.

Dynamic analyses of Glass-FRP pultruded portal frames subjected to a vertical load distribution were then performed. It was shown that geometrical effects arising from external loads may significantly reduce the natural frequencies, especially in the absence of out-of-plane bracing ($\cong -37\%$ for $q_z/q_{z,cr} = 0.5$). Moreover, strong reductions of natural frequencies were observed even for small participant additional masses. In fact, for pultruded structures, self weight typically is a small fraction of the total loads. It was then proved that neglecting shear strain effects leads to significant overestimates of buckling loads and natural frequencies ($\cong +20\%$). With reference to braced frames, sudden exchanges (frequency crossing) between in-plane and out-of-plane vibration mode shapes were observed. In particular, it was shown that the frequency crossing drastically decreases as the out-of-plane beam stiffness reduces.

Finally, the dynamic response of a footbridge composed by GFRP pultruded profiles was carried out. First and second natural frequency, associated to a lateral and to a vertical vibration mode, respectively, were reported as a function of the pedestrian traffic load. In this case, a not really significant influence of second-order effects was observed up to the characteristic value of the live load. A simple comparison with the typical pacing frequency values put in evidence that pedestrian traffic could excite neither lateral nor vertical vibrations.

Appendix 4.A – Mass matrix of element *H*32

The (14×14) consistent mass matrix of the *locking-free* Hermitian element adopted can be written in the form:

$$\mathbf{M} = \rho \begin{bmatrix} \mathbf{M}^w & \mathbf{0} & \mathbf{0} & \mathbf{0} \\ & \mathbf{M}^u & \mathbf{0} & \mathbf{M}^{u\omega} \\ & & \mathbf{M}^v & \mathbf{M}^{v\omega} \\ Sym & & & \mathbf{M}^\omega \end{bmatrix} \tag{4.A.1}$$

in which the submatrices lying on the main diagonal are symmetrical. All submatrices with the exception of $\mathbf{M}^w$ (2×2) are 4×4 matrices.

In particular, $\mathbf{M}^w$ is given by:

$$\mathbf{M}^w = \frac{Al}{6} \begin{bmatrix} 2 & 1 \\ 1 & 2 \end{bmatrix} \tag{4.A.2}$$

Matrix $\mathbf{M}^u$, see also the work of Kosmatka (1995), is given by:

$$M_{11}^{u} = M_{33}^{u} = \frac{252 J_y + A l^2 \left(78 + 147\phi_x + 70\phi_x^2\right)}{210 l \left(1 + \phi_x\right)^2} \tag{4.A.3}$$

$$M_{13}^{u} = \frac{-252 J_y + A l^2 \left(27 + 63\phi_x + 35\phi_x^2\right)}{210 l \left(1 + \phi_x\right)^2} \tag{4.A.4}$$

$$M_{12}^{u} = -M_{34}^{u} = \frac{-84 J_y \left(-1 + 5\phi_x\right) + A l^2 \left(44 + 77\phi_x + 35\phi_x^2\right)}{840 \left(1 + \phi_x\right)^2} \tag{4.A.5}$$

$$M_{14}^{u} = -M_{23}^{u} = -\frac{84 J_y \left(-1 + 5\phi_x\right) + A l^2 \left(26 + 63\phi_x + 35\phi_x^2\right)}{840 \left(1 + \phi_x\right)^2} \tag{4.A.6}$$

$$M_{22}^{u} = M_{44}^{u} = \frac{28 J_y l \left(4 + 5\phi_x + 10\phi_x^2\right) + A l^3 \left(8 + 14\phi_x + 7\phi_x^2\right)}{840 \left(1 + \phi_x\right)^2} \tag{4.A.7}$$

$$M_{24}^{u} = -\frac{-28 J_y l \left(-1 - 5\phi_x + 5\phi_x^2\right) + A l^3 \left(6 + 14\phi_x + 7\phi_x^2\right)}{840 \left(1 + \phi_x\right)^2} \tag{4.A.8}$$

Matrix $\mathbf{M}^{v}$ is obtained from $\mathbf{M}^{u}$ by replacing J_y and ϕ_x with J_x and ϕ_y respectively, and by changing sign to the terms with an odd index summation.

Similarly, $\mathbf{M}^{\omega}$ is obtained from $\mathbf{M}^{u}$ by replacing J_y, A and ϕ_x with J_ω, $\left(J_x + J_y + A x_S^2 + A y_S^2\right)$ and ϕ_ω respectively, and by changing sign to the terms with an odd index summation.

Matrix $\mathbf{M}^{u\omega}$ is given by:

$$M_{11}^{u\omega} = M_{33}^{u\omega} = \frac{A l y_S \left(156 + 147\phi_x + 147\phi_\omega + 140\phi_x\phi_\omega\right)}{420 \left(1 + \phi_x\right)\left(1 + \phi_\omega\right)} \tag{4.A.9}$$

$$M_{12}^{u\omega} = -M_{34}^{u\omega} = -\frac{A l^2 y_S \left(44 + 42\phi_x + 35\phi_\omega + 35\phi_x\phi_\omega\right)}{840 \left(1 + \phi_x\right)\left(1 + \phi_\omega\right)} \tag{4.A.10}$$

$$M_{13}^{u\omega} = M_{31}^{u\omega} = \frac{A l y_S \left(54 + 63\phi_x + 63\phi_\omega + 70\phi_x\phi_\omega\right)}{420 \left(1 + \phi_x\right)\left(1 + \phi_\omega\right)} \tag{4.A.11}$$

$$M_{14}^{u\omega} = -M_{32}^{u\omega} = \frac{A l^2 y_S \left(26 + 28\phi_x + 35\phi_\omega + 35\phi_x\phi_\omega\right)}{840 \left(1 + \phi_x\right)\left(1 + \phi_\omega\right)} \tag{4.A.12}$$

$$M_{21}^{u\omega} = -M_{43}^{u\omega} = \frac{Al^2 y_S \left(44 + 35\phi_x + 42\phi_\omega + 35\phi_x\phi_\omega\right)}{840\left(1 + \phi_x\right)\left(1 + \phi_\omega\right)} \tag{4.A.13}$$

$$M_{22}^{u\omega} = M_{44}^{u\omega} = -\frac{Al^3 y_S \left(8 + 7\phi_x + 7\phi_\omega + 7\phi_x\phi_\omega\right)}{840\left(1 + \phi_x\right)\left(1 + \phi_\omega\right)} \tag{4.A.14}$$

$$M_{23}^{u\omega} = -M_{41}^{u\omega} = \frac{Al^2 y_S \left(26 + 35\phi_x + 28\phi_\omega + 35\phi_x\phi_\omega\right)}{840\left(1 + \phi_x\right)\left(1 + \phi_\omega\right)} \tag{4.A.15}$$

$$M_{24}^{u\omega} = M_{42}^{u\omega} = \frac{Al^3 y_S \left(6 + 7\phi_x + 7\phi_\omega + 7\phi_x\phi_\omega\right)}{840\left(1 + \phi_x\right)\left(1 + \phi_\omega\right)} \tag{4.A.16}$$

Finally, $\mathbf{M}^{v\omega}$ is obtained from $\mathbf{M}^{u\omega}$ by replacing y_S and ϕ_x with x_S and ϕ_y respectively and by changing sign of the terms of the first and third row.

Chapter 5

Pultruded frames with semirigid connections

5.1 Introduction

In the nineties, extended research programs (Bank *et al.* 1990, Bank *et al.* 1994, Mosallam *et al.* 1994, Smith *et al.* 1999a) were aimed at understanding the behaviour of connections between FRP pultruded members. In fact, as is the case of steel frames, joint flexibility may have a very significant influence on the global behaviour of beam assemblages (Mottram & Bass 1994, Mottram & Zheng 1996, Turvey 1997), and structural design accounting for semirigid end-connections often turns out to be more economical than traditional approaches. Usually, bolted joints are preferred to adhesive bonding, due to higher assembling velocity, to the possibility of disassembling and re-assembling large parts of the structures, and to easier periodical inspection. In principle, bolted connections offer more ductile failure mechanisms but lower resistance; yet, the use of bonded FRP gussets reduces stress concentrations around the holes and significantly increases pin bearing capacity. Recently, Turvey and Cooper (2004) presented a comprehensive review of tests on bolted joints of GFRP profiles, including data about initial rotational stiffness, ultimate moments and ultimate rotations. It was clearly shown that standard (steel-type) connections are disadvantageous, due to the very low resistance offered by the web-to-flange junction of pultruded angle cleats. A significant improvement of the joint behaviour can generally be obtained by means of a single monolithic connection element like the cuff connections for box-section profiles (Smith *et al.* 1999a, Carrion *et al.* 2005a,b). Most of the experimental and numerical (Carrion *et al.* 2005b, Smith *et al.* 1999b) investigations hitherto carried out only consider joints connecting doubly-symmetric cross-section beams bent in the major stiffness plane. However, for a stability analysis, the joint three-dimensional behaviour is necessarily to be evaluated. Hence, an imperfection sensitivity analysis can be developed. In any case, a preliminary buckling analysis is necessary the evaluate the critical mode shapes and the consequent initial imperfections to be assigned. In the present chapter, a stability analysis of GFRP pultruded frames with semirigid connections is presented. The kinematical model presented in Chapter 3, based on a second-order approximation of the displacement field and accounting for the effects of shear deformations due to both nonuniform bending and torsion, is adopted. Once again,

the stability conditions are deduced via energy criterion, by imposing the positive definiteness of the second variation of the total potential energy. Moreover, *locking-free* finite elements of type *H*32 (§ 2.2.1) are used to interpolate the displacement functions unknown. The efficient numerical procedure developed by Shakourzadeh *et al.* (1999) is implemented to take the connection flexibility into account. The method resorts to a simple manipulation of the elastic stiffness matrix, so as to avoid additional connection elements (Blandford 1994). Hence, the inner resultants of the modified elements obtained are used to assemble the geometric stiffness matrix. The approach is quite general because the joint behaviour associated to membrane, shear, bending and torsion deformations as well as to cross-section warping can be taken into account. Finally, it can be demonstrated (see Appendix 5.A) that, for shear-undeformable doubly-symmetric profiles with semirigid moment-rotation behaviour, the modified elastic stiffness matrix reduces to the well known matrix of Monforton and Wu (1963), also reported by Xu (2005).

Aristizábal-Ochoa (2003, 2004, 2007) analyzed shear-deformable spatial beam assemblages with semirigid joints, providing closed-form expressions of critical loads. Yet, in those works doubly-symmetric compact cross-section beams were considered and, consequently, the effect of nonuniform torsion was neglected.

In the following, the influence of connection deformations on buckling loads and critical mode shapes of GFRP pultruded frames is emphasized. A variety of examples is presented, showing the role played by both in-plane and out-of-plane joint rotational flexibility, as well as by lateral bracing stiffness and by base-warping restraints.

5.2 Modeling of flexible joints

In structural analysis of plane frames, the torsional deformations of joints are usually neglected. Moreover, axial and shear joint deformations are also neglected since they are small compared to the bending deformation of most connections. Hence, for practical purposes, only the in-plane rotational deformation of beam-column connections (Fig. 5.1) are considered. On the other hand, a spatial stability analysis accounting for the flexural-torsional behaviour of members necessarily requires a three-dimensional modeling of joints. To this purpose, some authors (Carlberg *et al.* 1990, Blandford 1994) developed hybrid elements collecting the properties of a beam with rigid ends and of separate connection elements with possible warping deformations.
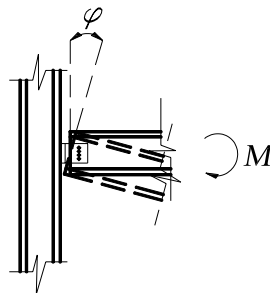

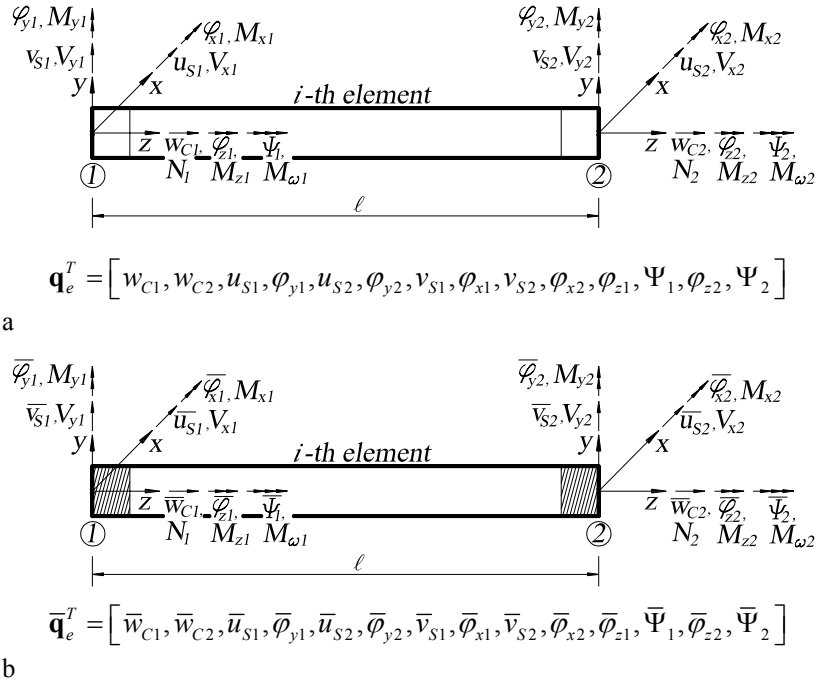Figure 5.1. Rotational deformation of a semirigid joint.

$$\mathbf{q}_e^T = \left[w_{C1}, w_{C2}, u_{S1}, \varphi_{y1}, u_{S2}, \varphi_{y2}, v_{S1}, \varphi_{x1}, v_{S2}, \varphi_{x2}, \varphi_{z1}, \Psi_1, \varphi_{z2}, \Psi_2 \right]$$

a

$$\overline{\mathbf{q}}_e^T = \left[\overline{w}_{C1}, \overline{w}_{C2}, \overline{u}_{S1}, \overline{\varphi}_{y1}, \overline{u}_{S2}, \overline{\varphi}_{y2}, \overline{v}_{S1}, \overline{\varphi}_{x1}, \overline{v}_{S2}, \overline{\varphi}_{x2}, \overline{\varphi}_{z1}, \overline{\Psi}_1, \overline{\varphi}_{z2}, \overline{\Psi}_2 \right]$$

b

Figure 5.2. Beam finite element with rigid (a) or semirigid (b) end connections, subjected to a set of nodal forces $\mathbf{r}_e$ where: $\mathbf{r}_e^T = \left[N_1, N_2, V_{x1}, M_{y1}, V_{x2}, M_{y2}, V_{y1}, M_{x1}, V_{y2}, M_{x2}, M_{z1}, M_{\omega1}, M_{z2}, M_{\omega2} \right]$.

In this way, additional degrees of freedom were generally introduced and static condensation is consequently required before assembling the global stiffness matrix (Lui & Chen 1986, Lui & Chen 1987, Goto & Chen 1987).

In order to save the number of degrees of freedom, a modified finite element including two elastically deformable ends is defined in this chapter, following the proposal of Shakourzadeh *et al.* (1999). Hence, with reference to the *i*-th element, the first-order equilibrium equation:

$$\mathbf{r}_e = \mathbf{K}_E^e \mathbf{q}_e - \mathbf{f}_e \tag{5.1}$$

is replaced by the relation:

$$\mathbf{r}_e = \overline{\mathbf{K}}_E^e \overline{\mathbf{q}}_e - \overline{\mathbf{f}}_e \tag{5.2}$$

where $\mathbf{r}_e$ is the vector of nodal forces; $\mathbf{q}_e$, $\mathbf{K}_E^e$ and $\mathbf{f}_e$ are the vector of nodal displacements, the elastic stiffness matrix and the equivalent load vector, respectively, of the element with rigid end connections (Fig. 5.2a), whereas $\overline{\mathbf{q}}_e$, $\overline{\mathbf{K}}_E^e$ and $\overline{\mathbf{f}}_e$ represent the vector of nodal displacements, the elastic stiffness matrix and the equivalent load vector, respectively, of the modified element (Fig. 5.2b).

In particular, vector $\overline{\mathbf{q}}_e$ takes the connection deformations into account by means of the additive relation:

$$\overline{\mathbf{q}}_e = \mathbf{q}_e + \mathbf{q}_J \tag{5.3}$$

where vector $\mathbf{q}_J$ is connected to $\mathbf{r}_e$ by the constitutive relation:

$$\mathbf{r}_e = \mathbf{K}_J \mathbf{q}_J \tag{5.4}$$

Assuming uncoupled joint constitutive relations yields the simplest form of matrix $\mathbf{K}_J$:

$$\mathbf{K}_J = \text{diag}\left\{K_{w1}, K_{w2}, K_{u1}, K_{u2}, K_{y1}, K_{y2}, K_{v1}, K_{v2}, K_{x1}, K_{x2}, K_{z1}, K_{z2}, K_{\Psi 1}, K_{\Psi 2}\right\} \tag{5.5}$$

where $i = 1, 2$ refers to the element end sections; coefficients K_{wi}, K_{ui} and K_{vi} represent the joint stiffnesses related to resultants N_i, V_{xi} and V_{yi}; coefficients K_{xi}, K_{yi} and K_{zi} are the joint rotational stiffnesses referred to resultants M_{xi}, M_{yi} and M_{zi} and, finally, $K_{\Psi i}$ represents the joint stiffness acting on cross-section warping. Substituting $\mathbf{q}_e = \overline{\mathbf{q}}_e - \mathbf{q}_J$ into Eq. 5.1 and remembering Eq. 5.4 yield:

$$\mathbf{r}_e = \mathbf{C}\mathbf{K}_E^e \overline{\mathbf{q}}_e - \mathbf{C}\mathbf{f}_e \tag{5.6}$$

where:

$$\mathbf{C} = \mathbf{K}_J \left(\mathbf{K}_J + \mathbf{K}_E^e\right)^{-1} = \left(\mathbf{I} + \mathbf{K}_E^e \mathbf{K}_J^{-1}\right)^{-1} \tag{5.7}$$

Comparing Eq. 5.6 with Eq. 5.2 yields stiffness matrix and equivalent load vector of the modified element:

$$\overline{\mathbf{K}}_E^e = \mathbf{C}\mathbf{K}_E^e; \qquad \overline{\mathbf{f}}_e = \mathbf{C}\mathbf{f}_e \tag{5.8}$$

It can be easily shown that the modified matrix $\overline{\mathbf{K}}_E^e$ still is symmetric. Moreover, the two limit cases of pinned and rigid connections can be re-obtained. In fact, the first case is recovered by setting the corresponding coefficient of matrix $\mathbf{K}_J$ equal to zero whereas, for rigid joints, $\mathbf{C} = \mathbf{I}$ makes Eq. 5.6 coincide with Eq. 5.1. The modified matrix $\overline{\mathbf{K}}_E^e$ based on the uncoupled constitutive relation 5.5 and obtained using the *locking-free* formulation $H32$ (§ 2.2.1) is reported in Appendix 5.A assuming semirigid connections for flexural rotations and warping displacements. In particular, for a plane bending problem, the reported matrix $\overline{\mathbf{K}}_E^e$ reduces, if shear deformations are neglected, to the matrix given by Monforton and Wu (1963).

To solve linearized buckling problems, the inner resultants obtained by means of the modified elastic stiffness matrix $\overline{\mathbf{K}}_E^e$ are used to build the geometric stiffness matrix (Shakourzadeh *et al.* 1999).
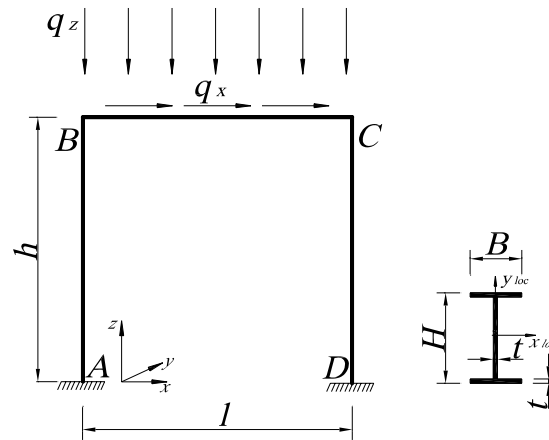
Figure 5.3. GFRP pultruded portal frame ($E = 25$ GPa, $G = E/10$) with $l = h = 3.0$ m. § 5.3.1: beam subjected to vertical load q_z acting along the beam top flange. Wide-flange profiles with $H = B = 203.2$ mm, $t = 9.5$ mm; $x_{loc(beam)}$ // y, $x_{loc(columns)}$ // x. § 5.3.2–5.3.6: beam subjected to a centroidal horizontal load q_x. I-section profiles with $H = 240.0$ mm, $B = 120.0$ mm, $t = 12.0$ mm; $x_{loc(beam)}$ // $x_{loc(columns)}$ // y.
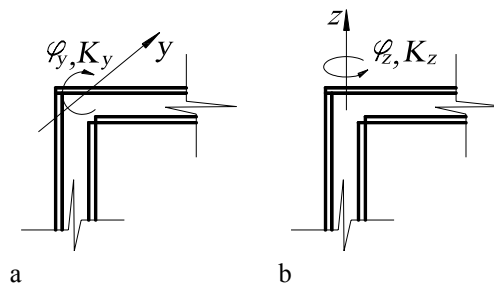

Figure 5.4. In-plane (a) and out-of plane (b) rotations and stiffnesses of the beam-column joint.

5.3 Buckling analysis of semirigid pultruded frames

In Chapter 3, a buckling analysis of FRP portal frames subjected to in-plane or lateral distributed loads was presented. Particular attention was paid to the influence of shear deformations and to the role of both out-of-plane bracing systems and base-warping restraints. At the beam-column connections, continuity was imposed on displacements and rotations whereas warping displacements were assumed to be totally unrestrained. The following numerical examples are intended to show the influence of the connection stiffness on the buckling behaviour of GFRP-pultruded portal frames (Fig. 5.3) subjected to vertical or horizontal loads uniformly distributed along the beam. Wide-flange and I-section profiles, showing $E = 25$ GPa and $G = E/10$, are adopted. Diagonal joint stiffness matrix 5.5, corresponding to uncoupled joint constitutive relations, is assumed. Due to the frame symmetry, joint stiffness values are referred to half frame only (nodes A and B of Fig. 5.3). Six cases are presented to show the influence of semirigid in-plane and out-of-plane rotational connections (ruled by K_{yB}
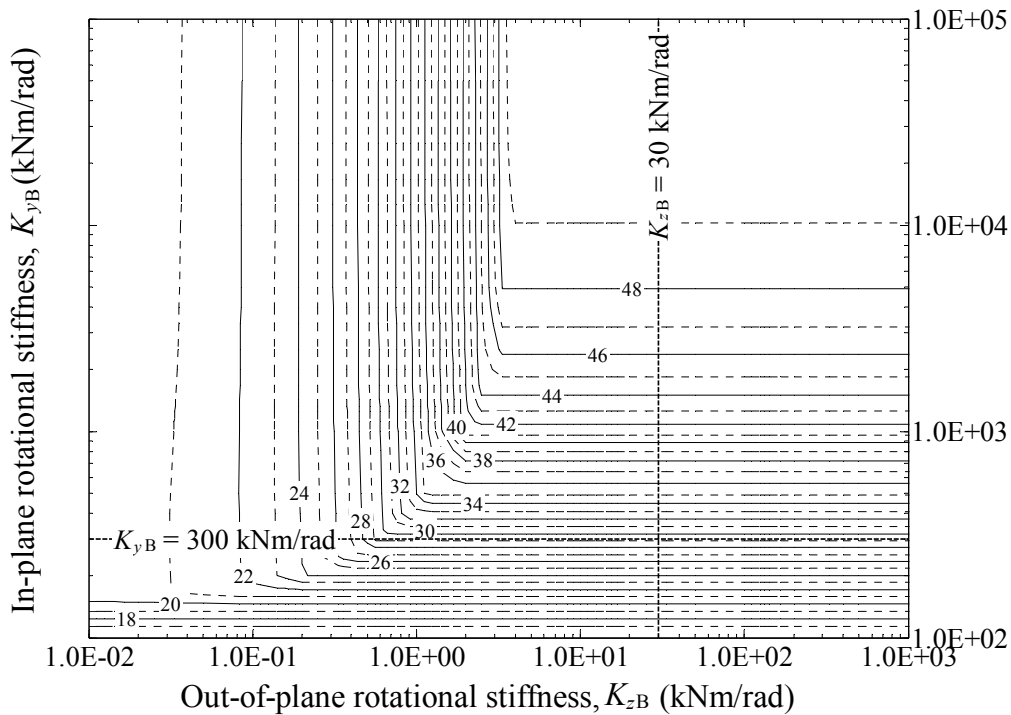
Figure 5.5. Portal frame of § 5.3.1 (no lateral bracing). Level curves of the buckling vertical load vs. in-plane (K_{yB}) and out-of-plane (K_{zB}) rotational stiffness at the beam-column joints.

and K_{zB}, respectively, Fig. 5.4), the role of lateral bracing at beam-column nodes (ruled by K_{brB}) and, finally, the influence of semirigid base-warping restraints (ruled by $K_{\Psi A}$). Four $H32$ finite elements for each member are adopted.

5.3.1 Critical vertical load for in-plane and out-of-plane semirigid joints

The first example is aimed at evaluating the buckling loads in the presence of semirigid in-plane and out-of-plane beam-column rotational joints (ruled by K_{yB} and K_{zB} respectively). A uniformly-distributed vertical load q_z is applied at the top flange of the beam. All shapes are wide-flange profiles and, in particular, the frame plane contains the maximum and the minimum second area moment of the beam and columns, respectively. No restraints are imposed on in-plane rotations ($K_{yA} = 0$). Furthermore, no lateral bracing ($K_{brB} = 0$) at the beam-column joints is introduced and warping displacements are considered fully restrained at the beam ends ($K_{\Psi B(beam)} \to \infty$) but left free at the column top sections ($K_{\Psi B(columns)} = 0$). The remaining degrees of freedom at the column bases are given null values.

The level curves of Figure 5.5 show the graph of the critical load $q_{z,cr}$ versus in-plane and out-of-plane rotational stiffness K_{yB} and K_{zB}. In particular, the section at $K_{yB} = 300$ kNm/rad of Figure 5.5 is shown in Figure 5.6, revealing a buckling shape exchange for $K_{zB} \cong 0.5$ kNm/rad. In fact, for $K_{zB} \le 0.5$ kNm/rad (curve a in Fig. 5.6), instability is characterized by flexural-torsional beam displacements associated with significant column torsional deformations (Fig. 5.7a) whereas, for $K_{zB/C} \ge 0.5$ kNm/rad (curve b in Fig. 5.6), in-plane antisymmetrical frame deflection occurs (Fig. 5.7b).
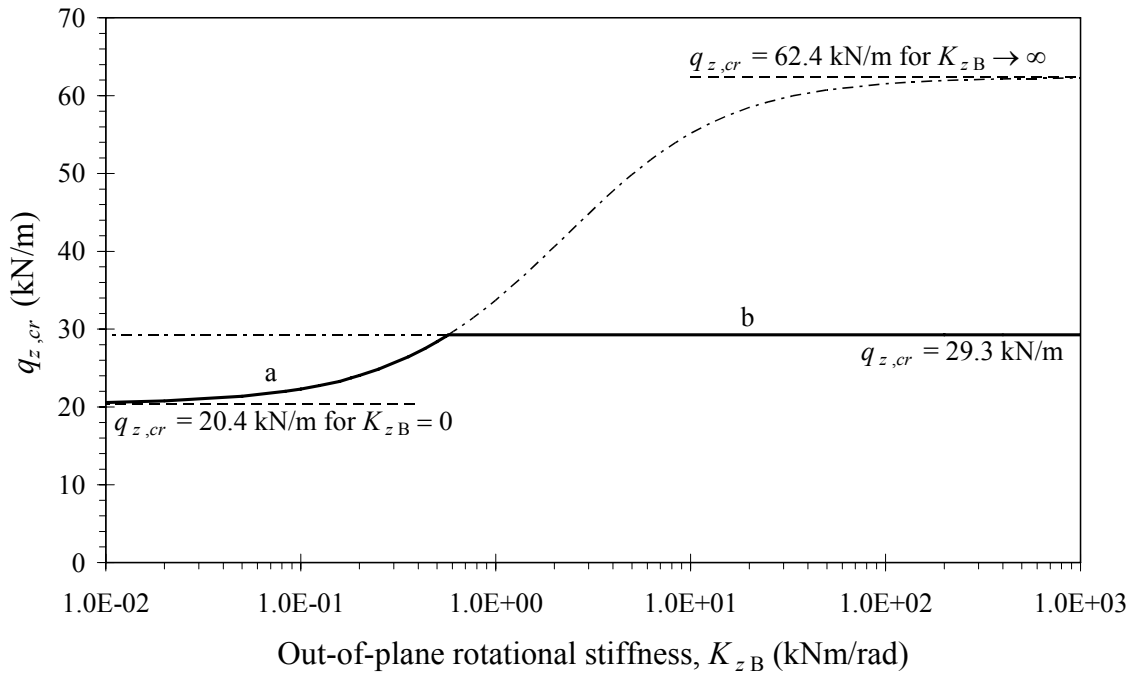
Figure 5.6. Critical vertical load of the portal frame of § 5.3.1 vs. out-of-plane rotational stiffness at the beam-column joints (K_{zB}). Section of level curves of Fig. 5.5 at $K_{yB} = 300$ kNm/rad. Curves a and b refer to the buckling modes shown in Fig. 5.7.
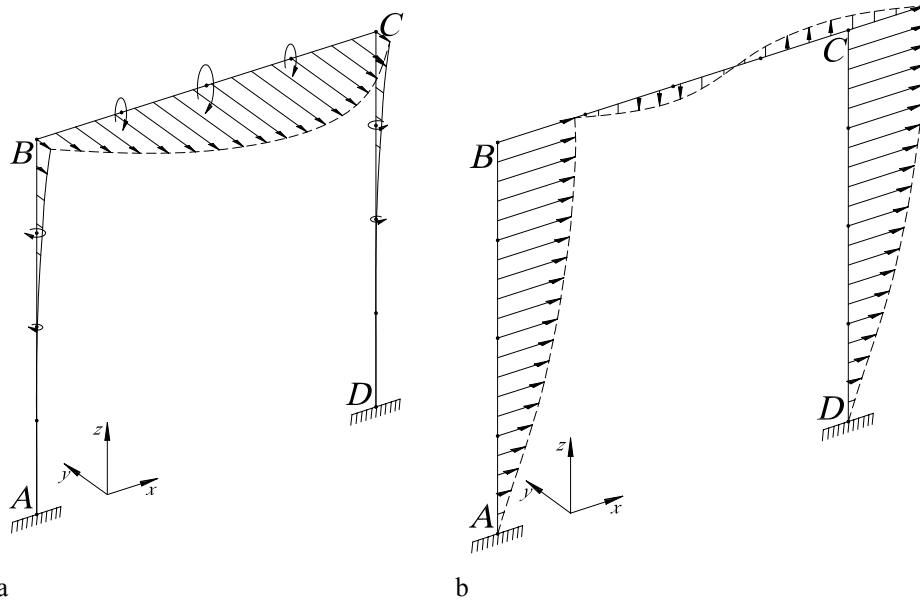

Figure 5.7. Buckling shapes of the portal frame of § 5.3.1 with no lateral bracing (load q_z uniformly distributed along the beam top flange). Straight and circular arrows indicate in- or out-of plane displacements and torsional rotations, respectively. Shapes a and b refer to curves a and b of Fig. 5.6, respectively.
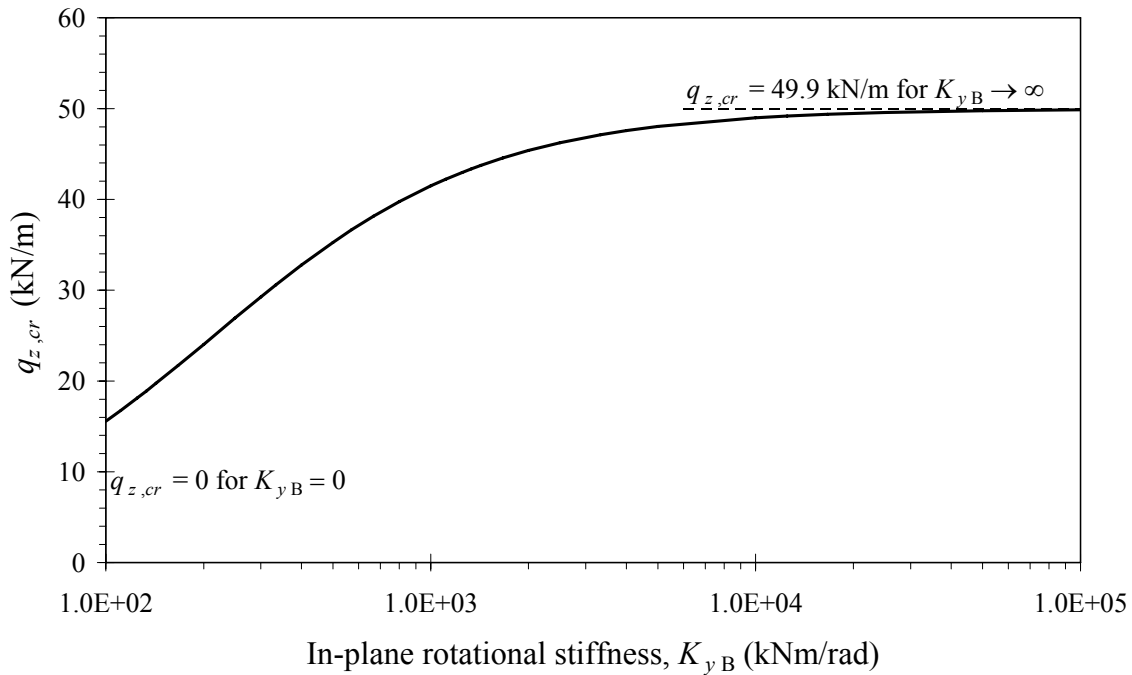
Figure 5.8. Critical vertical load of the portal frame of § 5.3.1 vs. in-plane rotational stiffness at the beam-column joints (K_{yB}). Section of the level curves of Fig. 5.5 at K_{zB} = 30 kNm/rad.

Figure 5.8 shows the section of the $q_{z,cr}$ plot (Fig. 5.5) at K_{zB} = 30 kNm/rad. In this case, for the whole interval $10^2 \leq K_{yB} \leq 10^5$ kNm/rad, the buckling shape is characterized by in-plane frame deflections. The buckling load ranges between $q_{z,cr}$ = 49.9 kN/m for $K_{yB} \rightarrow \infty$ and $q_{z,cr}$ = 0 for K_{yB} = 0 (four hinges at the frame nodes).

5.3.2 Critical horizontal load for in-plane and out-of-plane semirigid joints

In this example, a horizontal load q_x uniformly distributed along the beam is considered. The influence of in-plane (K_{yB}) and out-of-plane (K_{zB}) rotational stiffness at nodes B and C on the frame instability is analyzed. All members are I-section profiles presenting the maximum second area moment in the frame plane. Columns are assumed to be fully fixed but free to warp ($K_{\Psi A}$ = 0) at the base. Moreover, rigid lateral supports ($K_{brB} \rightarrow \infty$) and no warping restraints ($K_{\Psi B}$ = 0) are introduced at beam-column joints.

The pre-buckling state is characterized by an antisymmetrical deflection. In particular, for low values of the in-plane flexural stiffness K_{yB} at the beam-column nodes, each column tends to behave like a cantilever subjected to a transversal tip force at the free end. Viceversa, high values of joint flexural stiffness K_{yB} determine an antisymmetrical beam deflection associated to tensile and compressive forces in the adjacent columns.

The level curves of Figure 5.9 show the graph of the critical load $q_{x,cr}$ versus in-plane (K_{yB}) and out-of-plane (K_{zB}) joint rotational stiffness at node B (C). Sections of $q_{x,cr}$ graph for different values of the out-of-plane stiffness K_{zB} are reported in Figure 5.10. It should be noted that the buckling load is not a monotonic function of the in-plane stiffness K_{yB}.
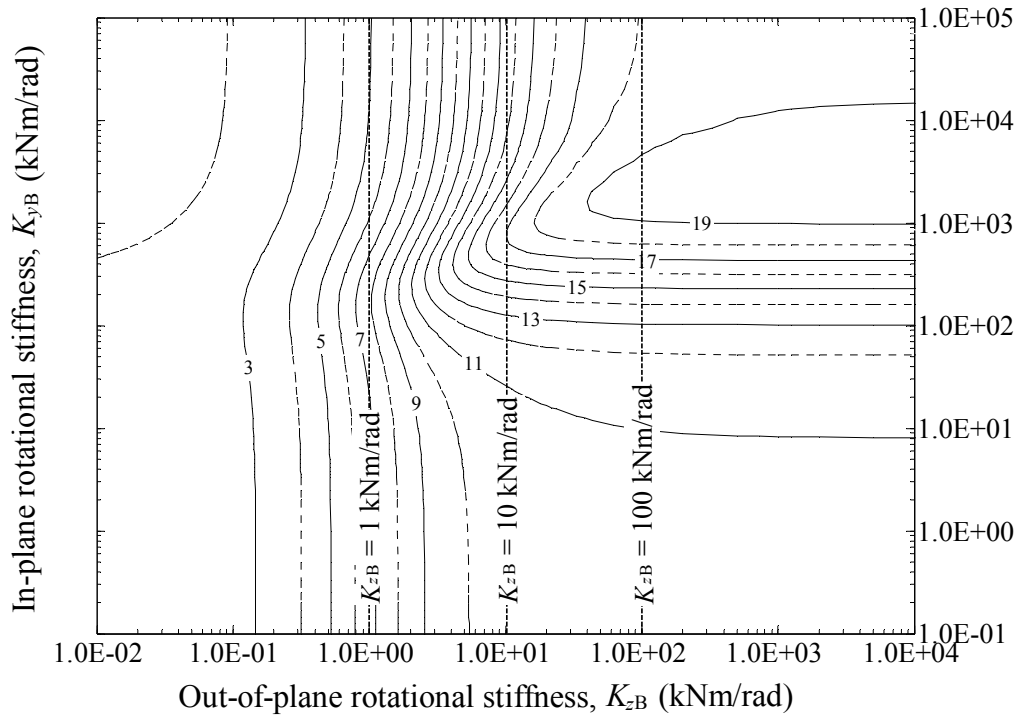
Figure 5.9. Portal frame of § 5.3.2 (rigid lateral bracing). Level curves of the buckling horizontal load vs. in-plane (K_{yB}) and out-of-plane (K_{zB}) rotational stiffness at the beam-column joints.
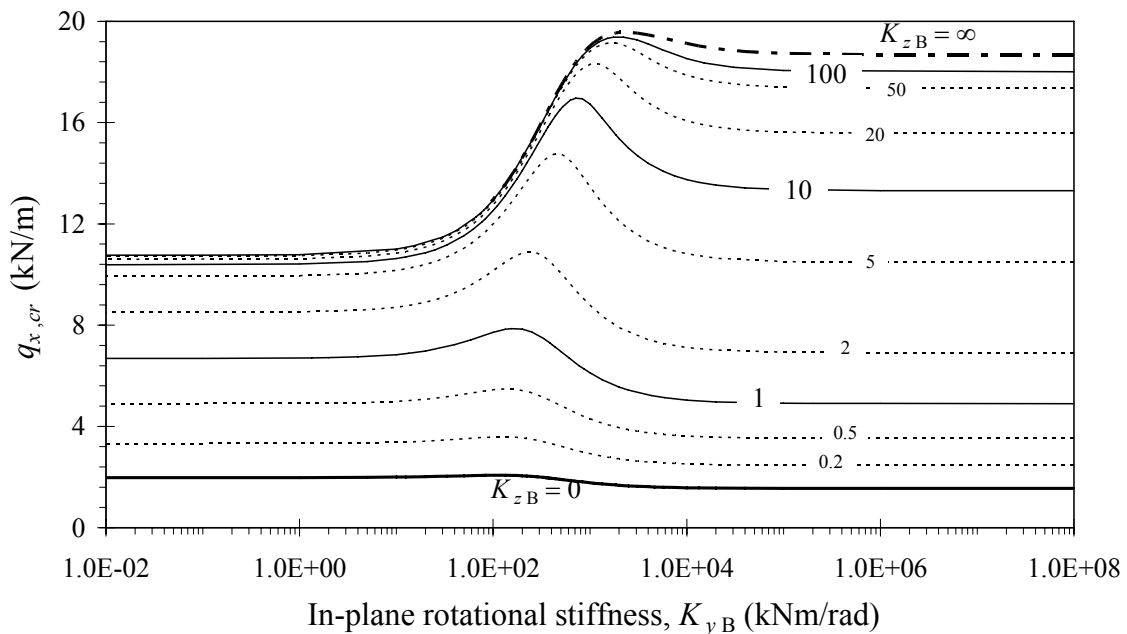

Figure 5.10. Critical horizontal load of the portal frame of § 5.3.2 vs. in-plane rotational stiffness at the beam-column joints (K_{yB}). Sections of the level curves of Fig. 5.9 for different values of the out-of-plane joint rotational stiffness K_{zB}.
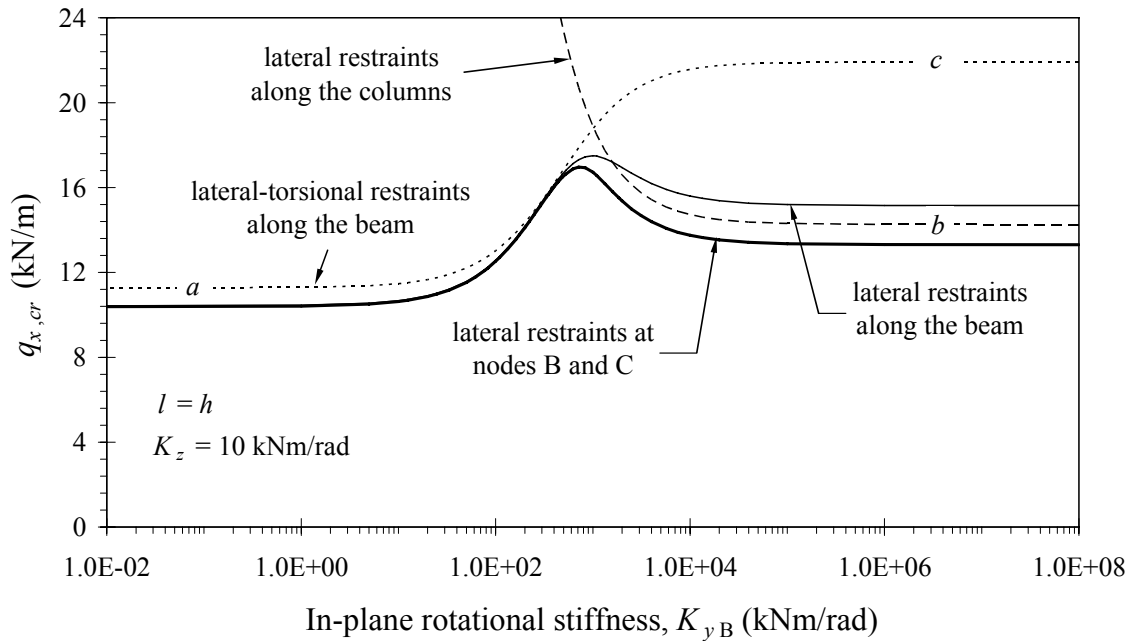
Figure 5.11. Critical horizontal load of the portal frame of § 5.3.2 with $K_{zB} = 10$ kNm/rad vs. in-plane rotational stiffness at the beam-column joints (K_{yB}) for different restraint conditions. Letters a, b and c correspond to the buckling shapes shown in Fig. 5.13.
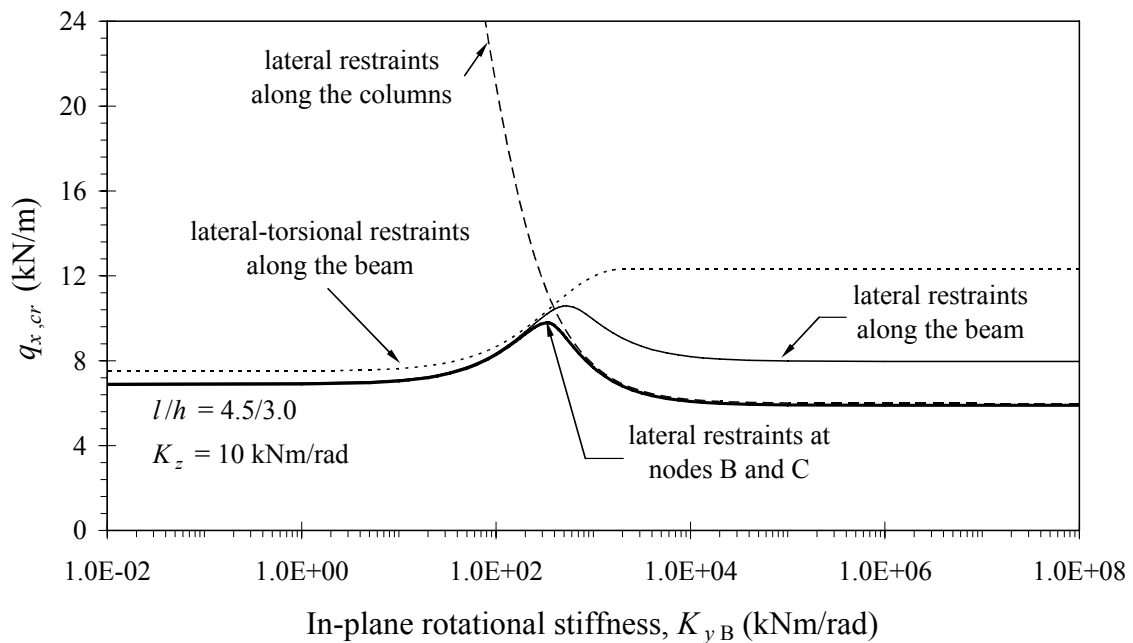

Figure 5.12. Critical horizontal load of a portal frame with $l = 4.5$ m, $h = 3.0$ m ($K_{zB} = 10$ kNm/rad) vs. in-plane rotational stiffness at the beam-column joints (K_{yB}) for different restraint conditions.

To explain this unusual response the buckling load was re-determined for $K_{zB} = 10$ (kNm/rad) assuming three different constraint conditions, i.e.: preventing both lateral and torsional displacements of the beam; lateral displacements of columns, and, finally, lateral beam displacements only. The curve $K_{zB} = 10$ of Figure 5.10 is compared with the response of the three limit cases in Figure 5.11. It can be observed that, for relatively low values of the in-plane joint stiffness, the buckling shape of the frame with lateral restraints at nodes B and C is essentially ruled by the flexural-torsional instability of the compressed column (Fig. 5.13a). Viceversa, as the in-plane joint stiffness increases, the frame response is ruled by the beam flexural-torsional instability (Fig. 5.13b). A similar response can be found assuming a ratio $l/h = 4.5/3.0$ (Fig. 5.12).
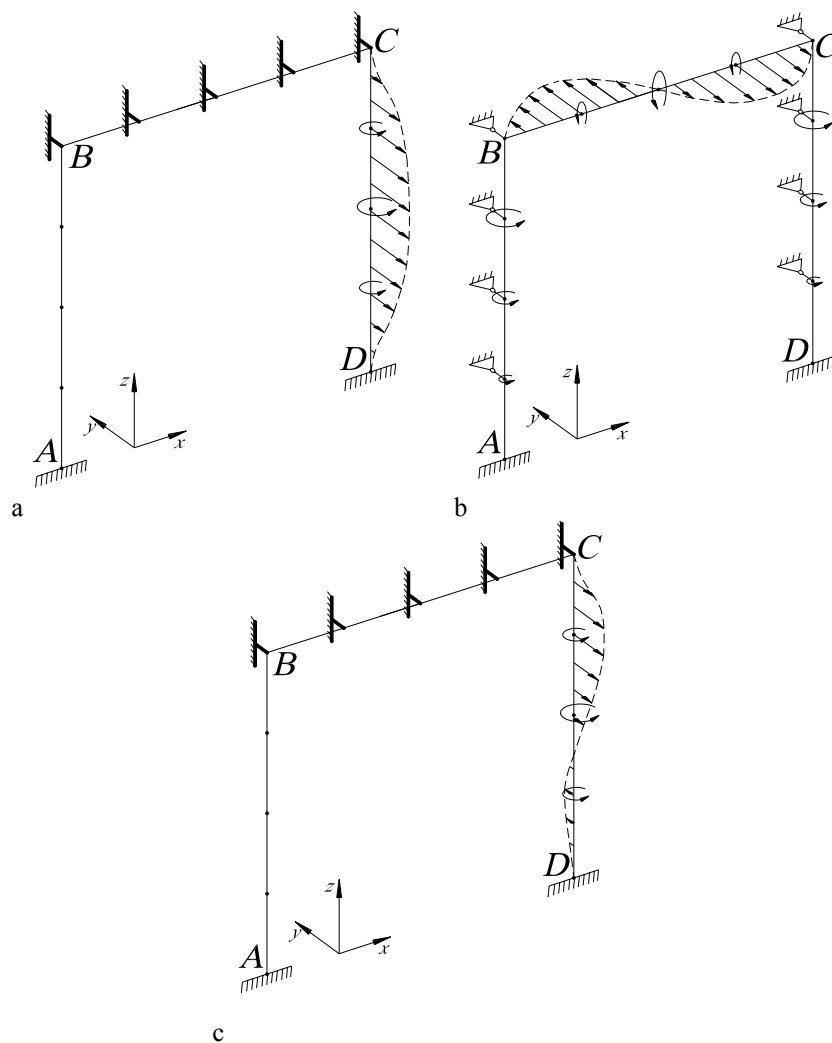

Figure 5.13. Buckling shapes of the portal frame of § 5.3.2 (load q_x uniformly distributed along the beam). a: lateral-torsional restraints along the beam, low in-plane joint stiffness K_{yB}. b: lateral restraints along the columns. c: lateral-torsional restraints along the beam, high in-plane joint stiffness K_{yB}.

5.3.3 Stiffness combined influence of in-plane rotational joints and base-warping restraints

Two more cases are analyzed for the frame of example 5.3.2 to combine the influence of in-plane rotational stiffness at the beam-column connections (ruled by K_{yB}) with that of the warping restraint stiffness at the column bases (ruled by $K_{\Psi A}$).

Figure 5.14 shows the level curves of the buckling load versus K_{yB} and $K_{\Psi A}$, assuming free out-of-plane relative rotations at the beam-column connections ($K_{zB} = 0$). In Figure 5.15, the critical horizontal load $q_{x,cr}$ is reported versus in-plane joint rotational stiffness K_{yB}, for some values of the base-warping restraint stiffness $K_{\Psi A}$. It can be noted that the degree of warping restraint at the column bases has a significant influence on the buckling load. For example, for $K_{yB} = 100$ kNm/rad setting $K_{\Psi A} = 1$ (10) kNm^3/rad makes $q_{x,cr}$ increase of about 28% (60%), with respect to analogous case with null warping restraint stiffness ($K_{\Psi A} = 0$). Furthermore, it could be verified that, for $K_{\Psi A} \geq 50$ kNm^3/rad, the frame behaves as if it were fully fixed at the base.

In turn, Figure 5.16 shows the level curves of the critical horizontal load $q_{x,cr}$ versus K_{yB} and $K_{\Psi A}$, assuming rigid beam-column connections for out-of-plane rotations ($K_{zB} \rightarrow \infty$). Sections of the contour plot of Figure 5.16 for some values of the base-warping restraint stiffness $K_{\Psi A}$ are reported in Figure 5.17.
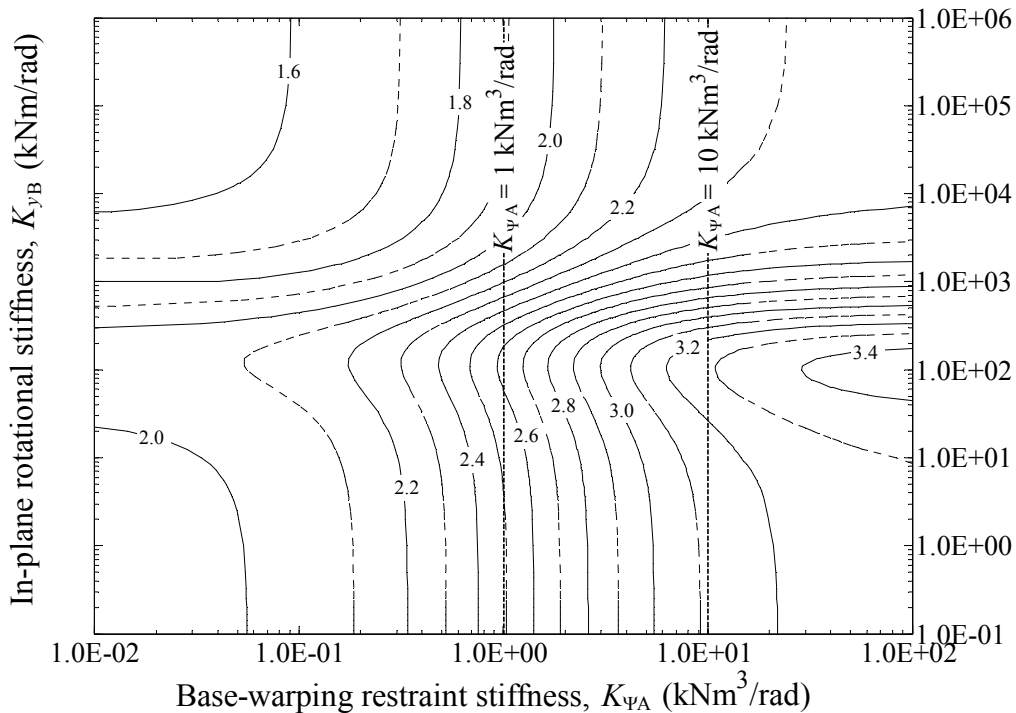

Figure 5.14. Portal frame of § 5.3.3 (rigid lateral bracing) with free out-of-plane rotations at the beam-column joints ($K_{zB} = 0$). Level curves of the buckling horizontal load vs. in-plane rotational stiffness at the beam-column joints (K_{yB}) and base-warping restraint stiffness ($K_{\Psi A}$).

Figure 5.15. Critical horizontal load of the portal frame of § 5.3.3 with $K_{zB} = 0$ vs. in-plane rotational stiffness at the beam-column joints (K_{yB}). Sections of the level curves of Figure 5.14 for different values of the base-warping restraint stiffness ($K_{\Psi A}$).
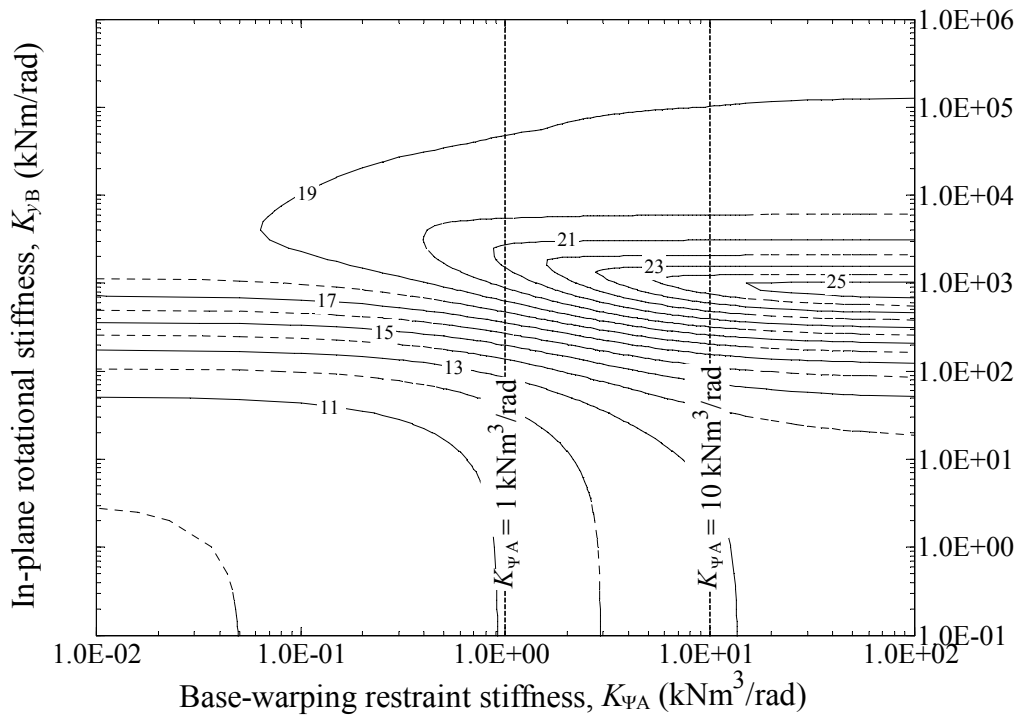
Figure 5.16. Portal frame of § 5.3.3 (rigid lateral bracing) with rigid out-of-plane rotations at the beam-column joints ($K_{zB} \to 0$). Level curves of the buckling horizontal load vs. in-plane rotational stiffness at the beam-column joints (K_{yB}) and base-warping restraint stiffness ($K_{\Psi A}$).
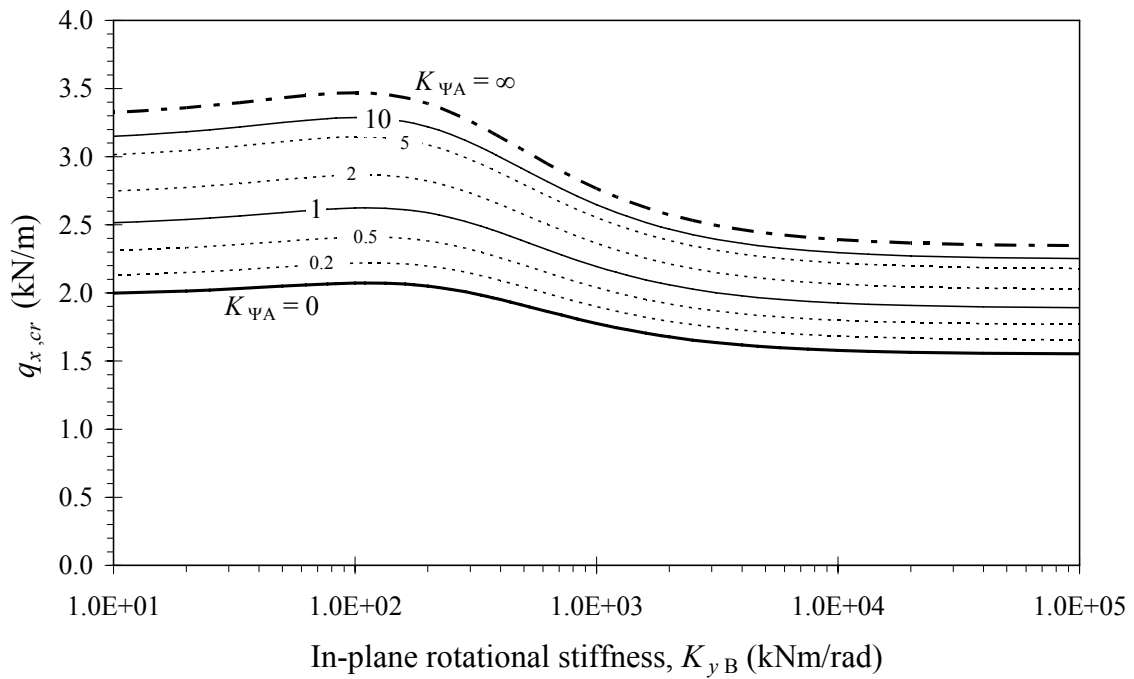
Figure 5.17. Critical horizontal load of the portal frame of § 5.3.3 with $K_{zB} \to 0$ vs. in-plane rotational stiffness at the beam-column joints (K_{yB}). Sections of the level curves of Figure 5.16 for different values of the base-warping restraint stiffness ($K_{\Psi A}$).
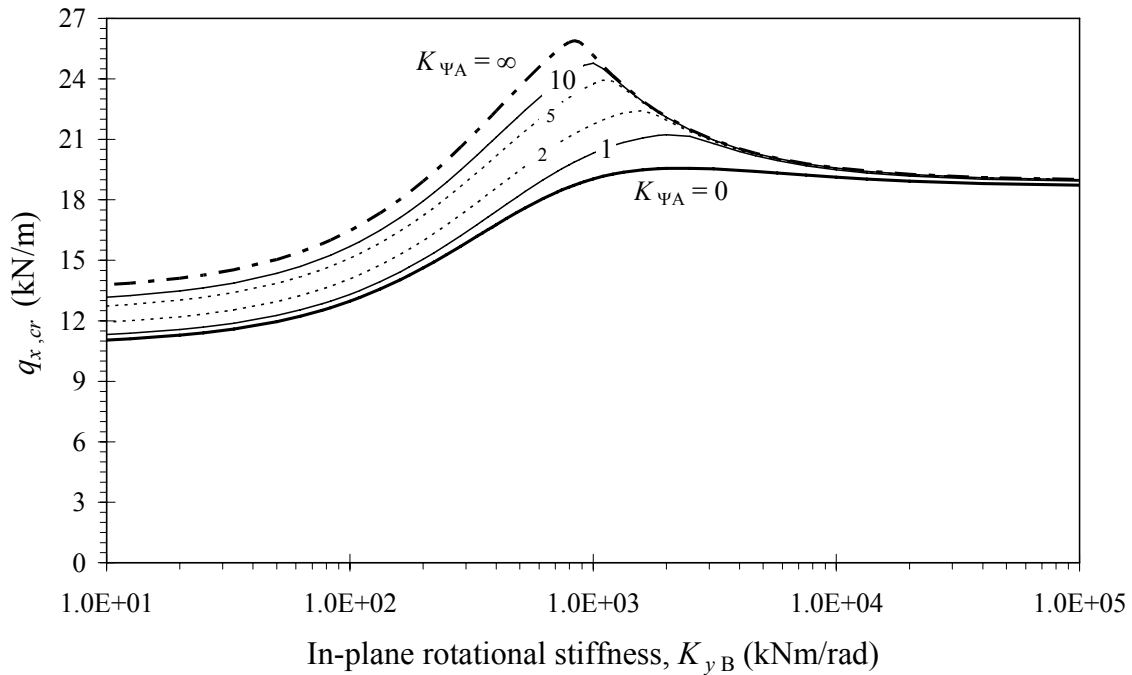
It can be observed that the case $K_{zB} \to \infty$ gives a buckling load even 10 times larger than the case $K_{zB} = 0$ (Figs. 5.14–5.15). Moreover, $q_{x,cr}$ takes the maximum value for $K_{yB} \cong 1 \cdot 10^3$ kNm/rad, more pronounced for high base-warping restraint stiffness. In fact, for $K_{yB} \leq 800$ kNm/rad, the buckling frame response mainly involves flexural-torsional displacements of the compressed column (C-D) and $q_{x,cr}$ increases with K_{yB}. On the contrary, for $K_{yB} \geq 1 \cdot 10^3$ kNm/rad and $K_{\Psi A} \geq 5$ kNm³/rad, the buckling shape is mainly characterized by antisymmetrical flexural-torsional displacements of the beam and $q_{x,cr}$ decreases with K_{yB}.

5.3.4 Stiffness combined influence of out-of-plane rotational joints and base-warping restraints

In this example, the critical horizontal load $q_{x,cr}$ is evaluated versus out-of-plane rotational stiffness at the beam column joints (K_{zB}) and warping restraint stiffness at the column bases ($K_{\Psi A}$), assuming semirigid in-plane beam-column connections with $K_{yB} = 450$ kNm/rad. The level curves of $q_{x,cr}$ and their sections for some values of the base-warping restraint stiffness $K_{\Psi A}$ are reported in Figures 5.18 and 5.19, respectively. Once again, the influence of the degree of base-warping restraint turns out to be significant. For example, for $K_{zB} = 100$ kNm/rad, setting $K_{\Psi A} = 1$ (10) kNm³/rad makes $q_{x,cr}$ increase of about 7% (26%), with respect to analogous case with null warping restraint stiffness ($K_{\Psi A} = 0$).
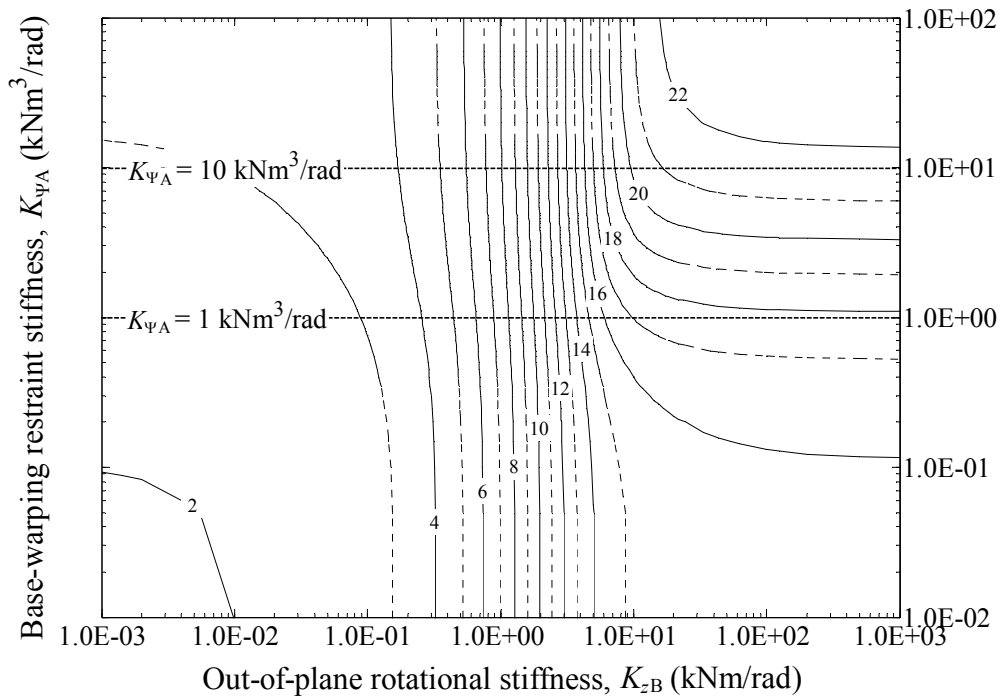
Figure 5.18. Portal frame of § 5.3.4 (rigid lateral bracing) with in-plane rotational stiffness of beam-column joints K_{yB} = 450 kNm/rad. Level curves of the buckling horizontal load vs. base-warping restraint stiffness ($K_{\Psi A}$) and out-of-plane rotational stiffness at the beam-column joints (K_{zB}).

Figure 5.19. Critical horizontal load of the portal frame of § 5.3.4 with K_{yB} = 450 kNm/rad vs. out-of-plane rotational stiffness at the beam-column joints (K_{zB}). Sections of the level curves of Fig. 5.18 for different values of the base-warping restraint stiffness ($K_{\Psi A}$).

5.3.5 Critical horizontal load in the absence of lateral bracings

In the present section, two more cases are analyzed, in the absence of lateral bracing systems ($K_{brB} = 0$), for free ($K_{\Psi A} = 0$) and totally prevented ($K_{\Psi A} \to \infty$) base-warping displacements. Correspondingly, Figures 5.20 and 5.21 show the level curves of the critical horizontal load $q_{x,cr}$ versus in-plane (K_{yB}) and out-of-plane (K_{zB}) rotational stiffness of the beam column connections. The analogous results in the presence of semirigid base-joints for warping displacements are not reported for the sake of brevity. The sections of the contour plots of Figures 5.20–5.21 and the buckling curves for some other values of the base-warping restraint stiffness $K_{\Psi A}$ are reported in Figure 5.22 for $K_{yB} = 450$ kNm/rad, showing that the base-warping restraints may determine a buckling load increase ranging between 62% and 68%.

Moreover, for values of K_{zB} about 2–4 kNm/rad, the buckling curves of Figure 5.22 show a sudden change in slope revealing a critical-shape exchange. In fact, before the change in slope, the buckling shape is mainly ruled by flexural-torsional instability of the compressed column (Fig. 5.23a), whereas, for greater values of K_{zB}, the frame buckles according to an out-of-plane antisymmetrical mode shape (Fig. 5.23b).

In Figure 5.24, the sections of the contour plots of Figures 5.20 ($K_{\Psi A} = 0$) and 5.21 ($K_{\Psi A} \to \infty$) and the buckling curves for some other values of the base-warping restraint stiffness $K_{\Psi A}$ are reported for $K_{zB} = 100$ kNm/rad, showing that, for $K_{\Psi A} > 2$ kNm^3/rad, the buckling load takes a maximum value for $K_{yB} \cong 3 \cdot 10^3$ kNm/rad.
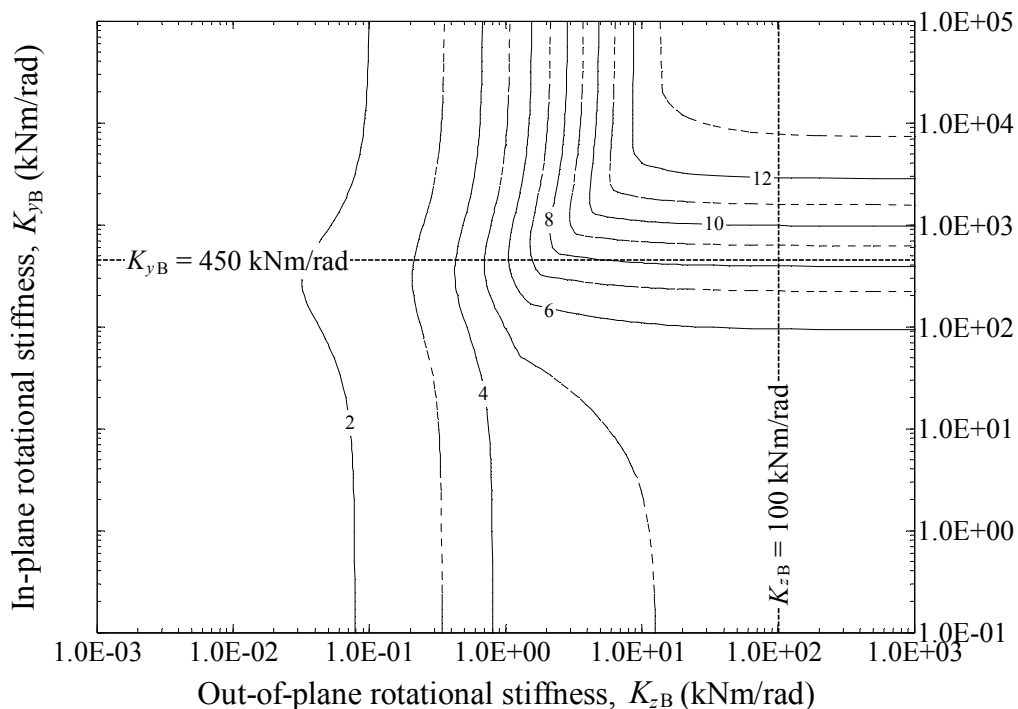
Figure 5.20. Portal frame of § 5.3.5 (no lateral bracing) with free base-warping displacements ($K_{\Psi A}$ = 0). Level curves of the buckling horizontal load vs. in- (K_{yB}) and out-of-plane (K_{zB}) rotational stiffness at the beam-column joints.
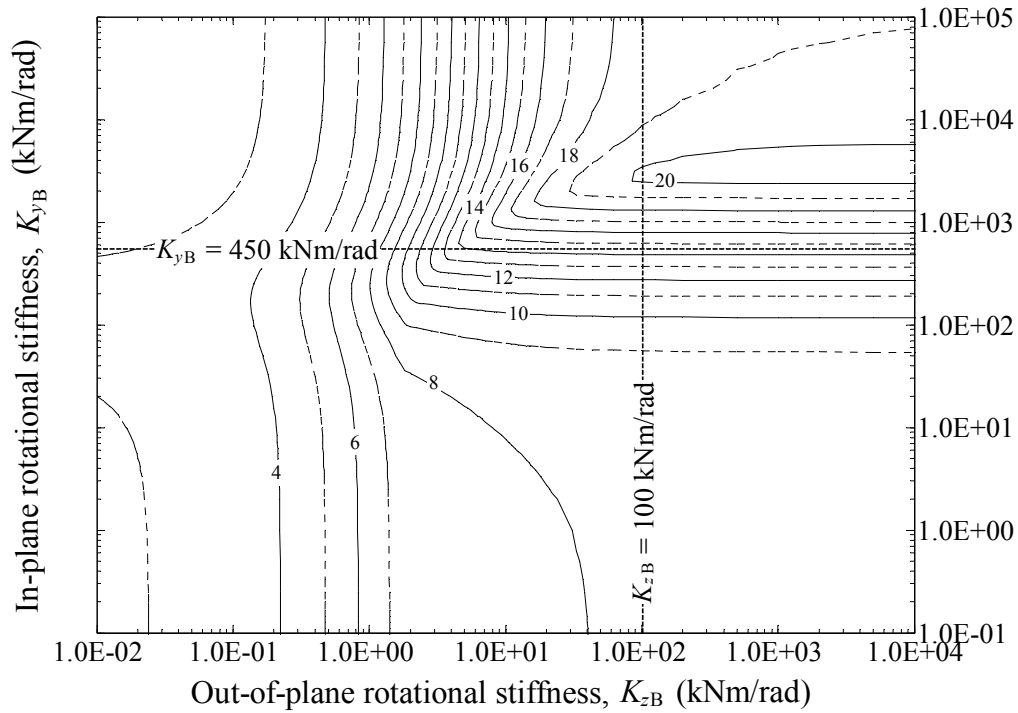
Figure 5.21. Portal frame of § 5.3.5 (no lateral bracing) with base-warping displacements totally prevented ($K_{\Psi A} \to \infty$). Level curves of the buckling horizontal load vs. in- (K_{yB}) and out-of-plane (K_{zB}) rotational stiffness at the beam-column joints.
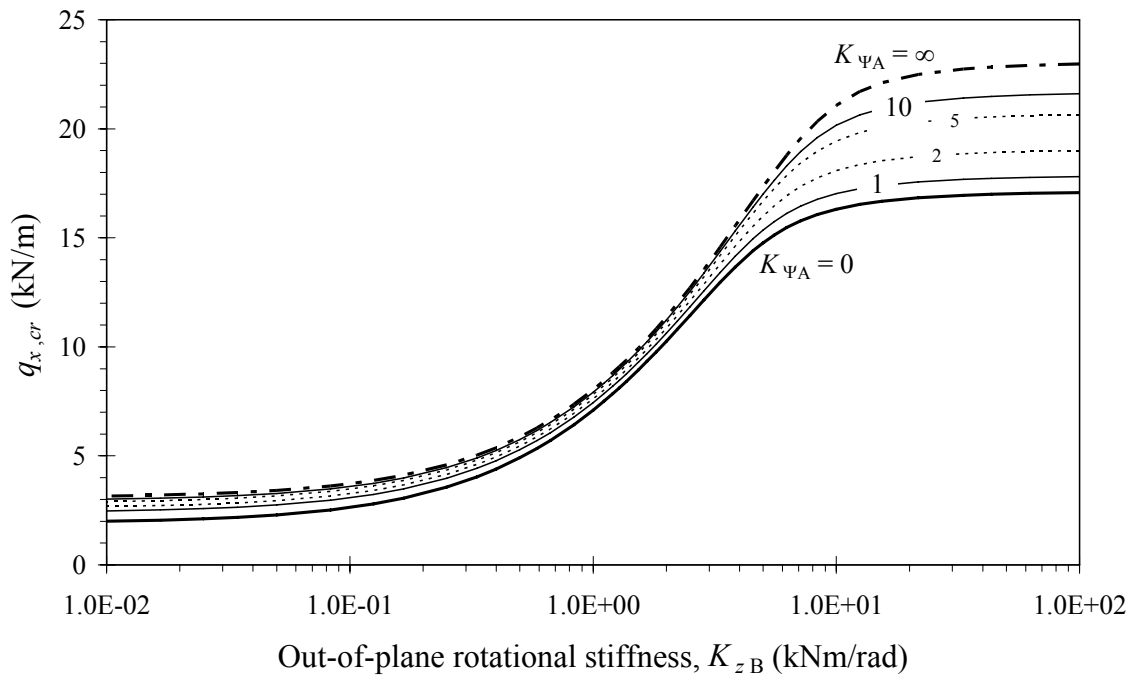

Figure 5.22. Critical horizontal load of the portal frame of § 5.3.5 vs. out-of-plane rotational stiffness at the beam-column joints (K_{zB}) for $K_{yB} = 450$ kNm/rad and different values of the base-warping restraint stiffness ($K_{\Psi A}$). Thick solid and dash-dot lines are sections of Figs. 5.20 and 5.21, respectively. Letters a and b correspond to the buckling shapes shown in Fig. 5.23.
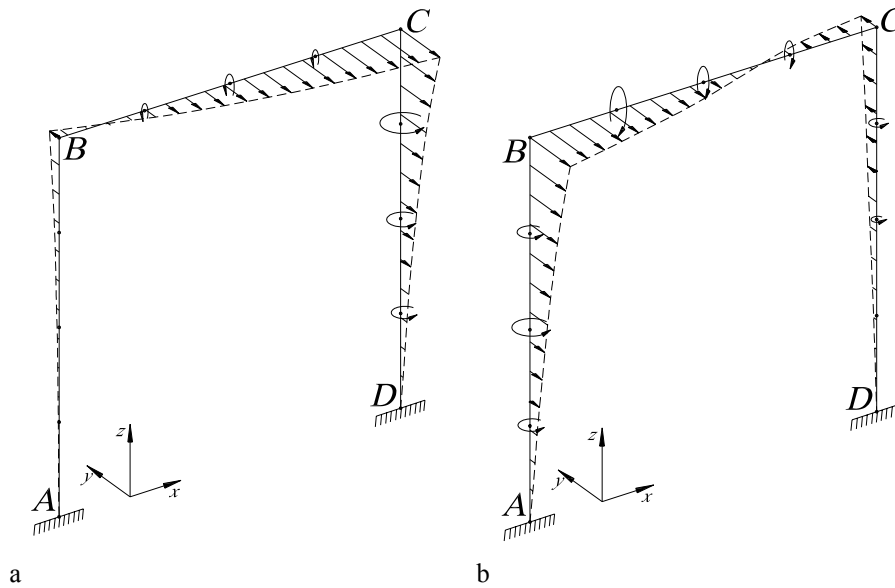
Figure 5.23. Buckling shapes of the portal frame of § 5.3.5 with no lateral bracing ($K_{brB} = 0$) and free base-warping displacements ($K_{\Psi A} = 0$). a: $K_{zB} < 2$ kNm/rad (curve a of Fig. 5.22). b: $K_{zB} > 2$ kNm/rad (curve b of Fig. 5.22).
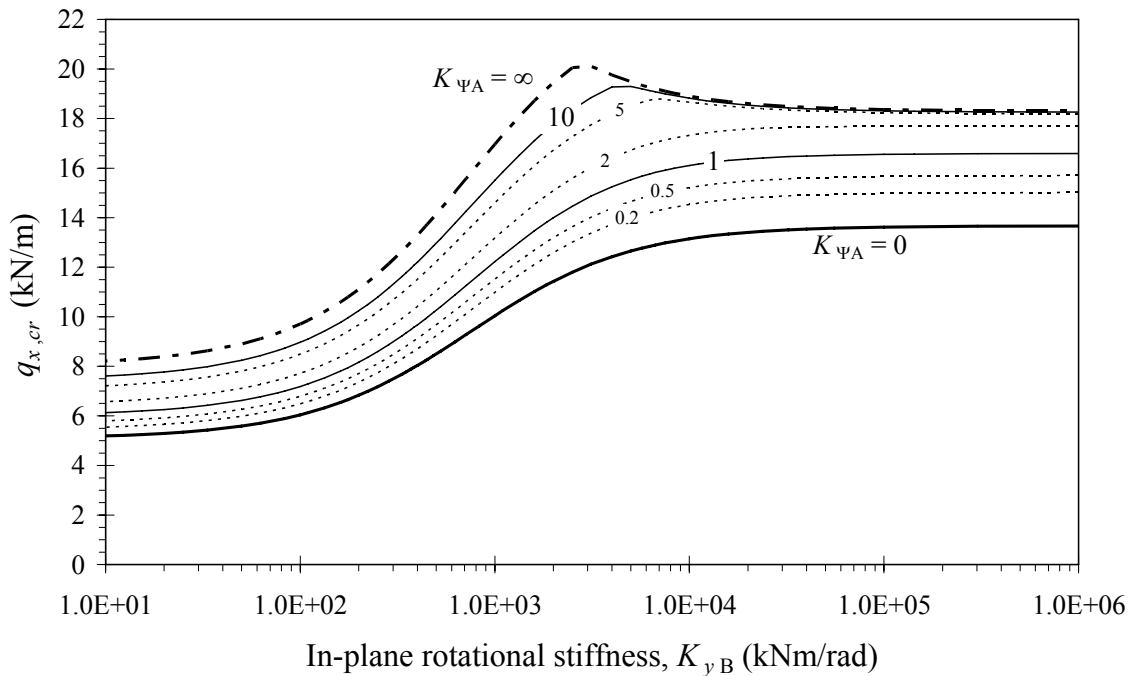
Figure 5.24. Critical horizontal load of the portal frame of § 5.3.5 vs. in-plane rotational stiffness at the beam-column joints (K_{yB}) for $K_{zB} = 100$ kNm/rad and different values of the base-warping restraint stiffness ($K_{\Psi A}$). Thick solid and dash-dot lines are sections of Figs. 5.20 and 5.21, respectively.
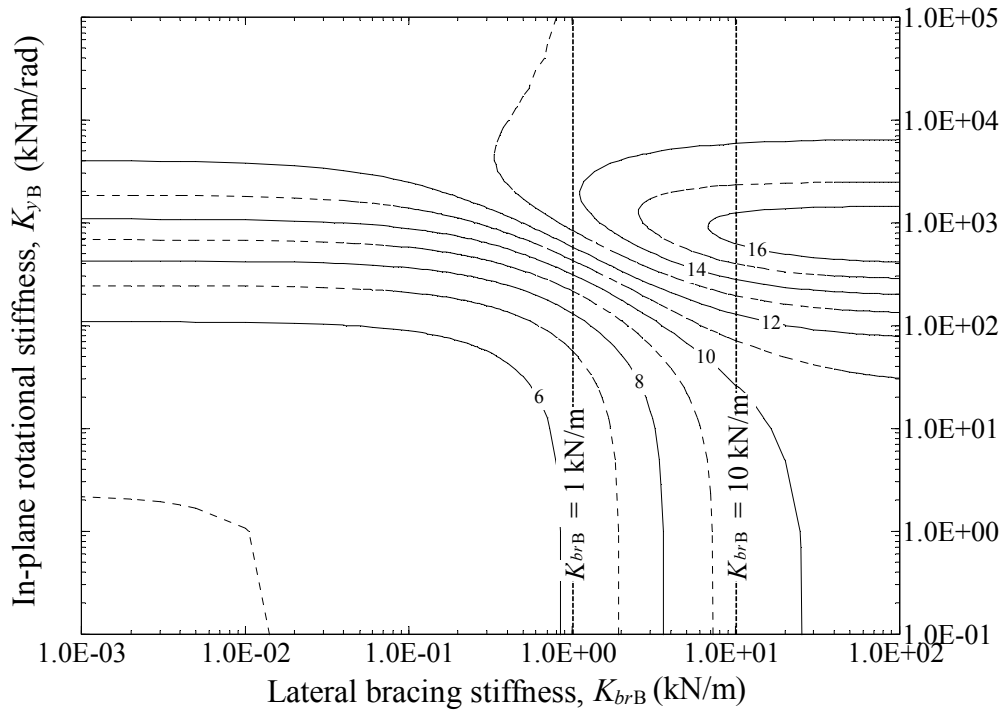
Figure 5.25. Portal frame of § 5.3.6 with unrestrained base-warping ($K_{\Psi A} = 0$) and out-of-plane rotational stiffness at the beam-column joints $K_{zB} = 10$ kNm/rad. Level curves of the buckling horizontal load vs. in-plane rotational stiffness (K_{yB}) and lateral bracing stiffness (K_{brB}) at the beam-column joints.
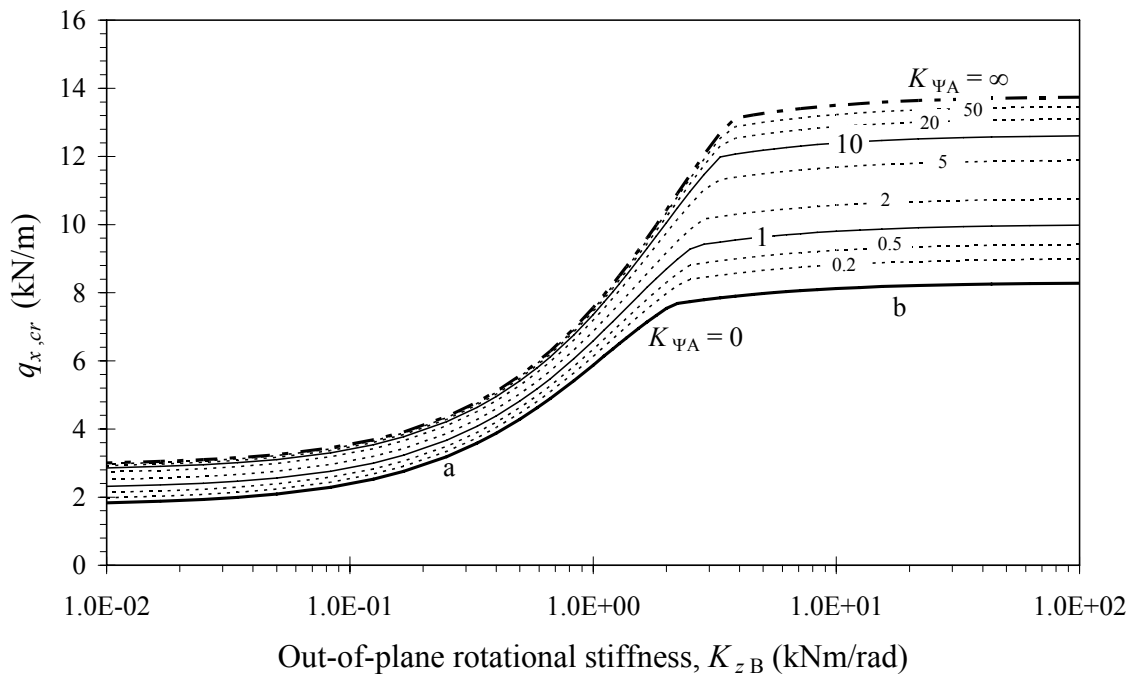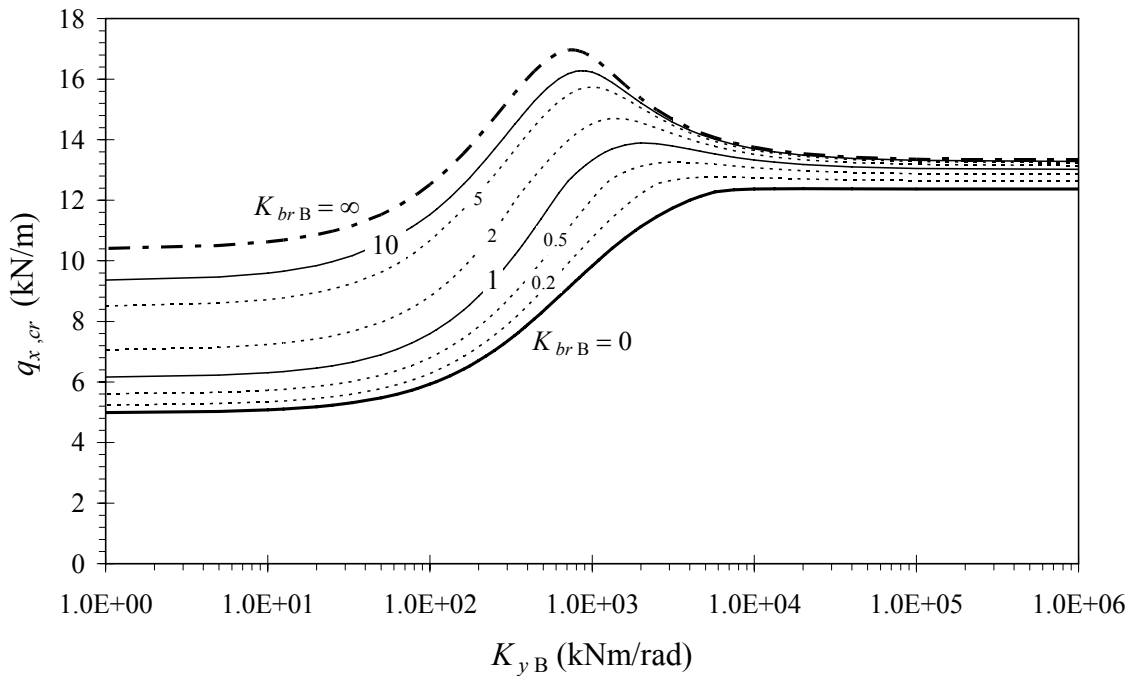

Figure 5.26. Critical horizontal load of the portal frame of § 5.3.6 vs. in-plane rotational stiffness at the beam-column joints (K_{yB}) for $K_{zB} = 10$ kNm/rad and $K_{\Psi A} = 0$. Sections of the level curves of Fig. 5.25 for different values of the lateral bracing stiffness (K_{brB}).
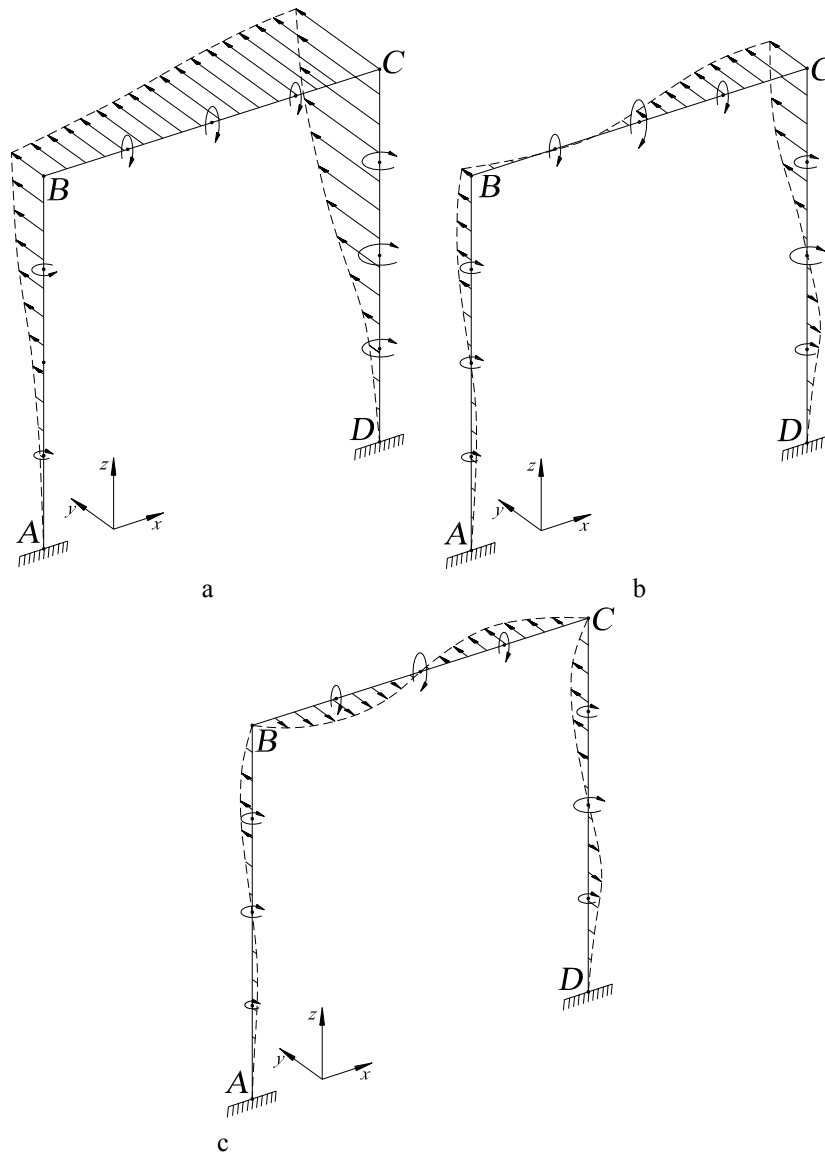
Figure 5.27. Buckling shapes of the portal frame of § 5.3.6 with in-plane rotational stiffness at the beam-column joints $K_{yB} = 2 \cdot 10^3$ kNm/rad. a: no lateral bracings ($K_{brB} = 0$). b: deformable lateral bracings ($K_{brB} = 10$ kN/m). c: rigid lateral bracings ($K_{brB} \to \infty$).

5.3.6 Critical horizontal load for deformable lateral bracings

The last example is aimed at evaluating the influence of deformable lateral bracings at joints B and C. In Figure 5.25, the level curves of the buckling horizontal load $q_{x,cr}$ versus in-plane rotational stiffness (K_{yB}) and lateral bracing stiffness (K_{brB}) are reported. In particular, semirigid out-of-plane beam-column joints ($K_{zB} = 10$ kNm/rad) and no base-warping constraints ($K_{\Psi A} = 0$) are assumed. Sections of the contour plot of Figure 5.25 for different values of K_{brB} are reported in Figure 5.26 for K_{yB} ranging between 1 and 10^6 kNm/rad. It should be observed that, for $K_{yB} \leq 1 \cdot 10^3$ kNm/rad, even small bracing stiffness values strongly increase the buckling load with respect to the unbraced

case (+88% for K_{brB} = 10 kN/m at K_{yB} = 10 kNm/rad). Figure 5.27 shows the buckling shapes corresponding to in-plane rotational stiffness K_{yB} = 2 · 10^3 kNm/rad and lateral bracing stiffness K_{brB} = 0, 10, ∞.

5.4 Second-order analysis

The formulation presented in Section 5.2 can easily be implemented for a nonlinear stability analysis, provided that Eq. 5.6 is rewritten in the following incremental form (Shakourzadeh *et al.* 1999):

$$\Delta \mathbf{r}_e = \mathbf{C} \mathbf{K}_T^e \Delta \overline{\mathbf{q}}_e - \mathbf{C} \mathbf{f}_e \tag{5.9}$$

where $\Delta \mathbf{r}_e$ is the increase of nodal element forces and $\Delta \overline{\mathbf{q}}_e$ represents the change of nodal displacements. Matrix $\mathbf{K}_T^e = \mathbf{K}_E^e + \mathbf{K}_G^e$ in Eq. 5.9 is the tangent stiffness matrix given, for each load increment, by the sum of elastic and geometric stiffness matrices. Matrix $\mathbf{C}$ takes now the form:

$$\mathbf{C} = \mathbf{K}_J \left(\mathbf{K}_J + \mathbf{K}_T^e \right)^{-1} = \left(\mathbf{I} + \mathbf{K}_T^e \mathbf{K}_J^{-1} \right)^{-1} \tag{5.10}$$

and $\overline{\mathbf{K}}_T^e = \mathbf{C} \mathbf{K}_T^e$ represents the modified tangent stiffness matrix accounting for the joint deformability. It is to be underlined that the method described is quite general, since any given joint constitutive relation may be implemented.

For example purposes, the GFRP pultruded frame of Figure 5.28a, subjected to two vertical point forces at the column tops, is analyzed. The horizontal force acting at node B simulates an imperfection. Rigid lateral bracings act at nodes B and C. A finite element model of the frame is built using four $H32$ elements per each member.
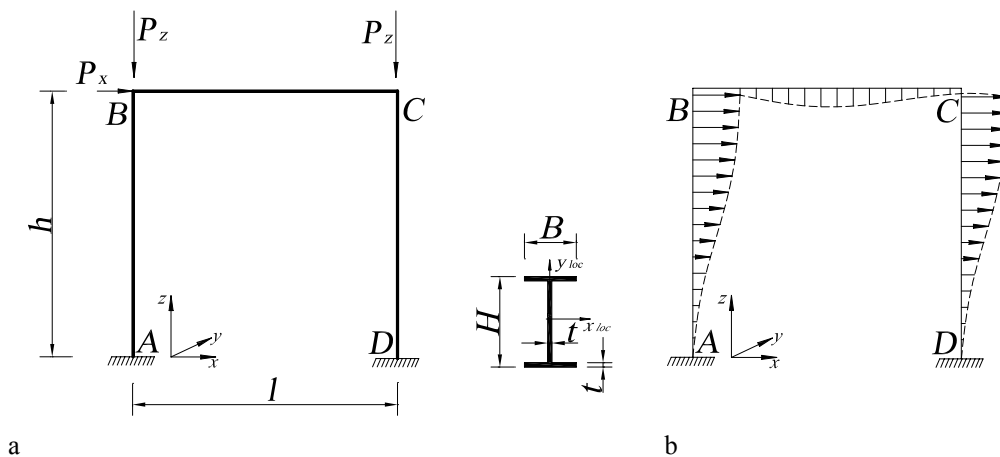
Figure 5.28. a: GFRP pultruded portal frame (E = 25 GPa, G = E/10) with l = 4.0 m, h = 3.0 m. Rigid lateral bracings are present at nodes B and C. Wide-flange profiles with H = B = 203.2 mm, t = 9.5 mm, $x_{loc(\text{beam})}$ // $x_{loc(\text{columns})}$ // y. Initial imperfection: P_x = 5 · 10^{-3} kN. b: instability mode.
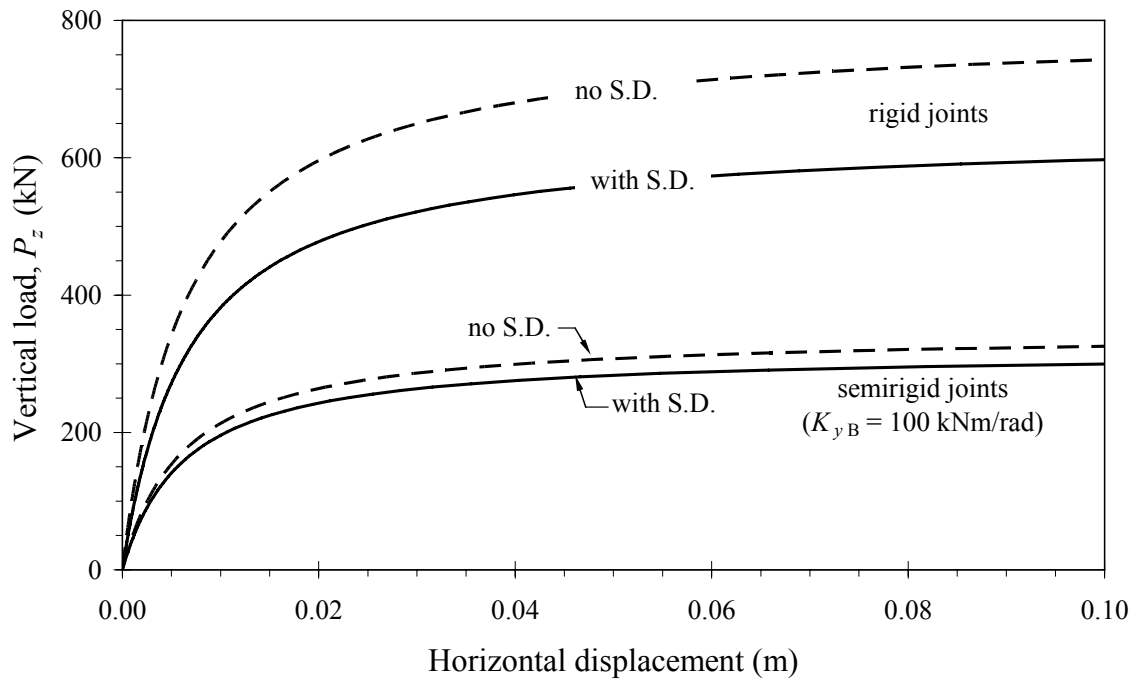
Figure 5.29. Vertical load vs. horizontal deflection for the GFRP portal frame of Fig. 5.28. Results including shear deformations (S.D.) or not. Comparison between rigid and semirigid joints.

The second-order stability analysis for increasing vertical forces is carried out by adopting an incremental-iterative Newton-Raphson procedure arrested as soon as the global tangent stiffness matrix becomes singular. Elastic and geometric stiffness matrices reported in Appendix 5.A and 3.A, respectively, are adopted. Two cases are solved, assuming rigid and semirigid (K_{yB} = 100 kNm/rad) joints. In particular, instability is ruled by the in-plane frame antisymmetrical deflection (Fig. 5.28b). The results in terms of applied vertical loads versus horizontal displacement of nodes B and C are reported in Figure 5.29. For comparison purposes, the corresponding plots obtained by neglecting shear deformations are also reported.

5.5 Conclusions

The buckling behaviour of frames composed by thin-walled FRP pultruded profiles with semirigid end connections was analyzed. The beam displacement field presented in Chapter 3, based on the second-order approximation of the finite rotation tensor and accounting for the shear deformations due to both nonuniform bending and torsion, was adopted. Resort to *locking-free* finite elements *H*32 (§ 2.2.1) was made to interpolate the displacement functions unknown. In order to take the joint flexibility into account, an efficient and quite general numerical procedure was implemented. The method consists of a simple manipulation of the element elastic stiffness matrix, so that no additional connection elements are required. In particular, connection semirigid behaviour due to axial, bending, torsion and cross-section warping effects can be easily modelled.

Moreover, neglecting shear deformations and non-uniform torsion, the modified stiffness matrix obtained (see Appendix 5.A) reduces to the well known matrix of Monforton and Wu (1963). Several examples showed the influence of joint flexibility on linear buckling analyses of GFRP portal frames subjected to in-plane horizontal or vertical loads uniformly distributed along the beam. It was observed that, for increasing out-of-plane rotational stiffness of the beam-column joints, sudden exchanges of the buckling shape occur: in particular, for unbraced frames under vertical load, it gets on from a prevailing flexural-torsional instability of the beam to the in-plane frame antisymmetrical deflection. Furthermore, in the case of horizontally-loaded frames, even a small base-warping restraint stiffness may significantly increase the buckling load. Finally, it was shown that the critical horizontal load is not a monotonic function of the in-plane rotational stiffness at the beam-column joints.

By rewriting the equilibrium equations in incremental form, the procedure described can be used to analyze the non-linear geometric behaviour of shear-deformable beam assemblages with any given joint constitutive law.

Appendix 5.A – Modified stiffness matrix of element *H*32

5.A.1 Modified stiffness matrix for semirigid warping and flexural connections

For a beam having a non-symmetric cross-section and generic end connections, the modified stiffness matrix $\bar{\mathbf{K}}_E^e$ can be represented in the form (superscript "*e*" omitted for simplicity):

$$\bar{\mathbf{K}}_E = \mathbf{C}\mathbf{K}_E = \begin{bmatrix} \bar{\mathbf{K}}_\mathbf{w} & \bar{\mathbf{K}}_\mathbf{wu} & \bar{\mathbf{K}}_\mathbf{wv} & \bar{\mathbf{K}}_\mathbf{w\omega} \\ & \bar{\mathbf{K}}_\mathbf{u} & \bar{\mathbf{K}}_\mathbf{uv} & \bar{\mathbf{K}}_\mathbf{u\omega} \\ & & \bar{\mathbf{K}}_\mathbf{v} & \bar{\mathbf{K}}_\mathbf{v\omega} \\ \text{Sym} & & & \bar{\mathbf{K}}_\mathbf{\omega} \end{bmatrix} \qquad (5.A.1)$$

Assuming uncoupled joint constitutive relations (Eq. 5.5) yields $\bar{\mathbf{K}}_\mathbf{wu}\left(=\bar{\mathbf{K}}_\mathbf{uw}\right)$ $=\bar{\mathbf{K}}_\mathbf{wv}\left(=\bar{\mathbf{K}}_\mathbf{vw}\right)=\bar{\mathbf{K}}_\mathbf{w\omega}\left(=\bar{\mathbf{K}}_\mathbf{\omega w}\right)=\mathbf{0}$. Moreover, the remaining off-diagonal submatrices vanish if doubly-symmetric cross-sections are considered (see Appendix 2.A). Finally, assuming K_{wi}, K_{ui}, K_{vi}, $K_{zi} \to \infty$ in Eq. 5.5, deformable joints for flexural rotations and warping displacements, and adopting the *locking-free* Hermitian formulation *H*32 reported in § 2.2.1 (linear functions for axial displacement), matrix $\bar{\mathbf{K}}_E^e$ takes the form:

$$\bar{\mathbf{K}}_E = \mathbf{C}\mathbf{K}_E = \text{diag}\left\{\bar{\mathbf{K}}_\mathbf{w}, \bar{\mathbf{K}}_\mathbf{u}, \bar{\mathbf{K}}_\mathbf{v}, \bar{\mathbf{K}}_\mathbf{\omega}\right\} \qquad (5.A.2)$$

where

$\overline{\mathbf{K}}_{\mathbf{w}} = \mathbf{K}_{\mathbf{w}}$ (see Eq. 2.A.2), $\qquad\qquad$ (5.A.3)

matrix $\overline{\mathbf{K}}_{\mathbf{u}}$ is given by:

$$\overline{K}_{\mathbf{u},11} = \overline{K}_{\mathbf{u},33} = -\overline{K}_{\mathbf{u},13} = 12EJ_y \left[EJ_y \left(K_{y1} + K_{y2} \right) + K_{y1}K_{y2}l \right] \big/ D_{\mathbf{u}}l^2 \qquad (5.A.4)$$

$$\overline{K}_{\mathbf{u},12} = -\overline{K}_{\mathbf{u},23} = 6EJ_y K_{y1} \left(2EJ_y + K_{y2}l \right) \big/ D_{\mathbf{u}}l \qquad (5.A.5)$$

$$\overline{K}_{\mathbf{u},22} = EJ_y K_{y1} \left[12EJ_y + K_{y2}l \left(4 + \phi_x \right) \right] \big/ D_{\mathbf{u}} \qquad (5.A.6)$$

$$\overline{K}_{\mathbf{u},24} = -EJ_y K_{y1} K_{y2}l \left(-2 + \phi_x \right) \big/ D_{\mathbf{u}} \qquad (5.A.7)$$

where:

$$D_{\mathbf{u}} = l^2 \left[12E^2 J_y^2 + K_{y1}K_{y2}l^2 \left(1 + \phi_x \right) + EJ_y l \left(K_{y1} + K_{y2} \right) \left(4 + \phi_x \right) \right] \qquad (5.A.8)$$

The terms $\overline{K}_{\mathbf{u},14} \left(= -\overline{K}_{\mathbf{u},34} \right)$ and $\overline{K}_{\mathbf{u},44}$ are obtained from $\overline{K}_{\mathbf{u},12}$ and $\overline{K}_{\mathbf{u},22}$, respectively, exchanging coefficients K_{y1} and K_{y2} with each other.

Matrix $\overline{\mathbf{K}}_{\mathbf{v}}$ is obtained from $\overline{\mathbf{K}}_{\mathbf{u}}$ by changing the sign of the terms whose indices give an odd summation integer and performing the substitutions $\phi_x \to \phi_y$, $J_x \to J_y$ and $K_{yi} \to K_{xi}$ ($i = 1, 2$).

Matrix $\overline{\mathbf{K}}_{\boldsymbol{\omega}}$ is given by:

$$\overline{K}_{\boldsymbol{\omega},11} = \overline{K}_{\boldsymbol{\omega},33} = -\overline{K}_{\boldsymbol{\omega},13} = N_{\boldsymbol{\omega},11} \big/ D_{\boldsymbol{\omega}}l^2 \qquad (5.A.9)$$

$$\overline{K}_{\boldsymbol{\omega},12} = -\overline{K}_{\boldsymbol{\omega},23} = N_{\boldsymbol{\omega},12} \big/ D_{\boldsymbol{\omega}}l \qquad (5.A.10)$$

$$\overline{K}_{\boldsymbol{\omega},22} = N_{\boldsymbol{\omega},22} \big/ D_{\boldsymbol{\omega}} \qquad (5.A.11)$$

$$\overline{K}_{\boldsymbol{\omega},24} = N_{\boldsymbol{\omega},24} \big/ D_{\boldsymbol{\omega}} \qquad (5.A.12)$$

where:

$$\begin{aligned} N_{\boldsymbol{\omega},11} = {} & 720E^2 J_\omega^2 \left(K_{\Psi 1} + K_{\Psi 2} + GJ_t l \right) \left(1 + \phi_\omega \right) \\ & + 12EJ_\omega l \left[GJ_t l \left(26K_{\Psi 2} + 6GJ_t l + 30K_{\Psi 2}\phi_\omega + 5GJ_t l\phi_\omega + 5K_{\Psi 2}\phi_\omega^2 \right) \right. \\ & \left. + K_{\Psi 1} \left(60K_{\Psi 2} + 26GJ_t l + 60K_{\Psi 2}\phi_\omega + 30GJ_t l\phi_\omega + 5GJ_t l\phi_\omega^2 \right) \right] \end{aligned}$$

$$+ GJ_t l^3 \Big[GJ_t l \left(9K_{\Psi 2} + GJ_t l + 10K_{\Psi 2}\phi_\omega + 5K_{\Psi 2}\phi_\omega^2 \right)$$
$$+ K_{\Psi 1} \left(72K_{\Psi 2} + 9GJ_t l + 120K_{\Psi 2}\phi_\omega + 10GJ_t l\phi_\omega + 60K_{\Psi 2}\phi_\omega^2 + 5GJ_t l\phi_\omega^2 \right) \Big] \tag{5.A.13}$$

$$N_{\omega,12} = -K_{\Psi 1} \Big[12EJ_\omega + l\left(6K_{\Psi 2} + GJ_t l \right) \Big] \Big[GJ_t l^2 + 60EJ_\omega \left(1 + \phi_\omega \right) \Big] \tag{5.A.14}$$

$$N_{\omega,22} = K_{\Psi 1} \Big[720E^2 J_\omega^2 \left(1 + \phi_\omega \right) + GJ_t l^3 \left(8K_{\Psi 2} + GJ_t l + 10K_{\Psi 2}\phi_\omega + 5K_{\Psi 2}\phi_\omega^2 \right)$$
$$+ 12EJ_\omega l \left(20K_{\Psi 2} + 6GJ_t l + 25K_{\Psi 2}\phi_\omega + 5GJ_t l\phi_\omega + 5K_{\Psi 2}\phi_\omega^2 \right) \Big] \tag{5.A.15}$$

$$N_{\omega,24} = -K_{\Psi 1}K_{\Psi 2}l \Big[60EJ_\omega \left(-2 - \phi_\omega + \phi_\omega^2 \right) + GJ_t l^2 \left(2 + 10\phi_\omega + 5\phi_\omega^2 \right) \Big] \tag{5.A.16}$$

$$D_\omega = 720E^2 J_\omega^2 \left(1 + \phi_\omega \right) + 12EJ_\omega l \Big[20K_{\Psi 2} + 6GJ_t l + 25K_{\Psi 2}\phi_\omega + 5GJ_t l\phi_\omega$$
$$+ 5K_{\Psi 2}\phi_\omega^2 + 5K_{\Psi 1} \left(4 + 5\phi_\omega + \phi_\omega^2 \right) \Big]$$
$$+ l^2 \Big[GJ_t l \left(8K_{\Psi 2} + GJ_t l + 10K_{\Psi 2}\phi_\omega + 5K_{\Psi 2}\phi_\omega^2 \right)$$
$$+ K_{\Psi 1} \left(60K_{\Psi 2} + 8GJ_t l + 120K_{\Psi 2}\phi_\omega + 10GJ_t l\phi_\omega + 60K_{\Psi 2}\phi_\omega^2 + 5GJ_t l\phi_\omega^2 \right) \Big] \tag{5.A.17}$$

The terms $\bar{K}_{\omega,14} \left(= -\bar{K}_{\omega,34} \right)$ and $\bar{K}_{\omega,44}$ are obtained from $\bar{K}_{\omega,12}$ and $\bar{K}_{\omega,22}$, respectively, exchanging coefficients $K_{\Psi 1}$ and $K_{\Psi 2}$ with each other.

It should be noted that pinned connections can be easily obtained by setting equal to zero the joint stiffness corresponding to the degrees of freedom to be released; on the contrary, matrix $\bar{K}_E$ reduces to the matrix of $H32$ finite element reported in Appendix 2.A in the case of rigid joints.

5.A.2 Simplified form in the absence of shear deformations

Assuming semirigid end connections for flexural rotations only and neglecting shear deformations ($\phi_x = \phi_y = 0$, see Eqs. 2.14, 2.17), modified submatrix $\bar{K}_u$ ($\bar{K}_v$) of Eq. 5.A.1 reduces to the well-known matrix of Monforton and Wu (1963), recently reported by Xu (2005). In fact, with reference, for example purposes, to bending into x-z plane, the condition $\phi_x = 0$ yields:

$$\bar{K}_u = K_u^{EB} C^{MW} \tag{5.A.18}$$

where K_u^{EB}, obtained from Eq. 2.A.3, represents the stiffness matrix of the classical Euler-Bernoulli element with rigid end-connections and C^{MW} is a correction matrix accounting for semirigid end rotations given by:

$$\mathbf{C}^{MW} = \frac{1}{l\left(4 - r_{y1}r_{y2}\right)} \begin{bmatrix} C_{11} & C_{12} & 0 & 0 \\ C_{21} & C_{22} & 0 & 0 \\ 0 & 0 & C_{33} & C_{34} \\ 0 & 0 & C_{21} & C_{44} \end{bmatrix} \tag{5.A.19}$$

where:

$$C_{11} = l\left(4r_{y2} - 2r_{y1} + r_{y1}r_{y2}\right) \tag{5.A.20}$$

$$C_{12} = -2l^2 r_{y1}\left(1 - r_{y2}\right) \tag{5.A.21}$$

$$C_{21} = 6\left(r_{y1} - r_{y2}\right) \tag{5.A.22}$$

$$C_{22} = 3lr_{y1}\left(2 - r_{y2}\right) \tag{5.A.23}$$

Moreover, coefficients C_{33} and C_{44} are obtained from C_{11} and C_{22}, respectively, exchanging r_{y1} and r_{y2} with each other, coefficient C_{34} is obtained from C_{12} changing the sign and exchanging r_{y1} and r_{y2} with each other and, finally, coefficients r_{yi} ($i = 1, 2$), representing the so-called "end fixity factors", are defined as:

$$r_{yi} = \left(1 + 3EJ_y \big/ K_{yi}l\right)^{-1} \tag{5.A.24}$$

References

Abramovich H. Natural frequencies of Timoshenko beams under compressive axial loads. *J. Sound Vibr*. 1992; **157**: 183-189.

Abramovich H and Ekishakoff I. Influence of shear deformation and rotatory inertia on vibration frequencies via Love's equations. *J. Sound Vibr*. 1990; **137**: 516-522.

Argyris JH, Dunne PC and Scharpf DW. On large displacement-small strain analysis of structures with rotational degrees of freedom. *Comput. Meths. Appl. Mech. Engng*. 1978; **14**: 401-451; ibid., 1978; **15**: 99-136.

Argyris JH et al. Finite element method—the natural approach. *Comput. Meths. Appl. Mech. Engng*. 1978; **17/18**: 1-106.

Argyris JH. Nonlinear finite element analysis of elastic systems under nonconservative loading—natural formulation. Part I. Quasistatic problems. *Comput. Meths. Appl. Mech. Engng*. 1981; **26**: 75-123.

Argyris JH. An excursion into large rotations. *Comput. Meths. Appl. Mech. Engng*. 1982; **32**: 85-155.

Aristizábal-Ochoa JD. Elastic stability and second-order analysis of three dimensional frames: effects of column orientation. *J. Eng. Mech. ASCE* 2003; **129**: 1254-1267.

Aristizábal-Ochoa JD. Column stability and minimum lateral bracing: effects of shear deformations. *J. Eng. Mech. ASCE* 2004; **130**: 1223-1232.

Aristizábal-Ochoa JD. Tension and compression stability and second-order analyses of three-dimensional multicolumn systems: effects of shear deformations. *J. Eng. Mech. ASCE* 2007; **133**: 106-116.

Bachmann H. Lively' footbridges – a real challenge. *Footbridge First International Conference*, Paris, 2002.

Back SY and Will KM. A shear-flexible element with warping for thin-walled open beams. *Int. J. Numer. Meth. Engng*. 1998; **43**: 1173-1191.

Baldacci R. *Fondamenti di meccanica dei solidi*. Utet, Torino, 1983.

Banerjee JR. Explicit modal analysis of an axially loaded Timoshenko beam with bending-torsion coupling. Journal of Applied Mechanics. 2000; 67: 307-313.

Banerjee JR, Guo S and Howson WP. Exact dynamic stiffness matrix of a bending-torsion coupled beam including warping. *Comput. Struct.* 1996; **59**: 613-621.

Bank LC. Shear coefficient for thin-walled composite beams. *Compos. Struct.* 1987; **8**: 47-61.

Bank LC, Mosallam AD and Gonsoir HE. Beam-to-column connections for pultruded FRP structures. *Serviceability and Durability of Constr. Mat. Proc., 1st Mat. Engrg. Congr.*, B. Suprenant, ed., ASCE 1990; Va.: 804-813.

Bank LC, Mosallam AD and McCoy GT. Design and performance of connections for pultruded frame structures. *J. Reinf. Plast. Comp.* 1994; **13**: 199-212.

Barbero EJ and DeVivo L. Beam-column design equations for wide-flange pultruded structural shapes. *Journal of Composites for Construction*. 1999; **3**: 185-191.

Barbero EJ and Malek T. Experimental Investigation of the beam-column behaviour of pultruded structural shapes. *J. Reinf. Plast. Comp.* 2000; **19**: 249-265.

Barbero EJ, Dede EK and Jones S. Experimental verification of buckling-mode interaction in intermediate-length composite columns. *Int. J. Solids Struct.* 2000; **37**: 3919-3934.

Barsoum RS and Gallagher RH. Finite element analysis of torsional-flexural stability problems. *Int. J. Numer. Meth. Engng.* 1970; **2**: 335-352.

Bauchau OA. A beam theory for anisotropic materials. *J. Appl. Mech. ASME* 1985; **52**: 416-422.

Bazant ZP and Cedolin L. *Stability of structures*. Oxford University Press, New York, 1st ed., 1991.

Bazoune A, Khulief YA and Stephen NG. Shape functions of three-dimensional Timoshenko beam element. *J. Sound Vibr.* 2003; **259(2)**: 473-480.

Bert C. Simplified analysis of static shear factors for beams of nonhomogeneous cross section. *J. Compos. Mat.* 1973; **7**: 525-529.

Blandford GE. Stability analysis of flexibly connected thin-walled space frames. *Comput. Struct.* 1994; **54**: 839-847.

Bokaian A. Natural frequencies of beams under compressive axial loads. *J. Sound Vibr.* 1988; **126**: 49-65.

Bokaian A. Natural frequencies of beams under tensile axial loads. *J. Sound Vibr.* 1990; **142**: 481-498.

Brooks RJ and Turvey GJ. Lateral buckling of FRP pultruded GRP I-section cantilevers. *Composite Structures*. 1995; **32**: 203-215.

Burgoyne CJ and Head PR. Aberfeldy bridge − An advanced textile reinforced footbridge. *TechTextil Symposium*, Frankfurt, 1993.

Capurso M. Sul calcolo delle travi di parete sottile in presenza di forze e distorsioni. Note I, II, III, IV. *La Ricerca Scientifica* 1964; **6**: 213-286 **7**: 5-106.

Capurso M. Influenza delle componenti di scorrimento nella deformazione delle travi di parete sottile con sezione aperta. *Giornale del Genio Civile* 1984; **122**: 127-144.

Carlberg RC, Blandford GE and Wang ST. Stability analysis of steel space frames with flexible connections and partial warping rigidity. *Proceedings of the SSRC Conference on the Stability of Bridges*. April 9-11, 1990, St. Louis, MO, 121-131.

Carrion JE, LaFave JM, and Hjelmstad KD. Experimental behaviour of monolithic composite cuff connections for fiber reinforced plastic box sections. *Compos. Struct.* 2005a; **67**: 333-345.

Carrion JE, Hjelmstad KD, and LaFave JM. Finite element study of composite cuff connections for pultruded box sections. *Compos. Struct.* 2005b; **70**: 153-169.

Chang S-P, Kim S-B and Kim M-Y. Stability of shear deformable thin-walled space frames and circular arches. *J. Eng. Mech. ASCE* 1996; **122**: 844-854.

Clark JW and Hill HN. Lateral buckling of beams. *Journal of the Structural Division*, ASCE. 1960; 86: 175-196.

CNR-DT 205/2007. Istruzioni per la Progettazione, l'Esecuzione ed il Controllo di Strutture realizzate con Profili Sottili Pultrusi di Materiale Composito Fibrorinforzato (FRP).

Corradi Dell'Acqua L. *Meccanica delle strutture*. Volume 1. *Il comportamento dei mezzi continui*. McGraw-Hill: Milano, 1992.

Corradi Dell'Acqua L. *Meccanica delle strutture*. Volume 3. *La valutazione della capacità portante*. McGraw-Hill: Milano, 1994.

Cortínez VH and Piovan MT. Vibration and buckling of composite thin-walled beams with shear deformability. *J. Sound Vibr.* 2002; **258**: 701-723.

Cortínez VH and Piovan MT. Stability of composite thin-walled beams with shear deformability. *Comput. Struct.* 2006; **84**: 978-990.

Cowper GR. The shear coefficient in Timoshenko's beam theory. *J. Appl. Mech.* 1966; **33**: 335-340.

Criesfield MA. *Non-linear finite element analysis of solid and structures*, volume 2: advanced topics. Wiley: Chichester, 1991.

Dallard P et al. London millennium bridge: pedestrian-induced lateral vibration. *Journal of Bridge Engineering.* 2001; **6**: 412-417.

Davalos JF, Qiao P and Salim HA. Flexural-torsional buckling of pultruded fiber reinforced plastic composite I-beams: experimental and analytical evaluations. *Comput. Struct.* 1997; **38**: 241-250.

De Lorenzis L and La Tegola A. Static behavior of pultruded fiber-reinforced polymer thin-walled beams. *Composite Structures* 2003a; **60**: 231-244.

De Lorenzis L and La Tegola A. A general approach to buckling of FRP pultruded profiles. *Proceedings of the International Conference Composites in Constructions.* Bios: Cosenza, 2003b.

De Lorenzis L and La Tegola A. Effect of applied stresses on global buckling of isotropic and transversely isotropic thin-walled members: theoretical analysis. *Composite Structures*. 2005; **68**: 339-348.

Dicuonzo A. Criteri di progetto per strutture realizzate con profili sottili pultrusi di materiale composito fibrorinforzato (FRP). Concezione strutturale, esecuzione e controllo di una struttura temporanea. PhD Thesis, University of Ferrara, 2008.

Dicuonzo A, Laudiero F, Maceri F, Minghini F and Tullini N. Design and construction of a temporary structure composed by FRP pultruded profiles. *4*[th] *International Conference on FRP Composites in Civil Engineering*, CICE, July 22-24, 2008, Zürich, accepted for presentation.

Eisenberger M. Derivation of shape functions for an exact 4 DOF Timoshenko beam element. *Commun. Num. Meth. Eng.* 1994; **10**: 673-681.

Eisenberger M. Dynamic stiffness vibration analysis using a higher-order beam model. *Int. J. Numer. Meth. Engng.* 2003; **57**: 1603-1614.

EN 1990:2002. Eurocode 0: Basis of structural design.

EN 1991-2:2003. Eurocode 1: Actions on structures - Part 2: Traffic loads on bridges.

Farchaly SH and Shebl MG. Exact frequency and mode shape formulae for studying vibration and stability of Timoshenko beam system. *J. Sound Vibr*. 1995; **180**: 205-227.

Feo L and Mancusi G. Modeling shear deformability of thin-walled composite beams with open cross-section. *Simulation Modelling Practice and Theory* 2005; in press.

Fiberline. *Design manual for structural profiles in composite materials*, Kolding, 2003.

Friedman Z and Kosmatka JB. An improved two-node Timoshenko beam finite element. *Comp. Struct.* 1993; **47**: 473-481.

Ghorbanpoor A and Omidvar B. Simplified analysis of thin-walled composite members. *J. Struct. Engng.* 1996; **122**: 1379-1383.

Ghugal YM and Shimpi RP. A review of refined shear deformation theories for isotropic and anisotropic laminated beams. *J. Reinf. Plast. Comp.* 2001; **20**: 255-272.

Giavotto V, Borri M, Mantegazza P, Ghiringhelli G, Carmaschi V, Maffioli G and Mussi F. Anisotropic beam theory and applications. *Comput. Struct.* 1983; **16**: 403-413.

Goto Y and Chen WF. On the computer-based design analysis for flexibly jointed frames. *J. Construct. Steel Research* 1987; **8**: 203-231.

Gunnlaugsson GA and Pedersen PT. A finite element formulation for beams with thin walled cross-section. *Comput. Struct.* 1982; **15**: 691-699.

Han SM, Benaroya H and Wei T. Dynamics of transversely vibrating beams using four engineering theories. *J. Sound Vibr*. 1999; **225**: 935-988.

Horgan CO. Recent developments concerning Saint-Venant's principle: an update. *Appl. Mech. Rev.* 1989; **42**: 295-303.

Horgan CO and Simmonds JG. Saint-Venant end effects in composite structures. *Composites Engng.* 1994; **4**: 279-286.

Howson WP and Williams FH. Natural frequencies of frames with axially loaded Timoshenko members. *J. Sound Vibr*. 1973; **26**: 503-515.

Hu Y, Jin X and Chen B. A finite element for static and dynamic analysis of thin-walled beams with asymmetric cross-sections. *Comput. Struct.* 1996; **61**: 897-908.

Hutchinson JR. Transverse vibrations of beams, exact versus approximate solutions. *J. Appl. Mech. ASME* 1981; **48**: 923-928.

Ibrahimbegović A. On FE implementation of geometrically nonlinear Reissner's beam theory: three-dimensional curved beam elements. *Comp. Meth. Appl. Mech. Eng.* 1993; **122**: 11-26.

Jones R. *Mechanics of composite materials.* McGraw-Hill: New York, 1975.

Keller T. Towards structural forms for composite fibre material. *Structural Engineering International* 1999: **9**.

Keller T. Fiber reinforced polymers in building construction. *Proceedings of International Association for Bridge and Structural Engineering Symposium, towards a better built environment*, Melobourne, 2002; CD-ROM.

Kim M-Y, Chang S-P and Kim S-B. Spatial stability and free vibration of shear flexible thin-walled elastic beams. I: analytical approach. *Int. J. Numer. Meth. Engng.* 1994; **37**: 4097-4115.

Kim M-Y, Chang S-P and Kim S-B. Spatial stability analysis of thin-walled space frames. *Int. J. Numer. Meth. Engng.* 1996; **39**: 499-525.

Kim M-Y, Chang S-P and Park H-G. Spatial postbuckling analysis of nonsymmetric thin-walled frames. I: theoretical considerations based on semitangential properties. *J. Eng. Mech. ASCE* 2001; **127**: 769-778.

Kim S-B and Kim M-Y. Improved formulation for spatial stability and free vibration of thin-walled tapered beams and space frames. *Eng. Struct*. 2000; **22**: 446-458.

Kim N-I and Kim M-Y. Exact dynamic/static stiffness matrices of non-symmetric thin-walled beams considering coupled shear deformation effects. *Thin-Wall. Struct.* 2005; **43**: 701-734.

Kim N-I, Shin DK and Kim M-Y. Exact lateral buckling analysis for thin-walled composite beam under end moment. *Engng. Struct*. 2007; **29**: 1739-1751.

Kim N-I, Shin DK and Kim M-Y. Improved flexural–torsional stability analysis of thin-walled composite beam and exact stiffness matrix. *Int. J. Mech. Sci.* 2007; **49**: 950-969.

Kollár LP and Springer GS. *Mechanics of composite structures*. Cambridge University Press: Cambridge, 2003.

Kollár LP. Flexural-torsional buckling of open section composite columns with shear deformation. *Int. J. Solids Struct.* 2001a; **38**: 7525-7541.

Kollár LP. Flexural-torsional vibration of open section composite beams with shear deformation. *Int. J. Solids Struct.* 2001b; **38**: 7543-7558.

Kosmatka JB. An improved two-node finite element for stability and natural frequencies of axial-loaded Timoshenko beams. *Comput. Struct.* 1995; **57**: 141-149.

Krenk S. *Lectures on thin-walled beams*. Department of Structural Engineering and Materials, Technical University of Denmark, 1998.

Laudiero F and Savoia M. Shear Strain Effects in Flexure and Torsion of Thin-walled-beams with Open or Closed Cross-section. *Thin-Wall. Struct.* 1990; **10**: 87-119.

Laudiero F and Zaccaria D. A consistent approach to linear stability of thin-walled beams of open section. *Int. J. Mech. Sci.* 1988a; **30**: 503-515.

Laudiero F and Zaccaria D. Finite element analysis of stability of thin-walled beams of open section. *Int. J. Mech. Sci.* 1988b; **30**: 543-557.

Lee J and Kim S-E. Flexural-torsional buckling of thin-walled I-section composites. *Comput. Struct.* 2001; **79**: 987-995.

Lee J and Kim S-E. Lateral buckling analysis of thin-walled laminated channel-section beams. *Comput. Struct.* 2002; **56**: 391-399.

Lee J, Kim S-E and Hong K. Lateral buckling of I-section composite beams. *Engng. Struct.* 2002; **24**: 955-964.

Leissa AW and So J. Comparisons of vibration frequencies for rods and beams from one-dimensional and three-dimensional analyses. *J. Acoust. Soc. Am* 1995; **98**: 2122-2135.

Lin ZM, Polyzois D and Shah A. Stability of Thin-walled Pultruded Structural Members by the Finite Element Method. *Thin-Wall. Struct.* 1996; **24**: 1-18.

Loughlan J and Ata M. The behaviour of open and closed section carbon fibre composite beams subjected to constrained torsion. *Composite Structures*. 1997; **1**: 631-647.

Lui EM and Chen WF. Analysis and behaviour of flexibly-jointed frames. *Eng. Struct.* 1986; **86**: 107-118.

Lui EM and Chen WF. Steel frame analysis with flexible joints. *J. Construct. Steel Research* 1987; **8**: 161-202.

Machado SP and Cortínez VH. Lateral buckling of thin-walled composite bisymmetric beams with prebuckling and shear deformations. *Engng. Struct.* 2005; **27**: 1185-1196.

Minghini F. Structural performances of arch FRP footbridges. *Footbridge Second International Conference*. Venice, 2005. CD-rom.

Minghini F, Tullini N and Laudiero F. Locking-free finite elements for shear deformable orthotropic thin-walled beams. *Int. J. Numer. Meth. Engng.* 2007; **72**: 808-834.

Minghini F, Tullini N and Laudiero F. Buckling analysis of FRP pultruded frames using locking-free finite-elements. *Thin-Wall. Struct.* 2008a; **46**: 223-241.

Minghini F, Tullini N and Laudiero F. Vibration analysis with second-order effects of FRP pultruded frames using locking-free elements, 2008b. Submitted for publication.

Minghini F, Tullini N, Laudiero F. Dynamic and buckling analysis of FRP portal frames using a locking-free finite element. *4th International Conference on FRP Composites in Civil Engineering*, CICE, July 22-24, 2008c, Zürich, accepted for presentation.

Monforton GR and Wu TS. Matrix analysis of semi-rigidly connected frames. *J. Struct. Eng. ASCE* 1963; **89**: 3713-3742.

Mosallam AD, Abdelhamid MK and Conway JH. Performance of pultruded FRP connections under static and dynamic loads. *J. Reinf. Plast. Comp.* 1994; **13**: 386-407.

Mottram JT and Aberle M. When should shear-flexible stability functions be used in elastic structural analysis?. *Proceedings of the Institution of Civil Engineers Structures & Buildings*. 2002; **152**: 31-40.

Mottram JT and Bass AJ. Moment-rotation behaviour of pultruded beam-to-column connections. *Proc. 12th ASCE Struct. Congr.*, ASCE 1994; Va.: 423-428.

Mottram JT and Zheng Y. State-of-the-art review on the design of beam-to-column connections. *Compos. Struct.* 1996; **35**: 387-401.

Mottram JT, Brown ND and Anderson D. Buckling characteristics of pultruded glass fibre reinforced plastic columns under moment gradient. *Thin-Wall. Struct.* 2003; **41**: 619-638.

Mottram JT. Determination of critical load for flange buckling in concentrically loaded pultruded columns. *Composites PartB: engineering*. 2004; **35**: 35-47.

Mukherjee S, Reddy JN and Krishnamoorthy CS. Convergence properties and derivative extraction of the superconvergent Timoshenko beam finite element. *Comput. Methods Appl. Mech. Engng.* 2001; **190**: 3475-3500.

Narayanaswami R and Adelman HM. Inclusion of transverse shear deformation in finite element displacement formulations. *AIAA Journal* 1974; **12**: 1613-1614.

Omidvar B. Shear coefficient in orthotropic thin-walled composite beams. *Journal of Composites for Construction ASCE* 1998; **2**: 46-56.

Ortúzar JM and Samartín A. Some consistent finite element formulations of 1-D beam models : a comparative study. *Adv. Engng. Soft.* 1998; **29**: 667-678.

Park SW, Fujii D and Fujiitani Y. A finite element analysis of discontinuous thin-walled beams considering non uniform shear warping deformation. *Comput. Struct.* 1997; **65**: 17-27.

Pecce M and Cosenza E. Local buckling curves for the design of FRP profiles. *Thin-Wall. Struct.* 2000; **37**: 207-222.

Pi Y-L and Bradford MA. Effects of approximations in analyses of beams of open thin-walled cross-section—part I: Flexural-torsional stability. *Int. J. Numer. Meth. Engng.* 2001; **51**: 757-772.

Pignataro M, Rizzi N and Luongo A. *Stabilità, biforcazione e comportamento postcritico delle strutture elastiche.* ESA, Roma, 1983.

Piovan MT and Cortínez VH. Mechanics of shear deformable thin-walled beams made of composite materials. *Thin-Wall. Struct.* 2007; **45**: 37-62.

Przemieniecki JS. *Theory of Matrix Structural Analysis*. McGraw-Hill: New York, 1968.

Qiao P, Zou G and Davalos JF. Flexural-torsional buckling of fiber-reinforced plastic composite cantilever I-beams. *Comput. Struct.* 2003; **60**: 205-217.

Reddy JN. *An introduction to the finite element method*. McGraw-Hill International Editions – Mathematics and Statistics Series, 1985.

Reddy JN. On locking-free shear deformable beam finite elements. *Comput. Methods Appl. Mech. Engng.* 1997; **149**: 113-132.

Reissner E. On non-uniform torsion of cylindrical rods. *J. Math. Phys.* 1952; **31**: 214-221.

Reissner E. A consistent treatment of transverse shear deformations in laminated anisotropic plates. *AIAA J.* 1972; **10**: 716.

Renton JD. A check on the accuracy of Timoshenko's beam theory. *J. Sound Vibr.* 2001; **245**: 559-561.

Roberts TM. Influence of shear deformation on buckling of pultruded fiber reinforced plastic profiles. *Journal of Composites for Construction ASCE*. 2002; **6**: 241-248.

Roberts TM and Al-Ubaidi H. Flexural and torsional properties of FRP pultruded fiber reinforced plastic I-profiles. *Journal of Composites for Construction ASCE* 2002; **6**: 28-34.

Roberts TM and Masri HM. Section properties and buckling behaviour of pultruded FRP profiles. *J. Reinf. Plast. Comp.* 2003; **22**: 1305-1317.

Rosenberg RM. *Analytical dynamics of discrete systems*. Plenum, New York, 2nd ed., 1980.

Rovira J, Ivorra S and Rovira J. Construction of a tower with pultruded FRP composites. *Journal of the International Association for Shell and Spatial Structures IASS* 2004; **45**: 109-117.

Sapkás Á and Kollár LP. Lateral-torsional buckling of composite beams. *Int. J. Solids Struct.* 2002; **39**: 2939-2963.

Savoia M and Tullini N. Torsional response of inhomogeneous and multilayered composite beams. *Composite Structures* 1993; **25**; 587-594.

Shakourzadeh H, Guo YQ and Batoz JL. A torsion bending element for thin-walled beams with open and closed cross sections. *Comput Struct* 1995a; **55**: 1045-1054.

Shakourzadeh H, Guo YQ, Batoz JL and Penserini P. On the non-linear elasto-plastic analysis of space frames undergoing large displacements. *Iran J. Sci. Technol.*, 1995; **19**: 219-232.

Shakourzadeh H, Guo YQ and Batoz JL. Modeling of connections in the analyses of thin-walled space frames. *Comput Struct* 1999; **71**: 423-433.

Sherbourne AN and Kabir MZ. Shear strain effects in lateral stability of thin-walled fibrous composite beams. *J. Eng. Mech. ASCE* 1995; **121**: 640-647.

Simo J.C. and Vu-Quoc L. A geometrically-exact rod model incorporating shear and torsion-warping deformation. *Int. J. Solids Structures*. 1991; **27**: 371-393.

Smith SJ, Parsons ID, and Hjelmstad KD. Experimental comparisons of connections for GFRP pultruded frames. *J. Compos. Constr.* 1999a; **3**: 20-26.

Smith SJ, Parsons ID, and Hjelmstad KD. Finite-element and simplified models of GFRP connections. *J. Struct. Eng. ASCE* 1999b; **125**: 749-756.

Sobrino JA and Pulido DG. A new glass-fiber reinforced-plastic footbridge. *Footbridge First International Conference*, Paris, 2002.

Song SJ and Waas AM. Effects of shear deformation on buckling and free vibration of laminated composite beams. *Composite Structures* 1997; **1**; 33-43.

SAP2000®. *Basic Analysis Reference Manual*. Computers and Structures, Inc: Version 9.0, Berkeley, 2004.

STRAUS7®. *Theoretical manual – theoretical background to the Straus7 finite element analysis system*. First edition, 2004.

Tanaka M and Bercin AN. Free vibration solution for uniform beams of nonsymmetrical cross section using Mathematica. *Comput. Struct.* 1999; **71**: 1-8.

Timoshenko SP. On the correction for shear of the differential equation for transverse vibrations of prismatic bars. *Phil. Mag.* 1921; **22**: 16-21.

Timoshenko SP. On the transverse vibrations of bars of uniform cross-section. *Phil. Mag.* 1922; **43**: 125-131.

Trahair NS. *Flexural-torsional buckling of structures*. E & FN SPON: London, 1993.

Tralli A. A simple hybrid model for torsion and flexure of thin-walled beams. *Comput. Struct.* 1986; **22**: 649-658.

Turvey GJ. Analysis of pultruded glass reinforced plastic beams with semi-rigid end connections. *Compos. Struct.* 1997; **38**: 3-16.

Turvey GJ and Cooper C. Review of tests on bolted joints between pultruded GRP profiles. *Proceedings of the Institution of Civil Engineers Structures & Buildings*. 2004; **157**: 211-233.

Vlasov ZZ. *Thin-walled elastic beams*. Israel Program for Scientific Translations: Jerusalem, 1961.

Vinson JR and Chou T-W. *Composite materials and their use in structures*. Applied Science Publishers: Ltd. London, 1975.

Volovoi VV, Hodges DH, Berdichevsky VL and Sutyrin VG. Asymptotic theory for static behaviour of elastic anisotropic I-beams. *Int. J. Solids Struct.* 1999; **36**: 1017-1043.

Washizu K. *Variational methods in elasticity and plasticity*. Pergamon Press, Oxford: 1982.

Xu L. *Semirigid frame structures*, in *Handbook of Structural Engineering, Chapter 23*, Second Edition, Chen WF and Lui EM (eds.), CRC Press, 2005.

Ziegler H. *Principles of structural stability*. Birkhäuser, Basel, 2nd ed., 1977.